molecules

Special Issue Reprint

Amphiphilic Molecules, Interfaces and Colloids

2nd Edition

Edited by
Plamen Tchoukov and Khristo Khristov

mdpi.com/journal/molecules

MDPI

Amphiphilic Molecules, Interfaces and Colloids: 2nd Edition

Amphiphilic Molecules, Interfaces and Colloids: 2nd Edition

Guest Editors

Plamen Tchoukov
Khristo Khristov

MDPI

Basel • Beijing • Wuhan • Barcelona • Belgrade • Novi Sad • Cluj • Manchester

Guest Editors
Plamen Tchoukov
Institute of Physical Chemistry
Bulgarian Academy of Sciences
Sofia
Bulgaria

Khristo Khristov
Institute of Physical Chemistry
Bulgarian Academy of Science
Sofia
Bulgaria

Editorial Office
MDPI AG
Grosspeteranlage 5
4052 Basel, Switzerland

This is a reprint of the Special Issue, published open access by the journal *Molecules* (ISSN 1420-3049), freely accessible at: https://www.mdpi.com/journal/molecules/special_issues/T9NBG8KT20.

For citation purposes, cite each article independently as indicated on the article page online and as indicated below:

Lastname, A.A.; Lastname, B.B. Article Title. *Journal Name* **Year**, *Volume Number*, Page Range.

ISBN 978-3-7258-8773-6 (Hbk)
ISBN 978-3-7258-8774-3 (PDF)
https://doi.org/10.3390/books978-3-7258-8774-3

© 2026 by the authors. Articles in this reprint are Open Access and distributed under the Creative Commons Attribution (CC BY) license. The reprint as a whole is distributed by MDPI under the terms and conditions of the Creative Commons Attribution-NonCommercial-NoDerivs (CC BY-NC-ND) license (https://creativecommons.org/licenses/by-nc-nd/4.0/).

Contents

About the Editors . . . . . **vii**

Plamen Tchoukov and Khristo Khristov
Amphiphilic Molecules, Interfaces and Colloids—2nd Edition
Reprinted from: *Molecules* **2026**, *31*, 2034, https://doi.org/10.3390/molecules31122034 . . . . . **1**

Saylor E. Blanco, Nathan Black, Margarita A. Alvarez, Kevin F. Morris, Mark A. Olson, Eugene J. Billiot and Fereshteh H. Billiot
Stereoisomeric Effects of Diammoniumcyclohexane Counterions on the Self-Assembly of Amino Acid-Based Surfactants
Reprinted from: *Molecules* **2025**, *30*, 4114, https://doi.org/10.3390/molecules30204114 . . . . . **5**

Remigiusz Zapolski, Monika Gasztych, Beata Jastrząb-Miśkiewicz, Alina Jankowska-Konsur and Witold Musiał
The Properties of the Monolayers of Sorbitan Lipids as Informative Factors on the Hydrophilic–Lipophilic Balance Value of Their Mixtures, Proposed for Dermatological Applications
Reprinted from: *Molecules* **2025**, *30*, 1841, https://doi.org/10.3390/molecules30081841 . . . . . **25**

Tatiana Slavova, Rumyana Stanimirova, Krastanka Marinova and Krassimir Danov
Cleansing Mechanisms and Efficacy on Artificial Skin
Reprinted from: *Molecules* **2025**, *30*, 1813, https://doi.org/10.3390/molecules30081813 . . . . . **39**

Joanna Kowalczuk, Oleg M. Demchuk, Mariusz Borkowski and Michał Bielejewski
Stabilisation of Nanosilver Supramolecular Hydrogels with Trisodium Citrate
Reprinted from: *Molecules* **2025**, *30*, 1613, https://doi.org/10.3390/molecules30071613 . . . . . **60**

Juan Doratt Mendoza, Jingwen Ding, Michelle Acosta Alvarez and Edgar Acosta
Yeast Viability in HLD–NAC-Designed Fully Dilutable Lecithin-Linker Microemulsions
Reprinted from: *Molecules* **2025**, *30*, 921, https://doi.org/10.3390/molecules30040921 . . . . . **76**

Iglika M. Dimitrova and Radomir I. Slavchov
Charge Regulation in Liquid Films Stabilized by Ionic Surfactants: Change in Adsorption with Film Thickness and Phase Transitions
Reprinted from: *Molecules* **2025**, *30*, 659, https://doi.org/10.3390/molecules30030659 . . . . . **102**

Joanna Le Thanh-Blicharz, Jacek Lewandowicz, Artur Szwengiel, Krystyna Prochaska, Hanna Maria Baranowska and Grażyna Lewandowicz
Insight into Oil-in-Water Emulsions Stabilized by Cross-Linked and Pregelatinized Starches: The Effect of Molecular Structure, Surface Activity and Proton Molecular Dynamics
Reprinted from: *Molecules* **2024**, *29*, 5626, https://doi.org/10.3390/molecules29235626 . . . . . **119**

Ryuju Suzuki, Keigo Kinoshita, Takeshi Miuchi, Masayuki Nishino, Yasuhiro Shimizu and Shigeru Deguchi
Exploring the Optical Properties of Carotenoid-Based Nanoparticles: The Role of Terminal Groups
Reprinted from: *Molecules* **2024**, *29*, 5456, https://doi.org/10.3390/molecules29225456 . . . . . **137**

About the Editors

Plamen Tchoukov

Plamen Tchoukov is an Associate Professor at the Institute of Physical Chemistry, Bulgarian Academy of Sciences. His current research interests focus on surface forces and stability mechanisms of emulsions, foams, and suspensions; the self-assembly of amphiphilic molecules; the application of green surfactants; oil-spill containment; functionalized colloidal systems for the delivery of bioactive agents; as well as colloidal and interfacial phenomena associated with CO_2 transport and storage pipelines. He holds an MSc degree in Physics from Sofia University and a PhD in Physical Chemistry from the Bulgarian Academy of Sciences, and continued his research as an NSERC Postdoctoral Visiting Fellow at Natural Resources Canada, and later as a Research Associate at the Department of Chemical and Materials Engineering, University of Alberta. He developed and applied state-of-the-art thin emulsion film instrumentation to study the stability of petroleum emulsions encountered during heavy oil extraction. This work contributed to a deeper understanding of the stability of water-in-crude oil emulsions, particularly the role of asphaltenes. Subsequently, in addition to his research on crude oil emulsions, he designed and built a novel Thin Film Force Apparatus (TFFA). This instrument enables the simultaneous measurement of film thickness profiles, bubble or droplet shape, contact angles, and interaction forces in thin liquid layers between approaching bubbles or droplets and solid surfaces. In addition to his academic work, Dr. Tchoukov has more than ten years of industrial experience in the development of specialty chemical formulations and in leading multidisciplinary teams addressing complex technological challenges.

Khristo Khristov

Khristo Khristov received his PhD in 1991 and, in 1993, he became Associate Professor at the Institute of Physical Chemistry, Bulgarian Academy of Sciences (IPC-BAS). He spent three years as visiting scientist (1997–1999; 2005–2006) at the University of Alberta, Edmonton, Canada. In 2008, Dr. Khristov became the Secretary of Scientific Council of IPC-BAS. He was a Member of the Organizing Committee of the IX International Conference on Surface and Colloid Science, 1997, Sofia, Bulgaria, and Scientific Secretary of Nanoscale Phenomena in Colloid and Interface Science Workshop (NPCIS 2007) in Plovdiv, Bulgaria. Dr. Khristov's scientific areas of interest include foam and foam films, emulsions and emulsion films, and dispersions stabilized by synthetic, polymeric, biopolymeric, and natural surfactants. While in the University of Alberta, he studied petroleum emulsions' properties and water/oil/water emulsion films, and acted as scientific adviser to two PhD students. He supervised three PhD students at the IPC-BAS. He was principal investigator on several international and national scientific projects, including with Oil Company ELF France, Syncrude-Canada, MaxPlanck Institute Germany, etc. Lately, he has been involved in studying the microrheological and microfluidic mechanical properties of blood cells. All these studies encompass more than 70 papers, including reviews in renown scientific journals (Q1 and Q2) and a book chapter in *Foam Films and Foams, Fundamentals and Applications* (2021, CRS Press) with over 1100 citations.

molecules

MDPI

Editorial

Amphiphilic Molecules, Interfaces and Colloids—2nd Edition

Plamen Tchoukov [1,2,*] and Khristo Khristov [1,*]

[1] Institute of Physical Chemistry, Bulgarian Academy of Sciences, "Acad. Georgi Bonchev" Str. Bl. 11, 1113 Sofia, Bulgaria
[2] National Centre of Excellence Mechatronics and Clean Technologies, 8 bul. Kliment Ohridski, 1756 Sofia, Bulgaria
* Correspondence: tchoukov@ipc.bas.bg (P.T.); khristov@ipc.bas.bg (K.K.)

1. Introduction

The relationship between the chemical structure and properties of amphiphilic molecules, their adsorption behavior and organization at interfaces, and the properties of colloidal systems are a primary research area for colloid chemistry, chemical engineering, and a wide range of industries, such as pharmaceuticals, food, resource extraction, and many others [1–3]. Studying the molecular structure–interfacial behavior relationships is also essential for understanding processes in living matter and the environment. The design of colloidal systems with the desired functionalities requires both knowledge of the interactions at the nano- and micro-scale level, and the thermodynamic state of the systems as a whole. In many processes of practical interest, the colloidal systems are far from equilibrium and dynamic properties, transient states, transport phenomena, and hydrodynamics are of interest. Besides the properties of interfaces, the colloidal stability is also governed by surface forces and drainage of thin liquid films between dispersed colloidal particles, which is strongly influenced by the mobility of the interfaces and Marangoni flows [4]. A wide range of experimental techniques, including interfacial, surface-force, optical, scattering, spectroscopic, and rheological, are typically employed to study different aspects of these complex systems.

There is increasing interest in the application of bio-based, sustainable and biodegradable amphiphilic molecules driven by increasing environmental awareness and new regulatory requirements [5]. Implementation of these new alternative chemistries, preferably derived from sustainable and renewable resources, requires extensive analytical and physicochemical characterization of their structure, behavior at the interfaces and in the bulk solutions.

Recently, it has become increasingly clear that the functionality of amphiphilic molecules is not determined solely by classical descriptors such as hydrophilic–lipophilic balance (HLB), critical micelle concertation (CMC), or packing parameters. Instead, their behavior is governed by the collective system free energy, which controls molecular self-assembly across multiple length and time scales. Computer simulations techniques like Molecular Dynamics (MD), Density Functional Theory (DFT), Dissipative Particle Dynamics (DPD), and AI-assisted generative models now make it possible to connect molecular architecture directly to properties such as adsorption, micellization, vesicle formation, interfacial rheology, thin-film stability, and transport properties.

This Reprint contains the collection of papers published in the Second Edition of the Special Issue of *Molecules* titled "Amphiphilic Molecules, Interfaces and Colloids". The presented collection includes research articles ranging from theoretical aspects of ionic effects on surface forces in thin liquid films, new green sustainable surfactants, and

insights into the relationship of molecular structure–interfacial–colloidal properties, to optimizations of cosmetic products and new testing procedures.

2. An Overview of the Contributions

Blanco et al. (Contribution 1) investigated the stereoisomeric effects of diammonium-cyclohexane (DACH) counterions on the self-assembly of amino acid-based surfactants (AAABs). Four AABSs derived from undecanoyl glycine, L-alanine, L-valine, and L-leucine were combined with six DACH counterions corresponding to the cis and trans isomers of 1,2-, 1,3-, and 1,4-DACH. Critical micelle concentrations and micelle sizes were determined by conductimetry and dynamic light scattering. The counterion binding degrees (β) were calculated to assess micelle stability and geometry-optimized DACH isomer structures were obtained using density functional theory (DFT). The authors found that, although the self-assembly tendencies followed the expected trend with increasing surfactant hydrophobicity, the trans-1,3-DACH counterion disrupted this trend, leading to higher CMCs values that were largely independent of the AABS side chain. The results highlight the important role of counterion structure in determining AABS behavior.

Zapolski et al. (Contribution 2) reported a thought-provoking correlation between HLB values of series of sorbitan esters (sorbitan monopalmitate, sorbitan tristearate, sorbitan monooleate, and sorbitan sesquioleate) and the parameters of the π–A Langmuir isotherm of their monolayers at water surface. The ratio between the slopes corresponding to the first and second stages of monolayer compression is determined and plotted against the calculated HLB values of the surfactants. A strong linear relationship is observed, with a coefficient of correlation 0.95.

Slavova et al. (Contribution 3) developed in vitro procedures using optical methods, artificial skin and model soils (sebum and dimethicone) for evaluation of the cleansing efficacy of formulations with applications in personal care. The authors conducted a systematic study on the soil removal mechanisms of formulations based on widely used in personal care surfactants disodium laureth sulfosuccinate (DSLSS), sodium laureth sulfate (SLES), sodium dodecyl sulfate (SDS), dodecyl trimethyl ammonium bromide (DTAB), and coco glucoside (CG). Nonionic CG removed dimethicone at a lower concentration than ionic surfactants. Combining CG with ionic surfactants improved cleaning at lower total concentrations. Two main mechanisms were outlined: emulsification and roll-up. The reported results have the potential for a direct application in product evaluation and the development process in the cosmetic industry.

Kowalczuk et al. (Contribution 4) reported positive synergetic effects of trisodium citrate (TSC) and silver nanoparticles (AgNPs) on the self-assembly of alanine derivative gelator (C12Ala) hydrogels. Thermal analysis (TGA/DSC), high-resolution nuclear magnetic resonance spectroscopy (HR-MAS NMR), and optical microscopy provided insights into the interactions and supramolecular assemblies of the studied three-component system. AgNPs alone disturb the C12Ala self-assembled structures; however, the presence of TSC molecules shields the gelator molecules from electrostatics interactions with the nanoparticles, allowing for the formation of stable hydrogels.

Mendoza et al. (Contribution 5) explored the application of self-microemulsifying delivery systems (SMEDS) formulated with a surfactant blend of lecithin (Le) and polyglycerol-10-caprylate (PG10C), which was mixed with ethyl oleate as an oil phase. This SMEDS was diluted with 0.9% w/v NaCl aqueous solution at different ratios and evaluated as a preservation media for dry instant yeast (Saccharomyces cerevisiae). The authors applied the hydrophilic–lipophilic difference and net-average curvature (HLD–NAC) model (available as an Excel-based tool) to predict the phase behavior of diluted SMEDS formulations.

https://doi.org/10.3390/molecules31122034

Dimitrova and Slavchov (Contribution 6) studied surface forces in thin liquid films (emulsion and foam films) stabilized by ionic surfactants and draining in a charge regulation regime, assuming the Davies isotherm charge regulation condition. The authors concluded that the thinning of a foam film can trigger a surface phase transition from a 2D liquid expanded state to a 2D gaseous state. This phase transition coincides with a simultaneous jump in the film thickness and the two different thickness states of the film could coexist in equilibrium. These theoretical predictions might serve as a guide for future experiments to confirm these effects.

Thanh-Blicharz et al. (Contribution 7) reported that the chemical and physical modification of starch leads to changes in the molecular structure, including an increase in molecular weight and the degree of branching, which in turn affect its to adsorption behavior at the water/oil interface, rheological properties, and consequently its ability to stabilize emulsions.

Suzuki et al. (Contribution 8) investigated nanoparticles (NPs) of naturally occurring food colorants (β-carotene, lycopene, astaxanthin, and lutein) prepared through a reprecipitation method. The study focused on understanding the role of the solvent used during reprecipitation for the molecular self-assembly and resulting properties of the nanoparticles. The authors found that the terminal groups of carotenoids significantly influence the intermolecular interactions, thereby altering the structural and optical properties of the NPs. These findings are expected to contribute to the development of new technologies for controlling the color properties of carotenoids, which are of considerable interest for food industry.

Author Contributions: Conceptualization, P.T. and K.K.; resources, P.T.; writing—original draft preparation, P.T. and K.K.; writing—review and editing, P.T. and K.K. All authors have read and agreed to the published version of the manuscript.

Acknowledgments: We wish to thank all the contributors to this Special Issue, all the reviewers for evaluating the submitted articles. P.T. acknowledges the financial support from project № BG16RFPR002-1.014-0006 "National Centre of Excellence Mechatronics and Clean Technologies," financially supported by the European Regional Development Fund under the "Research Innovation and Digitization for Smart Transformation" program 2021–2027.

Conflicts of Interest: The authors declare no conflicts of interest.

List of Contributions:

1. Blanco, S.E.; Black, N.; Alvarez, M.A.; Morris, K.F.; Olson, M.A.; Billiot, E.J.; Billiot, F.H. Stereoisomeric Effects of Diammoniumcyclohexane Counterions on the Self-Assembly of Amino Acid-Based Surfactants. *Molecules* **2025**, *30*, 4114. https://doi.org/10.3390/molecules30204114.
2. Zapolski, R.; Gasztych, M.; Jastrząb-Miśkiewicz, B.; Jankowska-Konsur, A.; Musiał, W. The Properties of the Monolayers of Sorbitan Lipids as Informative Factors on the Hydrophilic–Lipophilic Balance Value of Their Mixtures, Proposed for Dermatological Applications. *Molecules* **2025**, *30*, 1841. https://doi.org/10.3390/molecules30081841.
3. Slavova, T.; Stanimirova, R.; Marinova, K.; Danov, K. Cleansing Mechanisms and Efficacy on Artificial Skin. *Molecules* **2025**, *30*, 1813. https://doi.org/10.3390/molecules30081813.
4. Kowalczuk, J.; Demchuk, O.M.; Borkowski, M.; Bielejewski, M. Stabilisation of Nanosilver Supramolecular Hydrogels with Trisodium Citrate. *Molecules* **2025**, *30*, 1613. https://doi.org/10.3390/molecules30071613.
5. Doratt Mendoza, J.; Ding, J.; Acosta Alvarez, M.; Acosta, E. Yeast Viability in HLD–NAC-Designed Fully Dilutable Lecithin-Linker Microemulsions. *Molecules* **2025**, *30*, 921. https://doi.org/10.3390/molecules30040921.
6. Dimitrova, I.M.; Slavchov, R.I. Charge Regulation in Liquid Films Stabilized by Ionic Surfactants: Change in Adsorption with Film Thickness and Phase Transitions. *Molecules* **2025**, *30*, 659. https://doi.org/10.3390/molecules30030659.

7. Le Thanh-Blicharz, J.; Lewandowicz, J.; Szwengiel, A.; Prochaska, K.; Baranowska, H.M.; Lewandowicz, G. Insight into Oil-in-Water Emulsions Stabilized by Cross-Linked and Pregelatinized Starches: The Effect of Molecular Structure, Surface Activity and Proton Molecular Dynamics. *Molecules* **2024**, *29*, 5626. https://doi.org/10.3390/molecules29235626.
8. Suzuki, R.; Kinoshita, K.; Miuchi, T.; Nishino, M.; Shimizu, Y.; Deguchi, S. Exploring the Optical Properties of Carotenoid-Based Nanoparticles: The Role of Terminal Groups. *Molecules* **2024**, *29*, 5456. https://doi.org/10.3390/molecules29225456.

References

1. Wennerström, H.; Evans, D.F. *The Colloidal Domain: Where Physics, Chemistry, Biology, and Technology Meet*; John Wiley & Sons: Hoboken, NJ, USA, 2026.
2. Miller, R.; Guzmán-Solís, E. *Emulsions: From Single Interfaces to Applications*; CRC Press: Boca Raton, FL, USA, 2025.
3. Butt, H.-J.; Graf, K.; Kappl, M. *Physics and Chemistry of Interfaces*; John Wiley & Sons: Hoboken, NJ, USA, 2023.
4. Platikanov, D.; Exerowa, D. Fundamentals of foam films. In *Foam Films and Foams; Progress in Colloid and Interface Science*; Exerowa, D., Gochev, G., Platikanov, D., Liggieri, L., Miller, R., Eds.; CRC Press: Boca Raton, FL, USA, 2019; pp. 77–98.
5. Nagtode, V.S.; Cardoza, C.; Yasin, H.K.A.; Mali, S.N.; Tambe, S.M.; Roy, P.; Singh, K.; Goel, A.; Amin, P.D.; Thorat, B.R.; et al. Green Surfactants (Biosurfactants): A Petroleum-Free Substitute for Sustainability—Comparison, Applications, Market, and Future Prospects. *ACS Omega* **2023**, *8*, 11674–11699. [CrossRef] [PubMed]

Disclaimer/Publisher's Note: The statements, opinions and data contained in all publications are solely those of the individual author(s) and contributor(s) and not of MDPI and/or the editor(s). MDPI and/or the editor(s) disclaim responsibility for any injury to people or property resulting from any ideas, methods, instructions or products referred to in the content.

molecules

MDPI

Article

Stereoisomeric Effects of Diammoniumcyclohexane Counterions on the Self-Assembly of Amino Acid-Based Surfactants

Saylor E. Blanco [1], Nathan Black [2,*], Margarita A. Alvarez [1], Kevin F. Morris [3], Mark A. Olson [1], Eugene J. Billiot [1] and Fereshteh H. Billiot [1,*]

[1] Department of Physical and Environmental Sciences, Texas A&M University Corpus Christi, 6300 Ocean Dr., Corpus Christi, TX 78412, USA; sblanco3@islander.tamucc.edu (S.E.B.); mark.olson@tamucc.edu (M.A.O.)
[2] Department of Chemistry, University of Washington, 4000 15th Avenue NE, Seattle, WA 98195, USA
[3] Department of Chemistry, Carthage College, 2001 Alford Park Drive, Kenosha, WI 53140, USA
* Correspondence: nblack1@uw.edu (N.B.); fereshteh.billiot@tamucc.edu (F.H.B.)

Abstract: The impact of counterion structure, especially variations in constitutional and stereochemical isomers, on the properties and performance of AABSs remains under-explored. This study investigates how structural variations, particularly the stereochemistry of diammonium cyclohexane (DACH) counterions, influence the self-assembly behavior of AABSs. Four AABSs: undecanoyl-glycine, -L-alanine, -L-valine, and -L-leucine, were paired with six DACH counterions representing *cis*/*trans* isomers of 1,2-, 1,3-, and 1,4-DACH. Critical micelle concentrations (CMCs) were determined via conductimetry, and micellar sizes were measured using dynamic light scattering. The degree of counterion binding (β) was calculated to probe micelle stability, while geometry-optimized structures of the DACH isomers were obtained using density functional theory. Lastly, pH measurements were taken to probe the protonation of DACH counterions at their natural pH, where both the DACH counterion and AABS headgroups intrinsically behave as buffers. Results indicate that while surfactant hydrophobicity primarily dictates CMC in other AABS/DACH combinations, *trans*-1,3-DACH leads to consistently higher CMCs. This deviation likely arises from its structural conformation, which positions the amine groups an intermediate distance of ~4.4–4.5 Å apart, allowing a small fraction of divalently charged counterions to form strong electrostatic bridging pockets at the micelle interface. These interactions dominate over headgroup effects, leading to elevated and surfactant-independent CMC values. Regarding size and other unusual trends in the systems, *cis*- isomers formed slightly larger micelles, and *trans*-1,4-DACH induces abnormal aggregation in undecanoyl-glycine leading to temperature dependent gel formation. These findings highlight the significant influence of counterion structure on AABS behavior and support counterion design as a strategy for enhancing surfactant performance in sustainable applications.

Keywords: amino acid surfactants; diammonium counterions; critical micelle concentration; self-assembly; *cis*-*trans* counterion stereochemistry; biodegradable surfactants

1. Introduction

Traditional non-biodegradable surfactants, widely used in household, industrial, and agricultural applications, such as branched alkylbenzene sulfonates [1], alkylphenol ethoxylates [2], quaternary ammoniums [3,4], and perfluoroalkyl surfactants [5], pose significant

environmental risks due to their persistence in aquatic systems and potential toxicity to wildlife [6]. The demand for eco-friendly alternatives has driven interest in biodegradable surfactants derived from renewable resources. Amino acid-based surfactants (AABSs) offer a promising solution, as they are derived from amino acids and fatty acids, and thus exhibit biodegradability, low toxicity, and structural diversity [6–13]. Moreover, AABSs have a wide range of applications, including drug delivery, antibacterial formulations, cosmetics, agriculture, and household cleaning products [6–10]. Due to their ability to facilitate mixing of oil and aqueous phases, they are also used in material science and petroleum oil recovery, while maintaining environmental efficacy [8,11]. Their amphiphilic properties can be precisely tuned by modifying the amino acid type, hydrophobic tail, or counterion, allowing for the design of surfactants tailored to specific applications. This tunability is critical for optimizing performance while minimizing environmental impact. However, there has been limited systematic exploration into how structural modifications, particularly those generating constitutional and stereochemical isomers of divalent counterions, affect the properties and behaviors of AABSs.

A principal characteristic of a surfactant's aggregation capability is its critical micelle concentration (CMC), which can be significantly influenced by alterations to the surfactant's counterions. Micellar systems with low CMC values are commonly utilized in detergents and cleaning foams, where a low CMC enables greater dilution without sacrificing efficiency [14]. Surfactants can also self-assemble into bilayers forming vesicles with hollow interiors that can be used for drug delivery systems, and those with ultralow CMCs can effectively encapsulate hydrophobic drugs, enhancing their solubility [15,16]. The choice of counterion impacts many of these parameters, including micellar size, which is critical for applications requiring either precise targeting (small micelles) or high drug loading capacity (larger aggregates) [17–20]. Additionally, counterion properties such as size, steric bulk, charge, and spacer length between charged groups significantly affect the degree of counterion binding and, consequently, the stability of micellar structures. Studies indicate that factors like spacer length and *cis-trans* isomerization in counterion molecules notably influence micellar characteristics, including the formation of counterion binding pockets [13,21–27]. For instance, in micelles formed by alkyl and tetraalkyl ammonium sulfates, increasing monovalent counterion size from Li^+ to Cs^+ reduces electrostatic repulsion and enhances screening, thereby lowering the CMC and producing larger aggregates [28,29]. Thus, the tuning of surfactant properties by modifying counterions represents a crucial strategy in optimizing micelle-based systems.

This research aims to characterize four AABSs (Figure 1): undecanoyl-glycine (Und-Gly), undecanoyl-L-alanine (Und-Ala), undecanoyl-L-valine (Und-Val), and undecanoyl-L-leucine (Und-Leu) in the presence of six diammonium cyclohexane (DACH) counterions: (*cis*/*trans*)-1,2-DACH, (*cis*/*trans*)-1,3-DACH, and (*cis*/*trans*)-1,4-DACH (Figure 2). The use of cyclic isomers of diamine cyclohexane as counterions in amino acid–based surfactants has not been previously explored, particularly in relation to their effect on micellization. This manuscript is the first to describe these interactions, highlighting their importance in understanding how counterion structure influences surfactant self-assembly. The counterions are cyclohexane diamine and they differ in the location of the two amines on the ring. The AABSs differ in side chain length of their amino acid headgroup. The counterions were chosen as an extension of a previous study that investigated the micelle-binding of linear diammonium counterions bearing alkyl chains of differing lengths bridging the ammonium centers [21]. Here the six cyclic counterions are constitutional isomers differing in the position of their diammonium centers relative to each other in the 1,2-, 1,3-, and 1,4- positions with each existing as either a *cis*- or *trans*- diammonium stereoisomer. The CMC of each

AABS and counterion combination was measured by variable concentration conductimetry in natural pH, which is reported for each system along with the percent protonation of the counterions since these mixtures inherently act as buffers. From the conductimetry data, the degree of counterion binding (β) for each system was also calculated. Micellar size was measured using photon correlation spectroscopy/dynamic light scattering (DLS). Finally, density functional theory (DFT) was employed to calculate energy-minimized structures of the DACH counterions at two different protonation states.

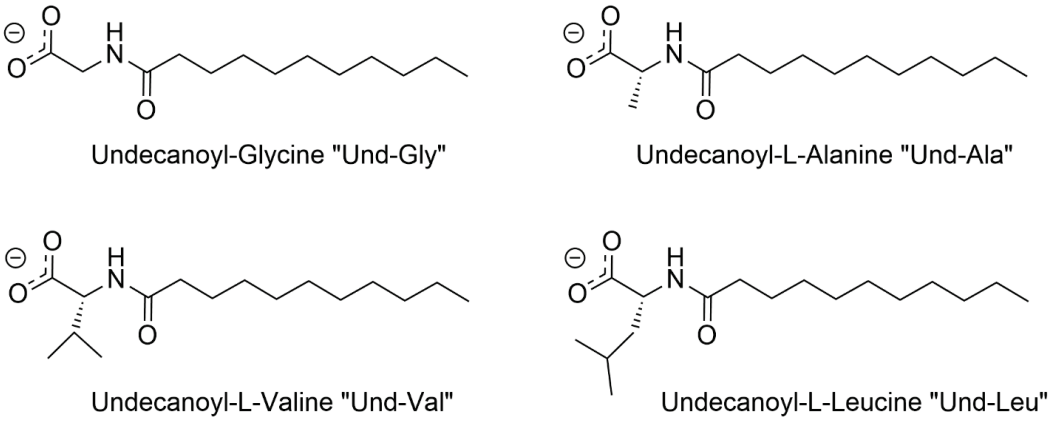

Figure 1. Structural representations of the carboxylate anions of the AABSs utilized in the study with their respective abbreviations.

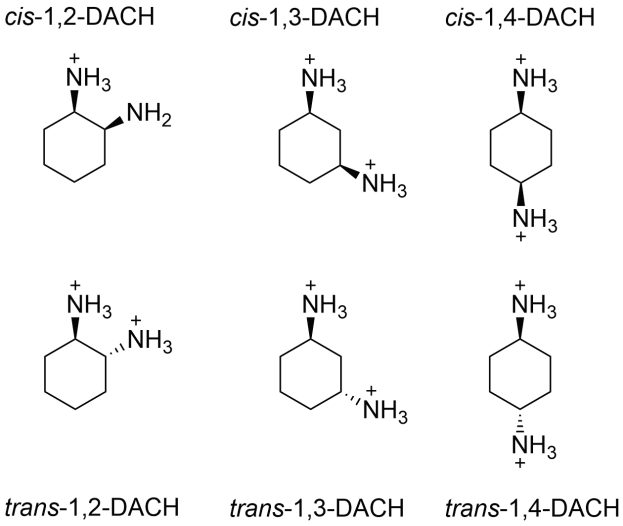

Figure 2. Structural representations of the *cis*- and *trans*- stereoisomers of 1,2-DACH, 1,3-DACH, and 1,4-DACH counterions. Fully protonated counterions are shown; however, the exact diamine charge will depend on the pH.

2. Results and Discussion

2.1. Structural Effects on Critical Micelle Concentration

CMC values were determined by conductimetry for surfactants Und-Gly, Und-Ala, Und-Val, and Und-Leu with each of the counterions, *cis*-1,2-DACH, *trans*-1,2-DACH, *cis*-1,3-DACH, *trans*-1,3-DACH, *cis*-1,4-DACH and *trans*-1,4-DACH (Figure 3, Table 1). It was determined that the CMCs of the surfactants decrease with increases in the length of the amino acid side chain in the presence of most counterions. For example, for solutions containing *cis*-1,2-DACH, the CMC steadily decreased from 15.9 mM to 8.0 mM as the

amino acid side chain length increased from Und-Gly to Und-Leu. This observation is likely due to the increased hydrophobic character associated with the larger amino acid side chains, which would promote micellization at lower concentrations to reduce unfavorable hydration interactions. Interestingly, this trend is not followed by the surfactant systems comprising *trans*-1,3-DACH. Rather, the CMCs for these systems ranged from 13.2 mM to 16.0 mM, with most values being statistically indistinguishable. This result suggests that *trans*-1,3-DACH binds to the micelles in such a way as to minimize the effect of varying headgroup hydrophobicity of each surfactant during micelle formation. Additionally, the CMC of Und-Gly in the presence of *trans*-1,4-DACH could not be measured at 25 °C due to its poor solubility and gel formation. Instead, a CMC of 15.1 mM was obtained, albeit at 60 °C. The insolubility of this system at 25 °C indicated that 1,4-DACH binds to Und-Gly in a way that promotes the self-assembly of larger aggregate morphologies at low temperatures. These assemblies can subsequently be disrupted at elevated temperatures. Overall, the data indicated that the structural parameters that influence CMC appear to be primarily driven by differences in the AABS side chains rather than counterion structure, with exceptions exhibited by both *trans*-1,3-DACH and *trans*-1,4-DACH.

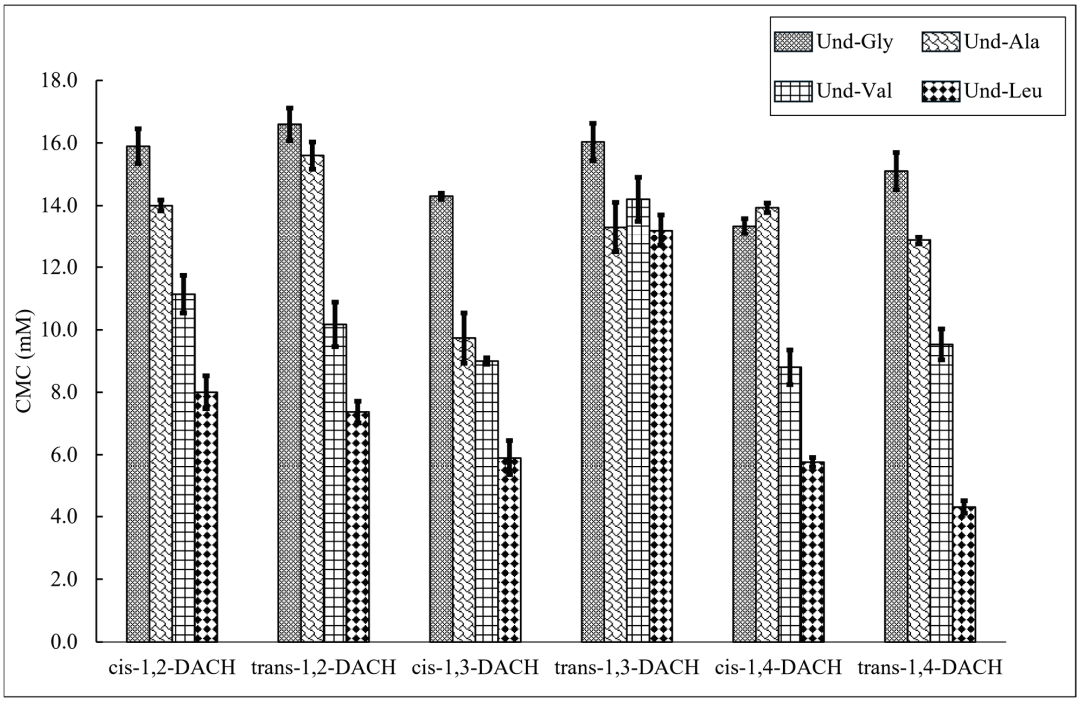

Figure 3. CMC values measured by variable concentration conductivity experiments for each AABS coupled with their respective DACH counterions. Data for Und-Gly with the *trans*-1,4-DACH counterion is not shown as it was insoluble at room temperature.

AABS CMCs are also selectively influenced by the stereochemistry of the DACH counterions. For example, the stereochemical identity, either *cis*- or *trans*-, of the 1,3-DACH counterions, greatly affects the CMC of their corresponding AABSs. In the case of Und-Leu, its CMC is 5.9 mM while accompanied by the *cis*-1,3-DACH counterion and 13.2 mM with the *trans*-1,3-DACH counterion. This result indicates that the relative spatial arrangement of the cationic 1,3-DACH ammonium centers, as determined by their stereochemistry, has a profound effect on AABS aggregation behavior. However, this is not true for both the 1,2-DACH and 1,4-DACH stereoisomers. In the case of 1,2-DACH stereoisomers, the CMCs of most AABSs are statistically indistinguishable. For example, CMCs of 8.0 ± 0.5 mM and 7.4 ± 0.4 mM were measured for Und-Leu in the presence of *cis*-1,2-

DACH and *trans*-1,2-DACH, respectively. It is likely that *trans*-1,3-DACH counterions have a different mechanism of micelle-binding, leading to CMCs that are largely independent of AABS side chain structure as discussed earlier.

Table 1. CMC of each AABS in the presence of the DACH counterions. $^{\alpha}$ Conformer (*ae*) refers to axial-equatorial diammonium conformer, and (*ee*) refers to the equatorial-equatorial diammonium conformer, $^{\beta}$ Measurements were taken at 60 °C.

Critical Micelle Concentration (CMC) (mM)				
Counterion (Conformer) $^{\alpha}$	**Surfactant**			
	Und-Gly	**Und-Ala**	**Und-Val**	**Und-Leu**
cis-1,2-DACH (*ae*)	15.9 ± 0.6	14.0 ± 0.2	11.1 ± 0.6	8.0 ± 0.5
trans-1,2-DACH (*ee*)	16.6 ± 0.5	15.6 ± 0.4	10.2 ± 0.7	7.4 ± 0.4
cis-1,3-DACH (*ee*)	14.3 ± 0.1	9.7 ± 0.8	9.0 ± 0.1	5.9 ± 0.6
trans-1,3-DACH (*ae*)	16.0 ± 0.6	13.3 ± 0.8	14.2 ± 0.7	13.2 ± 0.5
cis-1,4-DACH (*ae*)	13.3 ± 0.3	13.9 ± 0.2	8.8 ± 0.6	5.8 ± 0.2
trans-1,4-DACH (*ee*)	15.1 ± 0.7 $^{\beta}$	12.9 ± 0.1	9.5 ± 0.5	4.3 ± 0.2

Upon further analysis, the stereochemical influence of the DACH counterions on the CMC of the AABSs stems directly from the relative positions, axial (*a*) versus equatorial (*e*), of their diammonium centers that are inherent to the 1,2-, 1,3-, and 1,4-disubstituted cyclohexane structure as it adopts a chair conformation as either the *cis*- or *trans*- stereoisomer (Table 1). For example, *cis*-1,2-DACH is a C_1 symmetric meso compound that is optically inactive and structurally confined to existing as an axial-equatorial (*ae*) conformer, with the positioning of one ammonium center at an axial position and the other ammonium center at an equatorial position. Chair inversion of *cis*-1,2-DACH results in yet another *ae* conformer. *Trans*-1,2-DACH, on the other hand, possesses C_2 symmetry, is optically active, and can exist as both an *aa* or an *ee* conformer, but is energetically relegated to adopting an *ee* conformation in about 99:1 excess of *ee* to *aa* [30]. In a similar fashion to 1,2-DACH, *cis*-1,4-DACH is also a meso compound that is optically inactive and structurally confined to existing as an *ae* conformer, for which chair inversion results in yet another *ae* conformation. *Trans*-1,4-DACH is a C_{2h} optically inactive compound, that in the same manner as *trans*-1,2-DACH, is forced to exist as an *ee* conformer, whereby the chair inverted *aa* conformation is energetically unfavorable. The stereochemical similarities between 1,2- and 1,4-DACH is clear, whereby the *cis*- isomers for both 1,2- and 1,4-DACH exists as *ae* conformers, and the *trans* isomers for both 1,2- and 1,4-DACH exists as *ee* conformers. These stereochemical similarities a priori, account for the similar manner with which the *cis*- and *trans*- stereoisomers for both the 1,2-DACH and 1,4-DACH counterions interact with the AABSs, as previously mentioned. It should be noted that the exact conformation of the DACH counterions in solution may vary; however, the preference for each counterion with their respective *aa*, *ee*, and *ae* geometry is consistent.

The *cis*- and *trans*- structures of 1,3-DACH are stereochemical opposites with regard to *a* and *e* conformers as compared to 1,2- and 1,4-DACH [30,31]. *Cis*-1,3-DACH is a C_S symmetric meso compound that is optically inactive and exists exclusively as an *ee* conformer, for which the chair-inverted *aa* conformer is highly energetically unfavorable on account of 1,3-diaxial strain. *Trans*-1,3-DACH is C_1 symmetric, optically active, and structurally confined to existing as an *ae* conformer. Chair inversion of *trans*-1,3-DACH simply results in yet another *ae* conformer. As a result, both *cis*- and *trans*- isomers of 1,3-DACH interact with the AABSs in a fundamentally different manner than both the 1,2- and 1,4-DACH counterions.

2.2. Factors Affecting Micellar Hydrodynamic Diameter

To investigate the effect of the DACH counterions on the self-assembly of AABS into micellar aggregate structures, especially those with abnormal CMC measurements (*trans*-1,3-DACH and *trans*-1,4-DACH), the hydrodynamic diameters (H_D) of the micelles formed in solution were measured using DLS (Table 2). For most AABS-counterion pairs investigated, there is a modest increase in micellar size as the complexity of the AABS headgroup increases from Und-Gly to the Und-Leu. For example, the H_D of systems containing the *cis*-1,3-DACH counterion gradually rises from Und-Gly (2.0 nm) to Und-Leu (2.7 nm). The extended side chain structures associated with larger AABSs likely lead to minor steric repulsions between surfactant headgroups, causing the formation of slightly larger aggregates. This trend demonstrates that while AABS aggregation is largely governed by surfactant hydrophobicity, steric repulsions play a minor role in the self-assembly process.

Table 2. The hydrodynamic diameters of AABS micelles in the presence of DACH counterions. $^{\alpha}$ Measurements were taken at 60 °C.

Counterion	Size (nm)			
	Surfactant			
	Und-Gly	**Und-Ala**	**Und-Val**	**Und-Leu**
cis-1,2-DACH	2.3 ± 0.2	2.0 ± 0.2	2.0 ± 0.4	2.7 ± 0.6
trans-1,2-DACH	1.7 ± 0.2	1.7 ± 0.3	2.0 ± 0.2	2.3 ± 0.2
cis-1,3-DACH	2.0 ± 0.6	2.0 ± 0.2	2.7 ± 0.2	2.7 ± 0.2
trans-1,3-DACH	1.7 ± 0.2	1.7 ± 0.2	2.3 ± 0.3	2.3 ± 0.4
cis-1,4-DACH	2.0 ± 0.2	1.7 ± 0.2	2.7 ± 0.3	2.7 ± 0.3
trans-1,4-DACH	4.3 ± 0.3 $^{\alpha}$	2.7 ± 0.2	2.7 ± 0.2	3.1 ± 0.2

Micellar H_D also exhibits a dependence on the stereochemical identity of the DACH counterions. Namely, AABS micelles tend to be slightly larger when formed in the presence of a *cis*-1,2- and *cis*-1,3-DACH counterion compared to that of its *trans*- counterpart. Und-Gly exhibits H_D sizes of 2.3 and 1.7 nm in the presence of *cis*-1,2-DACH and *trans*-1,2-DACH, respectively. This difference is likely due to the altered spatial arrangements of the *cis*- versus the *trans*- counterions as they are situated and bound at the micellar surface. According to DFT calculations, which will be discussed in more depth in the next section, the inter-nitrogen distance for *cis*-1,2-DACH is 2.75 Å as compared to 2.73 Å for *trans*-1,2-DACH, at a pH where both stereoisomers predominantly exist in the +1 charged state. When bonding monovalently, the distance between the two amines is less relevant for variability of size than it is for DACH counterions with more linear protrusions. Moreover, the distance from the charged ammonium center to the furthest atom in the opposite direction on the molecule is 5.33 Å and 5.30 Å for *cis*- and *trans*-1,2-DACH counterions, respectively. Despite the odd behavior leading to consistent CMC values, there is no major exclusion of systems containing *trans*-1,3-DACH counterions from the other systems. The perpendicular, spatially extended binding configuration proposed here is consistent with the broader micellar expansion observed in systems incorporating *trans*-DACH counterions, particularly for the 1,3- and 1,4-substituted isomers, which adopt more linear or sterically extended geometries.

These minor differences between inter-nitrogen length however are likely not significant enough to cause size differences between *cis*- and *trans*- iteration of 1,2-DACH. This difference as well as size differences between the other *cis*- and *trans*- steroisomers is likely due to the altered spatial arrangements of the *cis*- versus the *trans*- counterions as they are situated and bound at the micellar surface. More specifically, both ammonium

centers of the *cis*-DACH counterion are oriented in the same relative direction with respect to the larger cyclohexane core. This arrangement optimizes ion-pairing during counterion condensation, allowing for the cationic *cis*-DACH ammonium center to bind to the anionic micellar surface in a way that positions their cyclohexane cores outward from the charged micelle. While one ammonium center is binding electrostatically, the neutral one forms a hydrogen bond with oxygen on the carboxylate group of the adjacent surfactant. From the perspective of the cyclohexane cores, this behavior can be described as "pushing" the ammonium centers toward the micellar surface. This behavior is consistent with our pH data, which indicates that most counterions exist predominantly in the +1 state rather than as fully +2 species. The *trans*-DACH counterions, however, orient their ammonium centers in opposing directions, causing the cyclohexane core and therefore the counterion to bind closer to the AABS headgroups. In this behavior, the cyclohexane cores can be described as "hugging" the micellar surface with their ammonium centers. The proposed "push" and "hug" binding modes of the DACH stereoisomers are depicted in Figure 4.

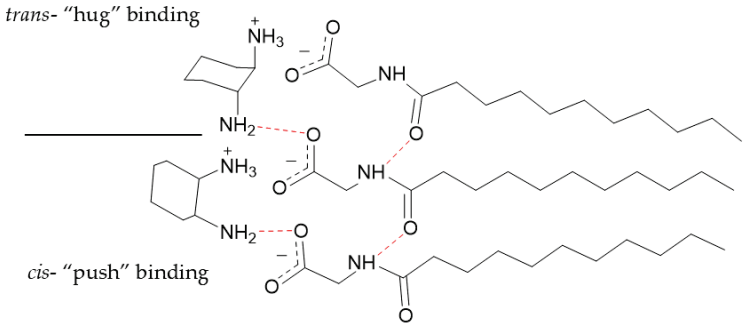

Figure 4. Graphical representation of the proposed binding of *cis*- and *trans*- DACH counterions to a micellar surface upon counterion condensation. Red dashed lines depict hydrogen bonding. Partially protonated counterions are shown; however, the exact diamine charge will depend on the pH.

This trend is not present for AABSs in the presence of 1,4-DACH counterions. For these systems, the measured H_D values for AABSs under the influence of *trans* counterions are larger than their *cis* counterparts. Und-Leu exhibits H_D sizes of 3.1 and 2.7 nm in the presence of *trans*-1,4-DACH and *cis*-1,4-DACH, respectively. This result is likely caused by the orthogonal positioning and relatively large distances between the cationic ammonium centers of the *trans*-1,4-DACH counterions, affectively hindering adoption of the "hug" binding mode. Rather, it is likely that only one of *trans*-1,4-DACH's ammonium centers binds to the micellar interface, while the other protrudes perpendicularly. Due to the opposite positioning of the ammonium centers on the cyclohexane core, it is likely that *cis*-1,4-DACH also binds in this monovalent orientation. This monovalent or perpendicular model of 1,4-DACH binding to AABS was also proposed by Fletcher et al. in an NMR study of counterion binding to undecylvaline leucinate micelles [23]. Altogether, these altered binding behaviors may explain the reversal in micellar H_D sizes induced by stereochemical identity of the 1,4-DACH counterions. This deviation of *trans*-1,4-DACH from the proposed "push" and "hug" binding modes can also be used to rationalize its abnormally low solubility (and associated binding interactions) with Und-Gly, as noted earlier.

To specifically probe the temperature-dependent morphologies of Und-Gly in the presence of *trans*-1,4-DACH, H_D measurements were made as a function of temperature, from 75 °C to 10 °C. Starting at 75 °C, the micelle H_D size remained stable at ~4.3 nm until the temperature reached 45 °C. Upon reaching 45 °C, the micellar H_D increased, ranging from 312.1 to 338.7 nm at and below 55 °C. The observed insolubility at lower temperatures

was likely due to the formation of these larger micellar morphologies, which then go on to fall out of solution.

Even when completely soluble at higher temperatures, the micelle H_D size (4.3 nm) is much larger than the other micellar aggregates. The observation of these relatively large aggregates, along with dramatic changes in micellar H_D with changes in temperature, support the conclusion that the interactions between Und-Gly and *trans*-1,4-DACH are different from those present in the other AABS-counterion pairs investigated. This difference can be explained by Und-Gly's small side chain, which enables strong hydrogen bonding between the amide function groups of contiguously assembled AABS molecules, leaving little space between adjacent headgroups. This crowding of Und-Gly's headgroups hinders the ability of *trans*-1,4-DACH counterions to bind to the micellar interface. Furthermore, because *trans*-1,4-DACH's predicted binding mode has only one ammonium center in contact with the anionic carboxylate site of the Und-Gly headgroup, its reduced charge-stabilization (compared to other DACH counterions) is likely unable to overcome the strong hydrogen bonding between the Und-Gly headgroups as depicted in Figure 5A. This does not present an issue for AABSs with increased headgroup separation leading to reduced hydrogen bonding strength and adequate room for counterion bonding as depicted in Figure 5B. The issue of steric hindrance between neighboring counterions is minimal for more compact or bent isomers due to their reduced exposure and lower interfacial charge density, despite perpendicular bonding.

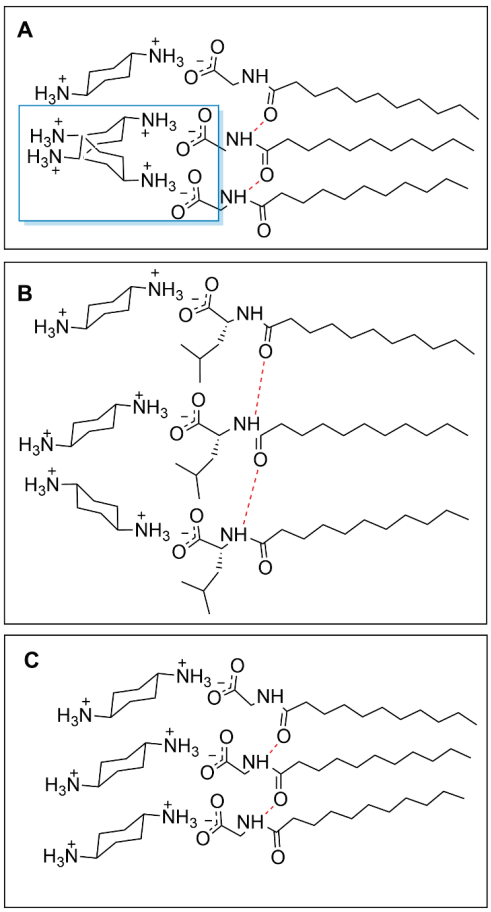

Figure 5. Structural representations of the proposed binding schema of Und-Gly with *trans*-1,4-DACH (**A**) the boxed region shows binding interference between counterions on adjacent surfactants, compared to Und-Leu with *trans*-1,4-DACH (**B**), and the organized alignment of Und-Gly with *trans*-1,4-DACH (**C**) leading to gel formation. Fully protonated counterions are shown; however, the exact diamine charge will depend on the pH.

The tight lamellar network of adjacent surfactants in Und-Gly/*trans*-1,4-DACH systems depicted in Figure 5C would therefore explain the insoluble gel formations that were observed at lower temperatures. At higher temperatures, increased thermal energy likely facilitates a more favorable alignment of the counterions by disrupting the amide hydrogen bonds in Und-Gly. The reduced repulsion allows the surfactants to pack more tightly and form elongated micelles as previously explained, giving rise to the increased size relative to other systems (4.3 nm) which is further emphasized upon the formation of a gel when cooling. The observed deviations in size therefore reflect the system's unique structural characteristics rather than temperature effects alone. This phenomenon of temperature-dependent gel formation has been observed in a variety of surfactant systems [32,33].

2.3. Degree of Counterion Binding

To investigate the efficacy of counterion condensation upon micelle formation, the degree of counterion binding (β) was calculated from conductimetry according to Equation (1) (Section 3.6) for each AABS and counterion pair (Figure 6, Table 3). For most DACH counterions, Und-Val consistently exhibited lower β values than the other AABSs. This observation is most pronounced when Und-Val was ion-paired with *cis*-1,3-DACH, for which β = 0.44, corresponding to 44% binding. AABSs Und-Ala and Und-Leu (Und-Val's structural neighbors) exhibited 65% and 59% binding, respectively. This result indicates that the steric bulk presented by Und-Val's amino acid side chain hinders DACH counterion binding in a manner that AABSs with similar side chains do not. Despite its steric bulk, Und-Leu does not exhibit a low degree of counterion binding. Its longer side chain leads to steric repulsion between AABS headgroups, giving the counterions greater access to the anionic carboxylate groups, thereby augmenting counterion binding. This selective reduction in Und-Val's counterion binding (compared to Und-Ala and Und-Leu) agrees with previous findings, albeit with AABSs coupled with linear diammonium counterions [21].

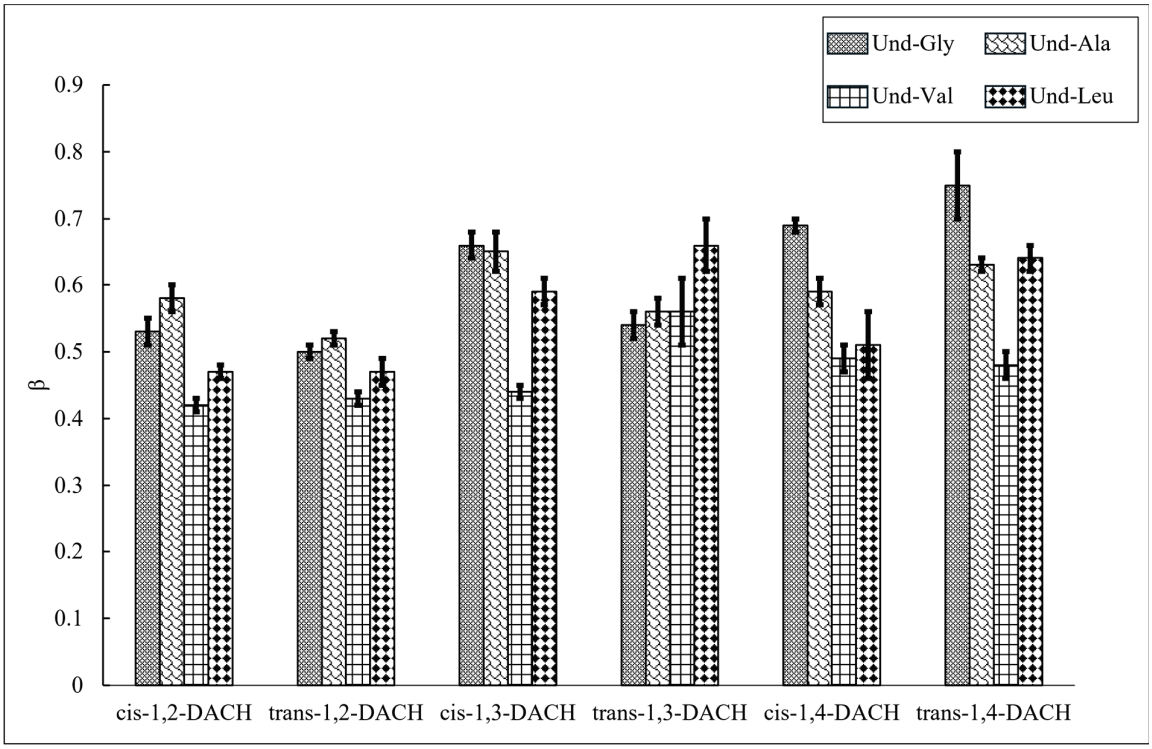

Figure 6. The degree of counterion binding (β) of each AABS with respect to DACH counterions.

Table 3. The degree of counterion binding (β) of each AABS in the presence of DACH counterion. [α] Measurements were taken at 60 °C.

Counterion	Degree of Counterion Binding (β)			
	Surfactant			
	Und-Gly	Und-Ala	Und-Val	Und-Leu
cis-1,2-DACH	0.53 ± 0.02	0.58 ± 0.02	0.42 ± 0.01	0.47 ± 0.01
cis-1,3-DACH	0.66 ± 0.02	0.65 ±0.03	0.44 ± 0.01	0.59 ± 0.02
cis-1,4-DACH	0.69 ± 0.01	0.59 ± 0.02	0.49 ± 0.02	0.51 ± 0.05
trans-1,2-DACH	0.50 ± 0.01	0.52 ± 0.01	0.43 ± 0.01	0.47 ± 0.05
trans-1,3-DACH	0.54 ± 0.02	0.56 ± 0.02	0.56 ± 0.05	0.66 ± 0.04
trans-1,4-DACH	[α] 0.75 ± 0.05	0.61 ± 0.01	0.48 ± 0.02	0.64 ± 0.02

AABS-*trans*-1,3-DACH salts undergo aggregation behavior that does not follow this general trend, as it exhibits an identical degree of micellar binding (56%) for both Und-Ala and Und-Val. In addition, the other β values measured for the *trans*-1,3-DACH counterion paired AABSs were not statistically different, indicating consistent binding behavior for the *trans*-1,3-DACH counterion regardless of the structure of the AABS side chain. This result can be explained by the inherent *ae* conformer structure of the *trans*-1,3-DACH counterion, which can accommodate a range of side chain lengths, from Und-Gly to Und-Leu, in interstitial space formed when bound and ion-paired to the micellar superstructure. This interstitial space may partially insulate AABS side chains from unfavorable hydration contacts, reducing the thermodynamic drive towards micellization.

In addition to its more favorable solubility in aqueous solutions, this dampening of the hydrophobic effect also contributes to the explanation as to why the CMCs of all 4 AABSs are similar and comparatively higher in the presence of the *trans*-1,3-DACH counterions, as previously discussed. The alteration of parallel and perpendicular binding contributes to a high β in par with the other AABSs/DACH systems. The hypothesized existence of the interstitial space formed upon micellar binding of *trans*-1,3-DACH counterions was further verified by considering the geometry-optimized structures of its diamine precursor obtained by DFT calculations. The resulting optimized structures for all the DACH counterion diamine precursors are presented in Figures 7 and 8 with a +1 and +2 charge.

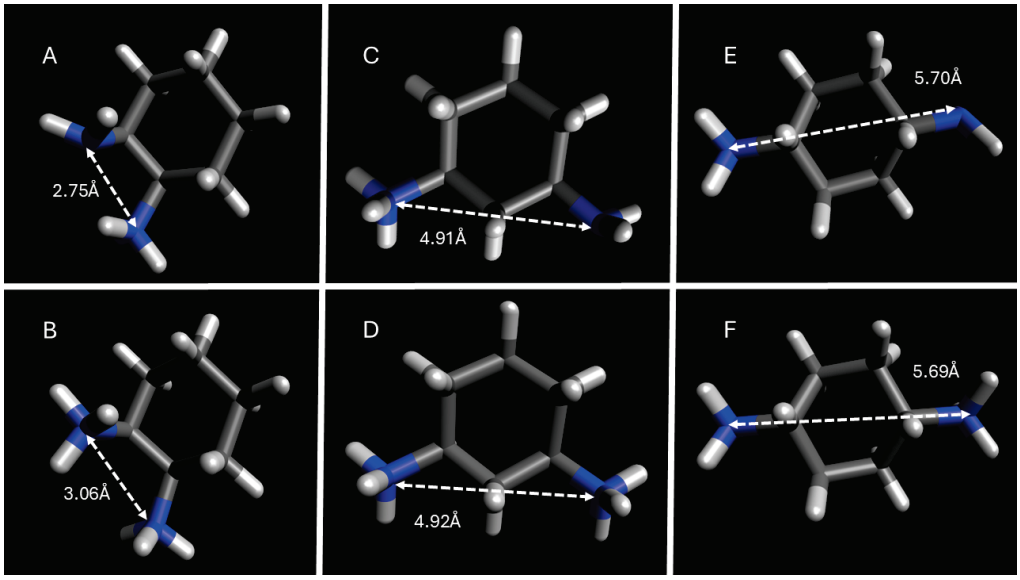

Figure 7. DFT geometry optimization of DACH counterions with the distance in angstroms between amines. (**A**). *cis*-1,2-DACH, (**C**). *cis*-1,3-DACH, (**E**). *cis*-1,4-DACH, all exhibiting a +1 charge, and (**B**). *cis*-1,2-DACH, (**D**). *cis*-1,3-DACH, and (**F**). *cis*-1,4-DACH all exhibiting a +2 charge.

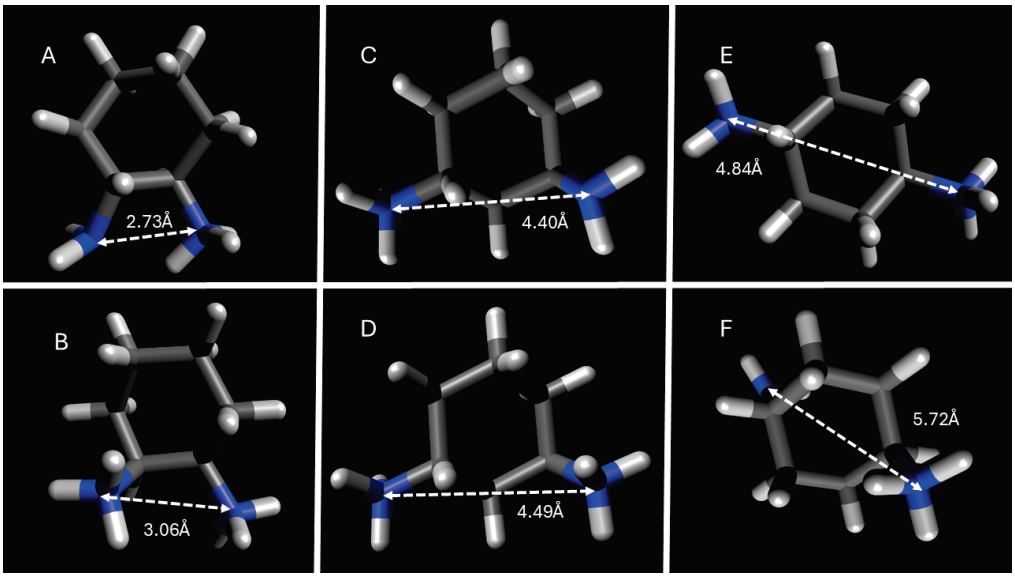

Figure 8. DFT geometry optimization of DACH counterions with the distance in angstroms between amines. (**A**). *trans*-1,2-DACH, (**C**). *trans*-1,3-DACH, (**E**). *trans*-1,4-DACH, all exhibiting a +1 charge, and (**B**). *trans*-1,2-DACH, (**D**). *trans*-1,3-DACH, and (**F**). *trans*-1,4-DACH all exhibiting a +2 charge.

Based on DFT calculations it was found that most of the DACH counterion diamine precursors have widely protruding amine groups, with the 1,4-DACH counterions having the widest protrusion. As previously stated, is likely that the diamine counterions bind parallel, with the neutral amine hydrogen bonding when the counterion is +1. The only exceptions to this trend are the 1,4-DACH counterions, which support the expected monovalent binding geometry from these diamines as previously explained. The high degree of counterion binding to the micellar superstructure for the 1,4-DACH counterions cannot be explained by the distance between its respective ammonium centers, but rather the higher availability for binding sites due to its perpendicular binding geometry as depicted in Figure 5. For the remaining DACH counterion diamine precursors, the geometrically optimized structures were used to calculate the distance between amine functional groups, as an approximate measure of interstitial space that can form upon counterion condensation to the micelle.

Intermediate distances (4.4–4.9 Å), as in *trans*-1,3-DACH, align well with carboxylate separations at the micelle surface, enabling parallel binding pockets that stabilize aggregation. These geometric constraints explain the unique electrostatic bridging behavior of *trans*-1,3-DACH and the resulting surfactant-independent CMC values.

2.4. pH Measurements and Calculations

It should be noted that there is some buffering capacity in the systems from both components: the counterion (DACH), which exists as a mixture of protonation states at the natural pH, and the surfactant, undecanoyl-(headgroup), also contributes to buffering through its ionizable carboxyl group, in the same way amino acids do. To investigate the percentage of counterions in each protonation state, the natural pH of AABS/DACH system, the pKas' of counterions were utilized in Equations (2)–(4). These equations quantify populations of the doubly protonated (+2), singly protonated (+1), and neutral (0) species. As described in Section 3.8, the resulting distributions are shown in Table 4.

Table 4. Calculated protonation state distributions (2^+, 1^+, 0) for AABS systems paired with various DACH counterions at natural pH. Values represent the mole fraction of each protonation state, calculated using Equations (2)–(4). * no data due to limited solubility at room temperature.

Surfactant	DACH Isomer	pH	pKa_1	pKa_2	+2%	+1%	0%
Und-Gly	*cis*-1,2-DACH	9.25 ± 0.05	6.13 [23]	9.93 [23]	0.06	82.67	17.27
Und-Ala		9.24 ± 0.09			0.06	82.99	16.94
Und-Val		9.44 ± 0.02			0.04	75.52	24.44
Und-Leu		9.27 ± 0.02			0.06	82.00	17.91
Und-Gly	*trans*-1,2-DACH	9.66 ± 0.01	6.47 [23]	9.94 [23]	0.04	65.55	34.4
Und-Ala		9.62 ± 0.01			0.05	67.6	32.35
Und-Val		9.71 ± 0.00			0.04	62.92	37.05
Und-Leu		9.61 ± 0.02			0.05	68.1	31.85
Und-Gly	*cis*-1,3-DACH	10.33 ± 0.04	8.29 [34]	10.3 [34]	0.44	48.06	51.5
Und-Leu		10.21 ± 0.07			0.66	54.8	44.54
Und-Val		10.31 ± 0.03			0.47	49.19	50.34
Und-Ala		10.33 ± 0.13			0.44	48.06	51.5
Und-Gly	*trans*-1,3-DACH	9.72 ± 0.02	8.54 [34]	10.36 [34]	5.10	77.21	17.69
Und-Ala		9.55 ± 0.03			7.80	79.83	12.36
Und-Val		9.90 ± 0.04			3.14	71.92	24.94
Und-Leu		10.03 ± 0.01			2.16	66.66	31.18
Und-Gly	*cis*-1,4-DACH	9.26 ± 0.07	9.4 [23]	10.8 [23]	57.30	41.51	1.2
Und-Ala		9.24 ± 0.10			58.45	40.44	1.11
Und-Val		9.44 ± 0.05			46.63	51.13	2.23
Und-Leu		9.28 ± 0.03			56.13	42.58	1.29
Und-Gly *	*trans*-1,4-DACH		9.4 [23]	10.8 [23]			
Und-Ala		9.93 ± 0.07			20.64	69.93	9.43
Und-Val		10.07 ± 0.07			15.27	71.43	13.3
Und-Leu		9.86 ± 0.07			23.72	68.42	7.86

Table 4 shows an estimation of the charge each counterion exhibits in the system as a percentage. For example, in Und-Gly/*cis*-1,2-DACH, 0.06% of the counterions in solution exhibit a +2 charge, while 82.67% exhibit a +1 charge and 17.27% are neutral. Because protonation depends on both pH and pKa, systems where the pH is lower than the pKa, will favor the divalent (+2) form. For example, in the UndAla-/*cis*1,4DACH system, the pH is 9.24 while the pKa is 9.40, resulting in a higher proportion (58.45 %) of divalent counterions. The majority of systems have counterions dominated by a +1 charge (41.51–82.99%). 1,2-, 1,3- DACH systems show that buffering from the $DACH^{2+}/DACH^{1+}$ couple is minimal, whereas the $DACH^{+}/DACH^{0}$ pair provides useful buffering, the opposite of this is true for 1,4- systems. This effect is likely due to the reduced electrostatic repulsion between the amines in the 1,4-systems, where initial protonation does not significantly hinder subsequent protonation. As a result, the molecule can more readily access multiple protonation states, thereby enhancing buffering in the +2/+1 region.

Systems containing *trans*-1,3-DACH have a small percentage of +2 charged counterions, while 1,4-DACH counterions have a much larger percentage (15.27–58.45%). Although most *trans*-1,3-DACH counterions exist in the +1 state at the experimental pH, a small fraction are protonated to the +2 state. Even a minimal amount of divalent counterions can dramatically influence micellar behavior due to their ability to effectively neutralize multiple charges and strong localization at the micellar interface [35,36]. It is likely that the small percentage of divalent counterions in *trans*-1,3-DACH systems have a high binding affinity. The spatial arrangement of amine groups and high binding affinity allows for selective interaction with the most negatively charged regions at the micelle interface first. This geometry favors the formation of parallel binding pockets due to a sufficient distance between amines and enhanced electrostatic complementarity with the carboxylate groups of the surfactant as depicted in Figure 9. This leads to the divalent binding pockets that

are sparsely placed, while the remaining positions at the charged interface are then filled by perpendicular binding monovalent *trans*-1,3-DACH counterions or parallel binding monovalent counterions forming binding pockets via hydrogen bonding as explained in Section 2.2. The electrostatic interactions, however, result in stronger binding than the parallel hydrogen bonding interactions, which differentiates the behavior of *trans*-1,3-DACH from that of the other DACH counterions. This stronger stabilization diminishes the influence of the surfactant's headgroup regardless of whether it is Gly, Ala, Val, or Leu. Because the electrostatic bridging interactions overwhelm the weaker headgroup-dependent forces, the micellization process is governed primarily by the *trans*-1,3-DACH geometry. This causes the energetic cost of micelle formation to become nearly identical across different surfactant headgroups, which explains the consistently similar CMC values observed for *trans*-1,3-DACH systems. The electrostatic bridging dominates the aggregation-driving forces. As a result, CMC values for *trans*-1,3-DACH systems remain consistently similar across different surfactants.

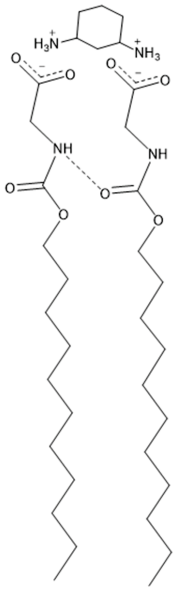

Figure 9. Parallel binding of *trans*-1,3-DACH counterion when exhibiting a +2 charge.

While the protonation state is significant for the *trans*-1,3-DACH counterions, it is less relevant for 1,4-DACH systems. Regardless of the protonation state of the 1,4-DACH counterions, it is likely that the divalent counterions do not contribute to parallel binding pockets due to their protruded geometry as further explained in Section 2.2.

3. Materials and Methods

3.1. Materials

Starting materials, reagents, and solvents were purchased from commercial suppliers and used without further purification. Deuterated solvents (Cambridge Isotope Laboratories, Tewksbury, MA, USA) for NMR spectroscopic analyses were used as received. Glycine, *L*-alanine, *L*-valine, and *L*-leucine (>97% purity) were purchased from Arcotein, Hoover, AL, USA. Undecanoic acid (>99%), N,N′-diisopropylcarbodiimide (>99%), N-hydroxysuccinimide (NHS; 98%), tetrahydrofuran (THF; ≥99.9%), sodium bicarbonate (≥99.7%), and hydrochloric acid (37%) were all obtained from Sigma-Aldrich, St. Louis, MO, USA. Deionized water with 18.0 mΩ conductivity (Millipore, Bedford, MA, USA) was used for synthesis and solution preparation. The DACH counterion were purchased

from the respective manufacturers: *cis*-1,2-DACH (AEchem Scientific Corporation, Downers Grove, IL, USA; >98% purity), (±)-*trans*-1,2-ADCH (Alfa Aesar, Haverhill, MA, USA; 99% purity), *cis*-1,3- DACH (TCI Chemicals, Tokyo, Japan, >98% purity), *trans*-1,3-DACH (TCI > 97.0% purity), *cis*-1,4- DACH (TLC Chemicals, Tokyo, Japan, >98.0%), *trans*- DACH (Aldrich Chemistry, ≥98.0% purity). The filters used are 0.020 μm Whatman PTFE syringe filters.

3.2. Analytical Techniques

^{1}H-NMR spectra were recorded on a Bruker Avance-II 300 MHz Ultrashield spectrometer (Bruker Corporation, Billerica, MA, USA) at 298 K. Chemical shifts are reported in ppm relative to the residual signal of the solvent. Conductivity measurements were carried out using a Vernier® conductivity probe (Vernier Scientific, Beaverton, OR, USA) and a jacketed beaker connected to a Scientific Caron™ 2050 recirculating bath (Caron Products & Services, Marietta, OH, USA), which maintained the temperature within ±0.05 °C of the set point. Dynamic light scattering (DLS) measurements were performed on a Malvern® Nano Series Zetasizer Nano-ZS (Malvern Panalytical Ltd., Malvern, UK) at a scattering angle (θ) of 173°. pH measurements were taken using a VWR® pHenomenal® pH 1100 L meter (VWR International, Radnor, PA, USA) equipped with a sympHony™ edition 1 pH probe (VWR International, Radnor, PA, USA).

3.3. Synthesis of AABSs and Their Respective DACH Counterions

The AABSs were synthesized following previously published methods, whereby undecanoic acid was first coupled with *N*-hydroxysuccinimide (NHS) to form an undecanoyl-NHS ester [21,37]. The undecanoyl-NHS ester was then subjected to amide formation upon coupling with each respective amino acid (Section S1 of the Supplementary Materials). The AABSs were then directly obtained by filtration after having been precipitated from solution with the addition of HCl. The precipitate was washed several times with deionized water to ensure complete removal of HCl residues, then freeze dried. The purity of the AABSs compounds was then verified using ^{1}H NMR spectroscopy (Section S2 of the Supplementary Materials).

3.4. Variable Concentration Conductivity Measurements

To CMC for each AABS/DACH system was obtained using variable concentration conductivity measurements. In a typical experiment, the conductivity of an initial 10 mL aqueous solution containing equimolar amounts of both AABS the corresponding diaminocyclohexane (40 mM) was measured. These counterions were extracted under nitrogen gas to prevent oxidation. A 1:1 molar ratio of surfactant to counterion was used, as pH-based speciation indicated that the counterion exists mainly in the +1 state, with only a minor fraction of +2 and some neutral species. This distribution results in an effective positive charge that is close to balancing the –1 charge of the surfactant. This solution was then diluted at intervals by removing 1 mL of sample from the solution and adding 1 mL of water via calibrated pipette to return the solution to its original volume. The solution conductivity was measured at each step along this dilution scheme, which was performed until a clear inflection in the linear relationship between conductivity and AABS/DACH concentration could be observed (Section S3 of the Supplementary Materials). This inflection point corresponded to the CMC and was identified from the intersection of two linear trendline equations. The Und-Gly/*trans*-1,4-DACH system could not be measured at room temperature (25 °C) due to poor solubility, even at concentrations significantly below 40 mM, so measurements were instead conducted at 60 °C.

3.5. Photon Correlation Spectroscopy/DLS Size Measurements

Micellar size for each AABS/DACH pair was determined using DLS. For each combination of AABS and DACH counterion, a 3 mL aqueous solution was prepared in 0.020 μm filtered deionized water at a concentration that was 5× the CMC at 25 °C. This filtered sample solution was then analyzed by DLS. The highest-intensity peak that was present in both the "by-volume" and "by-intensity" DLS spectra was taken as the average apparent micellar hydrodynamic diameter (Section S4 of the Supplementary Materials). Each sample was prepared and measured in triplicate, with each run consisting of the average of 12 different DLS scans. To explore the temperature-dependent solubility of the Und-Gly/*trans*-1,4-DACH system as mentioned in Section 2.2, hydrodynamic diameters were measured via DLS at 10 different temperatures from 10 to 75 °C. Measurements were taken once the internal Peltier-controlled system in the instrument indicated equilibration to the selected temperature. Based on previous studies, when comparing DLS measurements and DOSY NMR, no significant differences in hydrodynamic size were observed for our system; therefore, no additional measurements were included [38].

3.6. Degree of Counterion Binding Calculations

The degree of counterion binding (β) was calculated from the raw variable concentration conductivity data described in Section 2.3. By measuring the change in the slope of the solution conductivity as a function of AABS/DACH concentration, the degree of counterion binding was calculated using Equation (1) and according to previous studies [39]:

$$\beta = \frac{m_B - m_A}{m_B} \tag{1}$$

where m_B is the slope below the CMC and m_A is the slope above the CMC. β represents the fraction of charge-stabilized surfactants due to counterion condensation at the micellar-water interface, assuming no other simultaneous processes influence solution conductivity. Under this regime, β varies from 0 to 1, which, respectively, represent 0% and 100% counterion binding. This parameter, despite its underlying assumptions, is commonly used to compare counterion binding between different surfactant systems [21,22,39–43].

3.7. Density Functional Theory Calculations

To provide qualitative insights into the observed experimental results, DFT calculations were performed to identify energy-minimized geometries of the DACH diamine precursors in order to elucidate the binding modes of the DACH counterions using ORCA 6.0 software [44,45]. Hatree-Fock was used for preoptimization, prior to the final run. Then B3LYP-D4 functional was used to correlate DACH electron densities with their overall energies. The D4 component of the B3LYP-D4 functional represents a dispersion correction to the common B3LYP functional that was used to more accurately simulate weak van der Waals forces. This modified functional was used in conjunction with the DEF2-TZVP Opt TightSCF TightOpt basis set [46]. Opt TightSCF and TightOpt were used to ensure tight convergence and optimization. The conductor-like polarizable continuum model (CPCM) was used to implicitly simulate an aqueous environment. This optimization was performed for each DACH counterion diamine precursor and visualized thereafter using the software, Avogadro 2 [47] (Sections S5 and S6 of the Supplementary Materials). It is important to note that DFT calculations provide approximations for the systems being studied rather than direct values.

3.8. pH Measurements and Calculations

To investigate pH-dependent protonation of DACH counterions in the system, Equations (2)–(4) were utilized [48] (Section S7 of the Supplementary Materials). The pH measurements were taken at the CMC of each system with triplicate measurements being performed. It should be noted that the pH of the solutions was measured both before and after the CMC measurements, and no significant changes were observed. This stability reflects that the mixtures function as intrinsic buffer systems, since multiple protonation states of the counterions (and of the AABS headgroups) coexist under the experimental conditions. For the Und-Gly and *trans*-1,4-DACH surfactant solution, pH was not measured because the surfactant was not soluble at room temperature. The results from these calculations are presented in Table 4.

$$\alpha_{NH_3^+-R-NH_3^+} \sim \frac{[H^+]^2}{[H^+]^2 + K_{a1}[H^+] + K_{a1}K_{a2}} \tag{2}$$

$$\alpha_{NH_3^+-R-NH_2} \sim \frac{K_{a1}[H^+]}{[H^+]^2 + K_{a1}[H^+] + K_{a1}K_{a2}} \tag{3}$$

$$\alpha_{NH_2-R-NH_2} \sim \frac{K_{a1}K_{a2}}{[H^+]^2 + K_{a1}[H^+] + K_{a1}K_{a2}} \tag{4}$$

Each α represents the fraction of DACH counterions that exist in a given protonation state, expressed as a fraction of the total counterion concentration. The results from these equations can be interpreted qualitatively, as it should be considered that when two pKa values are similar, it is difficult to treat them as distinct protonation states due to overlapping protonation equilibria. Moreover, utilizing DACH pka values for calculations do not account for system specific behavior with the AABSs or micellization.

4. Conclusions

In conclusion, this study provides a comprehensive investigation into how stereochemical and constitutional isomerism of DACH counterions modulates the aggregation behavior of AABSs in their natural pH. Through CMC measurements, DLS, DFT calculations, and pH measurements we show evidence suggesting that both the side chain structure of AABSs and the spatial configuration of DACH counterions play pivotal roles in influencing micellar properties such as size, solubility, and degree of counterion binding.

While general trends in micellization were consistent with increasing surfactant hydrophobicity, the *trans*-1,3-DACH counterion uniquely disrupted this pattern, displaying CMCs and β values largely independent of AABS side chain identity. This deviation arises from its structural conformation and pH dependent protonation which showed a small fraction of diavalent counterions. For these counterions, the amine groups are an intermediate distance of ~4.4 Å apart, enabling the small fraction of divalently charged counterions to form strong electrostatic bridging pockets at the micelle interface. As a result, the counterion rather than the surfactant headgroup dictates the CMC. Conversely, the *trans*-1,4-DACH counterion induced abnormal solubility and gel formation in Und-Gly systems, attributed to hindered bidentate binding and enhanced inter-surfactant hydrogen bonding.

These findings suggest that the geometry of the counterion and the structure of the surfactant headgroup are closely linked, highlighting the importance of stereochemical design in controlling micellar systems. Because diamine counterions contain exchangeable hydrogen atoms, their protonation state is sensitive to pH. Consequently, changes in the pH

of the surfactant solution can strongly influence the self-assembly behavior of AABSs. This study expands our understanding of surfactant–counterion interactions by introducing a new class of cyclic counterions and suggesting how their structural isomerism may affect micellar organization. In future work, we plan to systematically investigate how pH and ionic strength impact the self-assembly and aggregation properties of AABSs in the presence of diamine counterions.

Supplementary Materials: The following supporting information can be downloaded at: https://www.mdpi.com/article/10.3390/molecules30204114/s1, Figure S1: Synesthetic scheme for undecanoyl-AABSs. Further information can be obtained on request; Figure S2: Und-Gly ^{1}H NMR spectrum in CD_3OD; Figure S3: Und-Ala ^{1}H NMR spectrum in CD_3OD; Figure S4: Und-Val ^{1}H NMR spectrum in CD_3OD; Figure S5: Und-Leu ^{1}H NMR spectrum in CD_3O; Figure S6: Conductivity vs. concentration data for Und-Gly, Und-Ala, Und-Val, and Und-Leu in the presence of *cis*-1,2-DACH at room temperature. Each point represents the average of three triplicate measurements. Similar trends were observed in the presence of other counterions. Full replicated data is available on request; Figure S7: Size distribution curve by intensity of 12 runs of Und-Leu with *cis*-1,3-DACH triplicate three taken at room temperature and 5x the CMC; Figure S8: Size distribution curve by volume of 12 runs of Und-Leu with *cis*-1,3-DACH triplicate three taken at room temperature and 5x the CMC; Section S1: Synthetic Scheme; Section S2: NMR Spectrums for Undecanoyl-AABSs; Section S3: CMC: Conductivity vs. Concentration Plots; Section S4: DLS Size Distribution Plots; Section S5: ORCA Geometry Optimization; Section S6: ORCA Geometry Optimized Coordinates; Table S1: Optimized systems: atom counts and calculated electronic energies of DACH counterions; Section S7: Derived pH Protonation Equation: Equations (S1)–(S23).

Author Contributions: Conceptualization, S.E.B., N.B., E.J.B., F.H.B., K.F.M. and M.A.O.; methodology, S.E.B., M.A.A., N.B., F.H.B., E.J.B. and K.F.M.; software, S.E.B.; validation, S.E.B., N.B., F.H.B., E.J.B., K.F.M. and M.A.O.; formal analysis, S.E.B., N.B., and F.H.B.; investigation, S.E.B., M.A.A., N.B., and F.H.B.; resources, F.H.B., E.J.B., K.F.M. and M.A.O.; data curation, S.E.B. and M.A.A.; writing—original draft preparation, S.E.B., M.A.A. and N.B.; writing—review and editing, S.E.B., N.B., F.H.B., E.J.B., K.F.M. and M.A.O.; visualization, S.E.B., M.A.A. and N.B.; supervision, N.B., F.H.B., E.J.B. and K.F.M.; project administration, F.H.B., E.J.B. and K.F.M.; funding acquisition, F.H.B., E.J.B., K.F.M. and M.A.O. All authors have read and agreed to the published version of the manuscript.

Funding: This research was funded by National Science Foundation grants #2203506 and #2203652 and by a Robert A. Welch Chemistry Departmental Grant #BT-0041 awarded to the Texas A&M University Corpus Christi Chemistry Program.

Institutional Review Board Statement: Not applicable.

Informed Consent Statement: Not applicable.

Data Availability Statement: The original contributions presented in this study are included in the article/Supplementary Materials. Further inquiries can be directed to the corresponding authors.

Acknowledgments: K.F.M. acknowledges the generosity and support of the Ralph E. Klingenmeyer family.

Conflicts of Interest: The authors declare no conflict of interest.

Abbreviations

The following abbreviations are used in this manuscript:

AABS	Amino Acid-Based Surfactant
DLS	Dynamic Light Scattering
CMC	Critical Micelle Concentration
DACH	Diamino Cyclo Hexane

Und-Gly	Undecanoyl-Glycine
Und-Ala	Undecanoyl-L-Alanine
Und-Val	Undecanoyl-L-Valine
Und-Leu	Undecanoyl-L-Leucine
DFT	Density Functional Theory

References

1. Badmus, S.O.; Amusa, H.K.; Oyehan, T.A.; Saleh, T.A. Environmental Risks and Toxicity of Surfactants: Overview of Analysis, Assessment, and Remediation Techniques. *Environ. Sci. Pollut. Res.* **2021**, *28*, 60987–61012. [CrossRef]
2. Raju, S.; Sivamurugan, M.; Gunasagaran, K.; Subramani, T.; Natesan, M. Preliminary Studies on the Occurrence of Nonylphenol in the Marine Environments, Chennai—A Case Study. *J. Basic Appl. Zool.* **2018**, *79*, 52. [CrossRef]
3. García, M.T.; Ribosa, I.; Guindulain, T.; Sánchez-Leal, J.; Vives-Rego, J. Biodegradability and Aquatic Toxicity of Quaternary Ammonium-Based Gemini Surfactants: Effect of the Spacer on Their Ecological Properties. *Chemosphere* **2016**, *154*, 155–160. [CrossRef]
4. Kim, S.; Ji, K.; Shin, H.; Park, S.; Kho, Y.; Park, K.; Kim, K.; Choi, K. Occurrences of Benzalkonium Chloride in Streams near a Pharmaceutical Manufacturing Complex in Korea and Associated Ecological Risk. *Chemosphere* **2020**, *256*, 127084. [CrossRef] [PubMed]
5. Ji, K.; Kim, Y.; Oh, S.; Ahn, B.; Jo, H.; Choi, K. Toxicity of Perfluorooctane Sulfonic Acid and Perfluorooctanoic Acid on Freshwater Macroinvertebrates (*Daphnia magna* and *Moina macrocopa*) and Fish (*Oryzias latipes*). *Environ. Toxicol. Chem.* **2008**, *27*, 2159–2168. [CrossRef]
6. Nagtode, V.S.; Cardoza, C.; Yasin, H.K.A.; Mali, S.N.; Tambe, S.M.; Roy, P.; Singh, K.; Goel, A.; Amin, P.D.; Thorat, B.R.; et al. Green Surfactants (Biosurfactants): A Petroleum-Free Substitute for Sustainability—Comparison, Applications, Market, and Future Prospects. *ACS Omega* **2023**, *8*, 11674–11699. [CrossRef]
7. Guo, J.; Sun, L.; Zhang, F.; Sun, B.; Xu, B.; Zhou, Y. Review: Progress in Synthesis, Properties and Application of Amino Acid Surfactants. *Chem. Phys. Lett.* **2022**, *794*, 139499. [CrossRef]
8. Bordes, R.; Holmberg, K. Amino Acid-Based Surfactants—Do They Deserve More Attention? *Adv. Colloid Interface Sci.* **2015**, *222*, 79–91. [CrossRef] [PubMed]
9. Ananthapadmanabhan, K.P. Amino-Acid Surfactants in Personal Cleansing (Review). *Tenside Surfactants Deterg.* **2019**, *56*, 378–386. [CrossRef]
10. Ansari, N.H.; Shahid, S.; Khan, M.S.; Rizvi, N.Z.; Iqubal, S.M.S.; Bahafi, A. Amino Acid-Based Biosurfactants: Promising and Ecofriendly Biomolecules for Attaining Sustainable Agriculture and Environmental Safety. *Colloid J.* **2025**, *87*, 78–100. [CrossRef]
11. Takassi, M.A.; Zargar, G.; Madani, M.; Zadehnazari, A. The Preparation of an Amino Acid-Based Surfactant and Its Potential Application as an EOR Agent. *Petrol. Sci. Technol.* **2017**, *35*, 385–391. [CrossRef]
12. Mayer, J.D.; Rauscher, R.M.; Fritz, S.R.; Fang, Y.; Billiot, E.J.; Billiot, F.H.; Morris, K.F. An Investigation of the Effect of pH on Micelle Formation by a Glutamic Acid-Based Biosurfactant. *Colloids Interfaces* **2024**, *8*, 38. [CrossRef]
13. Bhatt, J.; Rai, A.K.; Gupta, M.; Vyas, S.; Ameta, R.; Ameta, S.C.; Chavoshani, A.; Hashemi, M. Surfactants: An Emerging Face of Pollution. In *Micropollutants and Challenges*; Chavoshani, A., Hashemi, M., Amin, M.M., Ameta, S.C., Eds.; Elsevier: Amsterdam, The Netherlands, 2020; pp. 145–178. [CrossRef]
14. Abooali, D.; Soleimani, R. Structure-Based Modeling of Critical Micelle Concentration (CMC) of Anionic Surfactants in Brine Using Intelligent Methods. *Sci. Rep.* **2023**, *13*, 13361. [CrossRef] [PubMed]
15. Lu, Y.; Yue, Z.; Xie, J.; Wang, W.; Zhu, H.; Zhang, E.; Cao, Z. Micelles with Ultralow Critical Micelle Concentration as Carriers for Drug Delivery. *Nat. Biomed. Eng.* **2018**, *2*, 318–325. [CrossRef] [PubMed]
16. Lu, Y.; Zhang, E.; Yang, J.; Cao, Z. Strategies to Improve Micelle Stability for Drug Delivery. *Nano Res.* **2018**, *11*, 4985–4998. [CrossRef]
17. Torchilin, V.P. Structure and Design of Polymeric Surfactant-Based Drug Delivery Systems. *J. Control. Release* **2001**, *73*, 137–172. [CrossRef]
18. Wang, Q.; Atluri, K.; Tiwari, A.K.; Babu, R.J. Exploring the Application of Micellar Drug Delivery Systems in Cancer Nanomedicine. *Pharmaceuticals* **2023**, *16*, 433. [CrossRef]
19. Maboudi, A.H.; Lotfipour, M.H.; Rasouli, M.; Azhdari, M.H.; MacLoughlin, R.; Bekeschus, S.; Doroudian, M. Micelle-Based Nanoparticles with Stimuli-Responsive Properties for Drug Delivery. *Nanotechnol. Rev.* **2024**, *13*, 20230218. [CrossRef]
20. Farhoudi, L.; Hosseinikhah, S.M.; Vahdat-Lasemi, F.; Sukhorukov, V.N.; Kesharwani, P.; Sahebkar, A. Polymeric Micelles Paving the Way: Recent Breakthroughs in Camptothecin Delivery for Enhanced Chemotherapy. *Int. J. Pharm.* **2024**, *659*, 124292. [CrossRef]

21. Alvarez, M.A.; Black, N.; Blanco, S.E.; Reid, K.R.; Billiot, E.J.; Billiot, F.H.; Morris, K.F. Influence of Linear Diamine Counterions on the Self-Assembly of Glycine-, Alanine-, Valine-, and Leucine-Based Amphiphiles. *Molecules* **2024**, *29*, 4436. [CrossRef]
22. Maynard-Benson, A.; Alekisch, M.; Wall, A.; Billiot, E.J.; Billiot, F.H.; Morris, K.F. Characterization of Micelle Formation by the Single Amino Acid-Based Surfactants Undecanoic L-Isoleucine and Undecanoic L-Norleucine in the Presence of Diamine Counterions with Varying Chain Lengths. *Colloids Interfaces* **2023**, *7*, 28. [CrossRef]
23. Fletcher, J.; Mahant, G.; Witzleb, T.; Busche, R.; Garcia, M.; Fang, Y.; Billiot, E.J.; Billiot, F.H.; Morris, K.F. NMR Investigation of Counterion Binding to Undecyl LL-Leucinevalanate Micelles. *J. Dispers. Sci. Technol.* **2022**, *45*, 284–295. [CrossRef]
24. Garcia, M.; Black, N.; Billiot, E.; Billiot, F.; Morris, K.; Fang, Y. Chiral Recognition of Dansyl Derivatives with an Amino Acid-Based Molecular Micelle: A Molecular Dynamics Investigation. *Open J. Phys. Chem.* **2021**, *11*, 64–86. [CrossRef]
25. Ramos, Z.; Rothbauer, G.A.; Turner, J.; Lewis, C.; Morris, K.; Billiot, E.; Billiot, F.; Fang, Y. Comparison of Chiral Recognition of Binaphthyl Derivatives with L-Undecyl-Leucine Surfactants in the Presence of Arginine and Sodium Counterions. *J. Chromatogr. Sci.* **2019**, *57*, 54–62. [CrossRef]
26. Rothbauer, G.A.; Rutter, E.A.; Reuter-Seng, C.; Vera, S.; Billiot, E.J.; Fang, Y.; Billiot, F.H.; Morris, K.F. Nuclear Magnetic Resonance Investigation of the Effect of pH on Micelle Formation by the Amino Acid-Based Surfactant Undecyl L-Phenylalaninate. *J. Surfactants Deterg.* **2018**, *21*, 139–153. [CrossRef]
27. Lewis, C.; Hughes, B.H.; Vasquez, M.; Wall, A.M.; Northrup, V.L.; Witzleb, T.J.; Billiot, E.J.; Fang, Y.; Billiot, F.H.; Morris, K.F. Effect of pH on the Binding of Sodium, Lysine, and Arginine Counterions to L-Undecyl Leucinate Micelles. *J. Surfactants Deterg.* **2016**, *19*, 1175–1188. [CrossRef]
28. Ropers, M.H.; Czichocki, G.; Brezesinski, G. Counterion Effect on the Thermodynamics of Micellization of Alkyl Sulfates. *J. Phys. Chem. B* **2003**, *107*, 5281–5288. [CrossRef]
29. Benrraou, M.; Bales, B.L.; Zana, R. Effect of the Nature of the Counterion on the Properties of Anionic Surfactants. 1. CMC, Ionization Degree at the CMC and Aggregation Number of Micelles of Sodium, Cesium, Tetramethylammonium, Tetraethylammonium, Tetrapropylammonium, and Tetrabutylammonium Dodecyl Sulfates. *J. Phys. Chem. B* **2003**, *107*, 13432–13440. [CrossRef]
30. Talapatra, S.K.; Talapatra, B. *Basic Concepts in Organic Stereochemistry*; Springer: Cham, Switzerland, 2022.
31. Rossini, F.D.; Pitzer, K.S. Relabeling of the Cis and Trans Isomers of 1,3-Dimethylcyclohexane. *Science* **1947**, *105*, 647–648. [CrossRef] [PubMed]
32. Chu, Z.; Feng, Y. Thermo-Switchable Surfactant Gel. *Chem. Commun.* **2011**, *47*, 7191–7193. [CrossRef]
33. Xie, H.; Asad Ayoubi, M.; Lu, W.; Wang, J.; Huang, J.; Wang, W. A Unique Thermo-Induced Gel-to-Gel Transition in a pH-Sensitive Small-Molecule Hydrogel. *Sci. Rep.* **2017**, *7*, 8459. [CrossRef] [PubMed]
34. Fernandes, P.Z.; Petricevic, M.; Sobala, L.; Davies, G.J.; Williams, S.J. Exploration of Strategies for Mechanism-Based Inhibitor Design for Family GH99 Endo-α-1,2-Mannanases. *ACS Chem. Biol.* **2023**, *18*, 1474–1482. [CrossRef] [PubMed]
35. Dubin, P.L.; Chew, C.-H.; Davis, R.M. Competition between Monovalent and Divalent Counterions in Micelle Binding. *J. Colloid Interface Sci.* **1996**, *179*, 157–167. [CrossRef]
36. Sammalkorpi, M.; Karttunen, M.; Haataja, M. Ionic Surfactant Aggregates in Saline Solutions: Sodium Dodecyl Sulfate (SDS) in the Presence of Excess Sodium Chloride (NaCl) or Calcium Chloride ($CaCl_2$). *J. Phys. Chem. B* **2009**, *113*, 5863–5870. [CrossRef]
37. Lapidot, Y.; Rappoport, S.; Wolman, Y. Use of Esters of *N*-Hydroxysuccinimide in the Synthesis of *N*-Acylamino Acids. *J. Lipid Res.* **1967**, *8*, 142–145. [CrossRef]
38. Lewis, R.N.A.H.; McElhaney, R.N.; Pabst, G.; Hodzic, A.; Prenner, E.J. Temperature-Dependent Miscibility Behavior of Model Membrane Systems Consisting of a Phosphatidylcholine and a Saturated N-Acyl Amino Acid. *J. Surfactants Deterg.* **2016**, *19*, 1259–1274. [CrossRef]
39. Zana, R. Critical Micellization Concentration of Surfactants in Aqueous Solution and Free Energy of Micellization. *Langmuir* **1996**, *12*, 1208–1211. [CrossRef]
40. Jiang, N.; Li, P.; Wang, Y.; Wang, J.; Yan, H.; Thomas, R.K. Micellization of Cationic Gemini Surfactants with Various Counterions and Their Interaction with DNA in Aqueous Solution. *J. Phys. Chem. B* **2004**, *108*, 15385–15391. [CrossRef]
41. Ono, Y.; Kawasaki, H.; Annaka, M.; Maeda, H. Effects of Micelle-to-Vesicle Transitions on the Degree of Counterion Binding. *J. Colloid Interface Sci.* **2005**, *287*, 685–693. [CrossRef]
42. Bakshi, M.S.; Singh, J.; Kaur, J. Estimation of Degree of Counterion Binding and Thermodynamic Parameters of Ionic Surfactants from Cloud Point Measurements by Using Triblock Polymer as Probe. *J. Colloid Interface Sci.* **2005**, *287*, 704–711. [CrossRef]
43. Aggrawal, R.; Kumari, S.; Gangopadhyay, S.; Saha, S.K. Role of Different States of Solubilized Water on Solvation Dynamics and Rotational Relaxation of Coumarin 490 in Reverse Micelles of Gemini Surfactants, Water/12-s-12.2Br–(s = 5, 6, 8)/n-Propanol/Cyclohexane. *ACS Omega* **2020**, *5*, 6738–6753. [CrossRef]
44. Neese, F. The ORCA Program System. *WIREs Comput. Mol. Sci.* **2012**, *2*, 73–78. [CrossRef]

45. Neese, F.; Wennmohs, F.; Becker, U.; Riplinger, C. The ORCA Quantum Chemistry Program Package. *J. Chem. Phys.* **2020**, *152*, 224108. [CrossRef] [PubMed]
46. Weigend, F.; Ahlrichs, R. Balanced Basis Sets of Split Valence, Triple Zeta Valence and Quadruple Zeta Valence Quality for H to Rn: Design and Assessment of Accuracy. *Phys. Chem. Chem. Phys.* **2005**, *7*, 3297–3305. [CrossRef] [PubMed]
47. Hanwell, M.D.; Curtis, D.E.; Lonie, D.C.; Vandermeersch, T.; Zurek, E.; Hutchison, G.R. Avogadro: An Advanced Semantic Chemical Editor, Visualization, and Analysis Platform. *J. Cheminform.* **2012**, *4*, 17. [CrossRef] [PubMed]
48. Harris, D.C. *Quantitative Chemical Analysis*, 9th ed.; Macmillan: New York, NY, USA, 2011.

Disclaimer/Publisher's Note: The statements, opinions and data contained in all publications are solely those of the individual author(s) and contributor(s) and not of MDPI and/or the editor(s). MDPI and/or the editor(s) disclaim responsibility for any injury to people or property resulting from any ideas, methods, instructions or products referred to in the content.

molecules

MDPI

Article

The Properties of the Monolayers of Sorbitan Lipids as Informative Factors on the Hydrophilic–Lipophilic Balance Value of Their Mixtures, Proposed for Dermatological Applications

Remigiusz Zapolski [1], Monika Gasztych [1], Beata Jastrząb-Miśkiewicz [2], Alina Jankowska-Konsur [2] and Witold Musiał [1,*]

[1] Department of Physical Chemistry and Biophysics, Pharmaceutical Faculty, Wroclaw Medical University, Borowska 211, 50-556 Wroclaw, Poland; remigiusz.zapolski@gmail.com (R.Z.); monika.gasztych@umw.edu.pl (M.G.)

[2] University Centre for General and Oncological Dermatology, Wroclaw Medical University, Borowska 213, 50-556 Wroclaw, Poland; bajastrzab@gmail.com (B.J.-M.); alina.jankowska-konsur@umw.edu.pl (A.J.-K.)

* Correspondence: witold.musial@umw.edu.pl; Tel.: +48-71-784-02-28

Abstract: This study investigates the correlation between the hydrophilic–lipophilic balance (HLB) values and the π–A isotherm parameters of surfactant monolayers composed of sorbitan esters, specifically sorbitan monopalmitate, sorbitan tristearate, sorbitan monooleate, and sorbitan sesquioleate. The surfactant mixtures were prepared, and their π-A isotherms were recorded. The HLB values calculated for each mixture were in the range 2.10–6.70. The HLB values were compared to compression parameters, including the ratios of the slopes and the ratios of the intercepts, which were between 0.19 and 4.00 and between 0.64 and 1.77, respectively, across the monolayer compression stages. The findings indicate a significant relationship between HLB values and isotherm parameters, particularly for systems with sorbitan monooleate and sorbitan sesquioleate. A value of determination coefficient of 0.95 was found for the linear equation representing the slope ratios as a function of HLB, whereas the intercept ratios, as a linear function of HLB, gave a lower value of 0.71. The results allow for the use of the π–A Langmuir isotherm to experimentally estimate the value of the HLB in mixtures of the sorbitol esters of fatty acids, whose value is an important parameter in the selection of optimized topical and transdermal formulations, highlighting the specific formulations that enhance active substance delivery while minimizing skin irritation potential.

Keywords: surfactant; HLB; π–A isotherms; surface pressure measurements

1. Introduction

The effective delivery of active substances into and through the skin is crucial for various topical, transdermal, dermatological, and personal care applications. Although small, lipophilic molecules can traverse the skin with relative ease, the penetration of larger, hydrophilic molecules is significantly impeded by the stratum corneum's low permeability [1–3].

Chemical agents such as surfactants, fatty acids, esters, and amines can be employed to enhance penetration. These substances infiltrate the skin and disrupt the structural organization and packing of the lipids and proteins within the stratum corneum [1,4].

While chemical penetration enhancers effectively increase skin permeability for certain molecules, their use may be associated with irritation, limiting their applicability in practical scenarios [5,6].

Among these surfactants, the sorbitan esters from the so-called Span group, specifically sorbitan monopalmitate, sorbitan tristearate, sorbitan monooleate, and sorbitan sesquioleate, have garnered significant attention for their multifaceted applications in topical formulations [4,5]. The basic structural characterization of the molecules is presented below in Figure 1.

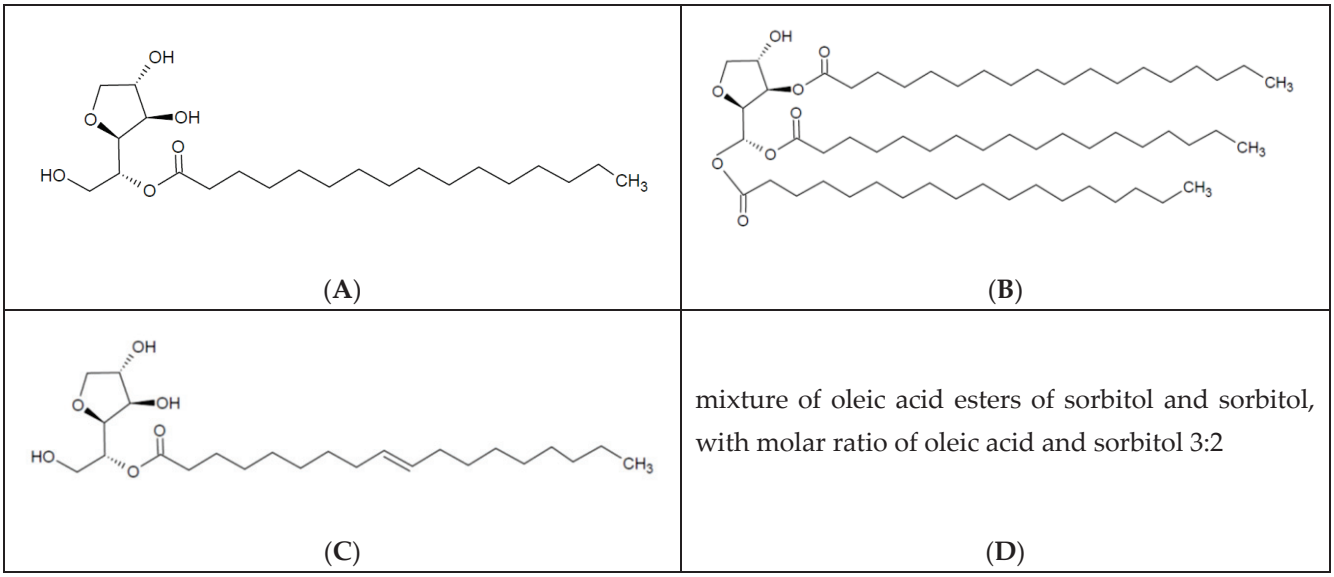

Figure 1. Schematic chemical structure of evaluated spans: (**A**) sorbitan monopalmitate (S40), (**B**) sorbitan tristearate (S65), (**C**) sorbitan monooleate (S80), and (**D**) sorbitan sesquioleate (S83).

Sorbitan monooleate is widely utilized in the formulation of oil-in-water emulsions, where it facilitates the solubilization of lipophilic drugs while improving the sensory attributes of creams and lotions [7]. Importantly, a recent study reported on cubosomes and hexosomes stabilized by sorbitan monooleate as a biocompatible nanoplatform for targeting skin metastatic human melanoma [8]. Similarly, sorbitan monopalmitate has been shown to enhance moisture retention in various topical applications, proving beneficial in formulations designed for dry or sensitive skin [7]. Furthermore, the study conducted by Abdelkader et al. focused on the formulation and optimization of lipid- and poloxamer-tagged niosomes for the dermal delivery of terbinafine. In this study, different lipids/surfactants with two different molar ratios were investigated with sorbitan monopalmitate-based niosomes. Both alternatives were identified as potential substitutes for cholesterol as bilayer membrane stabilizers for terbinafine, demonstrating superior antifungal activities in vitro, as indicated by the inhibition zones against Candida albicans ATCC 60913 [9]. Sorbitan tristearate and sorbitan sesquioleate are particularly effective in stabilizing emulsions and improving the delivery of active substances, making them suitable for formulations targeting dermatological conditions such as eczema [5,7,10]. Despite their benefits, the safety profiles of Span surfactants must be meticulously evaluated to mitigate potential adverse effects. While generally considered safe for topical use, some studies report skin irritation or sensitization, particularly at higher concentrations. For example, sorbitan sesquioleate, commonly incorporated in various highly potent to super-potent corticosteroids, has been reported as an important contact allergen [11,12]. Therefore,

careful formulation practices and thorough safety assessments are paramount to ensure the well-being of consumers using these surfactants.

A hydrophilic–lipophilic balance (HLB) value plays an important role in the prediction of the properties of a formulation, as well as being beneficial to production procedures. Depending on the substance which should be applied topically on the skin surface, various formulations may be developed to ensure proper or modified drug release and transport through the skin. The HLB level of the surfactant added to the biphasic or multicomponent mixture may enable the formation of creams or ointments with an internal structure governed by interfacial phenomena. The HLB value influences, i.a., the type of emulsion formed, o/w or w/o; in some cases, multiple emulsions may emerge. The programmed HLB value of some formulation components influences the solubility of the active pharmaceutical ingredient. The HLB scale is stretched between ca. 1, with antifoaming agents at the minimal edge, and ca. 20, with solubilizing agents [13–15]. The surfactants and their mixtures with HLB values of 3–6 have a potential to stabilize w/o emulsions, whereas the higher values between 8 and 16 usually favor the systems with o/w emulsions. Between the surfactants applied for the stabilization of the emulsions w/o there are nonionic surface-active components based on sorbitan and long chain fatty acids [16–19]. Within this group sorbitan monopalmitate, sodium tristearate, sodium monooleate, as well as sodium sesquioleate may be applied to formulate stable systems with a continuous lipid phase or as cofactors in other types of formulation for controlled drug delivery [20–23]. The basic properties of this group are gathered in Table 1.

Table 1. Selected properties of evaluated sorbitan esters.

AN	CSN	PG	NPG	NCC	NC	DB	M
S40	Sorbitan monopalmitate	1,4-sorbitan	Palmitic acid	16	1	N	402.57
S65	Sorbitan tristearate	1,4-sorbitan	Stearic acid	18	3	N	963.54
S80	Sorbitan monooleate	1,4-sorbitan	Oleic acid	18	1	Y	428.6
S83	Sorbitan sesquioleate *	1,4-sorbitan	Oleic acid	18	1.5	Y	1175.7

AN—abbreviated name, CSN—common synonym name, PG—polar group, NPG—nonpolar group, NCC—number of chain carbons, including carboxyl group, NC—number of chains per sorbitol molecule, DB—double bond, M—molar mass, and * indicates a mixture of oleic acid esters and hexitol anhydride.

An evaluation of an HLB value encounters numerous challenges. An HLB value can be interpreted as the fraction of hydrophilic functional groups compared to lipophilic functional groups, presented as a single number. However, determination of this value can be performed by both experimental and computational methods. Surface activity is a factor that is strongly related to the amphiphilic properties of molecules and can be related to the HLB value. In our former work, we investigated the possibility of excavating the HLB of surfactants systems from the data obtained in experiments on the monolayers of surfactants, using algorithms from the response surface methodology, and on the mixtures of sorbitan derivatives, with sorbitan monopalmitate as the main component, modified by the addition of other sorbitan esters [24]. The evaluation of dependency surface pressure–surface area was proposed by Langmuir and developed by numerous researchers [25]. On the other hand, the well-known parameters ascribed to the course of isotherms are the compression factor (E) or compression modulus, calculated as a ratio of surface pressure change ($\Delta\pi$) to area change (ΔS) at a certain surface area (A). The plot of E against S may be informative in terms of the mechanical properties of the monolayer [26].

$$E = -A\left(\frac{\Delta\pi}{\Delta A}\right)_T \tag{1}$$

The elastic properties of monolayers are presented in varied forms, including the reciprocal compression modulus, compressibility (*C*) [27].

$$C = \frac{1}{E} = -\frac{1}{A}\left(\frac{\Delta A}{\Delta\pi}\right)_T \tag{2}$$

However, the data are derived directly from the slopes of the graphs, which represent the change of the $\Delta\pi$ with the decreasing surface of the monolayer, as it was expressed by Vollhardt and Fainerman, so the basic approach is anchored in the slope of the linear surface pressure–surface area relationship [28].

The aim of this study was to search for distinct parameters of π-A isotherms that can reflect the HLB value in surfactant mixtures prepared based on sorbitan sesquioleate with other surfactants forming a sorbitan ester group. The specific aim was to evaluate the π-A isotherms of surfactant mixtures and to identify the relationship between the slopes or interceptions of the linear segments of π-A isotherms and the HLB values of the mixtures. The potential relationship could be used, after further validation, in a pioneering HLB quantification from a direct isotherm evaluation.

2. Results

2.1. Recorded Surface Pressure of Evaluated Monolayers

The surface pressure was measured in the range of a surface area of ca. 900–12,000 mm^2. The gathered data recorded for the monolayers containing various proportions of sorbitan monopalmitate and sorbitan sesquioleate were in the range between 0.9 and 60.9 mN/m, with the highest values through the entire process of compression recorded for the system which contained the surfactants in the proportion 0.72:0.28, respectively (Figure 2A, S4083D).

The monolayers composed of a mixture of sorbitan tristearate and sorbitan sesquioleate were characterized by surface pressures between 0.9 and 67.0 mN/m: however, the highest localization of an isotherm on the graph was recorded in the case of the monolayer composed of sorbitan tristearate only (Figure 2B, S6500A). The above-mentioned systems had the plots of a shape close to the often-recognized pattern of the so-called π-A isotherm, and characteristic inflection points were observed on part of the considered plots (Figure 2A,B). The course of the relationship between surface pressure and the monolayer surface of systems with sorbitan monooleate and sorbitan sesquioleate was shaped differently in comparison to the formerly presented case, with long parts of almost straight-line plots (Figure 2C).

As mentioned above, the sorbitan sesquioleate is a mixture of sorbitan monooleate and oleic acid. Two molecules of sorbitan monooleate are accompanied by one molecule of oleic acid. Actually, the combination of S80 with S83 should be considered as dilution of sorbitan monooleate by oleic acid; one added mole of sorbitan sesquiolete adds 1/3 mole of oleic acid, and 2/3 moles of sorbitan monoleate. The dilution is not very intensive, thus the plots on Figure 2C are shaped differently compared to Figure 2A,B. From Figure 2C and the proportions of S80 and S83, it may be concluded that the plots variability is less expressed, as in the case of S83 added to S40 or S65. The plots on Figure 2C are close to each other (cf. the scale on the y-axis of Figure 2C).

The range for the surface pressure was 1.1–46.6 mN/m. The highest values for surface pressure were recorded for the system composed of the surfactants in the molar composition 0.72:0.28, as in the case of the system composed on the base of sorbitan monopalmitate (S8083C).

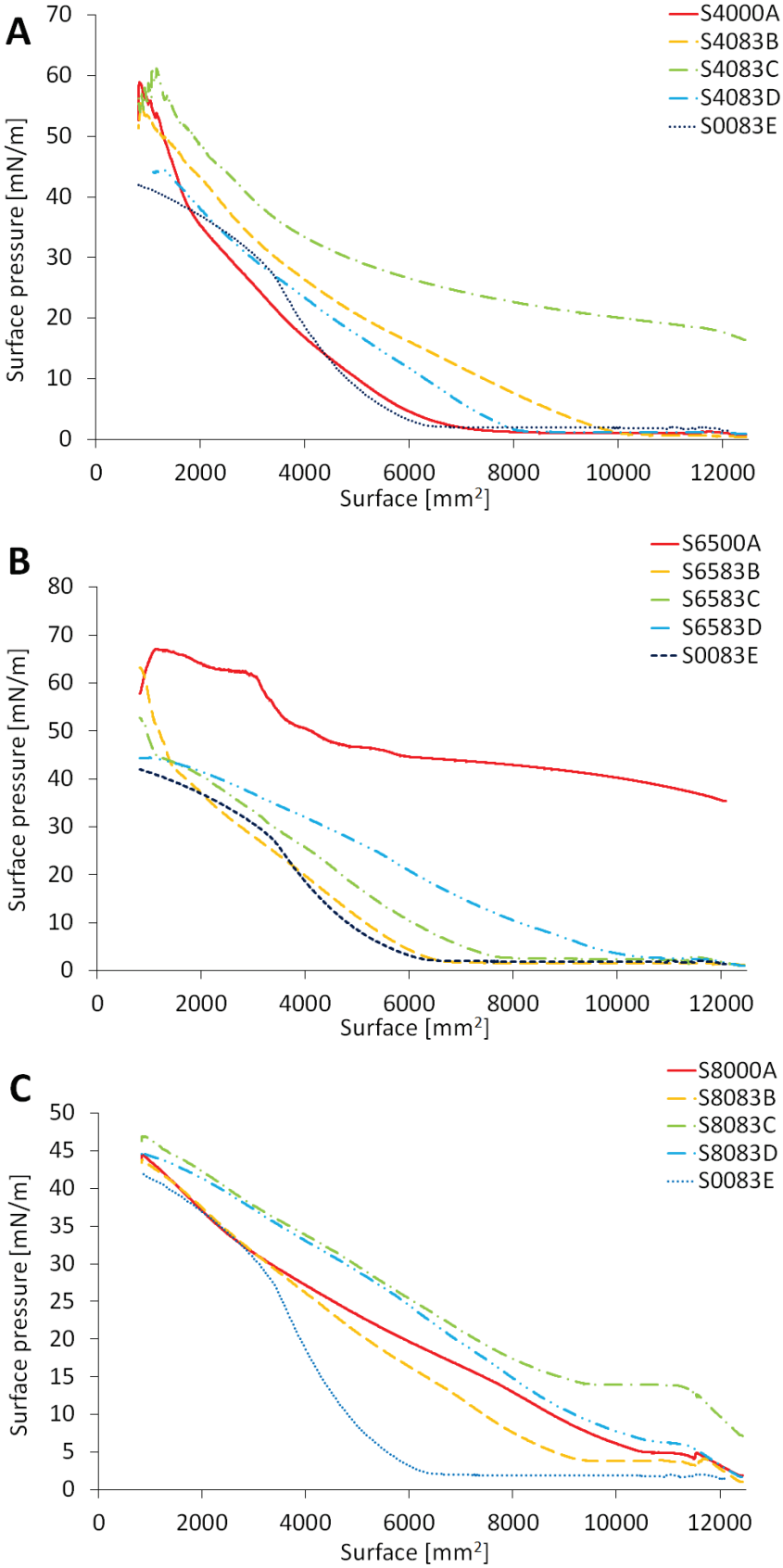

Figure 2. Exemplification of isotherms of evaluated sorbitan esters and the mixtures: S40:S83 (**A**), S65:S83 (**B**), and S80:S83 (**C**); the composition and abbreviations of presented isotherms are given in Table 5 in Section 4.

2.2. The Stages of Compression Identified by Linear Sections of the Plots

It was possible to distinguish on the plots the stages of the compression processes. The slopes, and the intercepts of the respective equations, which reflected the two main stages, were gathered in Table 2. The calculated slopes of the first stage of compression (a_1) were lower in standard numbers, when compared to the slopes calculated for the second stage of compression (b_1) for the preparations composed of sorbitan monopalmitate and doped by sorbitan sesquioleate (Table 2, S4000A-D). A similar tendency was observed for the intercepts of the y-axis; however, the monolayer composed of sorbitan sesquioleate only did not fit that tendency (Table 2, S0083E).

Table 2. Linear equations y = ax + b for the first (a_1, b_1) and second (a_2, b_2) observed stages on π–A isotherms of the assessed systems. The slope was calculated as μN/mm^3, and reflects the ratio π:A, whereas the intercept has a unit of mN/m, and reflects the intercept of the analyzed plot section with the y-axis. The composition of surfactants mixtures is presented in Table 5. The R2 is the determination coefficient.

Surfactants Mixture	Slope (a_1)	Intercept (b_1)	x_1 Intercept for y = 0	R^2	Slope (a_2)	Intercept (b_2)	x_2 Intercept for y = 0	R^2	Slopes Ratio a_1:a_2	Intercepts Ratio b_1:b_2
S4000A	-9.50×10^{-3}	54.12	5.70×10^3	0.9999	-2.63×10^{-2}	84.24	3.20×10^3	0.9986	2.77	0.64
S4083B	-9.90×10^{-3}	62.97	6.36×10^3	0.999	-1.36×10^{-2}	66.87	4.92×10^3	0.9834	1.37	0.94
S4083C	-1.13×10^{-2}	71.21	6.30×10^3	0.9975	-1.72×10^{-2}	79.99	4.65×10^3	0.9852	1.52	0.89
S4083D	-5.70×10^{-3}	46.14	8.09×10^3	0.9995	-9.50×10^{-3}	57.02	6.00×10^3	0.9996	1.67	0.81
S6500A	-2.16×10^{-2}	127.42	5.90×10^3	0.9947	-4.00×10^{-3}	72.17	1.80×10^4	0.9731	0.19	1.77
S6583B	-2.94×10^{-2}	85.031	2.89×10^3	0.9914	-5.19×10^{-2}	108.58	2.09×10^3	0.9932	1.77	0.78
S6583C	-7.80×10^{-3}	56.482	7.24×10^3	0.9994	-3.12×10^{-2}	79.535	2.55×10^3	0.9877	4.00	0.71
S6583D	-5.90×10^{-3}	56.184	9.52×10^3	0.9985	-5.00×10^{-3}	51.78	1.04×10^4	0.9998	0.85	1.09
S8000A	-4.10×10^{-3}	43.63	1.06×10^4	0.9994	-6.60×10^{-3}	50.30	7.62×10^3	0.9996	1.61	0.87
S8083B	-4.40×10^{-3}	42.94	9.76×10^3	0.9995	-5.90×10^{-3}	49.25	8.35×10^3	0.9992	1.34	0.87
S8083C	-4.20×10^{-3}	50.56	1.20×10^4	0.9981	-4.20×10^{-3}	50.58	1.20×10^4	0.9932	1.00	1.00
S8083D	-4.10×10^{-3}	49.64	1.21×10^4	0.9995	-2.40×10^{-3}	46.68	1.95×10^4	0.9964	0.59	1.06
S0083E	-1.33×10^{-2}	71.68	5.39×10^3	0.9992	-4.00×10^{-3}	45.45	1.14×10^4	0.9975	0.30	1.58

The acronyms and composition of evaluated systems are given in Table 5 in Section 4.

The maximal and minimal absolute values of the slopes for the preparations composed of sorbitan tristearate and doped with sorbitan sesquioleate in the first stage were 2.94×10^{-2} and 5.90×10^{-3}, respectively. The second stage of compression resembled absolute values in the range of 4.00×10^{-3} to 5.19×10^{-2}. The maximal and minimal interceptions represented the values of 127.42 and 51.78, respectively (Table 2, S6500A-D).

In the case of the monolayers prepared with the use of sorbitan monooleate and sorbitan sesquioleate (Table 2, S8000A-D), the absolute values of a_1 were closer to each other between 4.10×10^{-3} and 4.40×10^{-3}, compared to other types of mixtures. The absolute a_2 values were between 2.40×10^{-3} and 6.60×10^{-3}. The variability between the hypothetical first and second stages in the terms of intercepts (b_1, b_2) was less expressed, when compared to the preparations of sorbitan monopalmitate or sorbitan tristearate.

The determination coefficients for the selected linear sections of the graphs were in the ranges of 0.9914–0.9999 and 0.9731–0.9998, for the first and second stages of the process, respectively, as is presented in Table 2.

2.3. HLB Values of Evaluated Systems

In Table 3, we gathered the calculated values of the prepared surfactants mixtures, according to the values of HLB presented in the available bibliography. The highest levels of HLB were ascribed to the systems composed of sorbitan monopalmitate with sorbitan sesquioleate in the range between 4.25 and 5.62 (Table 3, S40:S83). The intermediate values were found for the systems comprising sorbitan monooleate and sorbitan sesquioletae, which were in the limits of 3.98–4.06 (Table 3, S80:S83). The lowest values were ascribed to the systems of sorbitan tristearate and sorbitan sesquioleate, i.e., 2.61–3.39 (Table 3, S65:S83). In the same table, we gathered the values of HLB for the systems with single surfactants, which were between 2.10 for the monolayer composed of sorbitan tristearate (S6500A) and 6.70 when the monolayer of sorbitan monopalmitate was considered (S4000A). The sorbitan monooleate and sorbitan sesquioleate were characterized by intermediate values of 4.30 and 3.70, respectively.

Table 3. Calculated HLB values of evaluated systems; the fractional HLB of the applied surfactants were treated as additive values. The basic data were established from the literature [29–31].

Monolayer type	S40:S83	HLB	S65:S83	HLB	S80:S83	HLB
Evaluated samples	S4000A	6.70	S6500A	2.10	S8000A	4.30
	S4083B	5.62	S6583B	2.61	S8083B	4.06
	S4083C	5.11	S6583C	3.01	S8083C	3.98
	S4083D	4.25	S6583D	3.39	S8083D	3.86
	S0083E *	3.70	S0083E *	3.70	S0083E *	3.70

* The HLBs are identical but were presented separately for clear evaluation; the composition of the evaluated mixtures of the surface-active agents are given in molar fractions.

3. Discussion

3.1. Recorded Surface Pressure of Evaluated Monolayers

The recorded isotherms of the monolayers composed of sorbitan monopalmitate only (Figure 2A, S4000A), as well as the sorbitan sesquioleate only (Figure 2B, S0083E) monolayers pass at similar values on the common graph; however, in the case of sorbitan sesquioleate, we did not observe any characteristic curve break, which is often ascribed to the destruction of the monolayer. Unfortunately, the data from the binary monolayers did not have conclusive results (Figure 2A, S4083B-D). However, the presence of sorbitan monopalmitate ensures the appearance of a characteristic peak in the isotherms of monolayers also containing sorbitan sesquioleate, which was observed below 2000 mm^2. It may be assumed that the sorbitan monopalmitate modified the structure of the monolayer to enable its breakage. In the case of pure sorbitan sesquioleate, the monolayer possibly possesses a high amount of spare space between the molecules, or its composition allows the layers to slide freely without breaking.

The apostasy from the standard shape of π-A in the case of S65500A sample is similar to the deviation of dioleoyl-sn-glycerophosphatidylcholine (DOPC) from dipalmitoyl-sn-glycerophosphatidylcholine (DPPC), observed by Anton et al. [32] during the study of a component of a pulmonary surfactant. In the case of S65 only, similar to the case of DOPC, the relatively huge nonpolar biforked chains may enable a systemic decrease in the monolayer surface area within a relatively stable surface pressure range. Oppositely, the DPPC was characterized by a decisive increase in surface pressure with the decrease in surface area. In the case of S65, the addition of a co-surfactant could diminish the range of stable surface pressure.

Doping sorbitan sesquioleate with a monolayer of sorbitan tristearate resulted in a very significant reduction of the surface pressure value (Figure 2B, S6583B). However, the further addition of sorbitan sesquioleate reversed the trend. The higher concentration of sorbitan sesquioleate moved the results (Figure 2B, S6583C,D) again towards the plot of the sorbitan tristearate monolayer (Figure 2B, S6500A). These phenomena confirm some interactions which could be further studied. The interactions between surfactants in a mixed monolayer are of high interest, and were studied, i.a., by Rosen and Zhou who assessed the $\beta\sigma$ parameter, for which a negative value may confirm positive forces between the molecules of the surfactant [33]. Due to Lu et al., the interactions may be elucidated by relative molecular bulk based on different numbers of acyl chains and POE substituents in the molecules of surfactants [34]. One of the reasons for the observed variability of the S65:S83 system may be the low aqueous solubility of sorbitan tristearate [35,36].

The isotherms obtained from the measurements of the surface pressure with the decreasing area of the monolayers formed of sorbitan monooleate (Figure 2C, S8000A), as well as sorbitan monooleate and sorbitan sesquioleate (Figure 2C, S8083B-D), revealed elongated plots, with parallel sections, whereas the monolayer collapse was rather vague. As was mentioned above, the lack of a distinct breakage of the curve, which was reflected by the low slope ratio a_1:a_2 in Table 2, may be attributed to the high fluidity of the systems with sorbitan sesquioleate. The addition of sorbitan monooleate would not influence the course of the isotherm much, due to the structural similarities of sorbitan monooleate and sorbitan sesquioleate. In this study, we limited the experimental design to the tests available in some basic industrial laboratories focused on application research.

3.2. Calculated HLB

The determination of HLB values by calculative and analytical methods is an important task, with high consequences for the preparative and analytical procedures applied for the dermatological forms of drugs. The possibility of a formation of the required type of emulsions, as well as the solubilizing properties of surfactants, is strictly connected with the deciding influence of HLB. The hydrophilic–lipophilic balance of the assessed systems may be calculated according to the equations given by Griffin [37] and discussed in detail, i.a., by Pasquali et al. [38]. Table 4 covers the mostly accepted values of HLB of the assessed surfactants, and the resulting HLB of their mixtures, calculated on an arithmetic basis. As is clear from Table 3, the increasing fractions of sorbitan sesquioleate stimulated a decrease in the HLB in the mixtures with sorbitan monopalmitate and with sorbitan monooleate. Oppositely, when sorbitan sesquioleate was gradually added to sorbitan tristearate, the HLB increased.

Table 4. Linear equation, y = ax + b, for the following relations: slope ratios v. HLB, and intercept ratios v. HLB, with values from Table 2; the plots are depicted in Figure 3.

Type of Composition	Slopes Ratio a_1:a_2 v. HLB		Intercepts Ratio b_1:b_2 v. HLB	
	Equation	Determination Coefficient	Equation	Determination Coefficient
S40:S83	y = 0.6349x − 1.6969	0.7204	y = −0.227x + 2.1244	0.5585
S65:S83	y = 0.0004x + 1.4185	3.0×10^{-8}	y = −0.0848x + 1.4352	0.0129
S80:S83	y = 2.3215x − 8.272	0.9468	y = −1.1015x + 5.4595	0.7118

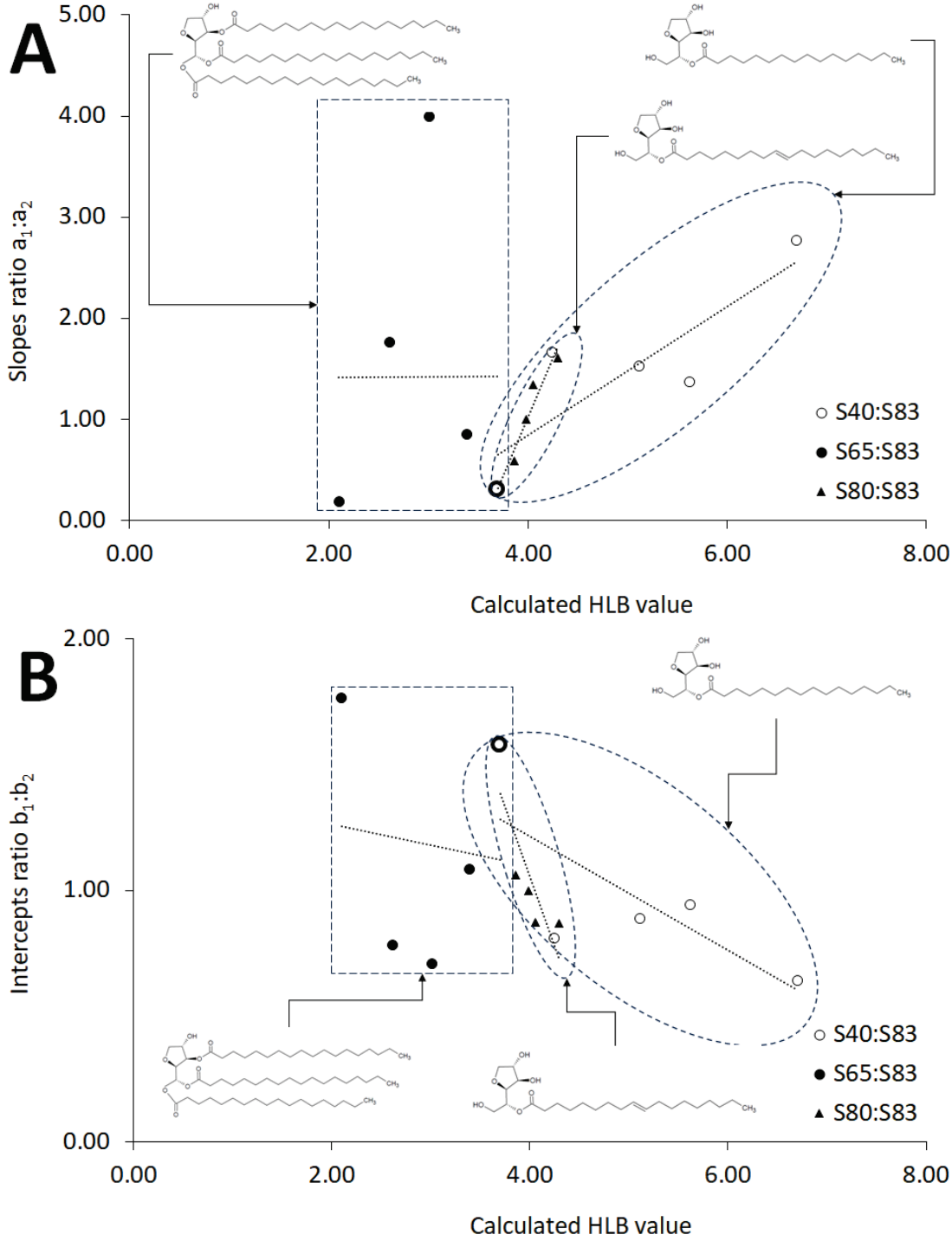

Figure 3. The influence of the calculated hydrophilic–lipophilic balance value (HLB) on (**A**) the ratio of the linear sections' slopes in the first and second stages of compression (a_1:a_2) and on (**B**) the ratio of the linear sections' y-intercepts (b_1:b_2), representing the individual stages of compression on π–A isotherms, detailed in the text. The acronyms S40:S83, S65:S83, S80:S83 describe the evaluated seria of assessed surfactant mixtures according to the Table 5—Section 4.

3.3. The Stages of Compression Identified by Linear Sections of the Plots in the Context of HLB Values

The course of the π–A isotherm is determined both by structural factors, as well as by the forces acting between the molecules densely packed in the late stages of compression [39]. In our previous work, we described the model, which may elucidate and predict

the values of HLB using elasticity modules and molecules surfaces [24]. However, we concentrated on another, more simplified approach to understand if there is linear coincidence between the direct parameters of π–A isotherms and an HLB value. Therefore, another set of surfactants was used. The selected surfactant systems were characterized by various basic HLB values (Table 2), and structures (Figure 1), different from those studied formerly by our team. The ratios of the slopes of the linear sections of the plots of the π–A isotherms, as well as the interceptions of the extrapolations of the sections, turned out to be the most promising (Figure 3 and Table 4).

The linear regression applied to the plot, which represented the relationship of the ratios of the slopes for HLBs, gave the highest determination coefficients for the systems with sorbitan monooleate and sorbitan sesquioleate (S80:S83, Table 4).

The lowest determination coefficient was definitely obtained for the seria of systems composed of sorbitan tristearate and sorbitan sesquioleate (S65:S83, Table 4). In the case of data obtained from the monolayers based on sorbitan monopalmitate and sorbitan sesquioleate (S40:S83, Table 4), the determination coefficients were on the intermediate level. Similar dependence was observed in the case of the interception ratios. However, the regression revealed that the most appropriate factor may be the slope ratio, which was 0.9468 for the S80:S83 system.

The high determination coefficient for the linear regression of the slope ratio and HLB in the case of the monolayers composed of monooleate derivatives (S80:S83) may be ascribed to the similarity in the components of sorbitan monooleate and sorbitan sesquioleate. In fact, sorbitan sesquioleate contains in its composition a fraction of sorbitan monooleate. Thus, the addition of the doping surfactant in this case alters non-extensively the monolayers' structure. Another factor which may add to the high determination coefficient may be the close HLB value of both surfactants, which are 3.70 and 4.30, respectively. In the system with the lowest determination coefficient, the molecular structures were more different in terms of the number of carbon chains attached to the sorbitan core, as well as the HLB values which were definitively distant at 2.10 and 6.70, respectively. The intermediate situation was ascribed to the system S40:S83, where both the distance between the HLB values as well as the structural differences were less expressed—both surfactants included one carbon chain connected to the sorbitan, although with varied bonds, and the sorbitan monopalmitate was saturated and the sorbitan sesquioleate was non-saturated. The relationship between π-A isotherms and HLB may be more easily assessed in the mixtures of surfactants with similar structural patterns in the future. According to the studies of other authors, amphiphilic properties may influence the behavior of compressed monolayers [40–43]. Thus, the range of HLBs may be of high importance in this process, which should be further developed based on the presented results, and the data gathered in our former work [24] for dermatological and pharmaceutical applications.

The proposed HLB evaluation method can enable a quick comparison of some new surfactants evaluated in Langmuir balance during the development of innovative surfactants and give practical insight into the properties of newly proposed or evaluated surfactants and surfactant mixtures. An interesting question is also whether the parameters important for the evaluation of the surfactant structure can also serve as an indicator of their direct application value.

4. Materials and Methods

4.1. Materials

Span 40 (sorbitan monopalmitate), Span 65 (sorbitan tristearate), Span 80 (sorbitan monooleate), Span 83 (sorbitan sesquioleate), and all of purity > 99% were purchased from

Merck, Warszawa, Poland. Deionized water with a conductivity below 2 μS/cm was used in the experiments. Solutions of surfactant mixtures for the monolayer preparations were prepared in chloroform (p.a. purity). Isopropyl alcohol (p.a. purity) was used to clean the Langmuir trough.

4.2. Composition of the Evaluated Mixtures of Surfactants

The assessed surfactants were dissolved in chloroform of p.a. purity. The stock solutions' concentrations were within the range of 1 mg/mL. Mixtures of the required molar fractions were obtained by mixing the calculated volumes of stock solutions immediately before application onto the subphase. The volume of the applied surfactant solutions was set at 5 microliters. The measurements were performed at 25 +/− 1 °C. The composition of the resulting solutions are presented in Table 5.

Table 5. Composition of evaluated surfactants systems.

Monolayer Type	S40:S83		Monolayer Type	S65:S83		Monolayer Type	S80:S83	
Components	Molar Fraction		Components	Molar Fraction		Components	Molar Fraction	
	S40	S83		S65	S83		S80	S83
S4000A	1.00	0.00	S6500A	1.00	0.00	S8000A	1.00	0.00
S4083B	0.84	0.16	S6583B	0.73	0.28	S8083B	0.80	0.20
S4083C	0.72	0.28	S6583C	0.48	0.52	S8083C	0.71	0.29
S4083D	0.39	0.61	S6583D	0.23	0.77	S8083D	0.50	0.50
S0083E *	0.00	1.00	S0083E *	0.00	1.00	S0083E *	0.00	1.00

* These compositions are identical but were presented separately for clear evaluations; the composition of the evaluated mixtures of surface-active agents are given in molar fractions.

4.3. Surface Pressure Measurements

The π-A isotherms were recorded in a Kibron Micro Trough (Kibron, Helsinki, Finland). A measuring element in the form of a platinum rod was flame-cleaned with a gas burner. FilmwareX 4.0 was used to control the experiment and to record the results. The calibration of the device is based on the tabulated value of the subphase surface tension and the standard mass of a detector. The chloroform (Merck, Warszawa, Poland) solution of the tested surfactants and their mixtures were placed 5 cm apart in distance and 5 cm away from one of the barriers. After completion of the evaporation of the solvent, which followed the 15 min of monolayer conditioning, the measurements started. Externally applied transparent coating protected the subphase against solid molecules from the air. The barrier speed was 14.5 mm/min.

4.4. Calculation of the Selected Parameters of the Evaluated π-A Isotherms

On the obtained plots of π-A isotherms, the segments representing the first and second stages of compression were selected according to the linear sections of the plots. The evaluated sets of data were limited to the segments with high Pearson's coefficients. The respective slopes and interceptions with the y-axis were calculated due to the linear equation $y = ax + b$, obtained from linear regression calculations.

4.5. Calculation of HLB of the Assessed Surfactants Mixtures

The HLB values were calculated according to the Griffin concept of the balance [14]. The fractional HLB of the applied surfactants were treated as additive values. The following

formula was used, where the index of HLB by Griffin of the selected surfactant (HLB_i) is multiplied by his weight fraction in the system (f_i):

$$HLB = \sum HLB_i \times f_i \tag{3}$$

5. Conclusions

We identified some possible patterns between the calculated values of HLB for the evaluated surfactants systems and the parameters of π–A isotherms obtained from monolayer compression studies. The selection of the ratio of the slope in the first stage of monolayer compression to the second stage of the layer compression enabled a comparison of the considered value of HLB to the recorded π–A isotherms. The relation of the calculated HLB values and the registered intercepts ratios was most remarkable in the case of the systems containing sorbitan monooleate and sorbitan sesquioleate. The relationship of the slope ratio to HLB was linear, with a coefficient of determination of 0.95, while the linearization of the relationship of the intercept ratio to HLB gave a lower coefficient of determination of 0.71. In the systems composed of spans 65 and 80, as well as the systems with spans 40 and 83, the relation was inexpressive. In summary, it is possible to reveal functional relationships that may enable the recovery of HLB from Langmuir monolayer studies, i.e., the slope and interception of the π-A isotherms. However, further studies with Langmuir balance are required to excavate more data on the relations between π-A isotherms and HLB value, including a visualization of the monolayers in Brewster angle microscopy or scanning electron microscopy.

Author Contributions: Conceptualization, R.Z. and W.M.; methodology, R.Z. and W.M.; formal analysis, R.Z., M.G., W.M. and A.J.-K.; investigation, R.Z. and W.M.; resources, W.M.; data curation, R.Z. and W.M.; writing—original draft preparation, R.Z., W.M., M.G., B.J.-M. and A.J.-K.; writing—review and editing, R.Z., W.M., M.G., B.J.-M. and A.J.-K.; visualization, R.Z., W.M. and B.J.-M.; supervision, W.M.; project administration, W.M.; funding acquisition, W.M. All authors have read and agreed to the published version of the manuscript.

Funding: This research was funded by Wroclaw Medical University—grants no: SUBK.D060.22.078 and SUBZ.D060.24.091.

Institutional Review Board Statement: Not applicable.

Informed Consent Statement: Not applicable.

Data Availability Statement: The original contributions presented in this study are included in the article. Further inquiries can be directed to the corresponding author.

Conflicts of Interest: The authors declare no conflicts of interest.

References

1. James-Smith, M.A.; Hellner, B.; Annunziato, N.; Mitragotri, S. Effect of surfactant mixtures on skin structure and barrier properties. *Ann. Biomed. Eng.* **2011**, *39*, 1215–1223. [CrossRef] [PubMed]
2. Pokhrel, D.R.; Sah, M.K.; Gautam, B.; Basak, H.K.; Bhattarai, A.; Chatterjee, A. A recent overview of surfactant-drug interactions and their importance. *RSC Adv.* **2023**, *26*, 17685–17704. [CrossRef]
3. Juhász, Á.; Ungor, D.; Berta, K.; Seres, L.; Csapó, E. Spreadsheet-based nonlinear analysis of in vitro release properties of a model drug from colloidal carriers. *J. Mol. Liq.* **2021**, *328*, 115405. [CrossRef]
4. Strati, F.; Neubert, R.H.H.; Opálka, L.; Kerth, A.; Brezesinski, G. Non-ionic surfactants as innovative skin penetration enhancers: Insight in the mechanism of interaction with simple 2D stratum corneum model system. *Eur. J. Pharm. Sci.* **2021**, *157*, 105620. [CrossRef] [PubMed]

5. Lanigan, R.S.; Yamarik, T.A.; Cosmetic Ingredient Review Expert panel. Final report on the safety assessment of sorbitan caprylate, sorbitan cocoate, sorbitan diisostearate, sorbitan dioleate, sorbitan distearate, sorbitan isostearate, sorbitan olivate, sorbitan sesquiisostearate, sorbitan sesquistearate, and sorbitan triisostearate. *Int. J. Toxicol.* **2002**, *21*, 93–112.
6. Badmus, S.O.; Amusa, H.K.; Oyehan, T.A.; Saleh, T.A. Environmental risks and toxicity of surfactants: Overview of analysis, assessment, and remediation techniques. *Environ. Sci. Pollut. Res. Int.* **2021**, *28*, 62085–62104. [CrossRef]
7. Korhonen, M.; Hirvonen, J.; Peltonen, L.; Antikainen, O.; Yrjänäinen, L.; Yliruusi, J. Formation and characterization of three-component-sorbitan monoester surfactant, oil and water-creams. *Int. J. Pharm.* **2004**, *269*, 227–239. [CrossRef]
8. Fornasier, M.; Krautforst, K.; Kulbacka, J.; Jönsson, P.; Murgia, S.; Bazylińska, U. Cubosomes and hexosomes stabilized by sorbitan monooleate as biocompatible nanoplatforms against skin metastatic human melanoma. *J. Colloid Interface Sci.* **2024**, *677*, 842–852. [CrossRef]
9. Abdelkader, H.; El-Wahab, A.A.; El-Gendy, A.O.; Abou-Taleb, H.A. Formulation and optimization of lipid- and Poloxamer-tagged niosomes for dermal delivery of terbinafine: Preparation, evaluation, and in vitro antifungal activity. *Pharm. Dev. Technol.* **2023**, *28*, 803–810. [CrossRef]
10. Sonwai, S.; Podchong, P.; Rousseau, D. Crystallization kinetics of cocoa butter in the presence of sorbitan esters. *Food Chem.* **2017**, *214*, 497–506. [CrossRef]
11. Asarch, A.; Scheinman, P.L. Sorbitan sesquioleate, a common emulsifier in topical corticosteroids, is an important contact allergen. *Dermatitis* **2008**, *19*, 323–327. [CrossRef] [PubMed]
12. Stingeni, L.; Foti, C.; Guarneri, F.; Corazza, M.; Cristaudo, A.; Ferrucci, S.M.; Gallo, R.; Martina, E.; Musumeci, M.L.; Napolitano, M.; et al. Contact allergy to SIDAPA baseline series allergens in patients with eyelid dermatitis: An Italian multicentre study. *Contact Dermat.* **2024**, *90*, 479–485. [CrossRef] [PubMed]
13. Boyd, J.; Parkinson, C.; Sherman, P. Factors affecting emulsion stability, and the HLB concept. *J. Colloid Interface Sci.* **1972**, *41*, 359–370. [CrossRef]
14. Kunieda, H.; Shinoda, K. Evaluation of the hydrophile-lipophile balance (HLB) of nonionic surfactants. I. Multisurfactant systems. *J. Colloid Interface Sci.* **1985**, *107*, 107–121. [CrossRef]
15. Pasquali, R.C.; Sacco, N.; Bregni, C. The studies on hydrophilic-lipophilic balance (HLB): Sixty years after William C. Griffin's pioneer work (1949–2009). *Lat. Am. J. Pharm* **2009**, *28*, 313–317.
16. Foo, K.S.; Bavoh, C.B.; Lal, B.; Mohd Shariff, A. Rheology impact of various hydrophilic-hydrophobic balance (HLB) index non-ionic surfactants on cyclopentane hydrates. *Molecules* **2020**, *25*, 3725. [CrossRef]
17. Michor, E.L.; Ponto, B.S.; Berg, J.C. Effects of reverse micellar structure on the particle charging capabilities of the span surfactant series. *Langmuir* **2016**, *32*, 10328–10333. [CrossRef]
18. Farooq, A.; Shafaghat, H.; Jae, J.; Jung, S.C.; Park, Y.K. Enhanced stability of bio-oil and diesel fuel emulsion using Span 80 and Tween 60 emulsifiers. *J. Environ. Manag.* **2019**, *231*, 694–700. [CrossRef]
19. Jiao, J.; Burgess, D.J. Rheology and stability of water-in-oil-in-water multiple emulsions containing Span 83 and Tween 80. *AAPS PharmSci* **2003**, *5*, 62–73. [CrossRef]
20. Satapathy, D.; Sagiri, S.S.; Pal, K.; Pramanik, K.J.D.M. Development of mustard oil-and groundnut oil-based span 40 organogels as matrices for controlled drug delivery. *Des. Monomers Polym.* **2014**, *17*, 545–556. [CrossRef]
21. Sakai, T.; Kurosawa, H.; Okada, T.; Mishima, S. Vesicle formation in mixture of a PEO-PPO-PEO block copolymer (Pluronic P123) and a nonionic surfactant (Span 65) in water. *Colloids Surf. A Physicochem. Eng. Asp.* **2011**, *389*, 82–89. [CrossRef]
22. Nakata, H.; Miyazaki, T.; Iwasaki, T.; Nakamura, A.; Kidani, T.; Sakayama, K.; Masumoto, J.; Miura, H. Development of tumor-specific caffeine-potentiated chemotherapy using a novel drug delivery system with Span 80 nano-vesicles. *Oncol. Rep.* **2015**, *33*, 1593–1598. [CrossRef] [PubMed]
23. Fujihira, A.; Shimizu, N. The effects of internal and receptor pH on the rate of drug release from water-in-oil emulsions. *Chem. Pharm. Bull.* **2014**, *62*, 64–71. [CrossRef] [PubMed]
24. Zapolski, R.; Musiał, W. The Response Surface Methodology for Assessment of HLB Values of Mixtures of Non-Ionic Surfactants Using Parameters from Their π-A Isotherms. *Molecules* **2024**, *29*, 2351. [CrossRef]
25. Fainerman, V.B.; Vollhardt, D. Equation of state for monolayers with additional phase transition between condensed phases of different compressibility. *J. Phys. Chem. B* **2009**, *113*, 6311–6313. [CrossRef]
26. Pan, W.; Chen, H.; Wen, G.; Giaouzi, D.; Pispas, S.; Zuo, J. Surface micelle structures and monolayer compression moduli of double hydrophilic block copolymer. *J. Phys. Chem. C* **2020**, *124*, 17150–17157. [CrossRef]
27. Keller, S.L. Miscibility transitions and lateral compressibility in liquid phases of lipid monolayers. *Langmuir* **2003**, *19*, 1451–1456. [CrossRef]
28. Vollhardt, D.; Fainerman, V.B. Progress in characterization of Langmuir monolayers by consideration of compressibility. *Adv. Colloid Interface Sci.* **2006**, *127*, 83–97. [CrossRef]

29. Schmidts, T.; Dobler, D.; Guldan, A.C.; Paulus, N.; Runkel, F. Multiple W/O/W emulsions—Using the required HLB for emulsifier evaluation. *Colloids Surf. A Physicochem. Eng. Asp.* **2010**, *372*, 48–54. [CrossRef]
30. Al-Sabagh, A.M. The relevance HLB of surfactants on the stability of asphalt emulsion. *Colloids Surf. A Physicochem. Eng. Asp.* **2002**, *204*, 73–83. [CrossRef]
31. Mahjoob, R.; Hakimzadeh, V.; Salehi, E.A.; Farmani, J. The interaction of polyglycerol esters with sorbitan tristearate, and sorbitan monostearate in structuring a low-saturated fat. *J. Food Meas. Character* **2022**, *16*, 4174–4184. [CrossRef]
32. Anton, N.; Pierrat, P.; Lebeau, L.; Vandamme, T.F.; Bouriat, P. A study of insoluble monolayers by deposition at a bubble interface. *Soft Matter* **2013**, *9*, 10081–10091. [CrossRef]
33. Rosen, M.J.; Zhou, Q. Surfactant-surfactant interactions in mixed monolayer and mixed micelle formation. *Langmuir* **2001**, *17*, 3532–3537. [CrossRef]
34. Lu, D.; Burgess, D.J.; Rhodes, D.G. Nonideality in mixed monolayers of sorbitan oleates is enhanced by elevated ionic strength. *Langmuir* **2000**, *16*, 10329–10333. [CrossRef]
35. Mortensen, A.; Aguilar, F.; Crebelli, R.; Di Domenico, A.; Dusemund, B.; Frutos, M.J.; Galtier, P.; Gott, D.; Gundert-Remy, U.; Leblanc, J.C. Re-evaluation of sorbitan monostearate (E 491), sorbitan tristearate (E 492), sorbitan monolaurate (E 493), sorbitan monooleate (E 494) and sorbitan monopalmitate (E 495) when used as food additives. *EFSA J.* **2017**, *15*, e04788.
36. Erni, P.; Fischer, P.; Windhab, E.J. Sorbitan tristearate layers at the air/water interface studied by shear and dilatational interfacial rheology. *Langmuir* **2005**, *21*, 10555–10563. [CrossRef]
37. Griffin, W.C. Classification of surface-active agents by HLB. *J. Soc. Cosmet. Chem.* **1949**, *1*, 311–326.
38. Pasquali, R.C.; Taurozzi, M.P.; Bregni, C. Some considerations about the hydrophilic–lipophilic balance system. *Int. J. Pharm.* **2008**, *356*, 44–51. [CrossRef]
39. Yu, Z.W.; Jin, J.; Cao, Y. Characterization of the liquid-expanded to liquid-condensed phase transition of monolayers by means of compressibility. *Langmuir* **2002**, *18*, 4530–4531. [CrossRef]
40. Kita-Tokarczyk, K.; Itel, F.; Grzelakowski, M.; Egli, S.; Rossbach, P.; Meier, W. Monolayer interactions between lipids and amphiphilic block copolymers. *Langmuir* **2009**, *25*, 9847–9856. [CrossRef]
41. Brezesinski, G.; Möhwald, H. Langmuir monolayers to study interactions at model membrane surfaces. *Adv. Colloid Interface Sci.* **2003**, *100–102*, 563–584. [CrossRef] [PubMed]
42. Fainerman, V.B.; Vollhardt, D. Penetration of Langmuir monolayers by soluble amphiphilic molecules. *Langmuir* **1999**, *15*, 1784–1790. [CrossRef]
43. Harris, J.; Rice, S.A. A molecular dynamics study of the structure of a model Langmuir monolayer of amphiphile molecules. *J. Chem. Phys.* **1988**, *89*, 5898–5908. [CrossRef]

Disclaimer/Publisher's Note: The statements, opinions and data contained in all publications are solely those of the individual author(s) and contributor(s) and not of MDPI and/or the editor(s). MDPI and/or the editor(s) disclaim responsibility for any injury to people or property resulting from any ideas, methods, instructions or products referred to in the content.

molecules

MDPI

Article

Cleansing Mechanisms and Efficacy on Artificial Skin

Tatiana Slavova [1], Rumyana Stanimirova [1], Krastanka Marinova [1,2,*] and Krassimir Danov [1,3]

[1] Department of Chemical & Pharmaceutical Engineering, Faculty of Chemistry & Pharmacy, Sofia University "St. Kliment Ohridski", 1164 Sofia, Bulgaria; tatiana_slavova@lcpe.uni-sofia.bg (T.S.); rs@lcpe.uni-sofia.bg (R.S.)

[2] Centre of Competence "Sustainable Utilization of Bio-Resources and Waste of Medicinal and Aromatic Plants for Innovative Bioactive Products" (BIORESOURCES BG), 1164 Sofia, Bulgaria

[3] Centre of Competence "Smart Mechatronics, Eco- and Energy Saving Systems and Technologies", 1164 Sofia, Bulgaria

* Correspondence: km@lcpe.uni-sofia.bg

Abstract: A systematic study on the mechanisms of cleansing artificial skin by solutions of widely used in personal care surfactants disodium laureth sulfosuccinate (DSLSS), sodium laureth sulfate (SLES), sodium dodecyl sulfate (SDS), dodecyl trimethyl ammonium bromide (DTAB), and coco glucoside (CG), is presented. The systematic characterization of soil removal from artificial skin revealed two primary cleansing mechanisms: emulsification and roll-up. Emulsification occurs in systems with very low interfacial tension, such as sebum in SLES solutions, while dimethicone soil was only removed by roll-up. The roll-up effectiveness depends on the surfactant's interfacial activity and its adsorption on the soiled surface. Thus, the strong adsorption of DTAB on the skin leads to dimethicone roll-up at a relatively high interfacial tension of 11 mN/m. The anionic and nonionic surfactants adsorbed less at the artificial skin surface, and the oil/water interfacial tension value lowering below 5 mN/m is necessary for the roll-up to occur. Nonionic CG removed dimethicone at a lower concentration than ionic surfactants. Combining CG with ionic surfactants improved cleaning at lower total concentrations. Surfactant mixtures are used to formulate simple cleansing formulations, whose performance is also investigated by the developed in vitro approach. The results obtained allow for a good rating of the formulations, which correlates well with the performance of the surfactant mixtures and their interfacial activity.

Keywords: skin cleansing mechanisms; roll-up; artificial skin; surfactant interfacial activity

1. Introduction

Nowadays, cleansing the skin is an innate concern for healthy skin with a good esthetic appearance. It provides removal of dirt, sebum, dead skin cells, cosmetic ingredients, e.g., dimethicone, pigments, etc. Cleansing and skin care play an important role in human psychological well-being and social interaction [1–3]. In the last decade, the cosmetic industry has provided myriads of products for skin cleansing based on various types and origins of the used surfactants, enormously enriched with "green" and "bio" sources, and their mixtures [4,5]. The efficacy and safety are the mandatory requirements for the surfactants and the raw materials included in the final products [1,3,4,6].

The human skin surface has been the subject of numerous studies in relation to the wetting of skin by water [7], surfactant mildness and skin irritation [1,4,8–10], and the surfactants' effect on the wetting and lipid composition [11–13]. The basic understanding

of any possible interactions and overall impact stems from the proper determination and interpretation of the skin surface energy [8,11–17]. In modern times, the organization of reliable in vivo investigations with humans requires a sufficient number of volunteers to be included. The obligatory ethical rules are met according to the Declaration of Helsinki (1964) and the subsequent revisions (World Medical Association, 1989) [18,19], which increase confidence in the applied procedures and the obtained data. As a result, the costs of the studies and the characterization of the product quality rise considerably. In contrast, in vitro efficacy tests are among the fastest and cheapest applied approaches. Various model surfaces (polymethyl methacrylate, hydrophobic glass, etc. [18,20]) have been used to characterize the cleansing efficacy of different compositions. New materials have been designed to better mimic the human skin surface [8,21,22].

The surface properties of the substrate to be cleaned have always been treated as the main governing factors for the proper choice of the detergent [20,23,24]. The physicochemical mechanisms of the soil removal from the skin and hair can be found briefly described in review papers and books [23–25], with detailed references to the pioneering publications. Varieties of in vitro skin models have been developed and improved in the last 20 years with the aim of decreasing the cost and risk, improving the model relevance, and accelerating the speed of substance testing, especially for topical drug delivery systems [26,27]. The robust skin models have been tested for a variety of cosmetic applications: skin tanning [28]; skin tribology characterization [29]; tactile skin perception [30]; spreading properties of emollients [31]; antiviral activity of organic acids [32], etc. Different cleaning protocols have been applied to model skin surfaces to support patent claims [33]. In the literature, the cleansing efficacy is mostly considered as a macroscopic characteristic, and to our knowledge, there are no discussions on the molecular mechanisms of soil removal and on the impact of the surfactant type on the particular mechanism.

Our investigation aims to demonstrate that model experiments with artificial skin could be applied and used to investigate the physicochemical mechanisms of soil removal, and to discriminate the effects of different types of surfactants in the cleansing compositions. For that purpose, we used the artificial skin Vitroskin® [34], which "has been formulated to have topography, pH, critical surface tension, chemical reactivity, and ionic strength that is similar to human skin". Although it has been used in many studies, only a single set of data has been found for its particular surface energy value [8]. Recently [35], we determined the surface energy of hydrated and non-hydrated Vitroskin® in order to compare the respective values with the available data for human skin in vivo, and to elucidate the effect of skin hydration. The hydration slightly increased the total surface energy of Vitroskin® (from 35.4 to 37.1 mN/m using the method of Wu [35,36]) and the obtained values are close to the value of 35.8 mN/m reported in [8] and to values for human skin (from 30 mN/m to 40 mN/m [14,17]). Thus, Vitroskin® is a suitable substrate to model the processes of human skin cleansing.

To distinguish the effects of different surfactant types, the following commercial surfactants are used in the present study: anionics, sodium laureth sulfate (SLES), disodium laureth sulfosuccinate (DSLSS), sodium dodecyl sulfate (SDS); cationic, dodecyl trimethyl ammonium bromide (DTAB); and nonionic coco glucoside (CG). The systematic investigations with two soils: sebum (a mixture of hydrocarbons, fatty acids, esters, etc.) and dimethicone (polydimethyl siloxane frequently added to skin and hair conditioning and decorative cosmetics [1,3,31]), demonstrate a clear impact of the compositions on the soil removal mechanisms and efficacy. In addition, the results with sample cleansing formulations manifest the benefits of the model experiments to real product development.

2. Results

2.1. Surface and Interfacial Tension Isotherms of the Used Surfactants

Surface properties of the surfactants were compared in order to further analyze the impact on their cleansing efficiency. The surface tension isotherms of four of the surfactants used in deionized (DI) water are shown in Figure 1a. Figure 1b represents the interfacial tension isotherms of the same surfactants at the water/dimethicone interface. The measurements were performed at 30 °C, in order to be close to the slightly warm water frequently used for skin cleansing. Weight concentrations are used on the plots since these are mostly used in practical applications and product preparations [3,20,33]. Note that the used concentrations correspond to the active substance in the raw material, which might not be the same as in the industrial recipes [33]. The comparison of the surface tension isotherms (Figure 1a) shows that disodium laureth sulfosuccinate (DSLSS) has the highest surface activity, whereas the cationic surfactant DTAB is the least surface active and has the highest critical micelle concentration (CMC). All CMC values from the surface tension isotherms (indicated by vertical dashed lines in Figure 1a) are listed in Table 1. The values of CMC for DTAB and coco glucoside (CG), determined from the interfacial tension measurements (Figure 1b), are also shown in Table 1, along with the pH range of all solutions (see Figures S1–S4).

Table 1. The critical micellar concentration (CMC) determined from the isotherms (Figure 1) at the air/solution and dimethicone/solution interfaces. The last column presents the pH range of the surfactant solutions used.

Surfactant	CMC, wt%		pH Range
	Air/Water	Dimethicone/Water	
CG	0.0037	0.0054	6.7–10.8
DSLSS	0.0012	>0.1	7.0–5.0
SLES	0.079	>0.1	7.0–6.0
DTAB	0.49	0.49	6.5–5.7

The determined CMCs of DTAB from the surface tension, the interfacial tension, and the electrolytic conductivity (Figure S1) data coincide well with the literature data [37–39]. The solid symbols for DTAB in Figure 1a are measured at 30 °C by the maximum bubble pressure method (MBPM), and the empty symbols show experimental data measured by the du Noüy ring method in Ref. [39] at 25 °C. The good coincidence of the CMCs suggests that the used sample of DTAB is relatively pure and does not contain additional indifferent electrolytes (salts). DTAB solutions have the highest surface tension and the highest interfacial tension (11 mN/m) with dimethicone above the CMC compared to the other surfactants.

The isotherm of the anionic sodium laureth sulfate (Figure 1a) has a pronounced minimum signifying the presence of nonionic admixtures [40], most probably due to hydrolysis [41,42]. The vertical dashed line in Figure 1a shows the CMC value obtained from the electrolytic conductivity data (Figure S2 and Table 1), which corresponds exactly to the CMC of pure SLES aqueous solutions, CMC = 0.079 wt% [43]. A neutral pH within the range of 6 to 7 is measured for SLES aqueous solutions. Note that the nonionic admixtures in SLES form micelles at 0.02 wt%. Mixed micelles containing both ionic and nonionic components appear for concentrations above 0.02 wt%, in which the molar fraction of the ionic component increases with the rise in concentration up to 0.079 wt% [44]. The oil solubility of

the nonionic admixture in SLES affects the interfacial tension (solution/dimethicone), and it decreases monotonically in the entire concentration range studied, reaching 6.5 mN/m at 5 wt%, as shown in Figure 1b. That is why no CMC value, but rather a CMC range for the dimethicone/water interface, is shown in Table 1 for SLES.

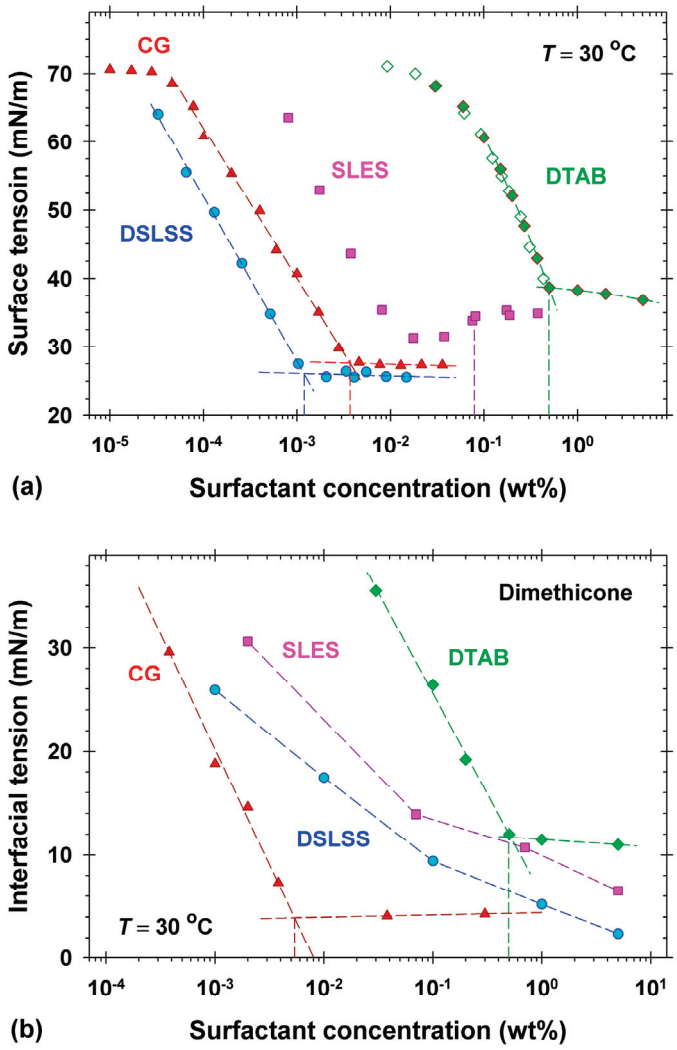

Figure 1. (**a**) Surface tension isotherms of DSLSS (disodium laureth sulfosuccinate), CG (coco glucoside), SLES (sodium laureth sulfate), and DTAB (dodecyl trimethyl ammonium bromide). All measurements were performed at 30 °C by the du Noüy ring method, except for DTAB, where the maximum bubble pressure method was applied. The empty green diamonds show experimental data measured by the du Noüy ring method in Ref. [39]. (**b**) Interfacial tension of selected solutions against dimethicone measured by the pendant drop method at 30 °C.

The used nonionic CG is a mixture of C8-C16 fatty alcohol glucosides with a low value of the CMC (0.0037 wt%, Figure 1a) determined from the surface tension isotherm. The higher CMC value (0.0054 wt%, Figure 1b) and the low interfacial tension (4.1 mN/m) above the CMC obtained from the interfacial tension isotherm show that, most probably, the admixtures of long-chain alcohols in the used CG sample are dissolved in the dimethicone [45]. The nonionic CG had a significant alkaline pH (Figure S3, Table 1). The high pH of glucoside surfactants typically results from the synthesis process that includes bleaching with either bleach or hydrogen peroxide [46].

The technical grade DSLSS is a mixture of surfactants with C10–C16 hydrocarbon tails and EO groups, which contains admixtures of the nonionic surface active laureth-2,

sodium sulfate, and sodium sulfite [47]. The surface tension isotherm of disodium laureth sulfosuccinate (Figure 1a) has no minimum, and the determined CMC (0.0012 wt%) is the lowest compared to the other surfactants. The relatively low values of the surface tension (26 mN/m) above the CMC might be a result of the presence of laureth-2. The very high molar conductivity below the CMC (Figure S4) suggests that the used DSLSS sample contains a high concentration of indifferent electrolytes (sodium sulfate). Note that disodium lauryl sulfosuccinate forms vesicles [48], and the respective surface tension monotonically decreases with the rise in concentration. In contrast, the surface tension isotherm of DSLSS has a well-pronounced kink point, and the CMC value is well determined. The available nonionic surface-active admixtures in the DSLSS sample are partially oil-soluble because the interfacial tension of DSLSS solution/dimethicone monotonically decreases with concentration, reaching the lowest value of interfacial tension (2.4 mN/m at 5 wt%) compared with the other surfactants. Similarly, for SLES, the CMC range for the dimethicone/water interface is shown in Table 1.

2.2. Oily Soils Removal from Vitroskin® in Single Surfactant Solutions

We performed direct observations of soil removal from Vitroskin® with two different soils—model sebum and dimethicone. The following mechanisms of soil removal were observed with the studied soils: emulsification of the sebum after contact with some of the surfactant solutions (Figure 2a), drop shrinking (rolling, Figure 2b,c), and eventual detachment (Figure 2c) in the case of dimethicone. No emulsification of the dimethicone drops on the skin was found, in contrast to the observations with sebum. The contact areas between the dimethicone drops and the substrate decrease slowly over time, t, to the equilibrium state (Figure 2b) or to the full drop detachment (Figure 2c), depending on the type of surfactants in the solutions. Figure 3a,b present the changes in the three-phase contact angle through the aqueous phase, θ, and the drop base diameter, d, with time, t, for a dimethicone droplet on artificial skin in a solution of 1 wt% SLES (squares) and 1 wt% (1:3) SLES+CG (stars). In the case of 1 wt% SLES aqueous solution, we did not observe detachments of the droplets from the substrate (cf. Figure 2b). Both the contact angle, θ, and the base diameter, d, decreased after the addition of the surfactant solution for about 60 s approaching their equilibrium values ($\theta = 61.85 \pm 0.35°$ and $d = 2.41 \pm 0.01$ mm determined with double exponential decay fit for the droplet shown on Figure 2b, squares on Figure 3). In the presence of a mixed 1 wt% (1:3) SLES+CG solution (Figure 2c), the three-phase contact angle and the drop base diameter continuously decreased for the initial 120 s from $\theta = 82°$ and $d = 3.2$ mm to $\theta = 44°$ and $d = 1.1$ mm (Figure 3). For 120 s $< t <$ 230 s, the contact angle slowly dropped to $\theta = 37°$, while the contact line shrank rapidly to the moment of the dimethicone drop detachment ($d = 0.4$ mm at $t = 230$ s), see Figure 3 and image number 4 in Figure 2c. This behavior exactly corresponds to the so-called "roll-up mechanism" of soil cleaning [23,25,49–51].

(a)

10 s **60 s** **120 s** **300 s**

Figure 2. *Cont.*

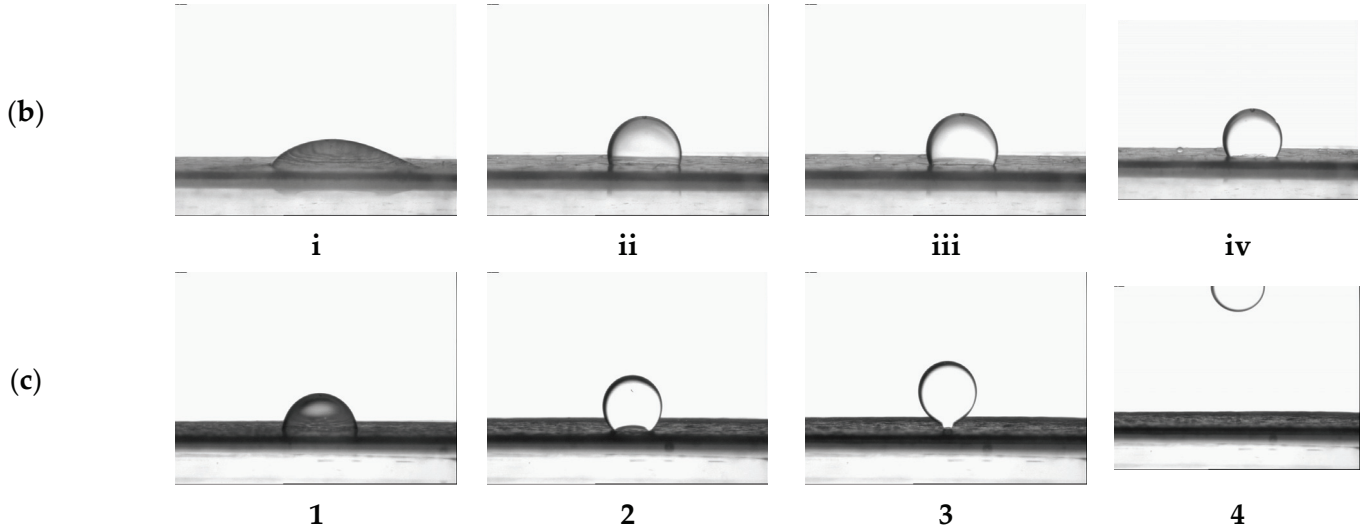

Figure 2. Images of (**a**) sebum soil at different times, as shown below each image, after immersion in a solution of 0.07 wt% SLES. (**b**) Dimethicone droplet after the addition of 1 wt% SLES solution; numbers under each image (**i**–**iv**) correspond to time, as shown on Figure 3. (**c**) Dimethicone droplet after the addition of 1 wt% 1:3 SLES+CG; numbers under each image (**1**–**4**) correspond to time, as shown on Figure 3.

The emulsification mechanism [23–25] was only observed with the sebum soil (as illustrated in Figure 2a) when the interfacial tension was low enough, as we have shown in our previous study [35]. The fatty acids present in the sebum most probably mix synergistically with some surfactants, forming complex amphiphilic structures and effectively decreasing the interfacial tension. Thus, we have observed emulsification with SLES at relatively low concentrations, while DSLSS has not been capable of emulsifying the sebum even at very high concentrations [35]. Further understanding of the surfactant–soil structuring could be performed with a complex instrumental investigation [52,53].

The roll-up mechanism observed with dimethicone soil allows for the straightforward comparison of surfactant efficiencies [35,49]. For that reason, we performed systematic observations of dimethicone droplets on Vitroskin® in single surfactant solutions varying the respective concentration from at least 10 times below the CMC up to 10× CMC.

The oily soil removal by the rolling-up mechanism is explained by the changes in surface energy and the interfacial tension, leading to simultaneous changes in the three-phase contact angle and the contact area [17,23,49,50]. At equilibrium, the contact angle through the water phase is related to the substrate water, γ_{SW}, and the substrate oil, γ_{SO}, surface energies and the water–oil, γ_{WO}, interfacial tension values by the Young–Laplace equation [17]:

$$cos\theta = (\gamma_{SO} - \gamma_{SW})/\gamma_{WO} \quad (1)$$

Thus, a plot of cosθ versus γ_{WO} appropriately illustrates the differences between the used surfactants and the wetting processes [16,35]. For convenience, the full drop detachment is typically denoted as cosθ = 1.

Figure 4 summarizes the experimental results for the dependence of cosθ on the interfacial tension (a) and on the surfactant concentration (b) for deposited dimethicone drops on artificial skin in aqueous surfactant solutions. Two series of measurements were performed with solutions of DTAB and DSLSS in 150 ppm hard water to explore the possible impact of the hardness ions on cleansing efficiency. The natural pH of CG solutions is approximately constant (pH = 10.5–10.8, Figure S3). CG solutions with pH

= 6 were also used in order to check the possible effect of pH on the dimethicone drop removal. The values of cosθ were taken at 300 s of contact of the dimethicone drop with the respective solution. If the drop's detachment occurred for t < 300 s, then we plotted cosθ = 1 in Figure 4. All experiments were conducted under static conditions without cross flows, additional mechanical forces, or agitation.

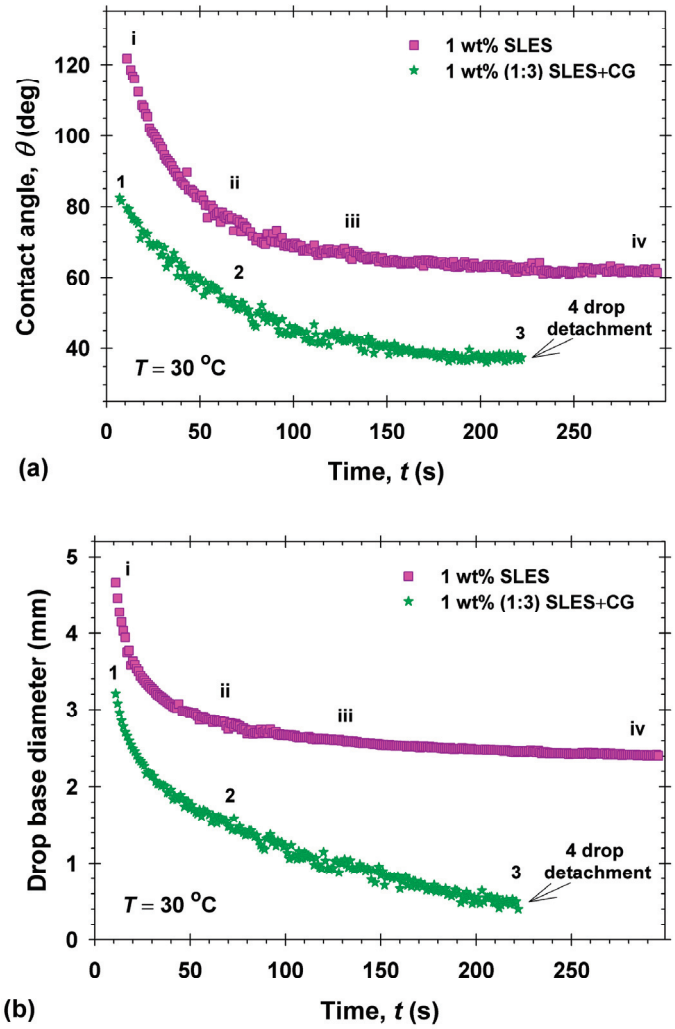

Figure 3. Three-phase contact angle (**a**) and drop base diameter (**b**) vs. time for 1 wt% SLES (no detachment of the oil drop, Figure 2b images corresponding to i, ii, iii, iv) and 1 wt% 1:3 SLES + CG (detachment of the oil drop, Figure 2c images corresponding to 1, 2, 3, 4).

The obtained dependence of cosθ on γ_{WO} (Figure 4a) clearly demonstrates the expected increase in the cosine with the decrease in the interfacial tension. Values of γ_{WO} below 5 mN/m were necessary for the complete drop detachment in the solutions of the anionic DSLSS and the nonionic CG solutions, as observed for 5 wt% DSLSS with γ_{WO} = 2.4 mN/m, and for 1 wt% CG with γ_{WO} = 4.4 mN/m. The interfacial tension of all used SLES solutions was larger than 5 mN/m (γ_{WO} = 5.6 mN/m at the highest concentration of 8 wt%, see Figure 1b), and drop detachments were not detected.

The dependence of cosθ on the surfactant concentration (Figure 4b) shows that the nonionic CG (either alkaline or at pH = 6) removes the dimethicone droplets from Vitroskin® at the lowest surfactant concentration compared to the ionic surfactants SLES, DSLSS, and DTAB. The best performance of CG is related to its highest interfacial activity, cf. Figure 1b.

CG decreases the interfacial tension, γ_{WO}, below 5 mN/m at the lowest concentration compared to all other surfactants. The efficacy of DTAB and DSLSS (both in DI and hard water) with respect to concentration is quite similar—the dimethicone droplets fully detach from the artificial skin for 5 wt% aqueous solutions. In the case of SLES, no dimethicone drop detachment was observed under the static experimental conditions, even at the highest experimental concentration of 8 wt% (squares in Figure 4a). SLES is known for its very low Krafft temperature and effectiveness in hard water [1,20,54], which is why its performance in hard water was not studied.

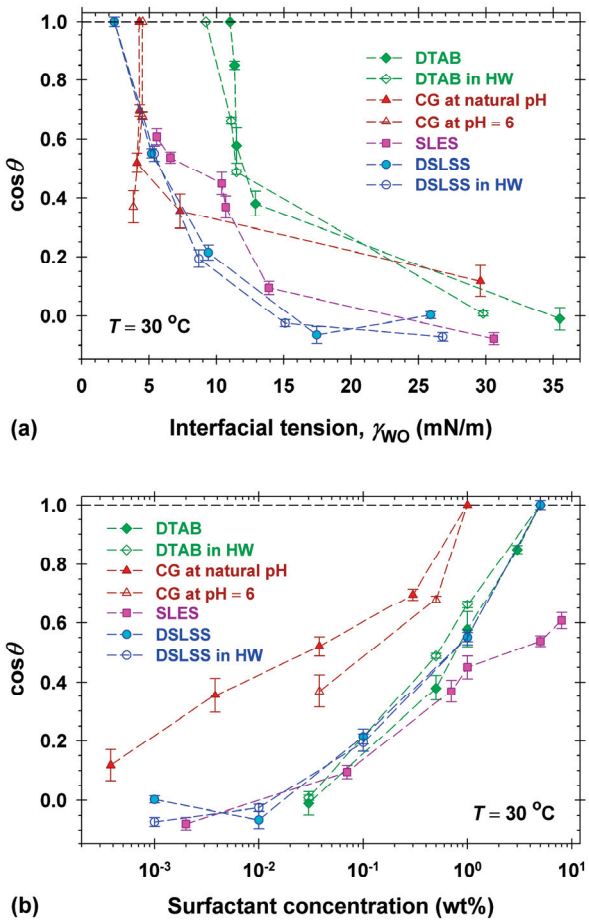

Figure 4. Cosine of the three-phase contact angle through the water phase, θ, of dimethicone droplets on Vitroskin® vs. (**a**) the interfacial tension, γ_{WO}, and (**b**) the surfactant concentration in the aqueous solutions. A series of solutions was prepared in DI water with the anionic surfactants SLES (squares) and DSLSS (circles), the nonionic surfactant CG (triangles), and the cationic surfactant DTAB (diamonds). The experimental results for two series with DSLSS (empty circles) and with DTAB (empty diamonds) in 150 ppm hard water (HW in the legend) are included. The measurements with CG solutions at fixed pH = 6 (empty triangles) are shown. All measurements were performed at 30 °C.

Notably, the drop's rolling up in DTAB solutions occurred at remarkably high interfacial tension of about 11 mN/m in both hard and DI water. Cationic surfactants and polymers are widely used as skin and hair conditioners [1,2,55] due to their preferential adsorption onto anionic surfaces. Thus, the adsorption of DTAB on the artificial skin is expected to decrease the surface energy γ_{SW}, and as a result, the dimethicone droplets detach from the substrate at relatively high values of γ_{WO}, see Equation (1). The electrolytic conductivity data (Figure S1) and the surface and interfacial tension isotherms (Figure 1) of

DTAB aqueous solutions suggested that the DTAB sample is relatively pure and there are no surface-active admixtures that could be dissolved in the dimethicone. Thus, the surface energy, γ_{SO}, does not depend on the DTAB concentration. Using Equation (1), we represent the Gibbs adsorption equation in the following form:

$$d(\gamma_{WO}cos\theta) = d(\gamma_{SO} - \gamma_{SW}) = -d\gamma_{SW} = k_B T \Gamma dlnC \quad (2)$$

Here, k_B is the Boltzmann constant, and Γ is the surface excess of the surfactant solution/artificial skin boundary.

Figure 5 shows the dependence of the product $\gamma_{WO} \cos\theta$ on the concentration C determined with solutions of DTAB. The dashed lines in Figure 5 correspond to the linear regression according to Equation (2). Both slopes obtained from the data in DI water and hard water are identical: Γ = 1.99 ± 0.05 μmol/m^2, and the regression coefficients are greater than 0.9995. The obtained surface excess, Γ, is two times lower than the saturation adsorption of DTAB at the solution/air interface [38,39], and it is comparable to values determined on other solid surfaces [56]. This amount is enough to substantially reduce the skin surface energy, γ_{WS}, and to allow for drop detachment at high interfacial tension, γ_{WO} (cf. Figure 4a). Note that the dependencies of $\gamma_{WO} \cos\theta$ vs. surfactant concentration for CG, SLES, and DSLSS (Figure S5) are scattered and cannot be described by Equation (2). Most probably, the presence of dimethicone soluble admixtures in these samples (Figure 1) affects the values of the surface energy, γ_{SO}, and the simple form of the Gibbs equation becomes inadequate to describe the respective surface excesses.

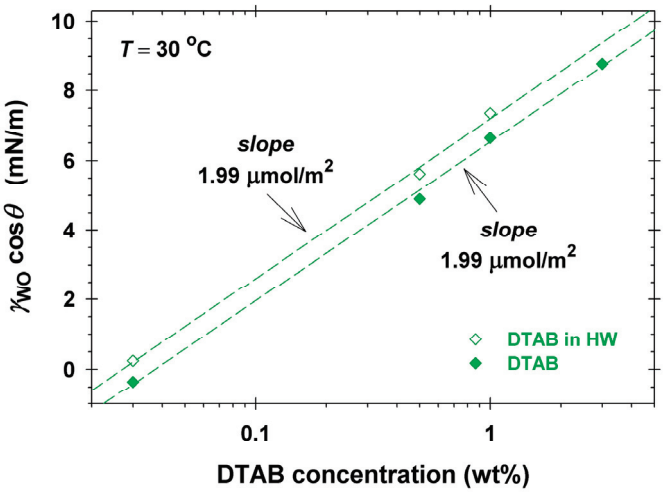

Figure 5. Difference between the surface energies γ_{SO} and γ_{SW} vs. DTAB concentration, C, see Equation (2), in DI water and in hard water. The lines represent the linear regression fit through the points. The adsorptions, Γ, determined from the slopes, are shown on the plot.

In summary, the experimental observations of the behavior of two different soils in different surfactant solutions allowed for the demonstration of two basic mechanisms of soil removal: emulsification and roll-up. The change in the contact angles of the dimethicone drops with the concentration and type of the surfactant outlined the most important factors for the roll-up to occur, namely the interfacial activity of the surfactants. Thus, CG, having the lowest interfacial tension (Figure 1b), has the best performance in removing dimethicone. Other surfactants, such as the used SLES with a low interfacial activity for dimethicone, showed good emulsification of sebum soil, most probably due to synergistic interaction with the fatty acids in the sebum. In practical applications, where different

types of soil are met [1,20,23,25], surfactant mixtures are usually set to ensure an optimal cleansing performance.

2.3. Dimethicone Soils Removal in Mixed Surfactant Solutions

We prepared mixtures of CG with the three ionic surfactants and performed systematic observations of dimethicone droplets rolling in the mixed surfactant solutions at natural pH to check the impact of the added ionics on the effectiveness of CG solutions.

Figure 6 shows results for the cosine of the aqueous three-phase contact angle with dimethicone droplets on Vitroskin® in DSLSS+CG solutions at anionic/nonionic ratios of 1:3 and 3:1. The obtained data are compared to those with the two surfactants alone, i.e., 1:0 (only DSLSS) and 0:1 (only CG) ratios. The natural pH values of all mixed DSLSS+CG solutions were in the range from 4.8 to 6.2, even at a 1:3 ratio between the two surfactants. The results with solutions of 1:3 and 0:1 DSLSS+CG were almost the same as interfacial tension (Figure 6a) and concentration (Figure 6b) dependencies, except at very low concentrations. One can conclude that the coco glucoside interfacial activity was dominant for the overall removal efficiency. With the 3:1 mixture, 3 wt% total surfactant concentration was necessary to decrease the interfacial tension below 5 mN/m and to roll-up the dimethicone drop. This total surfactant concentration (3 wt%) is lower than the necessary concentration for DSLSS alone (5 wt%) but higher than that for the 1:3 mixture (1 wt%).

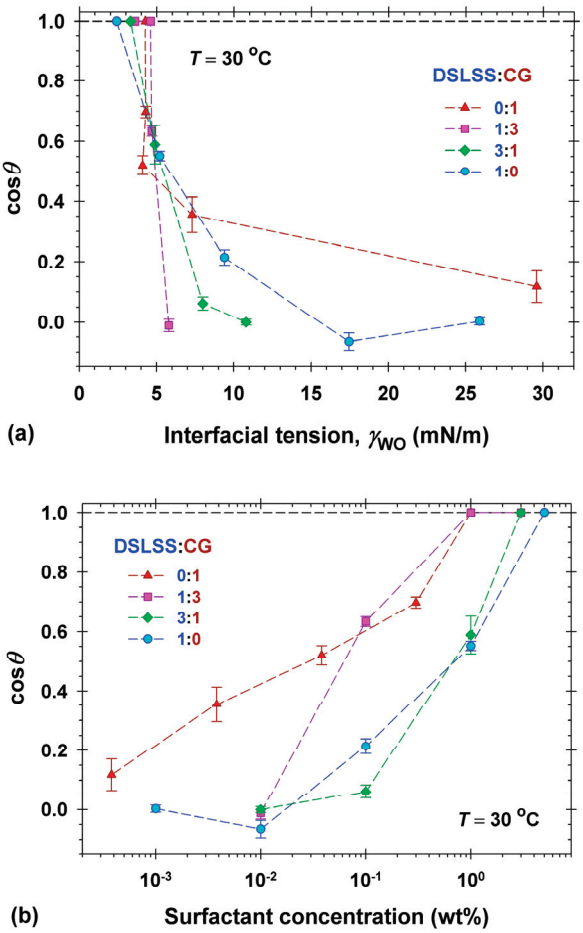

Figure 6. Cosine of the three-phase contact angle through the water phase, cosθ, of dimethicone droplets on Vitroskin® vs. (**a**) the interfacial tension, γ_{WO}, and (**b**) the total surfactant concentration in mixed solutions of DSLSS and CG at different ratios, as shown in the legend. All measurements were performed at 30 °C.

The behavior observed with the mixed solutions of SLES and CG (see the plots in Figure 7) was different compared to that of DSLSS and CG. First, the natural pH values of all mixed solutions were between 10 and 11, even at a 3:1 SLES+CG ratio, and the pHs are controlled by the available CG. Note that the removal efficiency of CG alone is approximately the same at natural pH and at pH = 6, see Figure 4. The mixtures with prevailing CG, i.e., 1:3, successfully detached dimethicone droplets at 1 wt% total surfactant concentration. The mixture with less CG, i.e., 3:1, had lower interfacial tension than SLES solutions (Figure 7a), but the decrease was not sufficient to observe drop roll-up. Note that the interfacial tension value, γ_{WO}, is not the only factor to influence the contact angle in this case. The mixed solution of 1:3 SLES:CG achieved complete oil removal at a concentration of 1 wt% and γ_{WO} = 6.3 mN/m, while in 8 wt% SLES solution with γ_{WO} = 5.5 mN/m no oil release was observed. In such case, one could expect change in the surface energy of the substrate, see Equation (1), where mixed adsorption layer is formed. The morphology of such layers depends on both structure and concentration of the surfactants [56] and could be a subject of detailed investigations in future studies.

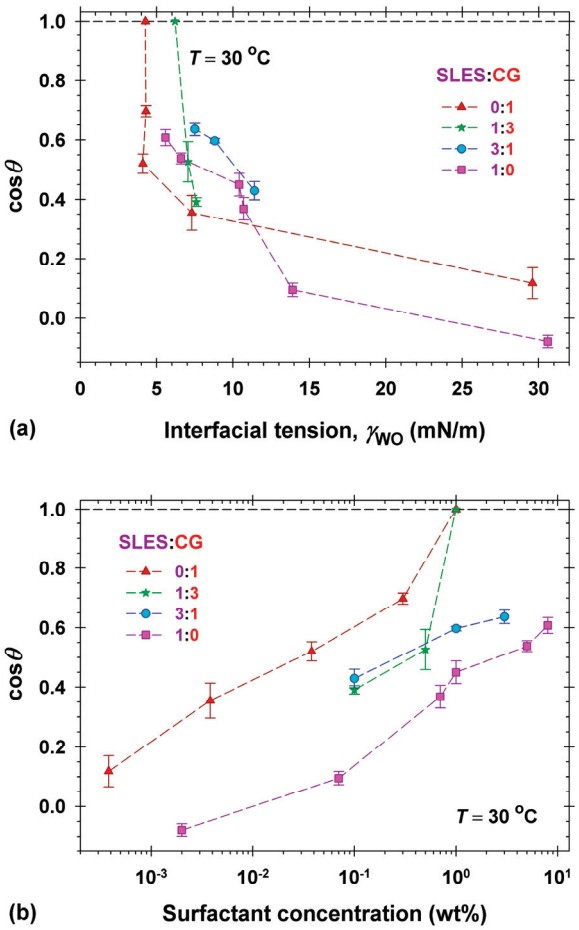

Figure 7. Dependence of the cosine of the three-phase contact angle, cosθ, of dimethicone droplets on Vitroskin® on (**a**) the interfacial tension, γ_{WO}, and on (**b**) the total surfactant concentration in mixed solutions of SLES and CG. All measurements were performed at 30 °C.

The effect of the cationic DTAB in the mixed DTAB+CG surfactant solutions on the detachment of dimethicone droplets deposited on Vitroskin® is shown in Figure 8, along with the results obtained for DTAB+CG at a ratio of 1:4. These solutions had an alkaline natural pH at concentrations higher than 0.5 wt% due to the prevailing concentration of CG.

The parallel measurements were performed by adjusting the pH of all studied solutions to pH = 6, and the obtained results are included in Figure 8. The lowest value of γ_{WO} of 3.2 mN/m was measured in the alkaline mixed solutions (see Figure 8a); however, the detachment of droplets was observed at 3 wt% total concentration in both alkaline and pH = 6, see Figure 8b.

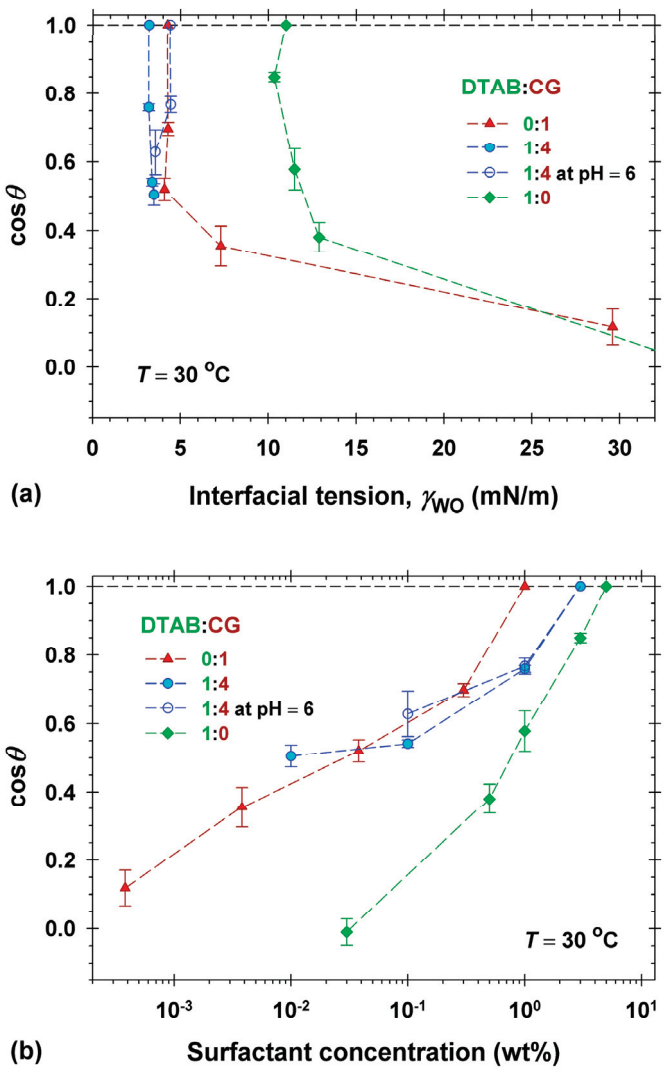

Figure 8. Cosine of the three-phase contact angle through the water phase, cosθ, of dimethicone droplets deposited on Vitroskin® vs. (**a**) the interfacial tension, γ_{WO}, and (**b**) the total surfactant concentration in mixed solutions of DTAB and CG (T = 30 °C).

The mixtures of CG with the anionic surfactants were very effective at an anionic/nonionic ratio of 1:3, and the dimethicone drop detachments occurred at a total concentration of 1 wt% (cf. Figures 6b and 7b). Thus, the synergistic mixing of CG with DSLSS and SLES at a ratio of 1:3 with respect to the dimethicone removal efficiency was observed. In contrast, the addition of DTAB to CG at a 1:4 ratio produced a less effective mixture, leading to drop detachments at a total concentration of 3 wt%. Thus, the antagonistic mixing of CG and DTAB takes place.

To compare directly the impact of the different ionic surfactants on the effectiveness of CG, we present cosθ as a function of the weight fraction of the nonionic CG in the respective mixtures at a total surfactant concentration of 1 wt%; see Figure 9. The addition of all ionic surfactants deteriorates the effectiveness of CG, as seen from the data. No

drop detachment was observed in any of the solutions containing the cationic DTAB. Best results were obtained with the mixture of DSLSS and CG, which is effective even at a 1:1 ratio. A peculiar minimum of cosθ versus the weight fraction of CG was observed for CG+SLES mixed surfactant solutions. To check whether this minimum was related to the specific interactions of the sulfate head or to the present nonionic admixture (cf. Section 2.1 and Figure 1b), we prepared a mixture with sodium dodecyl sulfate (SDS) at a 1:1 ratio. The results obtained (triangles on Figure 8) were quite comparable to those of the same ratio of SLES and CG. One could summarize that sulfate surfactants SLES and SDS have shown quite different dimethicone soil removal activity: the worst results were obtained at 50 to 60 weight percent sulfate surfactant in the mixtures with CG. The opposite effect has been observed with sebum: SLES showed the best performance by emulsification mechanisms at a relatively low surfactant concentration, most probably acting synergistically with components of the sebum. These results clearly illustrate the importance of the optimization step when formulating cleansing surfactant mixtures for a particular application.

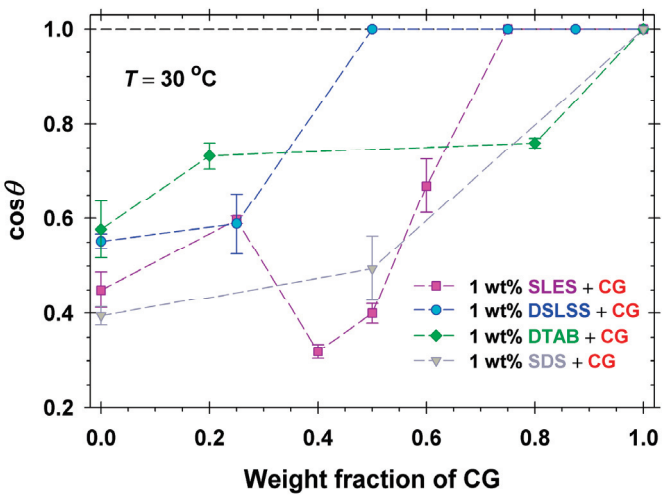

Figure 9. Cosine of the three-phase contact angle through the water phase of dimethicone droplets deposited on Vitroskin® vs. the weight fraction of CG in mixed surfactant solutions (CG with ionic surfactant) at a total concentration of 1 wt% and T = 30 °C.

2.4. Dimethicone Soils Removal in Model Cleansing Formulations

The cleansing products on the market contain not only surfactants but also humectants to avoid skin dryness, preservatives to ensure consumer safety, and perfume composition (PC) to have a pleasant scent [1–3,6,20]. All these additives might interact with the surfactants, leading to product and cleansing deterioration in some cases [3,57].

To demonstrate further the applicability of the proposed procedure to actual product development processes, we performed observations of dimethicone removal from Vitroskin® in simple cleanser formulations. The surfactant base of the formulations was selected using the results for the cleansing performance of the mixed systems presented in Section 2.3. Table 2 presents the compositions of five formulations labeled as F-G (CG containing), F-ES (SLES containing), F-SS (DSLSS containing), F-G+ES (containing a 1:1 mixture of CG and SLES), and F-G+SS (containing a 1:1 mixture of CG and DSLSS). Each formulation contains 12 wt% surfactant, 3 wt% glycerin (humectant), 1 wt% sodium benzoate as a preservative, 0.05 wt% perfume composition, and 1 wt% NaCl. Sodium chloride is a cheap raw material widely used as a rheology modifier for sulfate-containing cleansers [1,3,42,58,59]. We added NaCl with the same concentration to all formulations

to ensure relative formulation similarity (no electrolytes in the raw materials have been quantified). The pH of the formulations was adjusted in the range from 5 to 5.5 by means of citric acid. The formulations were prepared one day prior to use. The observations of dimethicone droplets on Vitroskin® were performed after a 12-fold dilution to a total surfactant concentration of 1 wt%. Note that the cleansing formulations with DSLSS (F-SS and F-G+SS) were turbid; however, after dilution, the turbidity was negligible, and optical observations were possible. The solutions of the surfactant DSLSS in water were transparent. The turbidity in the model cleanser formulations most probably resulted from specific interactions of DSLSS either with the preservative Na benzoate or with the used perfume composition.

Table 2. Composition of the model formulations of cleansing products.

	Composition, wt%				
Substances	**F-G**	**F-ES**	**F-SS**	**F-G+ES**	**F-G+SS**
water	qs to 100	qs to 100	qs to 100	qs to 100	qs to 100
CG	12	–	–	6	6
SLES	–	12	–	6	–
DSLSS	–	-	12	-	6
Glycerin	3	3	3	3	3
NaCl	1	1	1	1	1
Na Benzoate	1	1	1	1	1
Citric acid	qs	qs	qs	qs	qs
PC	0.05	0.05	0.05	0.05	0.05

The measured three-phase contact angles of dimethicone droplets on Vitroskin® in the 12-fold diluted model cleansers are shown in Table 3. For comparison, the contact angles measured with 1 wt% surfactant solutions in DI water are also shown. The determined values of the interfacial tension, γ_{WO}, and the pH of the solutions are included in Table 3. The pH slightly changed after the formulations were diluted with water, but the variations were less than 0.5 units, which is not expected to impact the results.

Table 3. Contact angle, θ, interfacial tension, γ_{WO}, and pH of aqueous surfactant solutions (no pH was adjusted, except for CG) and diluted formulations (see Table 2) at a total surfactant concentration of 1 wt%. Full drop detachment was observed when $\cos\theta = 1$.

Surfactants, 1 wt%	**Contact Angle, θ, deg**	**$\cos\theta$**	**γ_{WO}, mN/m**	**pH**
CG	0	1	4.5	6.0
F-G	0	1	4.5	5.6
SLES	63.3	0.45	10.4	6.8
F-ES	63.5	0.44	9.3	5.5
DSLSS	56.5	0.55	5.4	4.8
F-SS	61.2	0.48	5.2	4.7
1:1 CG+SLES	66.5	0.40	7.7	10.4
F-G+ES	61.3	0.48	7.3	5.5
1:1 CG+DSLSS	0	1	5.2	6.8
F-G+SS	47.1	0.68	4.3	4.8

The results in Table 3 show a very good correlation between the observed droplet behavior and the surfactant composition used, except for the mixture of DSLSS and CG (cf. the last two rows in the table). The weaker drop shrinkage, i.e., a higher contact angle, θ, in the formulations with DSLSS compared to the aqueous solutions of DSLSS, could be due to the deteriorating effect of the ingredients, seen as turbidity in these formulations.

Overall, the observations of dimethicone droplets on Vitroskin® in the prepared formulations confirmed the excellent drop removal by CG, the surfactant with the best interfacial activity. In addition, the issue of the possible negative impact of some formulation ingredients on the cleansing was well exhibited with the formulations of DSLSS.

3. Discussion

The comparison of the cleansing effectiveness of formulations in the model experiments we performed with dimethicone soil on Vitroskin® allowed for good discrimination between their performance: F-G > F-G+SS > F-G+ES ≈ F-SS ≥ F-ES. The obtained rating of the formulation's performance corresponds qualitatively well to the rating of its interfacial activity (cf. Figure 1b) and is very different from what one could expect based on the surface activity and the CMC values (Figure 1a). The absence of clear impact of the CMC on the surfactant performance is well known in the practice, and the optimization of products is mainly performed by direct examination of the cleaning of colored soils in vivo [18,19] or on selected surfaces [8,20,32,33], e.g., by cloth sweeping or by machine rubbing [18,19,33], and the effectiveness is measured by colorimetry [18–20,33]. Although the latter approach looks like a straightforward choice for the industry, it does not allow for the understanding of the intimate mechanisms and the role of the components in the process. The complication with the measurements in vivo represents another challenge, especially when developing makeup removers, for example. Some of the developed artificial skin models are a good alternative to use, as applied widely already [8,32,33]. The model experiments performed by us with Vitroskin® revealed further important details. The dimethicone removing capacity of the cationic surfactant DTAB was found to be comparable to that of the anionic DSLSS and much better than that of SLES (cf. Figure 4a). The determined adsorption of DTAB (1.99 μmol/m^2, see Figure 5) on the interface of artificial skin/water decreased most significantly the skin surface energy, allowing for dimethicone removal at relatively high interfacial tension (Figure 4b). Good cleaning properties have been documented for other cationics in detergent formulations [60,61]. Cationic surfactants are present in almost all contemporary micellar water products on the market.

Anionic and nonionic surfactants also adsorb on the skin surface; however, the adsorbed amount could not be determined quantitatively, as performed for the cationic DTAB (see Equation (2) and Figure 8), due to the presence of significant oil-soluble fractions that change the surface energy of the oil/skin interface as well. These oil-soluble admixtures influenced the interfacial activity and the overall dimethicone removal efficiency. The surfactant raw materials usually contain admixtures remaining after the synthesis and/or purification step of the substance [42]. These admixtures could significantly change the surface adsorption and cleaning efficacy, as demonstrated in the presented experimental results and analyses.

The interfacial activity and the cleansing depend on the soil phase as well. The anionic SLES decreased the interfacial tension sebum/water to less than 1 mN/m at not very high concentration, which resulted in sebum emulsification [35]. The same surfactant and a similar SDS could not decrease γ_{WO} enough to roll up dimethicone droplets. The other anionic DSLSS, which is frequently used as a substitute for sulfate surfactants in

contemporary cleansing products, successfully rolls up dimethicone from the artificial skin but could not remove sebum [35].

The optimization step of the surfactant mixtures is crucial for obtaining a good cleansing performance at a minimum surfactant concentration. Our model experiments showed that the mixture of CG and DSLSS (1:1) at a total concentration of 1 wt% was quite successful in dimethicone removal (Figure 9); however, the present perfume and/or preservative deteriorated the performance of their formulation (see Table 3). The addition of CG to DTAB also did not result in the best cleaning. Earlier investigators (see Ref. [23] and the references cited therein) have shown that when using scrubbing or wiping off, as in the application of the contemporary micellar water, a contact angle through the aqueous phase of less than 90° is already enough to ensure a good cleaning. Further upgrade of the applied in vitro methodology, by combining it with wiping off measurements and with a larger number of soils, could be applied to practical cleansing product optimization, bringing a deeper understanding of the role of the ingredients.

4. Materials and Methods

4.1. Materials

The following anionic surfactants were used: SLES (sodium laureth sulfate, commercial name Texapon N70, product of BASF, Ludwigshafen, Germany), DSLSS (disodium laureth sulfosuccinate, Texapon SB3KC, BASF, Ludwigshafen, Germany), and SDS (sodium dodecyl sulfate, SigmaAldrich, Darmstadt, Germany). The cationic DTAB (dodecyl trimethyl ammonium bromide, TCI, Zwijndrecht, Belgium) and the nonionic CG (coco glucoside, Plantacare 818 UP, BASF, Ludwigshafen, Germany) surfactants were also used in our studies. The structural formulas of the surfactants are shown in Table S1. Solutions of the surfactants were prepared in deionized (DI) water from an Elix purification system (Millipore, Darmstadt, Germany) and in hard water containing 150 ppm calcium and magnesium salts. Hard water was prepared according to the procedure after the US Environmental Protection Agency [62]. The used $CaCl_2$, $MgCl_2$, and $NaHCO_3$ were products of Sigma Aldrich.

The model soils were sebum and dimethicone (polydimethylsiloxane AK100, Wacker, Munich, Germany). The artificial sebum was prepared with the following composition [63,64]: 15% Squalene, 25% Wax esters, 2% Cholesteryl esters, 42% Triglycerides, 15% Fatty acids, 1% Cholesterol (all products of Sigma). Dimethicone was chosen as a model soil since it is a key component in decorative cosmetics, including products like lipsticks, gloss, etc. [1–3]. Structural formulas of the soil ingredients are shown in Table S2.

As an artificial skin, we used VitroSkin® (purchased from IMS, Bunnell, FL, USA). Pieces of size 1 × 2 cm were cut and used either dry or hydrated as advised by the producers [31]: 16 h in a closed chamber above a water–glycerin solution, 52 g glycerin in 298 g water.

For the preparation of the model cleansing formulation, we used glycerin (Valerus, Sofia, Bulgaria) as a humectant, inorganic salt NaCl (Sigma) as a thickener of the formulation, Na Benzoate (Valerus, Sofia, Bulgaria) as a preservative, and a perfume composition (Crisp spring, Luzi fragrance compounds). To adjust the desired pH of the solution, HCl (Sigma Aldrich, Darmstadt, Germany) or citric acid (Valerus, Sofia, Bulgaria) solutions were used.

4.2. Methods

4.2.1. Surface and Interfacial Tension Measurements, pH, and Conductivity Determination

Surface tension isotherms for the surfactants used in deionized water at 30 °C were determined using the du Noüy ring method with a K100 tensiometer (Kruess GmbH, Hamburg, Germany), equipped with an automatic dosing unit and a micro dispenser, and the maximum bubble pressure method with a BP100 (Kruess GmbH, Hamburg, Germany). The interfacial tension of the oils in the chosen surfactant solutions was measured using the pendant drop method with the Drop Shape Analyzer DSA100E (Kruess GmbH, Hamburg, Germany) at 30 °C. Note that the used artificial sebum was liquid at 30 °C.

The pH and conductivity of all solutions were measured by Fisherbrand™ accumet™ AB200 benchtop pH/conductivity meter at 30 °C.

4.2.2. Direct Observations of the Soil Removal from Vitroskin®

The observations of soil removal were conducted using the Drop Shape Analyzer DSA10 (Kruess GmbH, Hamburg, Germany) optical system. The methodology and experimental setup (Figure 10) were adapted after Yavrukova et al. [51]. The procedure was as follows: First, Vitroskin® substrate, hydrated in advance, was placed at the bottom of a 50 mL rectangular glass cuvette. Then, a 5 μL soil drop was deposited onto the substrate and allowed to rest for 5 min. Subsequently, 20 mL of surfactant solution at 30 °C was gently added to the cuvette. The shrinking of the contact area between the soil droplet and the substrate (including potential drop detachment) was monitored for 5 min (see Figures 2 and 3). Measurements with each surfactant solution or formulation were conducted at least twice, i.e., on two or more different substrates.

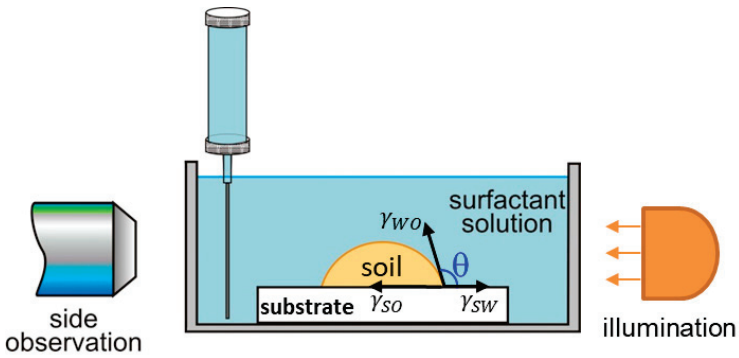

Figure 10. Scheme of experimental setup for direct observations of the soil removal from the surface of Vitroskin®. The glass cuvette with the soiled surface and the surfactant solution was mounted on the Drop Shape Analyzer DSA10 (Kruess GmbH, Hamburg, Germany), whose optical system was used for the observations. All experiments were performed at 30 °C.

5. Conclusions

The performed systematic characterization of soil removal from artificial skin by applying direct optical observations in different surfactant solutions allowed for the demonstration of two basic cleansing mechanisms: emulsification and roll-up. Emulsification occurred in systems with very low (below 1 mN/m) interfacial tension, γ_{WO}, as for the sebum and SLES solutions. Dimethicone soil was removed by the roll-up mechanism, and no emulsification was observed.

The effectiveness of the roll-up depends on the interfacial activity of the used surfactants and on their adsorption on the soiled surface. Thus, the cationic DTAB, adsorbing strongly on the artificial skin, was able to roll up dimethicone at γ_{WO} as high as 11 mN/m.

The anionic SLES and DSLSS, and the nonionic CG had lower adsorption on the skin than DTAB, but reduced the oil/water interfacial tension more significantly, and successfully rolled up dimethicone at γ_{WO} below 5 mN/m. The used DTAB did not contain oil-soluble components, as evidenced by the conductivity, surface, and interfacial tension measurements, which allowed for the determination of its adsorption of 1.99 μmol/m^2 on the Vitroskin® surface.

The nonionic CG fully removed the dimethicone from the skin at a lower concentration compared to the ionic surfactants used. The addition of some fraction of CG to the ionic surfactants was used to obtain good cleaning at decreased concentration of the anionics.

The developed in vitro procedure for cleansing efficacy characterization was applied to a series of simple cleansing formulations based on preselected surfactant mixtures and containing also humectant, salt, preservative, and perfume. The comparison of the cleansing effectiveness of formulations allowed for a good discrimination between their performance. Furthermore, their rating corresponded qualitatively well to the performance of the surfactant mixtures and to the rating of their interfacial activity.

Our investigation demonstrated well that model experiments with artificial skin could be applied and used to investigate the physicochemical mechanisms of soil removal, and to discriminate the effects of different types of surfactants in the cleansing compositions. Future applications of the developed approach to practical formulations would speed up the product development process and would allow for a fast evaluation of new raw materials.

Supplementary Materials: The following supporting information can be downloaded at: https://www.mdpi.com/article/10.3390/molecules30081813/s1. Figure S1. Electrolytic conductivity, κ, and pH of DTAB aqueous solutions vs DTAB molar concentration, *C*. Figure S2. Electrolytic conductivity, κ, and pH of SLES aqueous solutions vs SLES molar concentration, *C*. Figure S3. Electrolytic conductivity, κ, and pH of CG aqueous solutions vs CG molar concentration, *C*. Figure S4. Electrolytic conductivity, κ, and pH of DSLSS aqueous solutions vs DSLSS molar concentration, *C*. Figure S5. Dependence of $\gamma_{WO} \cos\theta$ on the surfactant concentration for CG, SLES, and DSLSS solutions. Table S1. Structural formulas of the used surfactants. Table S2. Structural formulas of the ingredients of the soils.

Author Contributions: Conceptualization, K.M.; methodology, R.S. and T.S.; investigation, R.S. and T.S.; data curation, T.S., R.S. and K.D.; writing—original draft preparation, R.S. and K.M.; writing—review and editing, K.M. and K.D.; supervision, K.M. and K.D. All authors have read and agreed to the published version of the manuscript.

Funding: The support of the Centre of Competence "Sustainable Utilization of Bio-resources and Waste of Medicinal and Aromatic Plants for Innovative Bioactive Products" (BIORESOURCES BG), project BG16RFPR002-1.014-0001, funded by the Program "Research, Innovation and Digitization for Smart Transformation" 2021–2027, co-funded by the EU, and the support of the National Science Fund of Bulgaria, Grant No. KP-06-N 79/4/2023, are greatly acknowledged.

Institutional Review Board Statement: Not applicable.

Informed Consent Statement: Not applicable.

Data Availability Statement: The data from this study are available upon request made to the corresponding author.

Acknowledgments: The authors acknowledge the equipment support of the European Regional Development Fund under the Operational Program "Scientific Research, Innovation and Digitization for Smart Transformation 2021-2027", Project CoC "Smart Mechatronics, Eco- and Energy Saving Systems and Technologies", BG16RFPR002-1.014-0005.

Conflicts of Interest: The authors declare no conflicts of interest.

References

1. Baki, G.; Alexander, K.S. *Introduction to Cosmetic Formulation and Technology*; John Wiley & Sons, Inc.: Hoboken, NJ, USA, 2015.
2. Abe, T. Psychology of Cosmetic Behavior. In *Cosmetic Science and Technology: Theoretical Principles and Applications*; Sakamoto, K., Lochhead, R.Y., Maibach, H.I., Yamashita, Y., Eds.; Elsevier: Amsterdam, The Netherlands, 2017; pp. 101–113. [CrossRef]
3. Mitsui, T. *New Cosmetic Science*; Elsevier Science: Amsterdam, The Netherlands, 1997.
4. Ananthapadmanabhan, K.P. Amino-Acid Surfactants in Personal Cleansing (Review). *Tenside Surf. Det.* **2019**, *56*, 378–386. [CrossRef]
5. Jahan, R.; Bodratti, A.M.; Tsianou, M.; Alexandridis, P. Biosurfactants, Natural Alternatives to Synthetic Surfactants: Physicochemical Properties and Applications. *Adv. Colloid Interface Sci.* **2020**, *275*, 102061. [CrossRef] [PubMed]
6. European Union. *Regulation (EC) No 1223/2009 of the European Parliament and of the Council of 30 November 2009 on Cosmetic Products*; European Union: Brussels, Belgium, 2009.
7. Ginn, M.E.; Noyes, C.M.; Jungermann, E. The Contact Angle of Water on Viable Human Skin. *J. Colloid Interface Sci.* **1968**, *26*, 146–151. [CrossRef] [PubMed]
8. Eudier, F.; Savary, G.; Grisel, M.; Picard, C. Skin Surface Physico-chemistry: Characteristics, Methods of Measurement, Influencing Factors and Future Developments. *Adv. Colloid Interface Sci.* **2019**, *264*, 11–27. [CrossRef]
9. Aßmus, U.; Banowski, B.; Brock, M.; Erasmy, J.; Fitzner, A.; Kortemeier, U.; Langer, S.; Munke, S.; Schmidt-Lewerkühne, H.; Segger, D.; et al. Impact of Cleansing Products on the Skin Surface pH. *IFSCC Mag.* **2013**, *16*, 17–24.
10. Hawkins, S.; Dasgupta, B.R.; Ananthapadmanabhan, K.P. Role of pH in Skin Cleansing. *Int. J. Cosmet. Sci.* **2021**, *43*, 474–483. [CrossRef]
11. Mavon, A.; Zahouani, H.; Redoules, D.; Agache, P.; Gall, Y.; Humbert, P. Sebum and Stratum Corneum Lipids Increase Human Skin Surface Free Energy as Determined from Contact Angle Measurement: A Study on Two Anatomical Sites. *Colloids Surf. B Biointerfaces* **1997**, *8*, 147–155. [CrossRef]
12. Mavon, A.; Redoules, D.; Humbert, P.; Agache, P.; Gall, Y. Changes in Sebum Levels and Skin Surface Free Energy Components Following Skin Surface Washing. *Colloids Surf. B Biointerfaces* **1998**, *10*, 243–250. [CrossRef]
13. German, G.K.; Pashkovski, E.; Dufresne, E.R. Surfactant Treatments Influence Drying Mechanics in Human Stratum Corneum. *J. Biomech.* **2013**, *46*, 2145–2151. [CrossRef]
14. Elkhyat, A.; Agache, P.; Zahouani, H.; Humbert, P. A New Method to Measure *In Vivo* Human Skin Hydrophobia. *Int. J. Cosmet. Sci.* **2001**, *23*, 347–352. [CrossRef]
15. Elkhyat, A.; Mavon, A.; Leduc, M.; Agache, P.; Humbert, P. Skin Critical Surface Tension: A Way to Assess the Skin Wettability Quantitatively. *Skin Res Technol.* **1996**, *2*, 91–96. [CrossRef]
16. Krawczyk, J. Surface Free Energy of the Human Skin and its Critical Surface Tension of Wetting in the Skin/Surfactant Aqueous Solution/Air System. *Skin Res. Technol.* **2015**, *21*, 214–223. [CrossRef]
17. Tsujii, K. Wetting and Surface Characterization. In *Cosmetic Science and Technology: Theoretical Principles and Applications*; Sakamoto, K., Lochhead, R.Y., Maibach, H.I., Yamashita, Y., Eds.; Elsevier: Amsterdam, The Netherlands, 2017; pp. 373–388. [CrossRef]
18. Elsner, P.; Seyfarth, F.; Sonsmann, F.; John, S.-M.; Diepgen, T.; Schliemann, S. Development of a Standardized Procedure for Testing the Efficacy of Workplace Cleansers. *Contact Dermat.* **2014**, *70*, 35–43. [CrossRef]
19. Sonsmann, F.K.; Strunk, M.; Gediga, K.; Schliemann, S.; Seyfarth, F.; Elsner, P.; Diepgen, T.L.; Kutz, G.; John, S.M. Standardization of Skin Cleansing *In Vivo*: Part II. Validation of a Newly Developed Automated Cleansing Device (ACiD). *Skin Res. Technol.* **2014**, *20*, 239–245. [CrossRef] [PubMed]
20. Lai, K.-Y. (Ed.) *Liquid Detergents*; Taylor & Francis Group: Boca Raton, FL, USA, 2005. [CrossRef]
21. Ali, A.; Ringstad, L.; Skedung, L.; Falkman, P.; Wahlgren, M.; Engblom, J. Tactile Friction of Topical Creams and Emulsions: Friction Measurements on Excised Skin and VitroSkin® using ForceBoard™. *Int. J. Pharm.* **2022**, *615*, 121502. [CrossRef] [PubMed]
22. Lir, I.; Haber, M.; Dodiuk, H. Skin Surface Model Material as a Substrate for Adhesion-to-Skin Testing. *J. Adhes. Sci. Technol.* **2007**, *21*, 1497–1512. [CrossRef]
23. Rhein, L. Surfactant Action on Skin and Hair: Cleansing and Skin Reactivity Mechanisms. In *Handbook for Cleaning/Decontamination of Surfaces*; Johansson, I., Somasundaran, P., Eds.; Elsevier: Amsterdam, The Netherlands, 2007; pp. 305–371. [CrossRef]
24. Cornwell, P.A. A Review of Shampoo Surfactant Technology: Consumer Benefits, Raw Materials and Recent Developments. *Int. J. Cosmet. Sci.* **2018**, *40*, 16–30. [CrossRef]
25. Lochhead, R.Y. Basic Physical Sciences for the Formulation of Cosmetic Products. In *Cosmetic Science and Technology: Theoretical Principles and Applications*; Sakamoto, K., Lochhead, R.Y., Maibach, H.I., Yamashita, Y., Eds.; Elsevier: Amsterdam, The Netherlands, 2017; pp. 39–76. [CrossRef]

26. Flaten, G.E.; Palac, Z.; Engesland, A.; Filipović-Grčić, J.; Vanić, Z.; Škalko-Basnet, N. In Vitro Skin Models as a Tool in Optimization of Drug Formulation. *Eur. J. Pharm. Sci.* **2015**, *75*, 10–24. [CrossRef]
27. Schmidt, F.F.; Nowakowski, S.; Kluger, P.J. Improvement of a Three-Layered In Vitro Skin Model for Topical Application of Irritating Substances. *Front. Bioeng. Biotechnol.* **2020**, *8*, 388. [CrossRef]
28. Jermann, R.; Toumiat, M.; Imfeld, D. Development of an in Vitro Efficacy Test for Self-Tanning Formulations. *Int. J. Cosm. Sci.* **2002**, *24*, 35–42. [CrossRef]
29. Bhushan, B. Nanotribological and Nanomechanical Properties of Skin with and without Cream Treatment using Atomic Force Microscopy and Nanoindentation. *J. Colloid Interface Sci.* **2012**, *367*, 1–33. [CrossRef] [PubMed]
30. Tang, W.; Zhang, J.; Chen, S.; Chen, N.; Zhu, H.; Ge, S.; Zhang, S. Tactile Perception of Skin and Skin Cream. *Tribol. Lett.* **2015**, *59*, 24. [CrossRef]
31. Douguet, M.; Picard, C.; Savary, G.; Merlaud, F.; Loubat-bouleuc, N.; Grisel, M. Spreading Properties of Cosmetic Emollients: Use of Synthetic Skin Surface to Elucidate Structural Effect. *Colloids Surf. B Biointerfaces* **2017**, *154*, 307–314. [CrossRef] [PubMed]
32. Turner, R.B.; Biedermann, K.A.; Morgan, J.M.; Keswick, B.; Ertel, K.D.; Barker, M.F. Efficacy of Organic Acids in Hand Cleansers for Prevention of Rhinovirus Infections. *Antimicrob. Agents Chemother.* **2004**, *48*, 2595–2598. [CrossRef]
33. DeMarco, G.M.; Ekman-Gunn, E.; Poccia, J.F., III. Gel Wipe Composition Comprising a Superabsorbent Gel Fiber. U.S. Patent US20160367102A1, 22 December 2016.
34. VITRO-SKIN® The Global Standard for Rapid, Predictive In Vitro Testing. Available online: https://ims-usa.com/vitro-skin-substrates/vitro-skin/ (accessed on 12 April 2025).
35. Marinova, K.; Slavova, T.; Stanimirova, R.; Danov, K. Artificial Skin Characterization for Cleansing Observation and Quantification. In Proceedings of the 33rd IFSCC Congress, Barcelona, Spain, 4–7 September 2023.
36. Wu, S. Calculation of Interfacial Tensions in Polymer Systems. *J. Polym. Sci.* **1971**, *34*, 19–30. [CrossRef]
37. Moulik, S.P.; Haque, M.d.E.; Jana, P.K.; Das, A.R. Micellar Properties of Cationic Surfactants in Pure and Mixed State. *J. Phys. Chem.* **1996**, *100*, 701–708. [CrossRef]
38. Christov, N.C.; Danov, K.D.; Kralchevsky, P.A.; Ananthapadmanabhan, K.P.; Lips, A. Maximum Bubble Pressure Method: Universal Surface Age and Transport Mechanisms in Surfactant Solutions. *Langmuir* **2006**, *22*, 7528–7542. [CrossRef]
39. Battal, T.; Shearman, G.C.; Valkovska, D.; Bain, C.D. Determination of the Dynamic Surface Excess of a Homologous Series of Cationic Surfactants by Ellipsometry. *Langmuir* **2003**, *19*, 1244–1248. [CrossRef]
40. Ranieri, D.; Preisig, N.; Stubenrauch, C. On the Influence of Intersurfactant H-Bonds on Foam Stability: A Study with Technical Grade Surfactants. *Tenside Surfact. Det.* **2018**, *55*, 6–16. [CrossRef]
41. Lunkenheimer, K.; Czichocki, G. On the Stability of Aqueous Sodium Dodecyl Sulfate Solutions. *J. Colloid Interface Sci.* **1993**, *160*, 509–510. [CrossRef]
42. O'Lenick, A.J. *Surfactants: Strategic Personal Care Ingredients*; Allured Publishing Corporation: Carol Stream, IL, USA, 2014; pp. 43–91.
43. Vollhardt, D.; Czichocki, G.; Rubert, R. Effect of the Molecular Structure on the Adsorption of Alkyl Ether Sulphates and Alkane Ether Sulphonates at the Air–Water Interface. *Colloids Surf. A* **1998**, *142*, 315–322. [CrossRef]
44. Danov, K.D.; Kralchevsky, P.A.; Ananthapadmanabhan, K.P. Micelle–Monomer Equilibria in Solutions of Ionic Surfactants and in Ionic–Nonionic Mixtures: A Generalized Phase Separation model. *Adv. Colloid Interface Sci.* **2014**, *207*, 17–45. [CrossRef]
45. Catanoiu, G.; Carey, E.; Patil, S.R.; Engelskirchen, S.; Stubenrauch, C. Partition Coefficients of Nonionic Surfactants in Water/n-Alkane Systems. *J. Colloid Interface Sci.* **2011**, *355*, 150–156. [CrossRef]
46. Varvil, J.; McCurry, P.; Pickens, C. Production of Alkyl Glucosides. In *Handbook of detergents. Part F: Production*; Zoller, U., Sosis, C., Eds.; CRC Press: Boca Raton, FL, USA, 2009; pp. 69–82.
47. Johnson, W.; Heldreth, B.; Bergfeld, W.F.; Belsito, D.V.; Hill, R.A.; Klaassen, C.D.; Liebler, D.C.; Marks, J.G.; Shank, R.C. Safety Assessment of Alkyl PEG Sulfosuccinates as Used in Cosmetics. *Int. J. Toxicol.* **2015**, *34*, 70S–83S. [CrossRef]
48. Matsuoka, K.; Noshiro, N.; Kuroki, H.; Tsuyuzaki, K.; Hashimoto, G. Vesicle Formation of Disodium Lauryl Sulfosuccinate. *J. Mol. Liq.* **2022**, *348*, 118422. [CrossRef]
49. Dillan, K.W.; Goddard, E.D.; McKenzie, D.A. Oily Soil Removal from a Polyester Substrate by Aqueous Nonionic Surfactant Systems. *J. Am. Oil Chem. Soc.* **1979**, *56*, 59–70. [CrossRef]
50. Kolev, V.L.; Kochijashky, I.I.; Danov, K.D.; Kralchevsky, P.A.; Broze, G.; Mehreteab, A. Spontaneous Detachment of Oil Drops from Solid Substrates: Governing Factors. *J. Colloid Interface Sci.* **2003**, *257*, 357–363. [CrossRef] [PubMed]
51. Yavrukova, V.I.; Shandurkov, D.N.; Marinova, K.G.; Kralchevsky, P.A.; Ung, Y.W.; Petkov, J.T. Cleaning Ability of Mixed Solutions of Sulfonated Fatty Acid Methyl Esters. *J. Surfact. Deterg.* **2020**, *23*, 617–627. [CrossRef]
52. Miller, C.A.; Raney, K.H. Solubilization-Emulsification Mechanisms of Detergency. *Colloids Surf. A* **1993**, *74*, 169–215. [CrossRef]

53. Raney, K.H.; Benton, W.J.; Miller, C.A. Optimum Detergency Conditions with Nonionic Surfactants. I. Ternary Water-Surfactant-Hydrocarbon Systems. *J. Colloid Interface Sci.* **1987**, *117*, 282–290. [CrossRef]
54. Lim, Y.S.; Stanimirova, R.D.; Xu, H.; Petkov, J. Sulphonated Methyl Ester a Promising Surfactant for Detergency in Hard Water Conditions. *HPC Today* **2016**, *11*, 47–51.
55. Fernández-Peña, L.; Guzmán, E. Physicochemical Aspects of the Performance of Hair-Conditioning Formulations. *Cosmetics* **2020**, *7*, 26. [CrossRef]
56. Zhang, R.; Somasundaran, P. Advances in Adsorption of Surfactants and their Mixtures at Solid/Solution Interfaces. *Adv. Colloid Interface Sci.* **2006**, *123–126*, 213–229. [CrossRef]
57. Halla, N.; Fernandes, I.P.; Heleno, S.A.; Costa, P.; Boucherit-Otmani, Z.; Boucherit, K.; Rodrigues, A.E.; Ferreira, I.C.F.R.; Barreiro, M.F. Cosmetics Preservation: A Review on Present Strategies. *Molecules* **2018**, *23*, 1571. [CrossRef]
58. Yavrukova, V.I.; Radulova, G.M.; Danov, K.D.; Kralchevsky, P.A.; Xu, H.; Ung, Y.W.; Petkov, J.T. Rheology of Mixed Solutions of Sulfonated Methyl Esters and Betaine in Relation to the Growth of Giant Micelles and Shampoo Applications. *Adv. Colloid Interface Sci.* **2020**, *275*, 102062. [CrossRef] [PubMed]
59. Mitrinova, Z.; Alexandrov, H.; Denkov, N.; Tcholakova, S. Effect of Counter-Ion on Rheological Properties of Mixed Surfactant Solutions. *Colloids Surf. A* **2022**, *643*, 128746. [CrossRef]
60. Yavrukova, V.; Cooban, E.; Blanco, I.; Pambou, E.; Marinova, K.; Petkov, J. Investigation of the detergency properties of mixtures of biocides and nonionic surfactants using a new simplified hard surface cleaning method. *J. Surf. Det.* **2025**, *28*, 389–397. [CrossRef]
61. Brycki, B.E.; Kowalczyk, I.H.; Szulc, A.M.; Brycka, J.A. Quaternary alkylammonium salts as cleaning and disinfectant agents. *Tenside Surfactant Deterg.* **2018**, *55*, 55–438. [CrossRef]
62. *Standard Operating Procedure for Preparation of Hard Water and Other Diluents for Antimicrobial Products*; Environmental Science Center: Ft. Meade, MD, USA, 2019; SOP Number: MB-30-02, 08-21-19.
63. Lu, G.W.; Valiveti, S.; Spence, J.; Zhuang, C.; Robosky, L.; Wade, K.; Love, A.; Hu, L.-Y.; Pole, D.; Mollan, M. Comparison of Artificial Sebum with Human and Hamster Sebum Samples. *Int. J. Pharm.* **2009**, *367*, 37–43. [CrossRef]
64. Walters, K.A.; Roberts, M.S. The Structure and Function of Skin. In *Dermatological and Transdermal Formulations*; Walters, K.A., Ed.; CRC Press: Boca Raton, FL, USA; Taylor and Francis Group: Boca Raton, FL, USA, 2002; pp. 1–40.

Disclaimer/Publisher's Note: The statements, opinions and data contained in all publications are solely those of the individual author(s) and contributor(s) and not of MDPI and/or the editor(s). MDPI and/or the editor(s) disclaim responsibility for any injury to people or property resulting from any ideas, methods, instructions or products referred to in the content.

molecules

MDPI

Article

Stabilisation of Nanosilver Supramolecular Hydrogels with Trisodium Citrate

Joanna Kowalczuk [1,*], Oleg M. Demchuk [2,*], Mariusz Borkowski [3] and Michał Bielejewski [1]

[1] Institute of Molecular Physics, Polish Academy of Sciences, M. Smoluchowskiego 17, 60-179 Poznań, Poland; michal.bielejewski@ifmpan.poznan.pl
[2] Faculty of Medicine, The John Paul II Catholic University of Lublin, 20-708 Lublin, Poland
[3] Jerzy Haber Institute of Catalysis and Surface Chemistry, Polish Academy of Sciences, Niezapominajek 8, 30-239 Kraków, Poland; mariusz.borkowski.edu@gmail.com
* Correspondence: joanna.kowalczuk@ifmpan.poznan.pl (J.K.); oleh.demchuk@kul.lublin.pl (O.M.D.)

Abstract: Designing supramolecular gelators with targeted properties is very difficult and mainly relies on structural modifications of known gelator molecules. However, very often, even minor modifications can result in the complete loss of gelation capabilities. In the present work, we have studied the influence and role of the silver nanoparticles (AgNPs) and trisodium citrate (TSC) additives on the self-assembly process of alanine derivative gelator (C_{12}Ala) and intermolecular interactions resulting in hydrogel systems of enhanced stability and sustainability. The effect of phase separation and diversity of supramolecular microstructures of gelator internal matrix on the composition of the investigated tricomponent system was studied thoroughly with thermal analysis methods (TGA/DSC), high-resolution nuclear magnetic resonance spectroscopy (HR-MAS NMR), and polarising optical microscopy (POM). The molecular mechanism of gelation and the interactions responsible for enhanced properties of nanosilver hydrogels was determined and described, indicating the synergistic role of TSC and AgNPs in the self-assembly process.

Keywords: *N*-lauroyl-L-alanine; C_{12}Ala; AgNPs; TSC; hydrogel; NMR; TGA; DSC

1. Introduction

Soft matter systems like physical gels/hydrogels find broad applications in fuels [1,2], food [3,4] and the pharmaceutical industry [5,6]. The critical parameter for successfully using these materials is their thermal and temporal stability, which depends strongly on the gelator structure and the additives incorporated in the gel. To this day, it remains impossible to predict whether a given molecule has solvent gelling properties or not. Gel research is primarily experimental work. However, sometimes a molecule that does not have solvent-gelling properties on its own acquires this property in the presence of another molecule. An example of such a molecule is *N*-lauroyl-L-alanine (C_{12}Ala), which on its own gels water very poorly and does not have the gelling properties of a hydrolate enriched with silver nanoparticles. However, the situation changes radically when the gelator–nanoparticle hydrolate system is enriched with a stabiliser molecule. Non-toxic hydrogels enriched with silver nanoparticles (AgNPs) constitute a group of materials with extremely high pharmaceutical potential [7]. In the case of AgNPs containing gels aside from the metal, the stabilators used in nanoparticle synthesis impact the gel properties. One of the most common stabilators used to synthesise negatively charged AgNPs is trisodium citrate (TSC) [8].

The biological activity of silver nanoparticles has been repeatedly confirmed in the fight against microorganisms (including bacteria, viruses, and fungi) or pathological human cancer cells [9–12]. The bioactive role of nanoparticles, including silver, depends strongly on their size and can have positive as well as negative effects on living organisms. The toxicology of nanoparticles is complicated, and the mechanism of hemotoxicity of silver nanoparticles, for example, is still not fully understood. It is unclear whether it results from the direct impact of nanoparticles on cells or from the release of silver ions. However, we can conclude that the smaller size of nanoparticles results in their more significant biological activity [13–16]. Another field where silver nanoparticles can be used is photodynamic cancer therapy (FTD). One of the effects of silver ions interactions with cells is the production of reactive oxygen species, especially their singlet form, which causes damage and cell death. The combination of a photosensitiser with silver nanoparticles leads to an increase in the efficiency of the production of free radicals in cells. One possible way to introduce photosensitisers into diseased areas is through the use of hydrogels [17,18]. Due to the alarming statistics of cancer cases, research on improving anti-cancer therapies is currently a civilisational challenge. We already know that antibiotics supported by nanoparticles improve the effectiveness of drugs, but we need personalised therapies with potentially higher therapeutic efficacy [19–22].

One of the known systems for delivering active substances to the body are gels [23]. A necessary condition for creating such systems for therapeutic purposes is the use of components (solvents and gelators) that have a neutral effect on the organism, can transform pharmaceuticals into an inactive gel form, and release and activate them at the targeted side. However, finding such a gelator to create non-toxic, durable, and stable systems is difficult. The best candidates are hydrogels, which use water to dissolve and immobilise the drug in the gel phase [24,25]. Recent research on different low-molecular-weight gelators showed that the representative of fatty acid amide C_{12}Ala displays the ability to create physical gels with varying types of solvents, including organic solvents, oils, emulsions (oil–water mixture) and water [26–30]. In particular, water is an important solvent that can create gel-based drug carrier systems enriched with gold and silver nanoparticles [9,31].

Although C_{12}Ala (LMWGs; low-molecular-weight gelators) has been shown to form hydrogels, it was found that their stability is time-limited. The pure hydrogel C_{12}Ala-H_2O undergoes phase separation within a few hours after gelation. The stable, homogeneous gel (verified by the inverse tube test) disintegrates and begins to resemble the structure of semolina or micellar fluid. While working on the C_{12}Ala gel enriched with silver nanoparticles, we noticed that after a few months of storing the C_{12}Ala-TSC hydrogel at 5 °C, the solid and liquid phases also began to separate, which resulted in the gravitational outflow of water from the sample. This effect does not bode well for the durability of the resulting gel but did not occur in the case of the gel enriched with nanoparticles. The sample enriched with TSC and AgNPs, tightly closed and stored at 5 °C retained its properties for 5 months. In the publication [9] (see Figure 5a,b), we see photos of upside-down vials with stored gels. The C_{12}Ala-TSC-AgNP sample looks homogeneous, but at the bottom of the vial with C_{12}Ala-TSC-H_20 gel (top of the image), we can see an area where water has accumulated, and the gel does not look homogeneous but rather resembles a "semolina" structure. So, the question arose about the effect of TSC and AgNPs on the internal structure of the gel and how TSC and silver nanoparticles contribute to its longer stability. In this work, the authors attempt to explain this phenomenon.

2. Materials and Methods

2.1. Hydrogel Preparation

The investigated samples of hydrogels were prepared according to the following procedures. The C_{12}Ala-H_2O hydrogels were obtained by dissolving 64 mg and 128 mg of the C_{12}Ala gelator [32] in 1 mL of deionised water to obtain 6 wt.% and 12 wt.% mixture concentrations, respectively. The dissolution was performed using a circulating water bath at 60 °C for 24 h. After dissolving the gelator molecules, the samples were cooled to room temperature for 12 h. The C_{12}Ala-TSC-H_2O hydrogels were prepared by dissolving 323 mg of TSC in 1 mL of deionised water, resulting in a molar concentration of Cm = 1.25 M. Next, the prepared solution of TSC was mixed with deionised water in a volume ratio of 0.5%/95.5% and used to prepare hydrogel samples with 6 wt.% and 12 wt.% concentrations of gelator. The procedure for dissolving the gelator in the prepared solution and obtaining the gel phase was the same as for the C_{12}Ala-H_2O system. The tube inversion test was performed to confirm no bulk flow. However, only the TSC-enriched sample retained its lack of flow over time. The C_{12}Ala-TSC-AgNP hydrogels were prepared by mixing 995 mL of AgNP water suspension and 5 mL of a 1.25 M water solution of TSC with 64 mg and 128 mg of gelator to obtain 6 wt.% and 12 wt.% hydrogels respectively. The silver nanoparticles with an average size of 30 nm (AgNPs) were synthesised as described in [9]. The chemical structures of the used compounds are depicted in Figure 1. The gelator dissolution process was carried out the same way as for other samples. As a result, we obtained three different gel systems: pure hydrogel C_{12}Ala-H_2O (not stable in the concentration of 6 wt.%), hydrogel enriched with TSC (C_{12}Ala-TSC-H_2O), and hydrogel enriched with TSC and silver nanoparticles, AgNPs, (C_{12}Ala-TSC-AgNPs). Without the addition of TSC, the C_{12}Ala molecule did not gel the nanoparticle solution containing AgNPs.

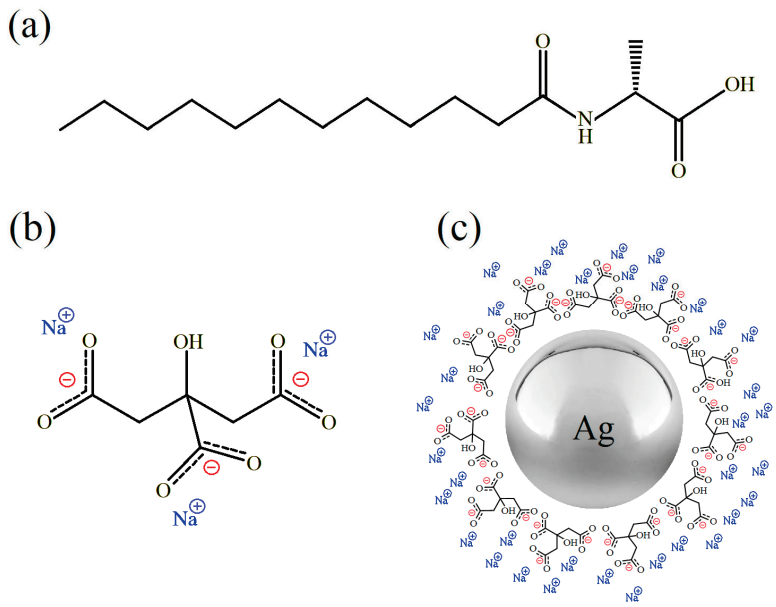

Figure 1. The chemical structure of (**a**) C_{12}Ala, (**b**) TSC, and (**c**) illustrative view of negatively charged silver nanoparticles stabilised by TSC.

2.2. Differential Scanning Calorimetry (DSC)

Differential scanning calorimetry (DSC) measurements were performed using a Perkin-Elmer DSC4000 instrument (Waltham, MA, USA). The measurements were conducted in a nitrogen atmosphere at a heating/cooling rate of 15 °C/min in the temperature range

of 20 to 100 °C. The heating and cooling rate of 15 K/min was slightly higher than the conventional 10 K/min to estimate the safe limit for storing samples in the gel state. The samples weighing approximately 14.4 mg and 12.4 mg for hydrogels with TSC and TSC-AgNPs, respectively, were loaded in hermetic crucibles. Three consecutive cycles of heating and cooling were recorded for each sample. The measurements allowed us to determine the characteristic endothermic and exothermic peaks for melting and gelation temperatures of the self-assembled matrices of the studied hydrogels.

2.3. Thermogravimetric Analysis (TGA/DTG)

Thermogravimetric analysis (TGA) was performed on a Perkin-Elmer TGA8000 device. The method allows for recording the mass loss of the sample during its thermal degradation. The measurements were performed under a nitrogen atmosphere for TSC and TSC-AgNP hydrogel samples at 10 °C/min heating rates in the temperature range of 20 to 1000 °C. The results were analysed according to the derivative method (DTG).

2.4. NMR Spectroscopy

The ^{13}C NMR spectra of the studied samples were recorded using a Bruker Avance III HD NMR spectrometer (Billerica, MA, USA) coupled to an 11.4 T superconducting magnet operating at 125.76 MHz for the carbon Larmour frequency. All experiments were recorded at room temperature using the solid-state technique for high-resolution NMR spectroscopy. The ^{13}C spectra were recorded using the ^{1}H-^{13}C CP-MAS technique to improve the S/N ratio for recorded signals. In the case of the C_{12}Ala gelator in the solid state, 2.5 mm zirconia rotors and 20 kHz spinning frequency were used for measurements. To record the ^{13}C NMR spectra of TSC solution and hydrogel samples, special 25 μL Kel-F inserts for 4 mm zirconia rotors and 5 kHz of spinning frequency were used. The lower spinning rate and special inserts were used to avoid the risk of mechanically destroying the gel state due to excessive centrifugal force and leakage of the solvent. The contact time during the cross-polarisation sequence was set to 1500 μs, the recycle delay was set to 15 s, and 2048 scans were accumulated, resulting in over 8 h of acquisition time per spectrum. The proton decoupling was achieved with a TPPM sequence at an 80 kHz radiofrequency field.

2.5. Microscopic Observation

The images of the gel microstructures were taken on an Olympus BX53 microscope (Tokyo, Japan). The pure, blank, and AgNP-enriched 12 wt.% gels were cast onto microscope slides and covered with a 130 nm thick coverslip. An image of the nanoparticle AgNP solution with the C_{12}Ala gelator was also taken for comparison. Images were taken immediately after the samples were placed on the slides.

3. Results

3.1. Calorimetric Tests (DSC)

To gain information on thermal events in the blank and silver-enriched sample, DSC scans were performed in the temperature range of 20 to 100 °C. Figure 2a,b show two heating–cooling cycles for blank (C_{12}Ala-TSC-H_2O) and silver-enriched (C_{12}Ala-TSC-AgNPs) gels.

The DSC examination revealed two characteristic peaks, gel–sol and gelation, for both samples. The gel–sol points were 64 °C and 65.5 °C for blank and silver-enriched gels, respectively. The gelation temperature varies from 35.5 °C to 34 °C in the second and third cooling cycles for the enriched sample, and for the blank sample, it remains more stable at 35.5 °C. This indicates silver nanoparticles' influence on the gelator molecules' organisation

in the gelation process. In each subsequent heating and cooling cycle, this process may take place slightly differently.

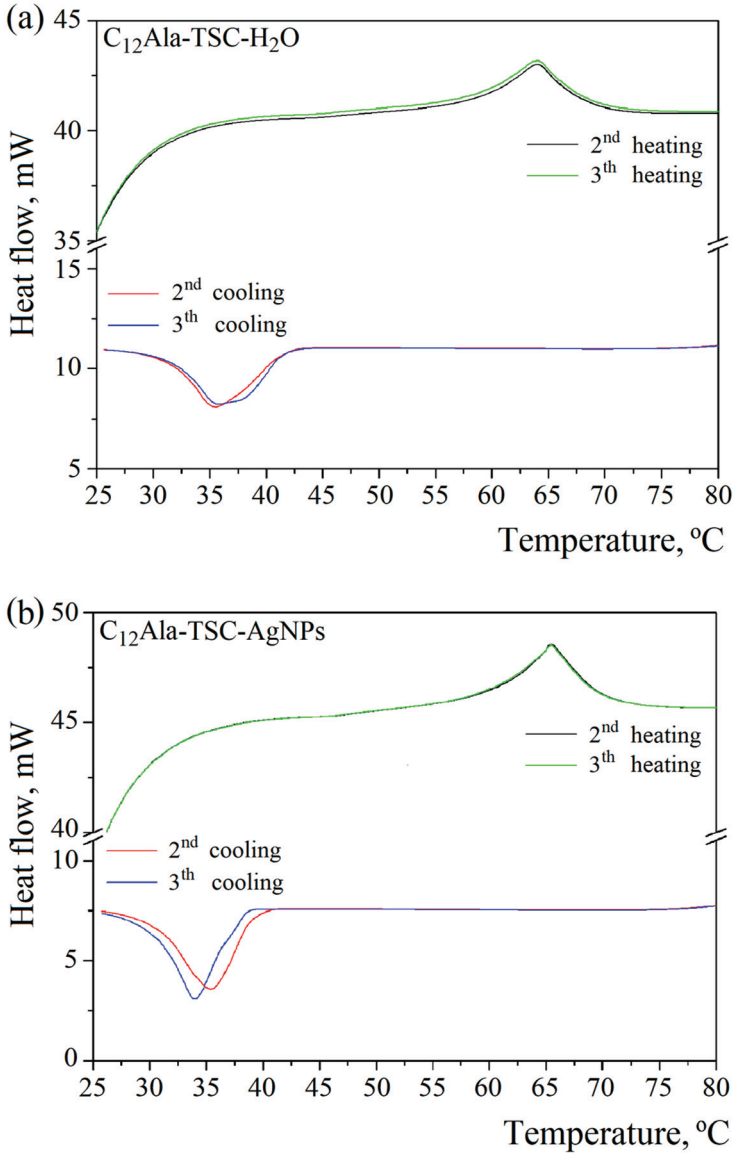

Figure 2. DSC curves of (**a**) C_{12}Ala-TSC-H_2O and (**b**) C_{12}Ala-TSC-AgNP gels.

3.2. Thermogravimetric Analysis (TGA + DTG)

Two (for liquid and solid phases) and three (for liquid, solid, and nanoparticles phases) characteristic peaks related to decomposition or evaporation (water) of individual components for the blank (C_{12}Ala-TSC-H_2O) and silver-enriched samples (C_{12}Ala-TSC-AgNPs), respectively, are visible on the TGA and DTG curves (Figure 3a,b). Figure 3c represents the DTG curves of TSC and C_{12}Ala powder. To compare the degradation temperatures of the individual phases of the systems, Figure 3d shows the normalised mass loss derivatives for both tested samples. The results do not include the pure C_{12}Ala-H_2O hydrogel sample because it disintegrated too quickly for its properties to be compared with the stable samples.

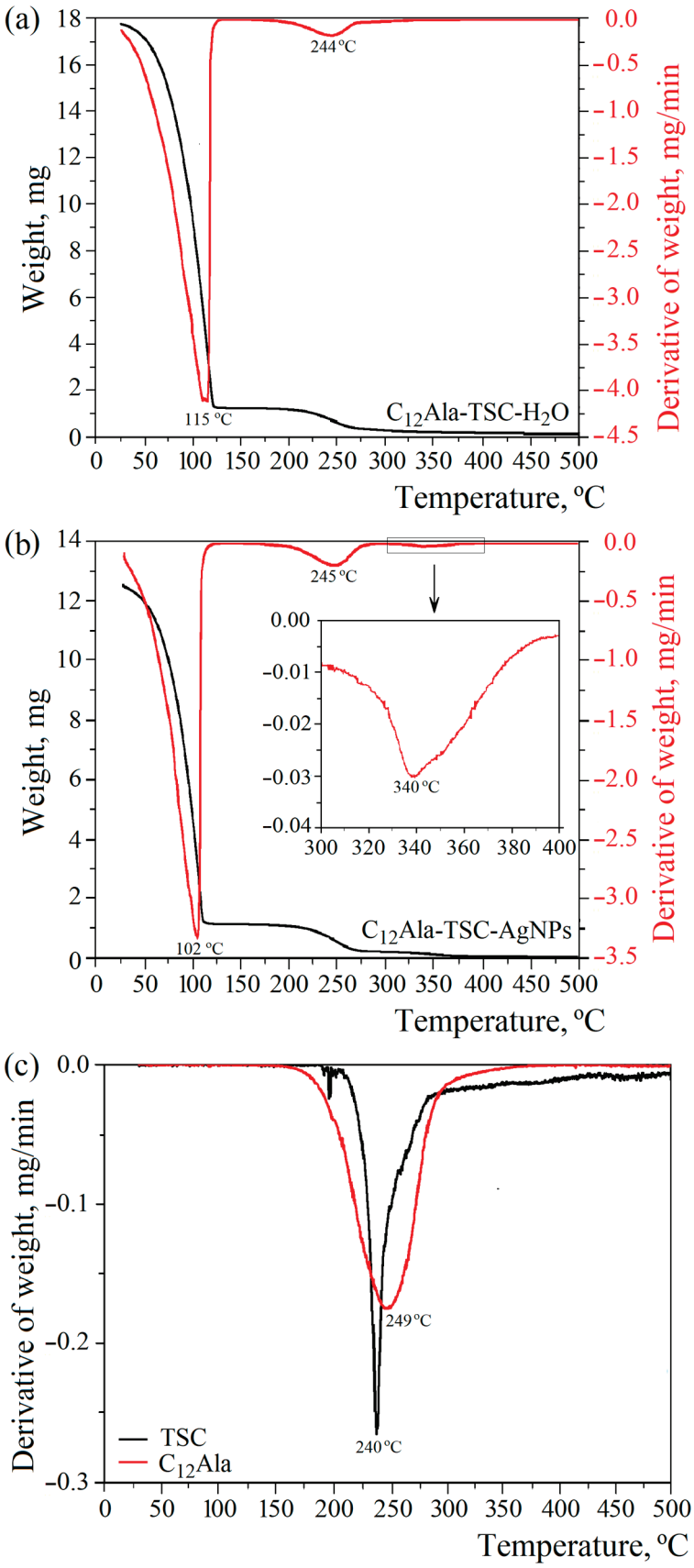

Figure 3. *Cont.*

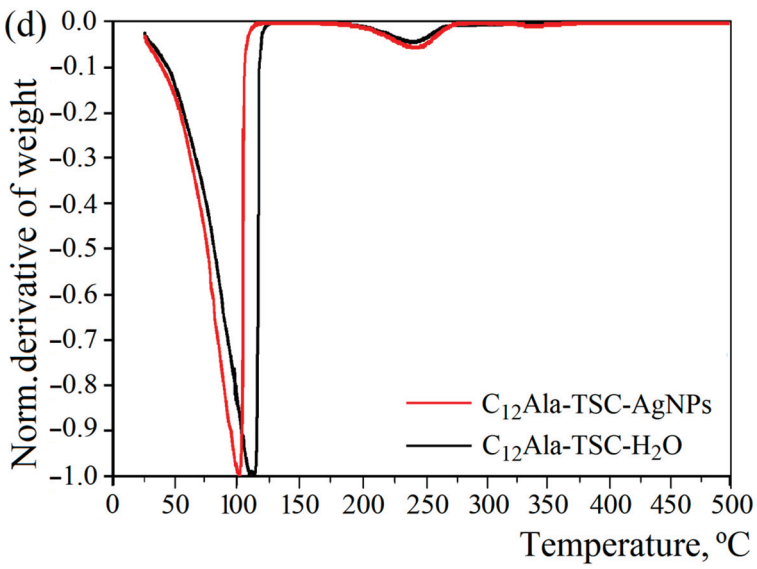

Figure 3. The 10 °C/min TGA and DTG thermograms of (**a**) C_{12}Ala-TSC-H_2O, (**b**) C_{12}Ala-TSC-AgNPs, (**c**) DTG curves of TSC and C_{12}Ala powder, and (**d**) normalised derivatives of weight loss of gel samples.

The addition of silver nanoparticles, AgNPs, to the hydrogel of C_{12}Ala with TSC influences the temperature water fraction evaporation. The DTG curves (Figure 3b) show a decrease in the inflection point related to the temperature at which the mass loss is the quickest by 13 °C in comparison to the silver-unenriched sample (Figure 3a). The maximum water evaporation rate occurs at 102 °C and 115 °C for the sample with and without silver nanoparticles, respectively. Two possible reasons can cause such behaviour: the intramolecular interactions between the AgNPs and the gelator matrix and the physical nature of the silver nanoparticles themselves. The intramolecular interactions with AgNPs can disturb the mechanism of physical bonding between the gelator molecules, causing a weakening of the gel strength. On the other hand, the physical properties of silver nanoparticles, namely lower heat capacity and higher heat transfer, can cause local heating and additionally weaken the physical bonds between C_{12}Ala molecules. Materials with low heat capacity and high thermal conductivity heat up faster and release accumulated energy more quickly. The heat capacity and thermal conductivity of water and silver are 4200 J/kg·K and 0.6 W/m·K and 237 J/kg·K and 429 W/m·K, respectively. Although adding AgNPs decreases the decomposition temperature, it increases the system's long-term stability at temperatures below 100 °C. The decomposition process observed at temperatures above 300 °C is related to the melting of AgNPs (Figure 3b, highlighted area). The total weight content of silver nanoparticles in the liquid fraction of the gel is 0.44 % (4.4 mg/mL). Uncrushed silver melts at a temperature of 960 °C. However, silver nanoparticles have a melting point of approximately 360 °C (depending on size), so we can conclude that the peaks visible in this temperature region correspond to the decomposition process of silver nanoparticles. The observed peak in the temperature range 175–275 °C is indistinguishable for TSC and C_{12}Ala due to the similar decomposition temperature of both materials, as shown in Figure 3c. The maximum rate of water evaporation is 3.32 mg/min at 102 °C and 4.10 mg/min at 115 °C for the enriched and blank samples, respectively.

3.3. ^{13}C CPMAS NMR

High-resolution NMR techniques were used to investigate the intra- and intermolecular interactions in all studied systems. The theoretical ^{13}C NMR spectra were calculated for isolated molecules of TSC and $C_{12}Ala$ based on their chemical structures to correctly assign and analyse the obtained experimental results. In Figure 4a,b, the obtained theoretical results are displayed in black, whereas the experimentally recorded spectra in the solid-state are presented in blue. The spectra recorded for $C_{12}Ala$ and TSC in the solid state are more complex, as they reveal intermolecular interactions between molecules, leading to splitting and additional resonance lines. Moreover, the static and random orientation of molecules with respect to the magnetic field causes a chemical shift anisotropy and line broadening due to dipole–dipole interactions. The broadening effects can be partially reduced using the magic angle spinning (MAS) technique, allowing the resonance lines to become distinguishable [33,34]. However, changes in chemical shielding caused by non-equivalent interactions between molecules can still be observed. The discrepancy between theoretical and experimental results originates from the fact that theoretical results do not account for the aforementioned effects. However, to test this assumption, we dissolved TSC and $C_{12}Ala$ in D_2O to diminish the intermolecular interactions by dispersing the investigated molecules in a liquid environment, thereby averaging out orientational dipolar interactions through increased rotational and translational molecular dynamics. The experimental ^{13}C NMR spectra obtained for diluted liquid samples of TSC and $C_{12}Ala$ are presented in Figure 4a,b in red. In the case of TSC, experimental and theoretical results show strong agreement, as expected for a small moleucule soluble in aqueous environments. For $C_{12}Ala$, although the agreement between theoretical and experimental data is much better, especially in the 170–180 ppm range, ir still shows some broadening effects due to residual intermolecular interactions. These observed effects indicate the self-assembly of these molecules, even if gelation does not occur without the addition of TSC, causing slower tumbling of molecules on the NMR timescale due to the formation of structures where diffusion is restricted by interactions. Therefore, the translational and orientational dynamics cannot effectively average out dipole–dipole interactions and the distinct orientation of groups of $C_{12}Ala$ molecules with respect to the external magnetic field. Therefore, it is natural to expect that the spectrum in D_2O will not exactly match the theoretical prediction for monomeric $C_{12}Ala$ (in black). On the other hand, to obtain a reasonable S/N ratio, the weight concentration of the gelator molecules in D_2O was 6% wt.%, which is relatively high, creating a viscous liquid. Sumita and Joykrishna showed that $C_{12}Ala$ can experience self-assembly already at a critical aggregation concentration (CAC) of 1.04 mM and at pH 12 or lower [35].

In Figure 4c, the experimental ^{13}C NMR spectrum for the $C_{12}Ala$-AgNP gel sample is presented in black, and the ^{13}C spectra for liquid samples of TSC and $C_{12}Ala$ are given in blue and red, respectively. The observed differences in the gel spectrum originate from the intermolecular interactions established in the self-assembly process during gelation in the presence of TSC molecules. Although we cannot detect the TSC signal directly in the gel sample because of the low concentration, we can see its influence indirectly through the interaction with the COO- groups of the $C_{12}Ala$ gelator in the spectral range from 170 to 180 ppm. The observed line at 176 ppm in the liquid sample of $C_{12}Ala$ has been split into two lines in the gel sample due to interaction with TSC, mediated by Na+ cation. The inset in Figure 4c shows the splitting and indicates the relative change in the line intensities relative to the line at 175 ppm, which is expected when a single line splits into more components, but the number of interacting spins remains the same. In the 25–10 ppm spectral range, differences between the spectrum of $C_{12}Ala$ in the gel and liquid state were detected. This region corresponds to the carbons in the hydrophobic tail

of the gelator molecule. Compared to the results for the liquid sample, in the gel sample, the spectrum has narrower lines and is less crowded. This indicates that the aliphatic chain's carbons exhibit a more uniform chemical environment, resulting in better-defined and uniform chemical shifts. Such a situation occurs when the chains become ordered relative to each other and create a uniform structure, e.g., a well-defined lamellar phase, where all the tails reassemble on the inside and polar groups on the outsides. Based on the obtained experimental results and theoretical spectra, we can conclude that TSC plays a crucial role by triggering the gelation process and interacting with the polar head of the gelator molecules through the sodium cations. The mutual influence of the TSC and AgNP electrostatic interactions on C_{12}Ala molecules also causes the ordering of the gelator hydrophobic tails into the lamellar phase.

Figure 4a,b show the ^{13}C CPMAS NMR spectra recorded for C_{12}Ala and TSC in the solid and D_2O solution state, together with theoretical spectra calculated for isolated molecules. Figure 4c shows experimental spectra of 1.25 M TSC and 6 wt.% of C_{12}Ala dissolved in D_2O and gel enriched with AgNPs.

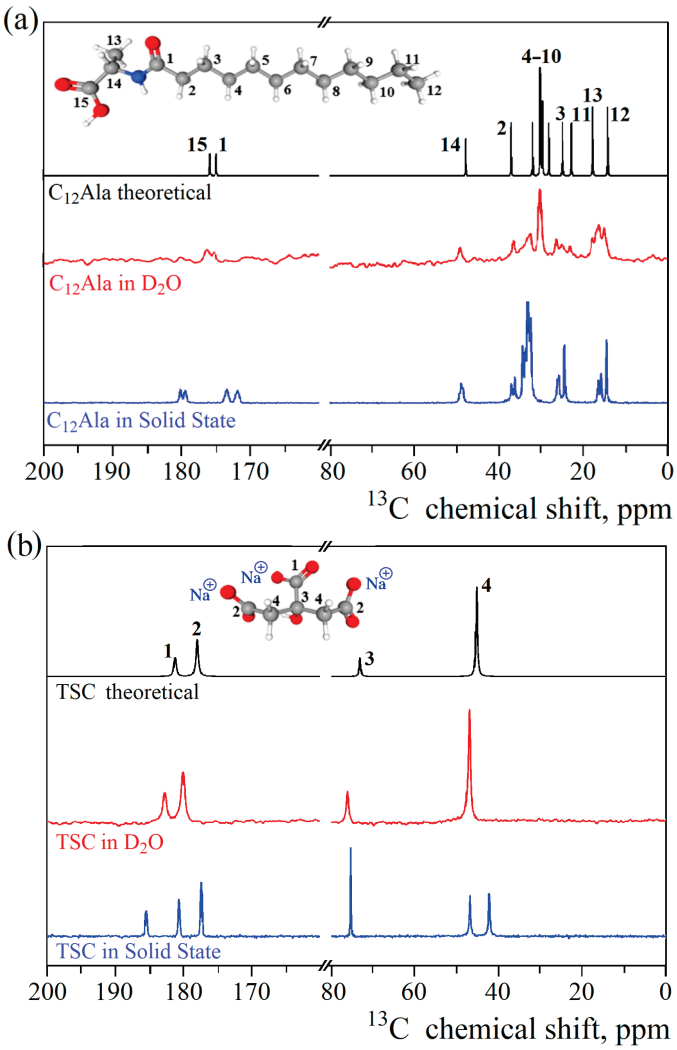

Figure 4. *Cont.*

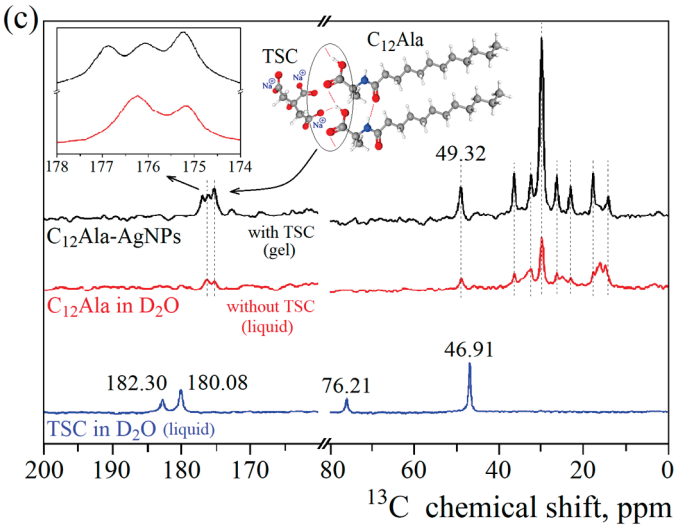

Figure 4. Theoretical and experimental ^{13}C CPMAS NMR spectra of solid and D_2O-dissolved $C_{12}Ala$ (**a**) and TSC (**b**), along with experimental spectra of TSC and $C_{12}Ala$ dissolved in D_2O and $C_{12}Ala$-AgNP gel (**c**).

3.4. Optical Images

To investigate the gelation process in the studied systems, images of the microstructures of the samples were recorded using polarising optical microscopy. Drops of the prepared compositions of the studied systems were cast onto amicroscopic plate, covered with glass coverslips, and subjected immediately to observation. The obtained results are presented in Figure 5. The differences between systems with and without TSC were clearly visible to the naked eye and confirmed by microstructure observation (Figure 5a,b vs. Figure 5c,d). The 12 wt.% mixture was used for the tests because 6 wt.% $C_{12}Ala$ in water (without TSC) did not form a stable gel with a microstructure that could be recorded in optical microscopy.

The polarising optical images were taken at 20× magnification with a field of view of 275 × 200 µm. The systems containing TSC self-assemble into microstructures that significantly differ from those formed without the addition of TSC. Although the added trisodium citrate is below 0.5 wt.% of the total mass, its influence on the intramolecular interactions between gelator molecules is substantial. The gelator solution with hydrolate $C_{12}Ala$-AgNPs, without TSC, does not exhibit gelling properties. In microscopic images, we can see clusters of gelator fibres surrounded by large pools of water (Figure 5a). In the case of the hydrogels without TSC, such as $C_{12}Ala$-H_2O (Figure 5b), the 12 wt.% of gelator molecules create rod-like aggregates that are loosely packed, resulting in significant areas where no aggregates are present. The small number of junction points between individual aggregates indicates the low thermal stability of the hydrogels created by the $C_{12}Ala$ gelator alone. In the absence of AgNPs, the aggregates of $C_{12}Ala$ stabilised by TSC create a dense mesh of rod-like aggregates of different thicknesses, lengths, and dendrimer-like shapes (Figure 5c). With the addition of silver nanoparticles to the systems, the interactions during the self-assembly process upon gelation change, leading to the creation of clusters of aggregates (Figure 5d). The shape of individual gelator aggregates also changes, assembling into thick, short, and straight rod-like shapes similar to the crystallites that create piles of random orientation. These piles can overlap and create regions of highly dense gelator aggregates and large free spaces in between. To explain such a change in aggregation pattern, we assume that the dispersed AgNPs become the nucleation centres for the aggregation of gelator molecules. The most crucial change

in the microstructure of the created hydrogels is observed upon the addition of TSC to systems, both in the presence and absence of AgNPs. Such a matrix contains many more junction points and interactions between aggregates, leading to higher thermal and time stability for the hydrogel. Similar to systems without TSC, adding silver nanoparticles to hydrogels containing TSC influences individual aggregates' shape and the created matrix's self-assembly pattern. The microstructure of C_{12}Ala-TSC-AgNP hydrogels consists of thin, long fibres of dendrimer-like shapes showing spatial ordering. The aggregates have a uniform size and form, indicating the role of AgNPs in the systems at the stage of aggregate formation and the supramolecular self-assembly process. A more uniform matrix in C_{12}Ala-TSC-AgNP hydrogels results in higher durability for the systems exposed to temperature and time. Very similar results were obtained in SEM images for 5 wt.% gels with and without AgNPs. In Figure 5a,b, in the publication [9], we can clearly see differences in the structure of the internal gel matrix.

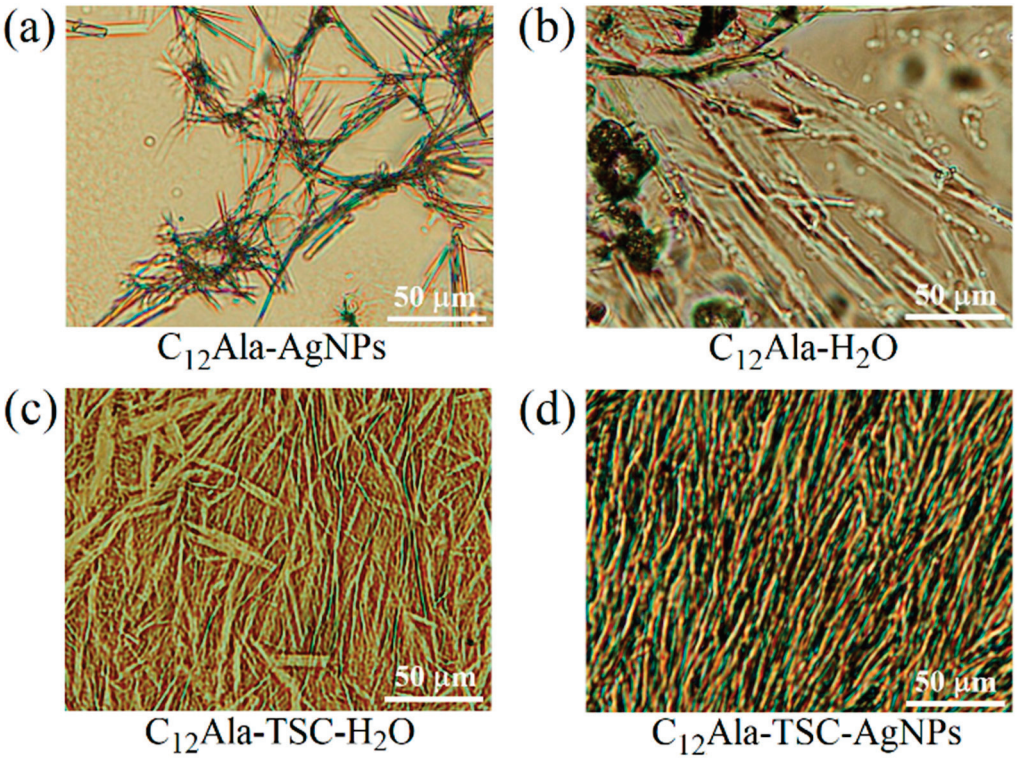

Figure 5. The polarising optical images of 12 wt% C_{12}Ala gels: C_{12}Ala-AgNPs (**a**), C_{12}Ala-H_2O (**b**), C_{12}Ala-TSC-H_2O (**c**), and C_{12}Ala-TSC-AgNPs (**d**).

4. Discussion

C_{12}Ala is an amphiphilic compound with a topological Polar Surface Area (PSA) equal to 66.4 Å^2 [32] and amino-acid-based surfactants [36] that has a hydrophobic hydrocarbon chain ending with a polar hydrophilic amine and carboxyl groups, so we can expect that, when in contact with polar solutions (e.g., water), it behaves in a characteristic way [37–40]. Figure 6 shows a simplified diagram of the interaction between neighbouring gelator molecules in different solvent polar conditions. The area of interaction of two neighbouring gelator molecules resembles a cone, with the hydrophobic part of the molecule at the top. C_{12}Ala, when in contact with water, forms micelles inside which the hydrophobic parts of the molecules are enclosed (see Figure 6a). Micelles form a colloidal system similar to lysols or emulsions, depending on the degree of dispersion. The addition of TSC to the

C_{12}Ala–H_2O solvent results in a lower polarity of gelator molecules; the area of interaction of two neighbouring gelator molecules then resembles a truncated cone, and the mutual interaction of the hydrophobic parts of the molecules decreases. In the tested blank and silver-enriched samples, there is one TSC molecule for approximately 13 C_{12}Ala molecules. This is sufficient to change the geometry of the mutual arrangement of the gelator particles. The micelle changes into a lamella system due to the interaction of TSC with C_{12}Ala (see Figure 6b), as indicated by the change in shape and the shift of the ^{13}C NMR peaks in the range of 170–180 ppm towards higher values, which is visible in the enlarged range in Figure 4c. The polar part of the gelator and silver nanoparticles chelated by TSC has a negative electric charge. Due to the Coulomb interaction, in the silver-enriched sample, C_{12}Ala-TSC-AgNPs, the nanoparticles have the ability to organise lamellar fibres into thicker layers, which are held together by their interaction with positively charged sodium ions. The lamella fibres change into a lamella layer system by interacting with AgNPs with C_{12}Ala (see Figure 6c). As a result, the gel system is expected to have longer, thicker, and more ordered solid fibrer. It should be remembered that the figure shows a schematic interaction of gelator molecules in the absence or presence of stabilisers such as TSC and AgNPs at CMC (critical micelles concentration—Figure 6a) and CAC (critical assembly concentration—Figure 6b,c). In a real system, the ratio of micelles, lamellae, and lamellar layers depends on the concentration of individual components in the sample, such as the gelator, stabiliser, and nanoparticles.

Now we can understand why, without a small addition of TSC, the C_{12}Ala gelator does not gel in the AgNP solution. Adding negatively charged AgNPs to the C_{12}Ala hydrogel causes structural changes in the gel. The AgNPs separate C_{12}Ala micelles from each other through electrical interaction. A pure hydrogel is formed by short lamellas and micelles, which form gelator clusters or single thin fibres dispersed in water. The disintegration of the pure hydrogel is visible shortly after gelation. In a short time (a few hours), the gelled sample changes into a structure resembling a "micellar fluid", suggesting an excess of micelles over lamellae in the system. The gelator aggregates precipitate from the gel, and the sample begins to flow. Still, this process is slower than that of a mixture of containing AgNP hydrolate combined only with the gelator C_{12}Ala without the participation of the TSC stabiliser. Adding negatively charged silver particles to the system causes an excess micelles of to form relative to the lamellas due to the Coulomb interaction with AgNPs. The fibres break into smaller, unconnected structures. A larger share of weakly interacting micelles in the sample and the separation of gelator fibres make it impossible for the system to gel. As a result, pure hydrogel without added TSC gels only for a short time, whereas the gel enriched with AgNPs without added TSC does not gel at all. This process is visible in Figure 5a,b. In a pure gel (Figure 5b), large pools of liquid are held together by interconnected gelator chains. Still, the Coulomb interaction with negatively charged AgNPs causes the separation of the gelator in the liquid phase (Figure 5a), and the gelation process becomes impossible. The addition of TSC causes an excess of lamellas over the micelles in this system, and the gel becomes more stable, creating short and twisted or unordered fibres in a rigid gel matrix, as seen in Figure 5c for the 12 wt.% gel and Figure 5a at [9] for the 5 wt.% gel. The appearance of lamellar layers also explains the change in the thermal decay rate of the system enriched with nanoparticles in the TGA measurement compared to the blank system. The temperature ranges and amplitudes of thermal degradation of the individual phases of the systems are always larger for samples enriched with nanoparticles than for the blank samples. Heat transfer through thick and long lamella layers occurs slower than in the case of thin and short fibres found in the blank sample. The fluctuation in the temperature of the silver-enriched

sample from 33 °C to 36 °C in the DSC measurement in subsequent cooling cycles also becomes understandable. The mutual arrangement of C_{12}Ala lamellae due to interaction with AgNPs and the formation of lamella layers may differ slightly in each heating and cooling cycle.

In the f C_{12}Ala hydrogel system enriched with silver nanoparticles, AgNPs, the addition of TSC molecules counteracts the electrostatic interaction between the gelator fibres and silver nanoparticles, thereby enabling gelation and maintaining the system's stability.

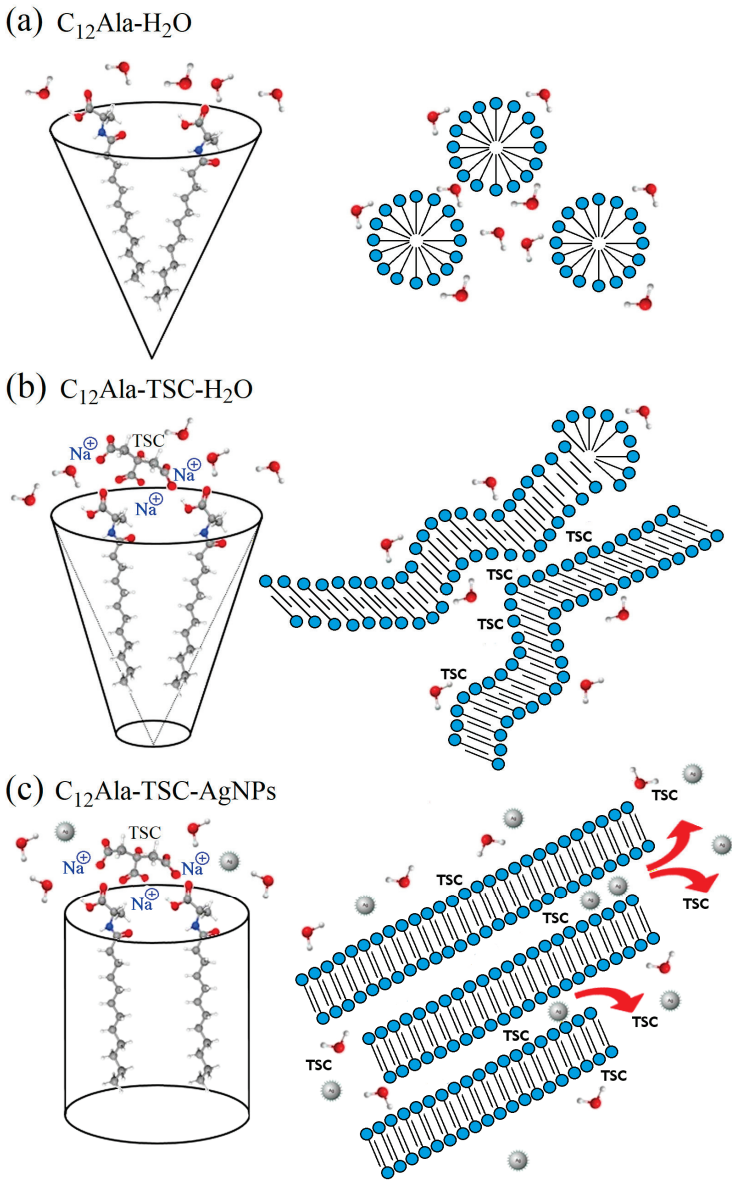

Figure 6. The simplified diagram of the interaction between neighbouring gelator molecules in different conditions: C_{12}Ala in water (**a**), C_{12}Ala with TSC in water (**b**), and C_{12}Ala with TSC in water solution of AgNPs (**c**).

5. Conclusions

The conducted research allowed us to answer the question about the mechanism of gelation and the intramolecular interactions between the liquid and solid phases in the pure hydrogel of C_{12}Ala, the hydrogel of C_{12}Ala-TSC, and the silver-enriched hydrogel of C_{12}Ala-TSC-AgNPs. The addition of TSC to water, which interacts with the polar part of the

gelator molecule and affects its polarity, changes the forming gel matrix's internal structure, and increases its stability. The C_{12}Ala hydrogel, with the addition of a 1.25M TSC water solution, exhibits greater thermal and time stability compared to the pure hydrogel due to the increased number of junction points between individual LMWG aggregates composing the internal matrix. A similar effect was observed in the system containing AgNPs. On the other hand, the presence of only silver nanoparticles in the hydrogel composition without TSC molecules causes the disintegration of the internal structure due to electrostatic interactions between the negatively charged nanoparticles and the micelles formed by the gelator molecules, preventing them from combining into a stable structure. In C_{12}Ala-TSC-AgNP hydrogels, the mutual interactions between TSC and AgNPs decrease the negative electrostatic influence of nanoparticles on the LMWG self-assembly process and lead to higher ordering of the created fibrilar aggregates, which increases the homogeneity and strength of the internal matrix. Consequently, we have obtained thermally and long-term stable hydrogels with a homogenous structure and AgNP distribution, improving the potential textural and organoleptic properties of potential pharmaceutical or cosmetic products. The identified role of the TSC molecules in shielding the gelator molecules from electrostatic forces that disturb the self-assembly process introduced by metallic nanoparticles paves the way for the preparation of hydrogel products enriched with other types of nanoparticles.

Author Contributions: Conceptualisation, J.K.; methodology, J.K. and M.B. (Michał Bielejewski); validation, J.K., M.B. (Michał Bielejewski) and O.M.D.; formal analysis, J.K. and M.B. (Michał Bielejewski); investigation, J.K., M.B. (Michał Bielejewski), O.M.D. and M.B. (Mariusz Borkowski); resources, O.M.D. and M.B. (Mariusz Borkowski); data curation, J.K.; writing—original draft preparation, J.K.; writing—review and editing, J.K., M.B. (Michał Bielejewski) and O.M.D.; visualisation, J.K. and O.M.D.; supervision, M.B. (Michał Bielejewski); project administration, J.K.; funding acquisition, O.M.D. All authors have read and agreed to the published version of the manuscript.

Funding: This research was partially funded by the Polish National Science Centre, grant number 2019/33/B/NZ7/01608.

Institutional Review Board Statement: Not applicable.

Informed Consent Statement: Not applicable.

Data Availability Statement: The raw data supporting the conclusions of this article will be made available by the authors on request.

Conflicts of Interest: The authors declare no conflicts of interest.

References

1. Glushkov, D.; Paushkina, K.; Pleshko, A. Gel Fuels: Praparing, Rheology, Atomization, Combustion. *Energies* **2023**, *16*, 298. [CrossRef]
2. Li, M.-G.; Wu, Y.; Cao, Q.-L.; Yuan, X.-Y.; Chen, X.; Han, J.-L.; Wu, W.-T. Rheological Properties of Organic Kerosene Gel Fuel. *Gels* **2022**, *8*, 507. [CrossRef] [PubMed]
3. Nicoletti Telis, V.R. *Biopolimer Engineering in Food Procesing*; CRC Press: Boca Raton, FL, USA, 2012; ISBN 9781439844946.
4. Zhi, L.; Liu, Z.; Wu, C.; Ma, X.; Hu, H.; Liu, H.; Adhikari, B.; Wang, Q.; Shi, A. Advances in preparation and application of food-grade emulsion gels. *Food Chem.* **2023**, *424*, 136399. [CrossRef]
5. Aggarwal, G.; Nagpal, M. Pharmaceutical Polymer Gels in Drug Delivery. In *Polymer Gels. Gels Horizons: From Science to Smart Materials*; Thakur, V., Thakur, M., Voicu, S., Eds.; Springer: Singapore, 2018; pp. 249–284. [CrossRef]
6. Siafaka, P.I.; Gündoğdu, E.A.; Cağlar, E.S.; Özgenç, E.; Gonzalez-Alvarez, M.; Gonzalez-Alvarez, I.; Okur, N.U. Polymer based Gels: Recent and Future Applications in Drug Delivery Field. *Curr. Drug Deliv.* **2023**, *20*, 1288–1313. [CrossRef]

7. Sharmin, E.; Batubara, A.S.; Tamboosi, B.A.; Al Khozay, E.B.; Alamoudi, M.K.; Al Aidaroos, O.Z.; Albenayan, J.A.; Lamfom, M.Y.; Sindi, A.A.H.; Al-Madboly, L.A.; et al. PVA nanocomposite hydrogel loaded with silver nanoparticles enriched Nigella sativa oil. *Inorg. Nano-Met. Chem.* **2021**, *52*, 1134–1142. [CrossRef]
8. Rammohan, A.; Kaduk, J.A. Trisodium citrate, $Na_3(C_6H_5O_7)$. *Acta Cryst.* **2016**, *E72*, 793–796. [CrossRef]
9. Kubiński, K.; Górka, K.; Janeczko, M.; Martyna, A.; Kwaśnik, M.; Masłyk, M.; Zięba, E.; Kowalczuk, J.; Kuśtrowski, P.; Borkowski, M.; et al. Silver Is Not Equal to Silver: Synthesis and Evaluation of Silver Nanoparticles with Low Biological Activity, and Their Incorporation into C12Alanine-Based Hydrogel. *Molecules* **2023**, *28*, 1194. [CrossRef]
10. Anjali Das, C.G.; Ganesh Kumar, V.; Stalin Dhas, T.; Karthick, V.; Govindaraju, K.; Mary Joselin, J.; Baalamurugan, J. Antibacterial activity of silver nanoparticles (biosynthesis): A short review on recent advances. *Biocatal. Agric. Biotechnol.* **2020**, *27*, 101593. [CrossRef]
11. Liao, C.; Li, Y.; Tjong, S.C. Bactericidal and Cytotoxic Properties of Silver Nanoparticles. *Int. J. Mol. Sci.* **2019**, *20*, 449. [CrossRef]
12. Ghiuță, I.; Cristea, D.; Croitoru, C.; Kost, J.; Wenkert, R.; Vyrides, I.; Anayiotos, A.; Munteanu, D. Characterization and antimicrobial activity of silver nanoparticles, biosynthesized using Bacillus species. *Appl. Surf. Sci.* **2018**, *438*, 66–73. [CrossRef]
13. Agnihotri, S.; Mukherji, S.; Mukherji, S. Size-controlled silver nanoparticles synthesized over the range 5–100 nm using the same protocol and their antibacterial efficacy. *RSC Adv.* **2014**, *4*, 3974–3983. [CrossRef]
14. Chen, L.Q.; Fang, L.; Ling, J.; Ding, C.Z.; Kang, B.; Huang, C.Z. Nanotoxicity of Silver Nanoparticles to Red Blood Cells: Size Dependent Adsorption, Uptake, and Hemolytic Activity. *Chem. Res. Toxicol.* **2015**, *28*, 501–509. [CrossRef] [PubMed]
15. Choi, J.; Reipa, V.; Hitchins, V.M.; Goering, P.L.; Malinauskas, R.A. Physicochemical characterization and in vitro hemolysis evaluation of silver nanoparticles. *Toxicol. Sci.* **2011**, *123*, 133–143. [CrossRef]
16. Riaz Ahmed, K.B.; Nagy, A.M.; Brown, R.P.; Zhang, Q.; Malghan, S.G.; Goering, P.L. Silver nanoparticles: Significance of physicochemical properties and assay interference on the interpretation of in vitro cytotoxicity studies. *Toxicol. Vitr.* **2017**, *38*, 179–192. [CrossRef]
17. Lucky, S.S.; Chee Soo, K.; Zhang, Y. Nanoparticles in Photodynamic Therapy. *Chem. Rev.* **2015**, *115*, 1990–2042. [CrossRef]
18. Kah, G.; Chandran, R.; Abrahamse, H. Biogenic Silver Nanoparticles for Targeted Cancer Therapy and Enhancing Photodynamic Therapy. *Cells* **2023**, *12*, 2012. [CrossRef] [PubMed]
19. Available online: https://www.who.int/news/item/01-02-2024-global-cancer-burden-growing--amidst-mounting-need-for-services (accessed on 10 September 2024).
20. Available online: https://www.who.int/news-room/fact-sheets/detail/antimicrobial-resistance (accessed on 10 September 2024).
21. Liu, G.; Yang, L.; Chen, G.; Xu, F.; Yang, F.; Yu, H.; Li, L.; Dong, X.; Han, J.; Cao, C.; et al. A Review on Drug Delivery System for Tumor Therapy. *Front. Pharmacol.* **2021**, *12*, 735446. [CrossRef]
22. Fornaguera, C.; García-Celma, M.J. Personalized Nanomedicine: A Revolution at the Nanoscale. *J. Pers. Med.* **2017**, *7*, 12. [CrossRef]
23. Sastri, T.K.; Gupta, V.N.; Chakraborty, S.; Madhusudhan, S.; Kumar, H.; Chand, P.; Jain, V.; Veeranna, B.; Gowda, D.V. Novel Gels: An Emerging Approach for Delivering of Therapeutic Molecules and Recent Trends. *Gels* **2022**, *8*, 316. [CrossRef]
24. Vigata, M.; Meinert, C.; Hutmacher, D.W.; Bock, N. Hydrogels as Drug Delivery Systems: A Review of Current Characterization and Evaluation Techniques. *Pharmaceutics* **2020**, *12*, 1188. [CrossRef]
25. Dang, Y.; Guan, J. Nanoparticle-based drug delivery systems for cancer therapy. *Smart Mater. Med.* **2020**, *1*, 10–19. [CrossRef]
26. Motulsky, A.; Lafleur, M.; Couffin-Hoarau, A.C.; Hoarau, D.; Boury, F.; Benoit, J.P.; Leroux, J.C. Characterization and biocompatibility of organogels based on L-alanine for parenteral drug delivery implants. *Biomaterials* **2005**, *26*, 6242–6253. [CrossRef]
27. Bhattacharya, S.; Pal, A. Physical Gelation of Binary Mixtures of Hydrocarbons Mediated by n-Lauroyl-L-Alanine and Characterization of Their Thermal and Mechanical Properties. *J. Phys. Chem. B* **2008**, *112*, 4918–4927. [CrossRef] [PubMed]
28. Pal, A.; Chhikara, B.S.; Govindaraj, A.; Bhattacharya, S.; Rao, C.N.R. Synthesis and properties of novel nanocomposites made of ingle-walled carbon nanotubes and low molecular mass organogels and their thermo-responsive behavior triggered by near IR radiation. *J. Mater. Chem.* **2008**, *18*, 2593–2600. [CrossRef]
29. Okesola, B.O.; Smith, D.K. Applying low-molecular weight supramolecular gelators in an environmental setting—Self-assembled gels as smart materials for pollutant removal. *Chem. Soc. Rev.* **2016**, *45*, 4226–4251. [CrossRef] [PubMed]
30. Miroslaw, B.; Demchuk, O.M.; Luboradzki, R.; Tyszczuk-Rotko, K. Low-Molecular-Weight Organogelators Based on N-dodecanoyl-L-amino Acids—Energy Frameworks and Supramolecular Synthons. *Materials* **2023**, *16*, 702. [CrossRef]
31. Kowalczuk, J.; Łapiński, A.; Stolarczyk, E.; Demchuk, O.M.; Kubiński, K.; Janeczko, M.; Martyna, A.; Masłyk, M.; Turczyniak-Surdacka, S. New Supramolecular Drug Carriers: The Study of Organogel Conjugated Gold Nanoparticles. *Molecules* **2021**, *26*, 7462. [CrossRef]

32. National Center for Biotechnology Information (2024). PubChem Compound Summary for CID 13854541, N-Lauroyl-L-Alanine. Available online: https://pubchem.ncbi.nlm.nih.gov/compound/N-Lauroyl-L-alanine (accessed on 22 October 2024).
33. Antzutkin, O.N. Sideband manipulation in magic-angle-spinning nuclear magnetic resonance. *Prog. Nucl. Mag. Reson. Spectrosc.* **1999**, *35*, 203–266. [CrossRef]
34. Brown, S.P. Probing proton-proton proximities in the solid state. *Prog. Nucl. Mag. Reson. Spectrosc.* **2007**, *50*, 199–251. [CrossRef]
35. Ghosh, A.; Dey, J. Effect of Hydrogen Bonding on the Physicochemical Properties andBilayer Self-Assembly Formation of N-(2-Hydroxydodecyl)-L-alanine inAqueous Solution. *Langmuir* **2008**, *24*, 6018–6026. [CrossRef]
36. Borkowski, M.; Orvalho, S.; Warszyński, P.; Demchuk, O.M.; Jarek, E.; Zawala, J. Experimental and theoretical study of adsorption of synthesized amino acid core derived surfactants at an air/water interface. *Phys. Chem. Chem. Phys.* **2022**, *24*, 3854–3864. [CrossRef] [PubMed]
37. Sorrenti, A.; Illa, O.; Ortuño, R.M. Amphiphiles in aqueous solution: Well beyond a soap bubble. *Chem. Soc. Rev.* **2013**, *42*, 8200–8219. [CrossRef] [PubMed]
38. Choucair, A.; Eisenberg, A. Control of amphiphilic block copolymer morphologies using solution conditions. *Eur. Phys. J. E* **2003**, *10*, 37–44. [CrossRef] [PubMed]
39. Alexandridis, P.; Lindman, B. *Amphiphilic Block Copolymers: Self-Assembly and Applications*; Elsevier Science: Amsterdam, The Netherlands, 2000; ISBN 0-444-82441-3.
40. Luo, C.; Yang, B.; Zhou, Y.; Yang, J.; Han, F.; Xu, B. Gelation properties and application based on amino acids gelators with four kinds of edible oils. *Colloids Surf. A* **2020**, *585*, 124184. [CrossRef]

Disclaimer/Publisher's Note: The statements, opinions and data contained in all publications are solely those of the individual author(s) and contributor(s) and not of MDPI and/or the editor(s). MDPI and/or the editor(s) disclaim responsibility for any injury to people or property resulting from any ideas, methods, instructions or products referred to in the content.

molecules

MDPI

Article

Yeast Viability in HLD–NAC-Designed Fully Dilutable Lecithin-Linker Microemulsions

Juan Doratt Mendoza , Jingwen Ding, Michelle Acosta Alvarez and Edgar Acosta *

Department of Chemical Engineering and Applied Chemistry, Faculty of Engineering and Applied Science, University of Toronto, Toronto, ON M5S 3E5, Canada; juan.doratt@mail.utoronto.ca (J.D.M.); jw.ding@alumni.utoronto.ca (J.D.)
* Correspondence: edgar.acosta@utoronto.ca

Abstract: Using microemulsions (μEs) as preservation media for cells was pursued in the 1990s; however, the difficulty in formulating biocompatible μEs and keeping unacclimatized cells alive for more than three days hindered developments in this area. This work explores the use of fully dilutable self-microemulsifying delivery systems (SMEDS) formulated with lecithin (Le) and polyglycerol-10-caprylate (PG10C) at a ratio of 2/5. This surfactant blend was mixed with ethyl oleate (EOL) at a ratio of 60 surfactant/40 EOL to produce a D60 dilution line. This D60 SMEDS was diluted with 0.9% w/v NaCl solution to produce lecithin-linker μEs (LLMs). The properties of the resulting LLMs were predicted using the hydrophilic–lipophilic-difference (HLD) and net-average curvature (NAC) model, indicating that LLMs with aqueous content from 5% to 60% are bicontinuous, confirmed via viscosity and conductivity. The largest yeast activity and viability obtained with LLMs were achieved with 30% aqueous content, resulting from the balance between having enough water for the effective transport of metabolites, enough SMEDS to contribute nutrients and lipids, and a low enough water to limit the partition of PG10C that, when present in the aqueous phase, inhibited yeast activity. For SMEDS, its low water activity ensured that the yeast remained dormant, keeping them alive for at least 10 weeks.

Keywords: yeast; microemulsion; lecithin; linkers; HLD–NAC; biologics

1. Introduction

Microemulsions (μEs) are surfactant–oil–water (SOW) systems that exist in thermodynamic equilibrium. μEs contain hydrophobic and hydrophilic compounds that could contribute to or hinder microorganism viability and activity. As a result, μEs could be used as a fermentation media, a disinfecting media, and possibly as encapsulating media/delivery system for cells. The main difficulty in formulating for any of these applications is understanding how the selection of surfactants and the proportion of the surfactant, oil, and water in the system can affect the viability and activity of microorganisms. This is the main question explored in this work using yeast as a model microorganism.

Luisi's group was one of the first to evaluate the activity of yeast in water-in-oil μEs formulated in three different SOW systems: (a) PEG-20-sorbitan trioleate (Tween 85) as surfactant and isopropyl palmitate (IPP) as oil, (b) azolectin (a form of lecithin) and IPP, (c) azolectin and hexadecane [1]. Luisi's group used yeast (*Saccharomyces cerevisiae*) because of its biotechnological importance, its relatively large size that facilitates the use of microscopy to evaluate the impact of μEs on viability, and its relative fragility. The

researchers found that, when holding the water/surfactant molar ratio (Wo) to 14, the original yeast has a greater viability in the formulation with azolectin and IPP and can survive for 3 days in that formulation. The authors determined that cells acclimatized to the μE environment could survive for 10 days. Hoppert et al. evaluated the photosynthetic activity of cyanobacteria and microalgae cells in water-in-oil μEs formulated with Tween 85 and sorbitan monooleate (Span 80) as surfactants and hexadecane as the oil phase [2]. In those experiments, the authors found that maximum photoactivity was obtained when Wo ranged from 80 to 180. The authors further proposed that in water-in-oil μEs, microorganisms are surrounded by a thin film of water with properties that are different from bulk properties but similar to the behavior of water in the confined environment of cells. The Luisi group also used the Tween 85-Span 80-hexadecane system as a suspension media for *Candida pseudotropicalis* and determined that these μEs, with Wo~10 to 20, can disperse the cells and promote anabolic and catabolic activity that used carbon from hexadecane (based on radiolabeled hexadecane) as a carbon source [3]. Prichanon et al. also used the Tween 85 + Span 80—hexadecane system to suspend *Mycobacterium* sp. [4]. In their work, the authors determined that higher water contents reaching Wo~25 could lead to better dispersion of the cells. Although their article refers to this dispersion of cells in μEs as an encapsulation process, the authors acknowledge that their main concern is the dispersion of the cells and not evaluating their survival or activity. In a follow-up article, the authors use these μEs as a way to suspend the heat-killed cells of *Mycobacterium* sp. where the released enzymes from the cells were capable of catalyzing epoxidation reactions [5].

The momentum of the research on microorganism viability in μEs was lost after the early 2000s, due to the limited viability of the cells after a few days of exposure to the μEs and the complexity of formulating biocompatible μEs with a wide range of Wo ratios. Furthermore, even if the cell remains alive, metabolic and anabolic processes will keep changing the composition of the μEs, leading to changes in the thermodynamic state of the μE, which can result in phase separation. At that point, the attention concentrated on hosting microbial cells in water-in-oil macro- or regular emulsions [6], on the evaluation of enzymatic activity in μEs, and the use of μEs (containing antimicrobial components) as antimicrobial formulations [7].

Much has changed since the early 2000s, including the development of the biocompatible lecithin-linker μEs (LLMs) [8]. There are two types of linkers: lipophilic linkers (LL, long-chain, C12+ amphiphiles with weakly hydrophilic headgroups such as alcohols, monoglycerols, and fatty acids) and hydrophilic linkers (HL, C6–C10 surfactant molecules with highly hydrophilic headgroups such as polyglycerols, polyethylene glycols, etc.). The advantage of using linkers is that it reduces the number of surfactants and co-surfactants in the formulation and allows for a broader selection of additives that can be biocompatible. Using lecithin (Le) as a surfactant, C8–C10 polyglycerols as HL, and glycerol monooleate as LL, Nouraei et al. formulated self-microemulsifying delivery systems (SMEDS) capable of increasing the intestinal absorption of ibuprofen by threefold [9]. SMEDS are water-free LLMs; in other words, SMEDS are surfactant–oil (SO) systems that, when diluted with water, form single-phase μEs. Fully dilutable SMEDS can provide the entire range of water to the surfactant mol ratio (Wo~ from 0 to 1000s), which was not possible when previous cell viability studies in μEs were conducted. Furthermore, although the work of Luisi's group pointed to azolectin (a form of lecithin) as the best surfactant, most of the other studies concentrated on polyethylene glycol (PEG) surfactants like Tween 85 because they are easier to formulate with those surfactants than with lecithin. The hydrophilic linker (HL), in particular, reduces the interfacial rigidity of lecithin membranes, allowing the formulation of lecithin μEs with a wide range of oils and aqueous solutions [8,10,11].

Nouraei et al. [9] also introduced the use of the hydrophilic–lipophilic difference and net-average curvature (HLD–NAC) model to predict the minimum surfactant (Le + HL + LL) to oil ratio required to produce SMEDS. The HLD model for non-ionic surfactants, such as the ones used in Nouraei et al. [9], is shown below:

$$HLD = b \cdot S - k \cdot EACN + c_T(T - 25\ ^\circ C) + Cc \quad (1)$$

The HLD indicates the approach to the phase inversion point (PIP) of emulsions and μEs. For SOW systems (emulsions and saturated μEs) with a water-to-oil ratio (WOR) between 1/3 and 3/1, negative HLDs indicate that water tends to be in the continuous phase. Positive HLDs correspond to SOW systems where the oil tends to be in the continuous phase. As the SOW system approaches HLD~0, the system tends to produce bicontinuous phases. The term b·S accounts for the salinity (S) of the system, measured in grams of NaCl per 100 mL, where b~0.13. The parameter "k" depends on the surfactant, but, for lecithin and linkers, k~0.16. EACN is the equivalent alkane carbon number of the oil; for n-alkanes between hexane and hexadecane, this is simply the number of carbon atoms in the chain, but, for any other oil, this is obtained from salinity scans [12]. The term c_T (T-25 °C) reflects the temperature dependence and, for PEG-based non-ionic surfactants, an increase in temperature results in a more hydrophobic SOW system (c_T~0.06 $^\circ C^{-1}$). However, for lecithin-linker μEs that are PEG-free, these systems are less temperature-dependent (c_T~0.01 $^\circ C^{-1}$) [8]. The term Cc in Equation (1) represents the surfactant's characteristic curvature value, indicating its inherent hydrophobicity. Surfactants that are more hydrophobic have more positive Cc values.

While the HLD is very useful, it does not explain the effect of surfactant concentration and does not, on its own, predict water or oil solubilization capacity or the μE phase boundary of ternary phase diagrams (TPDs). The NAC model, combined with the HLD, can predict these solubilization capacities and the single-phase boundary of TPDs, even for lecithin-linker μEs [13]. The NAC utilizes a mathematical model of two coexisting states to describe SOW systems. In one state, the aqueous phase is continuous where the oil solubilized has a solubilization radius Ro, and, in the other state, the oil phase is continuous where the aqueous phase solubilized has a solubilization radius Rw. This dual-state approach defines the net (Hn) and average (Ha) curvatures as follows:

$$H_n = \frac{1}{R_o} - \frac{1}{R_w} = \left(\frac{\phi_s}{3\phi_o} - \frac{\phi_s}{3\phi_w}\right)\left(\frac{a_s}{v_s}\right) = -\frac{HLD}{L} \quad (2)$$

$$H_a = \frac{1}{2}\left(\frac{1}{R_o} + \frac{1}{R_w}\right) = \frac{1}{2}\left(\frac{\phi_s}{3\phi_o} + \frac{\phi_s}{3\phi_w}\right)\left(\frac{a_s}{v_s}\right) \geq \frac{1}{\xi} \quad (3)$$

where ϕ_o, ϕ_w, ϕ_s are the volume fractions of oil, water, and surfactant in the SOW system. The ratio a_s/v_s is the interfacial area to molecular volume ratio of the surfactant. The surfactant tail length parameter, L, is fitted using experimental solubilization, but, for most surfactants, it is approximately 1.2 to 1.4 times the surfactant tail length [14]. The parameter ξ is the μE characteristic length, which indicates the maximum oil and water solubilization capacity of the SOW system. The combined HLD–NAC model is now used as an equation of state for μEs that can be used to define the optimal formulations for a given surfactant and oil composition.

Given the recent advances in fully dilutable, lecithin-linker SMEDS approach, which produces lecithin-linker μEs (LLM) upon dilution with aqueous solutions, and the HLD–NAC model to design these SMEDS; the question explored in this work is, can SMEDS or their resulting LLMs maintain unacclimatized yeast alive and active beyond the 3 days

reported in previous studies? We hypothesize that *Saccharomyces cerevisiae* will survive in the different microenvironments (reverse micellar, bicontinuous, and micellar systems) of LLMs). Confirmation of this hypothesis could open the doors for SMEDS and LLMs as delivery media for cells in applications such as probiotics delivery, for LLMs as solvent media in bioreactors for pharmaceutical applications, and for LLMs as adjuvants in remediation applications, such as oil spills [15].

To explore this hypothesis, we formulated LLMs using polyglyceryl-10 caprylate (PG10C, a HL), soy lecithin (Le, surfactant), and ethyl oleate (EOL, oil). The characteristic curvature (Cc) of Le and PG10C were obtained using surfactant μE phase scans using a C9E5 alkyl ethoxylated surfactant as a reference nonionic surfactant [12]. The EACN of EOL was obtained using a salinity μE phase scan using a C9E5 alkyl ethoxylated surfactant as a reference nonionic surfactant. A surfactant composition scan with Le, PG10C and EOL was then conducted and fitted using the HLD–NAC model to obtain the NAC parameters (L, ξ). These parameters were used to predict a TPD that could produce fully dilutable formulations using the lowest possible surfactant-to-oil ratio. The viability and activity of *Saccharomyces cerevisiae* along the fully dilutable line of the selected formulation were assessed via methylene blue cell staining and CO_2 production tests, respectively. The electrical conductivity and viscosity of μEs obtained along the dilution line were evaluated as a function of water content (and Wo ratio) to evaluate the microenvironment of each μE, considering the HLD–NAC predicted μE morphology.

2. Results and Discussions

2.1. Determination of HLD Parameters

Figure 1A presents a partial screenshot of the HLD–NAC spreadsheet used to fit the salinity scan for the equivalent alkane carbon number (EACN) of ethyl oleate (EOL), the oil used to prepare the lecithin-linker μEs (LLMs). The spreadsheet used was a modified version of the published HLD–NAC tutorial spreadsheet [16], which was designed for the salinity scan of a single ionic surfactant16. The salinities in column "I" (S = 10, 12, . . ., 26% NaCl) were used to calculate the HLD in column "L" using Equation (1). The HLD–NAC parameters for the OD5 reference surfactant are shown in cells B12 through B15. The HLD–NAC-predicted lower and upper μE levels (LL, UL) are included in columns "O" and "P". Cell I11 calculates the error between the predicted LL and UL and the experimental levels (red circles, UL; yellow circles LL). The fitted parameters were the EACN of EOL and the characteristic length (ξ) of the μE. The EACN = 7.6 obtained in Figure 1A is close to the EACN = 7.3 for EOL reported by Ontiveros and collaborators [17].

Figure 1B presents a partial screenshot of the HLD–NAC spreadsheet used to fit the surfactant composition scan for the characteristic curvature (Cc) of lecithin (Le, surfactant 1) mixed with OD5 (surfactant 2), maintaining S = 0.9% w/v NaCl (column "I"), and using limonene (EACN = 6) as the oil phase. The percentage of OD5 (in the mixture with Le) was gradually increased from 50 wt% to 90 wt% in 5% intervals (cells A17 to A25). For each composition, the molar fraction of surfactant 2 (xsurf2, cells B17 to B25) was calculated considering the molecular weights (MW, cells I7, J7) of each surfactant. The Cc of the mixture was then calculated in cells K17 to K25 using the linear mixing rule. The HLD of the SOW system was calculated using Equation (1) and Cc_{mix}. The parameters fitted in this case were the Cc of lecithin (cell I6) and the characteristic length (ξ, cell L12). The complete set of equations are included in the algorithm of Figure 2. The fitted Cc of +8.9 is higher than the published value of +5.5 [13]. Unpublished studies in our group show that the Cc of lecithin can range from +4 to +9 depending on the lecithin source, something common for a product derived from natural sources. Figure 1C presents a similar study for

PG10C, producing a Cc of −5.4, which is slightly less negative than Cc = −7.4, obtained in a previous study using 10% OD5 as a reference surfactant [15]. One important difference is that the 20% surfactant used in the current work tends to produce more accurate Cc values [18].

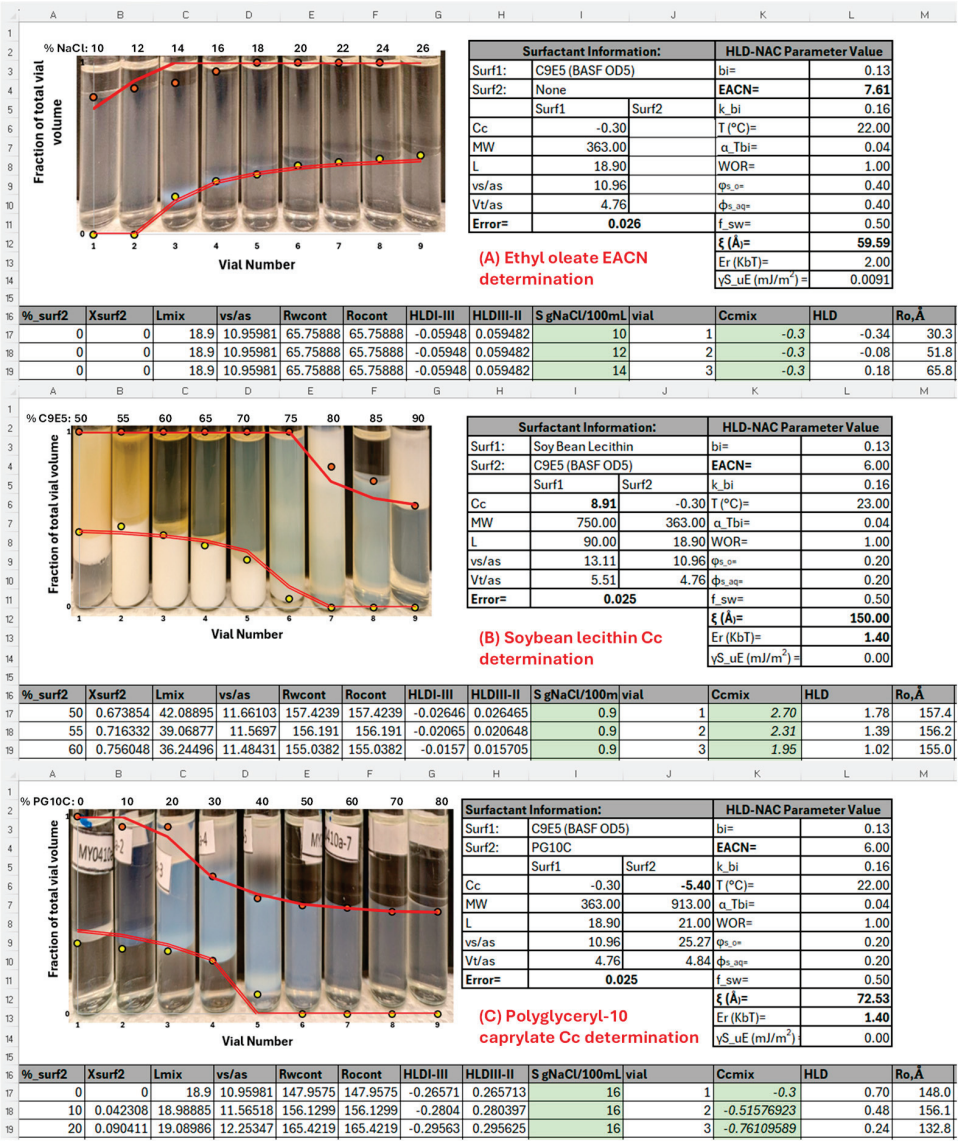

Surfactant Information:			HLD-NAC Parameter Value	
Surf1:	C9E5 (BASF OD5)		bi=	0.13
Surf2:	None		**EACN=**	**7.61**
	Surf1	Surf2	k_bi	0.16
Cc	-0.30		T (°C)=	22.00
MW	363.00		α_Tbi=	0.04
L	18.90		WOR=	1.00
vs/as	10.96		φ_{s_o}=	0.40
Vt/as	4.76		ϕ_{s_aq}=	0.40
Error=	**0.026**		f_sw=	0.50
			ξ (Å)=	**59.59**
			Er (KbT)=	2.00
			γS_uE (mJ/m^2) =	0.0091

%_surf2	Xsurf2	Lmix	vs/as	Rwcont	Rocont	HLDI-III	HLDIII-II	S gNaCl/100mL	vial	Ccmix	HLD	Ro,Å
0	0	18.9	10.95981	65.75888	65.75888	-0.05948	0.059482	10	1	*-0.3*	-0.34	30.3
0	0	18.9	10.95981	65.75888	65.75888	-0.05948	0.059482	12	2	*-0.3*	-0.08	51.8
0	0	18.9	10.95981	65.75888	65.75888	-0.05948	0.059482	14	3	*-0.3*	0.18	65.8

Surfactant Information:			HLD-NAC Parameter Value	
Surf1:	Soy Bean Lecithin		bi=	0.13
Surf2:	C9E5 (BASF OD5)		**EACN=**	6.00
	Surf1	Surf2	k_bi	0.16
Cc	**8.91**	-0.30	T (°C)=	23.00
MW	750.00	363.00	α_Tbi=	0.04
L	90.00	18.90	WOR=	1.00
vs/as	13.11	10.96	φ_{s_o}=	0.20
Vt/as	5.51	4.76	ϕ_{s_aq}=	0.20
Error=	**0.025**		f_sw=	0.50
			ξ (Å)=	**150.00**
			Er (KbT)=	**1.40**
			γS_uE (mJ/m^2) =	0.00

%_surf2	Xsurf2	Lmix	vs/as	Rwcont	Rocont	HLDI-III	HLDIII-II	S gNaCl/100m	vial	Ccmix	HLD	Ro,Å
50	0.673854	42.08895	11.66103	157.4239	157.4239	-0.02646	0.026465	0.9	1	*2.70*	1.78	157.4
55	0.716332	39.06877	11.5697	156.191	156.191	-0.02065	0.020648	0.9	2	*2.31*	1.39	156.2
60	0.756048	36.24496	11.48431	155.0382	155.0382	-0.0157	0.015705	0.9	3	*1.95*	1.02	155.0

Surfactant Information:			HLD-NAC Parameter Value	
Surf1:	C9E5 (BASF OD5)		bi=	0.13
Surf2:	PG10C		**EACN=**	6.00
	Surf1	Surf2	k_bi	0.16
Cc	-0.30	**-5.40**	T (°C)=	22.00
MW	363.00	913.00	α_Tbi=	0.04
L	18.90	21.00	WOR=	1.00
vs/as	10.96	25.27	φ_{s_o}=	0.20
Vt/as	4.76	4.84	ϕ_{s_aq}=	0.20
Error=	**0.025**		f_sw=	0.50
			ξ (Å)=	**72.53**
			Er (KbT)=	**1.40**
			γS_uE (mJ/m^2) =	0.00

%_surf2	Xsurf2	Lmix	vs/as	Rwcont	Rocont	HLDI-III	HLDIII-II	S gNaCl/100mL	vial	Ccmix	HLD	Ro,Å
0	0	18.9	10.95981	147.9575	147.9575	-0.26571	0.265713	16	1	*-0.3*	0.70	148.0
10	0.042308	18.98885	11.56518	156.1299	156.1299	-0.2804	0.280397	16	2	*-0.51576923*	0.48	156.1
20	0.090411	19.08986	12.25347	165.4219	165.4219	-0.29563	0.295625	16	3	*-0.76109589*	0.24	132.8

Figure 1. (**A**) Salinity scan used to obtain the Equivalent Alkane Carbon Number (EACN) of ethyl oleate (oil) using pentaethylene glycol nonyl ether (C9E5 or OD5, surfactant 1); the numbers on top of each vial represent the %w/v NaCl (salinity) in the aqueous phase. (**B**) Surfactant composition scan with lecithin (SBlec, surfactant 1) and reference surfactant C9E5 (surfactant 2) using limonene (EACN = 6) as oil and a 0.9% w/v NaCl aqueous phase; the numbers on top of each vial represent the wt% of C9E5 (surf2) in the mixture with lecithin (wt%surf1 = 100 − wt%surf2). (**C**) Surfactant composition scan with reference surfactant C9E5 (surfactant 1) and polyglycerol-10 caprylate (PG10C, surfactant 2) using limonene (EACN = 6) as oil and a 0.9% w/v NaCl in the aqueous phase; the numbers on top of each vial represent the wt% of PG10C (surf2) in the mixture with C9E5 (surf1). The orange and yellow dots are the experimental determination of the lower level (LL) and upper level (UL) boundaries of the µE phases. The solid red lines are predictions of the lower level (LL) and upper level (UL) boundaries of the µE phases predicted by the HLD–NAC programmed in the HLD–NAC tutorial [16], using the algorithm explained in Figure 2.

Figure 2 presents the algorithm used to generate the μE boundary (red) lines for composition (x2 or x_{surf2}) phase scans. The algorithm starts by setting the temperature (T), salinity (S, g NaCl/100 mL), the HLD–NAC parameters for surfactants 1 and 2: their characteristic curvature (Cc_1, Cc_2), volume to area ratio ($(vs/as)_1$, $(vs/as)_2$), salinity factors (b_1, b_2), EACN factors (k_1, k_2), temperature factors (c_{T1}, c_{T2}), tail lengths (L_1, L_2), and the total surfactant volume fraction added to the aqueous phase (φ_s), the μE characteristic length (ξ), and the fraction of the surfactant volume that contributes to the aqueous (f_{sw}) and oil (f_{so}) volume compartments.

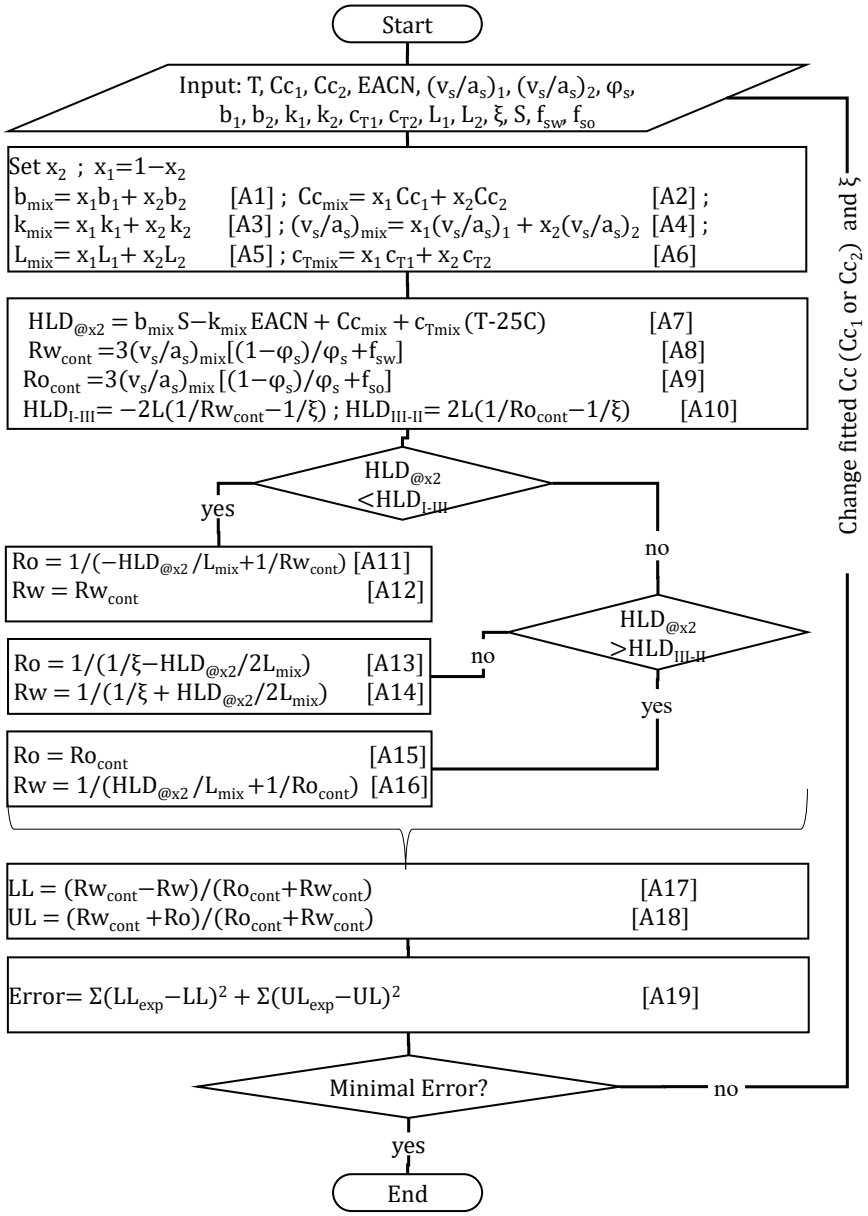

Figure 2. HLD–NAC algorithm to calculate the lower level (LL) and upper level (UL) of μEs produced in composition (x_2) phase scans at water/oil volume ratio (WOR) of 1/1.

Equations (A1) through (A6) in Figure 2 are used to obtain the surfactant parameters for the mixture with a given molar fraction of surfactants 1 and 2 (x_1, x_2). Equation (A7) calculates the HLD of the surfactant mixture with composition x_2. Equations (A8) and (A9) present the solubilization radii for the continuous aqueous and oil phases (Rw_{cont}, Ro_{cont}, respectively). Equation (A10) is used to calculate the $HLD_{I–III}$ at the transition from

Type I (water-continuous) to Type III (bicontinuous middle phase) μEs, and the $HLD_{III–II}$ from Type III to Type II (oil-continuous) μEs. For Type I μEs, Equations (A11) and (A12) calculate the solubilization radii of oil (Ro) and water (Rw), respectively. For Type III μEs, Equations (A13) and (A14) calculate the solubilization radii of oil (Ro) and water (Rw), respectively. For Type II μEs, Equations (A15) and (A16) calculate the solubilization radii of oil (Ro) and water (Rw), respectively. These solubilization radii are then used in Equations (A17) and (A18) to calculate the lower (LL) and upper (UL) limits of the μE, expressed as volume fractions of the total volume of the SOW system. Equation (A19) calculates the deviation (error) between the experimental μE boundaries (LL_{exp}, UL_{exp}) and the HLD–NAC predicted LL and UL. To minimize the error, the fitted parameters (Cc_1 or Cc_2, and ξ) are adjusted. The input parameters and the fitted values in the composition scans of Figure 1B,C are shown in the screenshots presented in those figures. For the composition scans in Figure 3A,C, the L_{mix} was not calculated from composition but set to 90 Å, reflecting the synergism of lecithin-linker scans [9,13]. For the systems of Figure 3A,C the characteristic length was set to ξ = 90 Å.

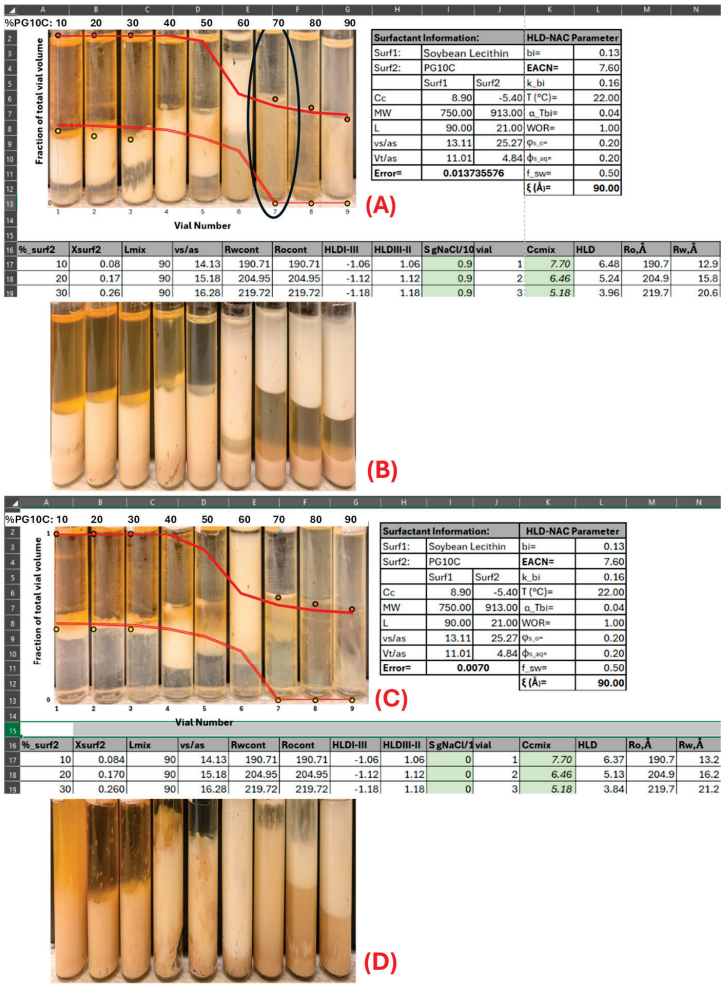

Surfactant Information:			HLD-NAC Parameter	
Surf1:	Soybean Lecithin		bi=	0.13
Surf2:	PG10C		EACN=	7.60
	Surf1	Surf2	k_bi	0.16
Cc	8.90	-5.40	T (°C)=	22.00
MW	750.00	913.00	α_Tbi=	0.04
L	90.00	21.00	WOR=	1.00
vs/as	13.11	25.27	$\phi_{s,o}$=	0.20
Vt/as	11.01	4.84	$\phi_{s,aq}$=	0.20
Error=	0.013735576		f_sw=	0.50
			ξ (Å)=	90.00

%_surf2	Xsurf2	Lmix	vs/as	Rwcont	Rocont	HLDI-III	HLDIII-II	S gNaCl/10	vial	Ccmix	HLD	Ro,Å	Rw,Å
10	0.08	90	14.13	190.71	190.71	-1.06	1.06	0.9	1	7.70	6.48	190.7	12.9
20	0.17	90	15.18	204.95	204.95	-1.12	1.12	0.9	2	6.46	5.24	204.9	15.8
30	0.26	90	16.28	219.72	219.72	-1.18	1.18	0.9	3	5.18	3.96	219.7	20.6

Surfactant Information:			HLD-NAC Parameter	
Surf1:	Soybean Lecithin		bi=	0.13
Surf2:	PG10C		EACN=	7.60
	Surf1	Surf2	k_bi	0.16
Cc	8.90	-5.40	T (°C)=	22.00
MW	750.00	913.00	α_Tbi=	0.04
L	90.00	21.00	WOR=	1.00
vs/as	13.11	25.27	$\phi_{s,o}$=	0.20
Vt/as	11.01	4.84	$\phi_{s,aq}$=	0.20
Error=	0.0070		f_sw=	0.50
			ξ (Å)=	90.00

%_surf2	Xsurf2	Lmix	vs/as	Rwcont	Rocont	HLDI-III	HLDIII-II	S gNaCl/1	vial	Ccmix	HLD	Ro,Å	Rw,Å
10	0.084	90	14.13	190.71	190.71	-1.06	1.06	0	1	7.70	6.37	190.7	13.2
20	0.170	90	15.18	204.95	204.95	-1.12	1.12	0	2	6.46	5.13	204.9	16.2
30	0.260	90	16.28	219.72	219.72	-1.18	1.18	0	3	5.18	3.84	219.7	21.2

Figure 3. (**A**) Surfactant composition scan using mixtures of lecithin (surfactant 1) and PG10C (surfactant 2) in an aqueous phase containing 0.9% w/v NaCl. (**B**) Surfactant composition scan of panel A with 5 wt% yeast in aqueous phase. (**C**) Surfactant composition scan using mixtures of lecithin (surfactant 1) and PG10C (surfactant 2) in an aqueous phase containing 0.9% w/v NaCl and 25% w/v sucrose. (**D**) Surfactant composition scan of panel C with 5 wt% yeast in aqueous phase. The numbers on top of each vial represent the wt% of PG10C (surf2) in the mixture with lecithin (wt%surf1 = 100 − wt%surf2).

2.2. Lecithin–Hydrophilic Linker (Le–HL) Phase Scans

Phase behavior studies of mixtures of lecithin (Le) and hydrophilic linker (HL, PG10C) were conducted to determine the lecithin-to-hydrophilic linker ratio required to produce water-dilutable μEs with the maximum possible oil solubilization. To estimate the HLD–NAC parameters L and ξ for lecithin-linker μEs, the Le-PG10C composition scan shown in Figure 3A was performed using EOL as the oil phase. The inversion points from water-in-oil μEs (vials 1 through 5 in Figure 3A) to oil-in-water μEs (vials 7 through 9) predicted by the HLD–NAC model was set by the EACN and Cc parameters obtained in Figure 1. The parameters L and ξ only help to fit the water or oil solubilization capacity of the μEs. The value of L = 90 Å is consistent with the value of L obtained from other lecithin-linker μEs [9,13]. The relatively low value of ξ = 90 Å compared to previous Le–LL–HL μEs (with ξ~200 Å) is likely due to the lack of a lipophilic linker (LL) [13].

Vials 1 through 6 in Figure 3A still display metastable emulsions (white phases) even after four heating cycles and 6 weeks of settling. This behavior is typical of lecithin μEs, especially those with low HL (PG10C, in this case) content. The surfactant mixture of vial #7 in Figure 3A has 70 parts PG10C, 30 parts Le, and a total surfactant concentration of 20 wt%. This vial is highlighted with an oval in Figure 3A because this is the approximate composition selected for ternary phase diagrams. At this surfactant composition, we do not observe metastable emulsions; the μE is continuous in the aqueous phase, which suggests that it can be further diluted with the aqueous phase, and the amount of oil solubilization is the maximum.

The phase scan in Figure 3B is the same scan as Figure 3A, but with 5% yeast added to the aqueous phase. The picture was taken one day after yeast addition. Overall, the phase behavior did not seem to be impacted by the addition of yeast, as the yellow tinge of the oil phases in vials #1 through #5 in Figure 3B are similar to the corresponding vials in Figure 3A. This yellow tinge is indicative of the presence of lecithin and PG10C in the oil, which is otherwise colorless. The presence of the surfactant in the oil phase is a signature for water-in-oil μEs. Similarly, the yellow tinge in the aqueous phases of vials 7 through 9 in Figure 3A,B are indicative of oil-in-water μEs. In all the vials, there was evidence of some level of yeast activity even though no sucrose was added. This is consistent with previous observations that yeast can use some of the oil, and perhaps the surfactants, as carbon sources for aerobic respiration [3].

Figure 3C presents a surfactant composition scan similar to that of Figure 3A, except that the aqueous phase contains 25 wt% sucrose. Using the same HLD–NAC parameters used in Figure 3A, the HLD–NAC predicted phase volumes in Figure 3C largely agree with the experimental values, except that vial #5 developed a middle phase μE, and vial #7 presented what appears to be a second phase in the aqueous phase, but this phase turned into a single clear aqueous phase with mild mixing. Given that sucrose is not interfacially active, it is not a surprise that it did not substantially affect the phase behavior of LLMs. One interesting observation is that, despite the increase in aqueous phase viscosity caused by the addition of sucrose, the system in Figure 3C produced less stable emulsions than the system of Figure 3A, a phenomenon that is worth exploring in future studies and may be related to the hydration of the lecithin headgroups.

Figure 3D shows the same scan as Figure 3C after adding 5% yeast. Evidence of vigorous CO_2 production started within 10 min of yeast addition in vials # 5, 6, and 7. Due to the relatively large amount of gas produced, the caps of each vial were left loose to prevent pressure buildup. The picture in Figure 3D was taken 24 h after introducing the yeast showing that fermentation took place in all the vials. There was evidence that, for vials # 4 through 9, the evolution of CO_2 was large enough to produce a froth that carried a portion of the liquid out of the vials.

2.3. Ternary Phase Diagram (TPD)

The composition scan in Figure 3A pointed to 70 parts HL (PG10C) to 30 parts Le as a possible composition to explore as candidate SMEDS. The composition used to develop the TPD was slightly different, 5 parts HL to 2 parts Le (equivalent to 71.4% PG10C), where the slightly higher HL content was expected to contribute to preventing the formation of metastable phases. Figure 4 presents the TPD obtained experimentally, along with pictures of the vials obtained at the different compositions explored. The black dots in Figure 4, corresponding to the D60 dilution line (SDL = 60), show the fully dilutable single phase μEs (the LLMs). The pictures of the vials at SDL = 60 containing 60% and 80% aqueous solution appear as two-phase systems, but a minor swirl turns the entire system into a homogeneous and clear single phase, suggesting that these systems are close to the multiple-phase boundary but solubilize all the oil and water. The systems at SDL = 80% are highly viscous and show birefringence when set in cross-polarized light filters, suggesting the presence of hexagonal or lamellar liquid crystals. The white phases observed at SDL = 20 and 40 indicate the presence of stable emulsions of unsolubilized oil.

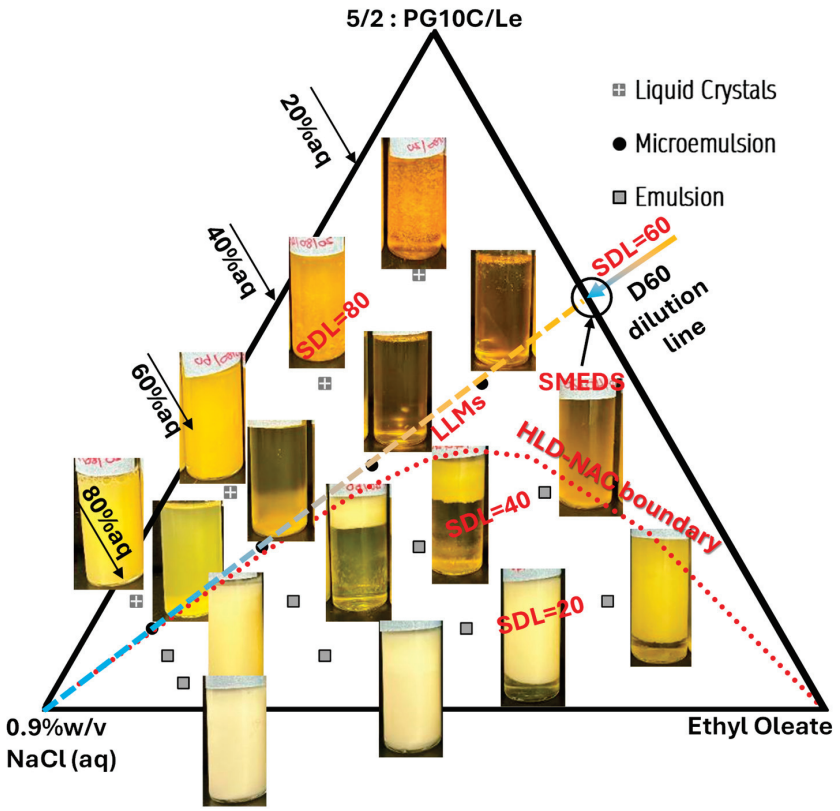

	A	B	C	D	E	F	G	H	I	J
1		Surfactant Information:			HLD-NAC Parameters					
2		Surf1:	Surf2:	Mixed:	Input		Pre-set or adjusted		Calculated	
3		Soybean Lecithin	PG10C	Surf	EACN=	7.60	fso=	0.01	HLD=	-1.94
4	grams	2.00	5.00	7.00	k=	0.16	fsw=	0.2	HLDi_iii=	-2.00
5	moles	0.0027	0.0055	0.0081	Cc=	-0.72	ξ (Å)=	90	HLDiii_ii=	2.00
6	mol_frac	0.33	0.67	1.00	c_T(1/°C)=	0.04	L (Å)=	90	Ro_d=	45.73
7	Cc	8.90	-5.40	-0.72	b=	0.13			Rw_d=	2817.30
8	vs/as (Å)	13.10	25.30	21.30	vs_as (Å)=	21.30				
9	MW (mol/g)	750.00	913.00	859.21	S (%NaCl)=	0.90				
10					T(°C)=	22.00				

Figure 4. Ternary phase diagram (TPD) for PG10C + lecithin (5 to 2 mass ratio) as surfactant (top vertex), ethyl oleate as oil (right vertex) and an aqueous phase containing 0.9% NaCl (left vertex). SDL = 60 or D60 indicates 60% of total surfactant in mixture with ethyl oleate to produce the water-free

SMEDS. Lecithin-linker μEs (LLMs) are SMEDS diluted with aqueous saline solutions. The screen shot at the bottom was from a modified version of the HLD–NAC tutorial Excel file used to predict HLD–NAC boundary, shown as a dotted line [16]. The algorithm for this calculation is shown in Figure 5.

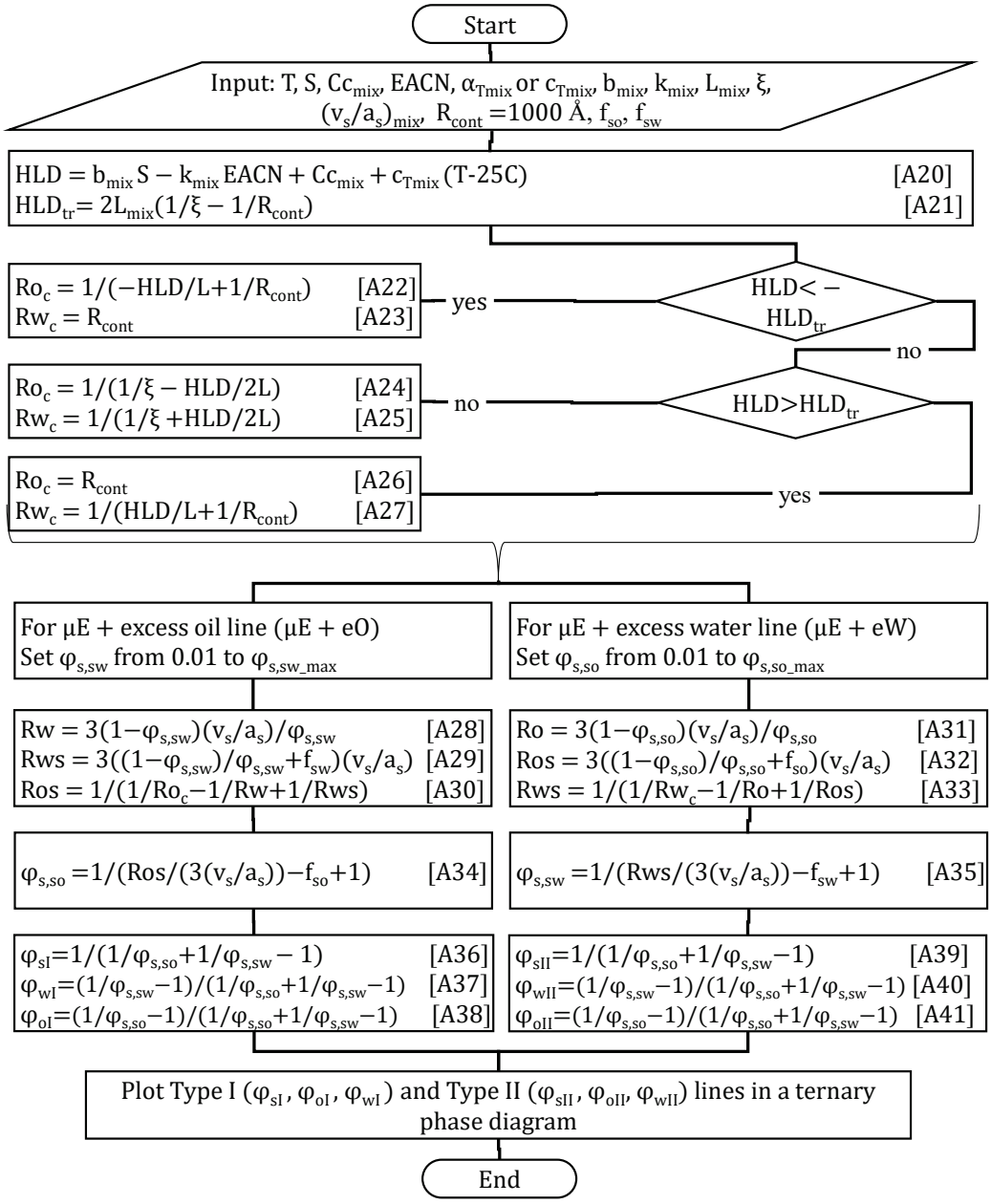

Figure 5. HLD–NAC algorithm to calculate the μE solubilization boundaries with excess oil (μE + eO) and with excess water (μE + eW) in a ternary phase diagram (TPD).

The dotted line in Figure 4 shows the HLD–NAC-predicted phase boundary for μEs coexisting with an excess oil phase (μE + eO lines) obtained using the input parameters shown in the screenshot included at the bottom of Figure 4. This screenshot was taken from a modified version of the HLD–NAC spreadsheet included in the HLD–NAC tutorial [16]. Figure 5 shows the algorithm used to generate the TPD lines. The input of the algorithm are the temperature (T), salinity of the system (S), oil EACN, and the mixed HLD–NAC parameters for the selected composition (x_2): the characteristic curvature (Cc_{mix}), volume to area ratio ($(vs/as)_{mix}$), salinity factor (b_{mix}), EACN factor (k_{mix}), temperature factor (c_{Tmix}),

tail length (L_{mix}), and the μE characteristic length (ξ) and fraction of the surfactant volume that contributes to the aqueous (f_{sw}) and oil (f_{so}) volume compartments. The algorithm requires the solution of the HLD–NAC in highly diluted conditions. This highly diluted case requires setting a high solubilization radius for the continuous phase (R_{cont} = 1000 Å, and this becomes Ro_{cont} or Rw_{cont}, depending on the HLD).

Equation (A20) in Figure 5 is used to calculate the HLD of the system. Equation (A21) is used to calculate the transition $HLD_{III–II}$ (HLDtr = $HLD_{III–II}$) under dilute conditions, and under dilute conditions $HLD_{I–III} = -$HLDtr. Equations (A22) and (A23) calculate the solubilization radii under dilute conditions for oil (Ro_d) and water (Rw_d), respectively, in Type I μEs. Equations (A24) and (A25) are used to obtain Ro_d and Rw_d in Type III μEs. Equations (A26) and (A27) are used to obtain Ro_d and Rw_d in Type II μEs. After obtaining Ro_d and Rw_d, there are two solubilization boundary lines that one can obtain; one is the saturated μE coexisting with excess oil (μE + eO) line, and the line of saturated μE coexisting with excess water (μE + eW). For the μE + eO line, one starts by setting the volume fraction of the surfactant mixture as if all the surfactant was only present in the aqueous phase ($\varphi_{s_sw} = v_{surf}/(v_{surf} + v_{water})$) between 0.01 and a maximum value ($\varphi_{s_sw,max}$). The value of $\varphi_{s_sw,max}$ can be found by trial and error because, when $\varphi_{s_sw} > \varphi_{s_sw,max}$, a portion of the predicted boundary line (beyond $\varphi_{s_sw,max}$) produces unrealistic results. The published tutorial spreadsheet [16] contains a protocol to find $\varphi_{s_sw,max}$. After setting φ_{s_sw}, the solubilization radius of water (Rw) is found with Equation (A28). Equation (A29) calculates the radius of solubilization of water, including the surfactant contribution to the aqueous phase compartment (Rws). To construct TPDs, one uses the principle that the net curvature is the same under dilute ($Hn = 1/Ro_d - 1/Rw_d$) or concentrated ($Hn = 1/Ros - 1/Rws$) conditions. Equation (A30) uses $1/Ro_d - 1/Rw_d = 1/Ros - 1/Rws$ to calculate Ros with the previously calculated Ro_d, Rws, and Rw_d = Rw. With the value of Ros, one can now calculate the surfactant volume fraction in the oil phase, as if all of the surfactant were only present in the oil phase ($\varphi_{s_so} = v_{surf}/(v_{surf} + v_{oil})$). Once one obtains φ_{s_so} for the set value of φ_{s_sw}, one can find the volume fraction of the surfactant in the system ($\varphi_{sI} = v_{surf}/(v_{surf} + v_{water} + v_{oil})$) using Equation (A32), the volume fraction of water in the system ($\varphi_{wI} = v_{water}/(v_{surf} + v_{water} + v_{oil})$) using Equation (A33), and the volume fraction of oil in the system ($\varphi_{oI} = v_{oil}/(v_{surf} + v_{water} + v_{oil})$) using Equation (A34). By setting a range of φ_{s_sw} values and repeating the steps in (A28) through (A34), then a set of compositions (φ_{sI}, φ_{oI}, φ_{wI}) can be obtained and plotted to obtain the μE + eO line. This is what led to the red dotted line in Figure 4. A similar set of calculations can be performed for the μE +eW line (Equations (A35) through (A41)), but, since the system of Figure 4 is at the I-III boundary, only the μE +eO line is relevant.

For the system in Figure 4, the only adjusted parameters in the algorithm were the fraction of the surfactant volume that contributes to the volume of the "aqueous" (f_{sw}) and "oil" (f_{so}) compartments. To illustrate the meaning of f_{sw} and f_{so}, let us consider a system containing 3 mL of oil, 2 mL of surfactant, and 5 mL of water. If f_{sw} = 0.4 and f_{so} = 0.1, the volume of the aqueous compartment is 5 mL (from water) + 2 × 0.4 mL (from the surfactant) = 5.8 mL, and the volume of the oil compartment is 3 mL (from oil) + 2 × 0.1 mL (from the surfactant) = 3.2 mL. Initially, it was thought that $f_{sw} + f_{so} = 1$, but, after fitting various TPDs, it has become evident that this sum is often less than 1 [9,13]. For the HLD–NAC predicted boundary in Figure 4, f_{so} was set to 0.01 because any higher value would move the boundary beyond SDL = 60, and f_{sw} was set to 0.2 because any higher value would predict that, at SDL = 40 and 20% aqueous phase, the system would be a single phase μE. The physical significance of $f_{sw} + f_{so} \leq 1$ needs further exploration, but

it suggests that a portion of the volume of the surfactant cannot be used to accommodate the curvature of the oil and aqueous compartments.

2.4. Conductivity and Viscosity Along SDL = 60 (D60) Dilution Line

According to Nouraei et al. [9,13], fully dilutable lecithin-linker microemulsions can form three distinct microenvironments as the aqueous phase increases—reverse micellar, bicontinuous, and micellar—whose transitions are reflected in conductivity and viscosity measurements. These properties help to experimentally identify when the system moves between oil-continuous, bicontinuous, and water-continuous phases. Figure 6 provides a visual representation of these microenvironments. One aspect that should be clarified is that, lecithin in SMEDS, due to the presence of HL and oil, does not exist in the form of rigid layers like those in liposomes or bilayers.

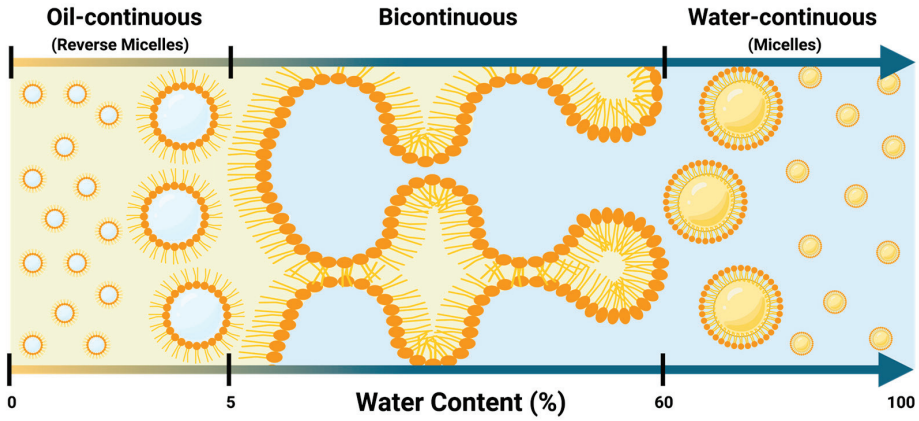

Figure 6. Schematic representation of lecithin-linker μEs (LLMs) transitioning from oil-continuous (reverse micellar) structures to bicontinuous phases at approximately 5% water content and from bicontinuous to micellar (water-continuous) systems at around 60% water content, according to the information in Figure 7 (Created in BioRender. Doratt, J., accessed on 4 January 2025, https://BioRender.com/a21a732).

Figure 7 shows the relative conductivity and viscosity of LLMs (SDL = 60 in Figure 4) as a function of the aqueous phase content (Figure 7A) and the water-to-surfactant molar ratio (Wo, Figure 7B). The reference conductivity was the conductivity of water containing the same electrolyte concentration (based on total volume) as the diluted μEs, and the reference viscosity was the viscosity of water at 20 °C. The green lines were obtained using equations developed for bicontinuous polymer systems. The relative conductivity ($\sigma_{relative}$) was predicted as [19]:

$$\frac{\sigma_{bicontinuous}}{\sigma_{aqueous}} = \sigma_{relative} = \frac{\varphi_{aqueous}}{\tau} = \frac{\varphi_{aqueous}}{\left(\frac{2-\varphi_{aqueous}}{\varphi_{aqueous}}\right)} \quad (4)$$

The term $\varphi_{aqueous}$ is the volume fraction of the aqueous phase, and τ is the tortuosity. The tortuosity expression included in the last term of Equation (4) is the Mackie–Meares equation for ion transport in polymer networks [20]. The dashed green line shows the predicted relative conductivity using Equation (4).

According to Figure 7, for systems containing up to 20 wt% aqueous phase, the relative conductivity predicted by Equation (4) matches the experimental data. It is important to keep in mind that Equation (4) was obtained by combining two equations derived for bicontinuous polymers, where the polymer network is immobile. On the other hand, μEs are dynamic systems where the oil and water domains are constantly fluctuating.

This suggests that, at least for systems with less than 20% aqueous phase, the mobility of the aqueous environment is rather limited, but, after 20% water, the larger experimental conductivity can be explained by the greater mobility of μE environments compared to fixed bicontinuous polymeric environments.

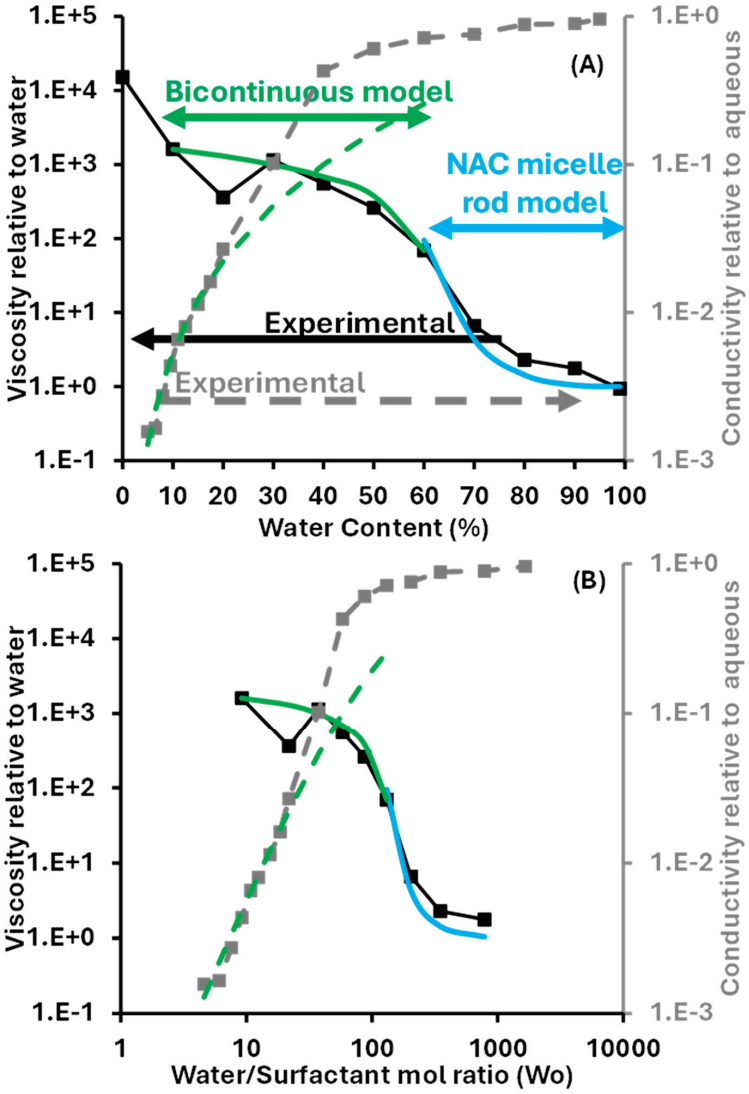

Figure 7. Relative conductivity (dashed line) and viscosity (solid line) of fully dilutable μEs (SDL = 60 or D60 in Figure 4) as a function of (**A**) water content expressed as volume % in the system, and (**B**) water to surfactant molar ratio (Wo). The green lines represent the conductivity and viscosity predicted bicontinuous polymer models, and the blue line represents the relative viscosity predicted via the HLD–NAC model using the dilute rigid rods model.

Considering that Equation (4) was designed for bicontinuous systems, the close match with the experimental data at low water content suggests that, even with as low as 5% aqueous content, the μEs are bicontinuous. The HLD–NAC can help evaluate if, conceptually, bicontinuous μEs are even possible at this low water content. To this end, we need to consider the solubilization radii for oil and water, including the surfactant volume contribution, Ros and Rws [9]:

$$\mathrm{Ros} = 3\left(\frac{\phi_o}{\phi_s} + f_{so}\right)\left(\frac{v_s}{a_s}\right);\ \mathrm{Rws} = 3\left(\frac{\phi_w}{\phi_s} + f_{sw}\right)\left(\frac{v_s}{a_s}\right) \quad (5)$$

When one obtains a single phase μE (i.e., a composition above the solubilization boundary line) the net curvature (Hn) is no longer controlled by HLD but is calculated with Equation (2) using the solubilization radii of Equation (5); Hn = (1/Ros − 1/Rws). Similarly, the average curvature is calculated using Equation (3) with the solubilization radii of Equation (5); Ha = (1/2)·(1/Ros + 1/Rws). With Hn and Ha, the size and shape of oil-swollen micelles (positive Hn) or water-swollen reverse micelles (negative Hn) can be calculated, assuming that these swollen micelles or reverse micelles have a cylindrical body with hemispherical caps. The radius (R_d) and length (L_d) of the cylinders is calculated as [21]:

$$R_d = \frac{2Ha - \sqrt{4Ha^2 - 2Ha \cdot |Hn|}}{Ha \cdot |Hn|} \tag{6}$$

$$L_d = 2 \cdot R_d \cdot \left(2 - \frac{|Hn \cdot R_d|}{|Hn \cdot R_d| - 1}\right) \tag{7}$$

For a system with near zero curvature, when $|Hn| < 1/R_d$, Equation (7) produces negative L_d values, signifying that the system cannot exist as a water-continuous or oil-continuous system, and instead, a bicontinuous μE is obtained. For the D60 (SDL = 60) dilution line, with a given level of water dilution, for example, 20% water (φ_w = 0.2), the surfactant fraction is $\varphi_s = (1 - \varphi_w) \cdot SDL/100 = 0.8 \times 0.6 = 0.48$; then, for the oil, $\varphi_s = (1 - \varphi_w) \cdot (100 - SDL)/100 = 0.32$. Using f_{so} = 0.01, f_{sw} = 0.2, and v_s/a_s = 21.3 Å (see Figure 4 bottom—NAC input table), and these volume fractions, Ros and Rws are calculated using Equation (5), then Hn and Ha are calculated. Using Equations (6) and (7), R_d and L_d are calculated. Using this procedure, negative L_d values were obtained along the D60 dilution line, from 5 wt% water to just below 60% water, suggesting that all of these systems are bicontinuous. This NAC prediction is consistent with the close match between the experimental relative conductivity and the relative conductivity predicted by the bicontinuous polymer model (Equation (4)).

The radius (R_d) and length (L_d) of the swollen micelles and reverse micelles along the dilution line can also be used to predict the viscosity of the μEs, assuming that they behave as dilute rods [21]:

$$\mu_{relative} = \frac{\mu_{\mu E}}{\mu_0} = \left(1 + \frac{\phi_{solubilized}}{\pi}\left(\frac{L_d}{R_d}\right)^2\right) \tag{8}$$

The term $\mu_{\mu E}$ is the μE viscosity, μ_0 is the viscosity of the solvent (water for oil-in-water μEs), and $\varphi_{solubilized}$ is the volume fraction of the solubilized phase (the oil, and the surfactant contribution to the oil compartment, for oil-in-water μEs). The solid blue line in Figure 7 was obtained using Equation (8). The close match between the predicted relative viscosity (no fitting parameters) and the experimental relative viscosity for a water content of 60% or more suggests that the NAC model accurately captures the changes in the size and shape of oil-swollen micelles along the dilution line. This observation is consistent with previous evaluations that considered not only relative viscosity but also particle size evaluated using dynamic light scattering and neutron scattering [9,13,21]. To predict the relative viscosity in the bicontinuous region (solid green lines in Figure 7), a linear bicontinuous polymer melt model was used [22]:

$$\mu_{relative} = \frac{1}{\mu_{reference}}\left(\mu_1\phi_1 + \mu_2\phi_2\right) \tag{9}$$

The reference fluid for the relative viscosity in Figure 7 is water at 20 °C (μ_{ref} = 1 mPa·s). Fluid 1 was taken as the μE obtained with 10% water (μ_1 = 1600 mPa·s), and fluid 2 was taken as the μE obtained with 60% water (μ_2 = 70 mPa·s). Overall, this linear approximation matches well with the experimental values, except for the dip in measured viscosity at 20% water. A second set of viscosity measurements was undertaken with systems containing 8% yeast, and the viscosity obtained was nearly identical to those obtained from yeast-free systems, except for the systems with 70% water or more, where the viscosity of the yeast suspension was two to three times larger than the viscosity of the yeast-free system. The dip in viscosity at 20% water was also observed in this second set of measurements. At this point, the origin of the dip in viscosity at 20% water is not clear and should be explored in future studies.

2.5. Yeast Dispersibility

Figure 8 illustrates the dispersibility of yeast (*Saccharomyces cerevisiae*) in LLMs obtained along the D60 dilution line, with an increasing aqueous phase from 0% to 100%. At a 0% aqueous phase, the yeast was unable to disperse, settling at the bottom of the vial. When a sample was taken from the middle of the vial, 15 min after 8% of yeast was dispersed, no yeast cells were observed, suggesting that yeast may not be activated in water-free systems and remain dormant in a dry state. At a 5 wt% aqueous phase, a significant portion of the cells remained suspended in the system, suggesting that yeast was activated in those systems. Yeast cells require a water activity of at least 0.61 to be activated [23]. Although water activity was not measured, previous studies with ionic μEs reveal that, at water-to-surfactant mol ratio (Wo) as small as 2.5 (~3 wt% aqueous in LLMs), the activity of water is 0.79 [24]. This suggests that, for LLMs with 5% water, yeast cells are activated (and suspended in the process), which is to be expected considering that instant dry yeast cells were used in this study. Full and stable yeast dispersion was achieved from 20% aqueous content and above. From 30 to 60 wt% aqueous, the micrographs showed yeast clusters in bicontinuous μEs. For the water-continuous μEs (>60 wt% aqueous), the cells were homogeneously dispersed.

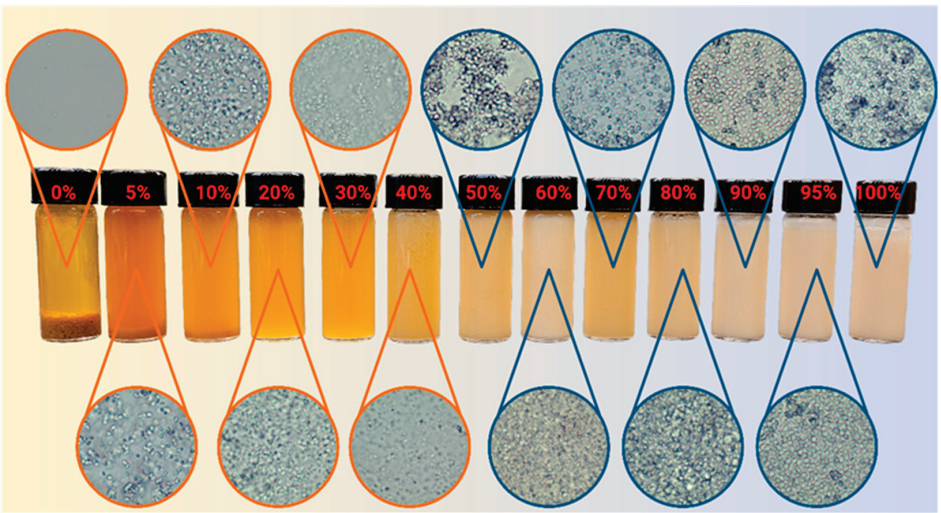

Figure 8. Dispersibility of 8% yeast suspension in LLMs produced along the D60 (SDL = 60) dilution line in Figure 4. The percentage indicated corresponds to the percentage of the aqueous phase in the LLM. The circles show the bright field micrographs obtained using a 20× objective.

2.6. Yeast Viability and Activity

Figure 9 shows the relative activity of 8% yeast suspensions in aqueous solutions of lecithin (Le, system "A"), hydrophilic linker PG10C (HL, system "B"), Le + HL (system "C"), and in an LLM (Le + HL + EOL, system "D") produced along the D60 dilution line with the 80% aqueous phase. This 80% aqueous phase dilution was selected as a reference point because it produced well-dispersed cell suspensions in aqueous-continuous environments. The relative activity was calculated in reference to the CO_2 production by an 8% yeast suspension in a saline (0.9% *w*/*v* NaCl) solution. The data in Figure 9 show that lecithin does not significantly reduce the activity of yeast. It should be clarified that lecithin on its own can only be dispersed in the saline solution and is not fully dissolved. The system with hydrophilic linker (HL, PG10C) and the system with the mixture of HL and Le deactivated the yeast. Microscope images did not show signs of mechanical damage to the cells; however, it is known that surfactants can fluidize cell membranes, an effect that is similar to heat-induced cell death [25,26].

Lecithin	✓		✓	✓
PG10C		✓	✓	✓
Oil (EO)				✓
Saline	✓	✓	✓	✓
Balloon	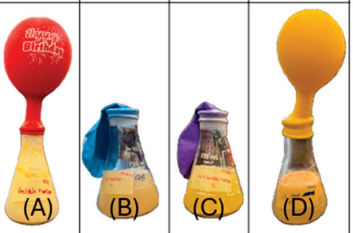			
Activity (%)	95	0	0	40

Figure 9. Relative yeast activity in control samples: (**A**) 3.4 parts Le/80 parts (by mass) saline, (**B**) 8.6 HL (PG10C)/80 saline, (**C**) (3.4 Le + 8.6 HL)/80 saline, (**D**) (3.4 Le +8.6 HL+ 8 parts oil (ethyl oleate)/80 saline. The composition of (**D**) corresponds to an 80% aqueous dilution along the D60 line in Figure 4. Each of these systems containing 8% yeast were left for 24 h before mixing with a sucrose solution (25 g suspension + 75 g sucrose). The balloons show the CO_2 production after another 24 h. The relative activity compares the volume of CO_2 produced in each case and the volume produced by a suspension of 8% yeast in saline solution (0.9% *w*/*v* NaCl).

Hydrophilic linkers have been reported to reduce interfacial rigidity substantially [10]. This may explain the strong deactivating effect of HL alone or in combination with lecithin. However, once the full μE (LLM) is produced with the addition of EOL (the oil), then a substantial fraction of the activity is still retained. This partial activity may be explained by the fact that the presence of the oil creates an oil-water interface where the HL can be adsorbed, discouraging HL from primarily adsorbing on the surface of cell membranes. In other words, the addition of EOL likely reduced the activity of the HL in the aqueous phase.

Figure 10 presents the activity and viability (assessed via the methylene blue staining method) of yeast suspensions in LLMs along the D60 line. The aqueous phase content is presented in Figure 10A as wt% and in Figure 10B as water/surfactant mole ratio (Wo). At 0% aqueous content (i.e., the SMEDS at D60), the yeast exhibited relatively high activity, producing the equivalent of 82.7 ± 5.0% of the CO_2 produced by yeast suspended in saline solution (the reference suspension) for 24 h before the addition of the sucrose solution. Considering that yeast was not dispersible in SMEDS, suggesting that yeast was not activated, the large activity obtained once the sucrose solution was added indicates

that SMEDS served as a dry preservation media for yeast. In LLMs with 5% aqueous content, the viability was 59.9 ± 2.8%, and the activity was 62.6 ± 4.5%, suggesting that a significant portion of the yeast cells remained alive despite partial dispersion observed in Figure 8 for this system. As the aqueous content increased to 10% (Wo~10), the activity and viability drastically decreased to 37.7 ± 3.5% and 23.8 ± 1.7%, respectively, but the activity and viability bounced back to 76.7 ± 7.4% and 71.2 ± 4.0%, once the aqueous content reached 20% (Wo~22). Yeast activity reached a peak (93.3 ± 3.2%) in LLMs with 30% aqueous content (Wo~37) while maintaining a relatively high viability (75.1 ± 2.1%). From there, further increases in water content in the LLM resulted in a gradual decrease in activity and viability, reaching a plateau of about 30% activity once the LLM reaches a 70% aqueous content. The viability also reduces slightly, but, in most cases, the viability remains above 50%.

Hopper et al. investigated the photosynthetic activity (measured as O_2 generation) of cyanobacteria and green algae as a function of Wo in Tween 85-Span 80-hexadecane μEs, finding that there was no activity when Wo was less than 50 and maximum activity at Wo~80 to 1802. The authors posed that Wo > 50 was needed to activate the cells; however, for yeast, even Wo~3 should be enough to activate the cells. The high activity found at Wo~0 suggests that, in a dry state, the yeast remains dormant in SMEDS but is quickly activated once in contact with the sucrose solution. The minimum activity and viability found at Wo~10 in Figure 10B suggests that, during the 24 h incubation of yeast in the LLM with 10% aqueous, there was some level of metabolic activity (supported by the evidence of metabolic activity in the sugar-free systems in Figure 3B) that produced metabolites (possibly alcohols and fatty acids), but, given the small amount of water and the poor transport, these metabolites could have concentrated to toxic levels [27].

As the aqueous content in the LLM increases beyond Wo~10, the increased volume of water solubilized likely helped dilute and transport metabolites (illustrated by the increased conductivity in Figure 7B when Wo > 10) during the 24 h incubation period before the yeast was set in contact with the sucrose solution.

Much like Hopper et al., we were not able to identify a clear reason for the existence of an optimal Wo for cell activity (Wo~37 in our case). At Wo less than 37, increasing Wo increases the transport of aqueous metabolites (Figure 7B), but, after Wo~37, there are only marginal increases in conductivity and transport through the aqueous phase. On the other hand, increasing Wo decreases the amount of SMEDS (Le + PG10C + EOL) in the LLM, which means it decreases the ratio of SMEDS to yeast. The data suggest that the Le–HL–EOL system plays a role in kickstarting the metabolic processes (Figure 3B) in yeast. This observation is consistent with a previous study where a Le-PG10C-Span80 formulation designed as an oil spill dispersion media maintained the biodegradation in a nutrient-deprived cell growth media, suggesting that the carbon, phosphor, and nitrogen in lecithin served as nutrients for the cells [15]. Another study showed that the addition of small amounts of lecithin could improve alcohol production in yeast fermentation, which was explained in terms of lecithin being used as a lipid source to form new cell membranes (aid in yeast cell division) [28]. The idea that the SMEDS lipids help kickstart the fermentation in yeast is also supported by the findings of Pfammatter et al., who observed a 4-fold increase in cell counts in the first 24 h that yeast cells were exposed to Tween85-Span80-hexadecane μEs containing 3% of an aqueous 0.9% w/v NaCl solution without added nutrients [3]. In fact, their work shows that, when the yeast (*C. pseudotropicalis* in their case) was exposed to 0.9% w/v NaCl solution without surfactants and without nutrients, there was only about 1.5-fold increase in cell counts after 24 h of incubation. The same work showed, using

C^{14}-labeled hexadecane, that, during the incubation period, some of this oil was used as a carbon source for aerobic respiration.

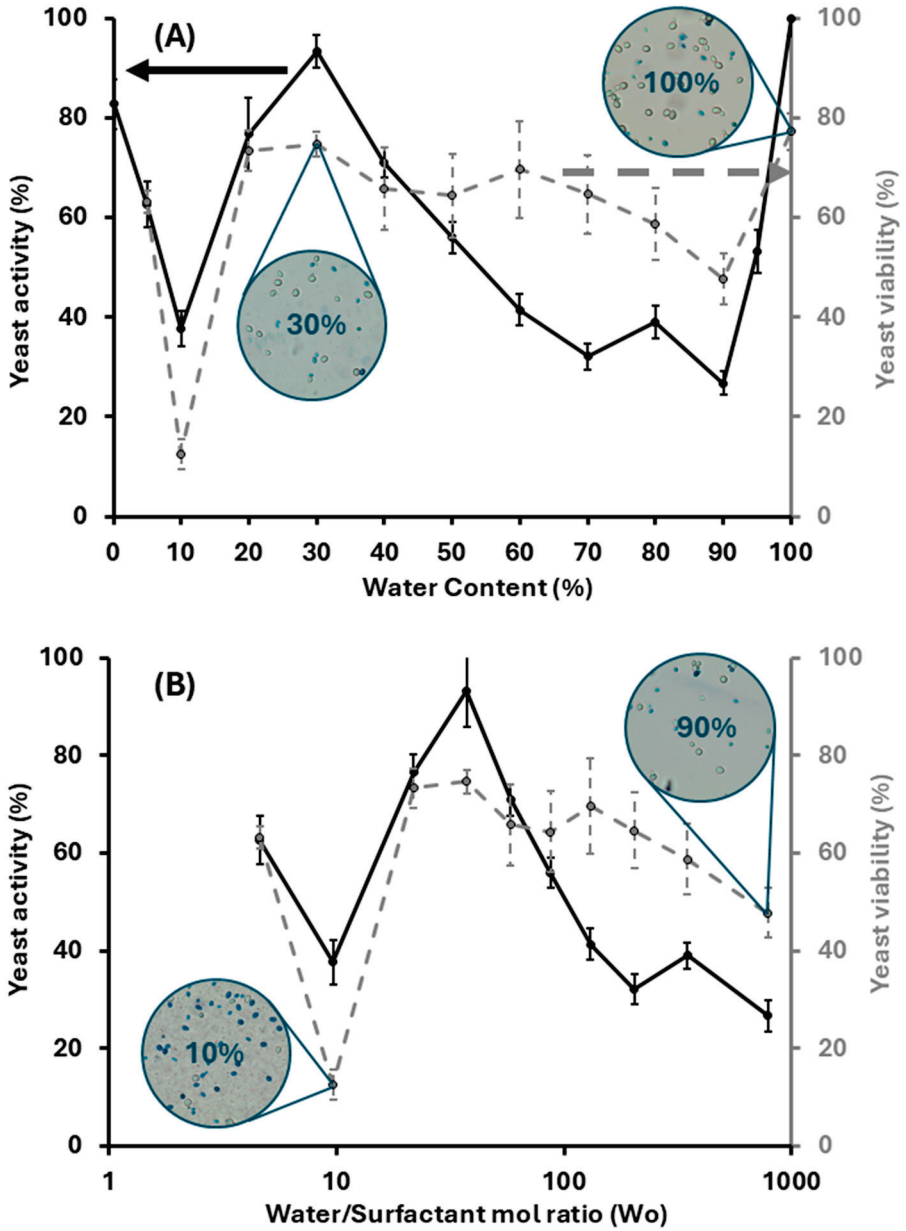

Figure 10. Yeast activity and viability as a function of water content (**A**) and water-to-surfactant ratio, Wo, (**B**)—along the dilution line D60 illustrated in Figure 4. The left vertical axis (black solid line) represents yeast activity, measured by the amount of CO_2 produced over 24 h after feeding the yeast-loaded (loading: 8% *w*/*w*) LLMs (previously exposed to the formulation for 24 h with a 25% *w*/*v* sucrose solution. The right vertical axis (gray dashed line) shows yeast viability following the same exposure and feeding protocol. The viability was determined by staining the dead yeast cells with a 0.1% aqueous methylene blue, as shown in the micrographs for the LLM systems containing 10%, 30%, 90% and 100% of the aqueous phase.

Another factor to consider when interpreting Figure 10 is that hydrophilic linkers, like PG10C, tend to remain partially present in the aqueous phase even in LLMs10. Therefore, the more water in the system (increasing Wo), the more hydrophilic linker (PG10C) will end in the aqueous phase. As we learned from Figure 9, when PG10C is in the aqueous

phase, PG10C tends to suppress yeast activity. This also explains why the LLM with 90% aqueous phase has the lowest yeast activity, but with 100% aqueous (only saline solution, no Le-PG10C-ethyl oleate), then, the activity is the largest observed with these systems.

2.7. Long-Term Storage in SMEDS and LLMs

The activity of yeast in SMEDS and selected LLMs was evaluated as a function of incubation time (the time before the yeast + LLM or SMEDS was exposed to the sucrose solution) to determine how long one could store yeast in these systems before there is a significant decrease in activity, assessed in terms of CO_2 production. Figure 11 presents the activity of yeast in LLMs containing 0% (SMEDS), 30%, 80%, and 100% (only aqueous phase) 0.9% w/v NaCl solution.

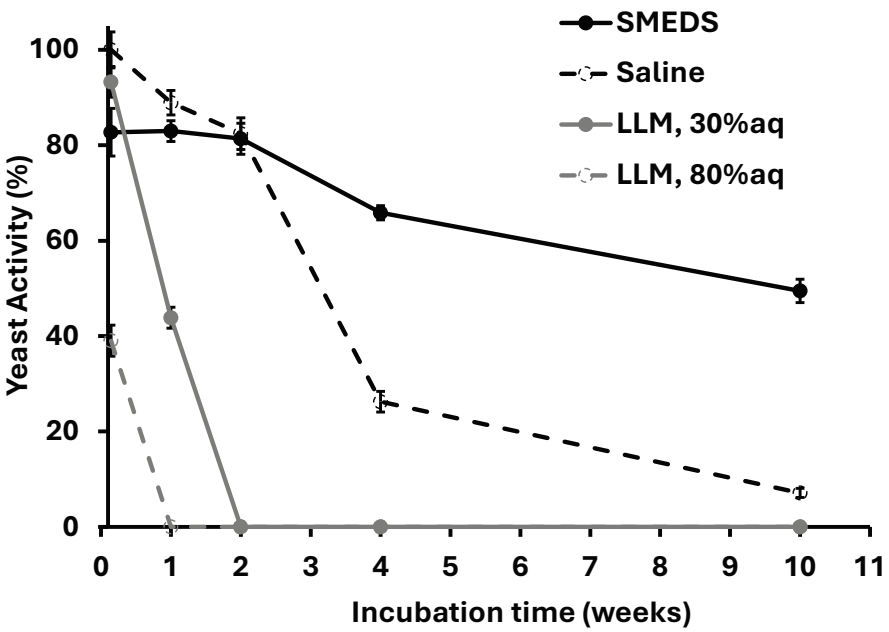

Figure 11. Yeast activity in LLMs (measured by the amount of CO_2 produced after exposure to sucrose solution) versus the incubation time of the yeast in SMEDS or LLMs before contacting with the 25% sucrose solution.

The system with 100% aqueous phase produced the largest activity after one day of incubation. However, as the incubation time increased over 2 weeks, the activity reduced substantially. This decline may indicate that, despite the stabilizing effect of the saline environment, the absence of nutrients over time gradually impaired cellular functions and viability, resulting in diminished metabolic activity. The LLMs with 80% and 30% aqueous content show a precipitous decrease in activity that is unlikely to be associated with the lack of nutrients as Le and EOL serve that function, but rather the problem of metabolite build-up and the presence of the hydrophilic linker (PG10C) in the water that tends to suppress yeast activity, as shown in Figure 9.

For the LLM with 30% aqueous phase, it is remarkable that the yeast was still active after 1 week of incubation, answering part of the research question that LLMs can extend the survival of unacclimatized yeast beyond the 3 days reported for other μE formulations1. The D60 SMEDS (0% LLM) shows a gradual decline in activity, decreasing from 82.73 ± 4.99 in Week 0 to 49.50 ± 2.46 by Week 10. This observation then answers the second part of the research question that SMEDS can substantially extend the survival of unacclimatized yeast beyond the 3 days reported for previous μE formulations. The slow decrease in

yeast activity in SMEDS, compared to the LLMs, is likely associated with the low water activity in the D60 SMEDS since yeast cells are known to remain dormant when the water activity is lower than 0.61 [23]. Recent work shows that when yeast cells enter a dormancy stage due to dehydration (the process used to make dry powder yeast), the cells enter a solid-like state triggered by an acidification of the cytoplasm that results in a widespread macromolecular assembly of proteins and sugars, causing the cytoplasm to gel [29]. Since dry powder yeast cells are added to SMEDS (no water added), then, as long as the SMEDS remain dry, the lack of water keeps the yeast dormant. The gradual loss of yeast activity in SMEDS might be associated with water absorption from air over the 10-week period since the formulation was stored in ambient air (T~25 °C, ~50% relative humidity), protected with Parafilm™ film, which has low but non-zero water vapor permeability [30]. One fundamental difference between dry yeast powder (that remains stable for one year or more if the package seal is not compromised) and the yeast in SMEDS is that the yeast powder does not have nutrients, thus absorption of water from air is not likely to result in activation. However, in SMEDS, lecithin and EOL are nutrients, and the absorption of water from air is likely to result in premature yeast activation. Future stability tests are planned to keep track of water activity in SMEDS under different storage conditions and its impact on cell viability and activity. If water absorption is involved, then appropriate storage and packing/sealing must be considered.

Another potential explanation for the gradual decrease in yeast activity in SMEDS is the potential effect of the hydrophilic linker (HL) on the yeast cell wall. The prolonged exposure of dormant cells to the HL in SMEDS could allow enough time for HL molecules to diffuse into cell membranes, fluidizing the membrane, following a similar deactivation mechanism proposed to explain the results in Figure 9B,C [25,26]. The viability of dry dormant cells diminishes when the membranes are fluidized and is often reflected in lower glass transition temperature of the cell membrane [30,31]. Future stability tests are planned to keep track of the effect of HL on cell membrane fluidity, assessed via glass transition temperature, for cells stored in SMEDS. If HL-induced membrane fluidization is involved, then alternative formulations with different HL, or different HL/Le ratios, or membrane protectants, such as albumin, could be considered, as well as producing acclimatized cells that are resistant to the potential HL effects.

One additional factor that was not fully considered in this work was the effect of shear on cell death induced by mechanical stresses. The mixing used in this work was relatively mild (vortex-mixing), and no cell rupture was observed in any of the images, even in systems with low cell viability. However, the use of high-shear processing technologies, such as high-pressure homogenization, can lead to mechanically induced yeast cell rupture [32]. For such cases, the lubrication phenomena in localized high shear environments are likely to play a role, and the potential effects of surfactants, and μEs, on lubrication should be considered. In some cases, surfactants have been shown to display "superlubricity effects" that might help yeast cells survive high shear environments [33].

3. Materials and Methods

3.1. Materials

The chemicals used in the formulation of the lecithin-linker microemulsions included MiliQ water (18 Ω) obtained from Milli-Q® IQ 7000 Ultrapure Water Purification System, Sigma-Aldrich (Oakville, ON, Canada); ethyl oleate (98%), which was purchased from Fisher Scientific (Mississauga, ON, Canada); L_α-granular soybean lecithin, granular (from soybean oil), which was purchased from Thermo Fisher Scientific-Across Organics (Mississauga, ON, Canada); sodium chloride (>99.0%), sucrose (≥99.5%), methylene blue

hydrate (≥95.0%), and limonene (97%, racemic mixture), which were purchased from Sigma-Aldrich (Oakville, ON, Canada); polyglyceryl-10-caprylate (Polyaldo® 10-1-CC, 97%), which was donated by Azelis Canada (Brampton, ON, Canada); surfactant pentaethylene glycol nonyl ether (C9E5 or Dehydol® OD-5, 100% active), which was donated by BASF North America (Wyandotte, MI, USA); and *Saccharomyces cerevisiae*, which was purchased from a local store as baker's yeast, Fleischmann's® quick-RISE instant dried yeast manufactured by AB Mauri Food Inc. (St. Louis, MO, USA). Plastic balloons were sourced from Pioneer Ballon Canada Ltd. (Hamilton, ON, Canada). All chemicals were used as received without further purification.

3.2. Methods

3.2.1. Estimation of HLD and NAC Parameters for Lecithin-Linker Microemulsions

A salinity scan was conducted to estimate the EACN of ethyl oleate (EOL) using the surfactant C9E5 at 40 wt% in the aqueous phase, a water-to-oil ratio (WOR) of 1:1, and a total volume of 6 mL. For C9E5 concentrations of 20 wt% or higher, the characteristic curvature (Cc) was −0.3, determined via salinity scans with limonene as the oil phase. All vials were gently agitated and allowed to equilibrate for two weeks before any observations were recorded. Phase volumes were then analyzed using a modified HLD–NAC model Excel spreadsheet to fit EACN and ξ [16].

In a separate composition scan, the Cc of lecithin (Le) and the hydrophilic linker polyglyceryl-10-caprylate (PG10C) was assessed by mixing each surfactant with C9E5 (reference) and limonene (EACN = 6), at WOR = 1:1, total volume of 6 mL, and 20 wt% total surfactant. The aqueous phase salinity was 0.9% w/v NaCl. After two weeks of stabilization, phase volumes were again fitted with a modified HLD–NAC model to determine the Cc and ξ values.

3.2.2. Lecithin–Hydrophilic Linker Phase Scans

To determine the HLD–NAC parameters (L and ξ in Equations (2) and (3)) for the Le + HL (PG10C) system with ethyl oleate, a composition scan was carried out at 20 wt% total surfactants in the aqueous phase, varying the HL from 10% to 90% in 10% increments. The water-to-oil ratio (WOR) was kept at 1:1 (6 mL total), with a salinity of 0.9 g NaCl per 100 mL in the aqueous phase (S = 0.9%). After two weeks of room-temperature equilibration, most samples still formed gel-like emulsions. They were then heated to 80 °C for one hour (no mixing), cooled, and allowed to equilibrate for another week; this cycle was repeated four times before images were taken. The phase volumes were fitted with a modified HLD–NAC model.

Since the yeast activity involves the use of sucrose as a substrate, it is important to assess whether sucrose affects the Le + HL microemulsion phase behavior. The effect of sucrose on the Le + HL microemulsion phase behavior was determined by repeating the scan described above with the addition of 25% w/v sucrose in the aqueous phase (still at S = 0.9%). After taking pictures and observations of the scans containing the sucrose, 0.15 g of baker's yeast (5 wt% in the aqueous phase) was added to each vial to gauge whether yeast metabolism influences the phase behavior of the Le + HL microemulsions.

3.2.3. Construction of the Ternary Phase Diagram (TPD)

To construct the ternary phase diagram and determine the minimum surfactant concentration for a fully dilutable pathway, binary mixtures were prepared along the surfactant–oil axis of the TPD by varying the total surfactant (Le + HL) to ethyl oleate (EOL) weight ratio from 10% to 90% respectively (or vice versa). These surfactant–oil blends, without added

water, serve as self-microemulsifying delivery systems (SMEDS) candidates. The percentage of surfactant in the surfactant–oil mixture is referred to as the Surfactant Dilution Line (SDL); for instance, SDL = 60 corresponds to 60% surfactant and 40% oil (the D60 line for simplicity). The surfactant blend (lecithin + polyglyceryl-10 caprylate) was held at a 2:5 ratio, identified from prior phase scans.

To create dilution lines between 5% and 95% (w/w) aqueous phase, a 0.9% w/v NaCl solution was added to each surfactant–oil mixture in glass vials, followed by gentle hand shaking. The dilution behavior was observed within two hours and after two weeks of equilibration. Samples that remained as clear, single-phase solutions without birefringence under cross-polarized light were classified as microemulsions (μEs). These results were then mapped onto a pseudo-ternary phase diagram, with EOL at the right vertex, the surfactant blend at the top vertex, and the 0.9% w/v NaCl solution at the left vertex.

3.2.4. Preparation of Le–HL μEs (LLMs) and Yeast-Loaded LLMs Along SDL = 60

Ethyl oleate, lecithin, and PG10C were mixed at 40%, 17.1%, and 42.9% w/w, respectively, using a magnetic stirrer at 80 °C for 30 min to ensure complete solubilization of lecithin and PG10C in ethyl oleate and form the D60 SMEDS. The D60 SMEDS was then diluted with the 0.9% w/v NaCl solution to produce a final aqueous content from 0% to 100% by weight, producing the LLMs. The solutions were mixed until clear, homogeneous mixtures were obtained. Each μE was labeled according to its aqueous content (e.g., 0%, 5%, 10%, etc.). Dry yeast (*Saccharomyces cerevisiae*) was rehydrated in the corresponding saline solution fraction of the sample for 15 min at room temperature prior to use (no rehydration was used for 0% aqueous). The rehydrated yeast slurries were then added to each μE to a final dried yeast concentration of 8.0% (w/w). The yeast-loaded microemulsion mixtures were thoroughly mixed using a vortex mixer for 2 min to ensure uniform distribution. Each sample was allowed to stand for at least 24 h at room temperature before any measurement was taken.

3.2.5. Electrical Conductivity Studies

Conductivity measurements of single-phase μEs for SDL = 60 (D60) were obtained through a LabQuest 2 standalone interface (Vernier Science Education, Beaverton, OR, USA) equipped with a conductivity probe (CON-BTA, Vernier Science Education, USA). A control sample made of MiliQ water and increasing concentrations (0–100%) of saline solution (NaCl 0.9% w/v) was also measured. All dilution samples were measured in triplicates.

3.2.6. Viscosity

The viscosity of the single-phase lecithin-linker μEs (D60 LLMs) and yeast-loaded μEs (D60 LLM/Yeast), diluted with an aqueous phase containing 0.9% w/v NaCl, was measured along the D60 path using a Carri-Med CSL2 rheometer (TA Instruments, New Castle, DE, USA). A 2-degree cone geometry with a diameter of 4 cm and a gap of 60 μm was employed. Temperature control was maintained at 25 °C using a Peltier plate. The measurements were performed in flow mode, with shear rates varying from 0.1 to 100 s^{-1}.

3.2.7. *Saccharomyces cerevisiae* Dispersibility in Le-HL μEs

The dispersibility of the yeast within each microemulsion formulation was assessed visually. After the 24 h incubation period, the samples were inspected for signs of yeast settling or sedimentation. Samples were classified into three categories: "Fully Dispersed", "Partially Dispersed", or "Not Dispersed", based on the visual homogeneity of the mixture. Microscopy was conducted to evaluate the dispersibility of yeast within the LLMs. Small

aliquots from each sample were placed onto glass slides (VWR Inc., Mississauga, ON, Canada) and covered with micro cover glass (VWR Inc., Mississauga, ON, Canada). Images were captured using an Olympus BX51 optical microscope equipped with an Olympus U-CMAD3 camera adapter (Olympus Corporation, Tokyo, Japan) and an AmScope MD35 camera (AmScope Company, Irvine, CA, USA) at 20× magnification. Microscopic images were analyzed to assess the dispersion of yeast cells, the presence of clusters, and any structural patterns within the μEs. Images were categorized based on the uniformity of yeast distribution and the presence of any clustering behavior.

3.2.8. *Saccharomyces cerevisiae* Activity

The yeast activity test was adapted from Agee and Rowland [34] who developed the test as a demonstration lab for the activity of S. cerevisiae by keeping track of the volume of CO_2 produced using balloons that inflate with the CO_2 produced according to the well-known biochemical pathway for alcoholic fermentation involving yeast as a catalyst, which is expressed in Equation (10), where 1 mole of glucose turns into 2 moles of ethanol and 2 moles of carbon dioxide.

$$C_6H_{12}O_6 \overset{\text{yeast}}{\rightarrow} 2\,C_2H_5OH + 2\,CO_2 \tag{10}$$

Twenty-five grams of the LLM (including the SMEDS only, i.e., LLM with 0% aqueous) were added to 250 mL conical flasks. Dry yeast cells (2.0 g) were mixed with the LLMs. The following day, 75.0 g of a sucrose solution (25% w/v sucrose in 0.9% w/v NaCl) were added to the mixture. A helium-grade balloon was placed over the opening of the conical flask and sealed with Parafilm. The flask was gently shaken to ensure that the yeast was evenly distributed with no remaining lumps. After 24 h, the circumference of the balloon was measured and recorded to calculate the volume of CO_2 produced during fermentation. The CO_2 produced was taken as a measurement of cell metabolic activity.

3.2.9. *Saccharomyces cerevisiae* Viability

The methylene blue test consists of exposing 50 μL of the LLM yeast suspension with 50 μL of a solution of 0.1 wt% methylene blue in water and incubating this mixture for 5 min [35,36]. Live yeast cells contain reductases that turn methylene blue colorless, which is something that dead cells cannot accomplish. After the incubation time, samples of the resulting suspension were observed using the Olympus BX51 optical microscope in brightfield mode with a 20× objective. The live and dead cells were manually counted, making sure that the total number of cells per image was at least 30. The percentage of live cells was calculated as the number of live cells (unstained) divided by the total number of cells times 100%. For each yeast-LLM suspension, at least five pictures per sample were taken, and two samples were evaluated. The average percentage of live cells and the standard deviation (shown as error bars) were reported.

4. Conclusions

This study explored the viability and activity of dry instant yeast (*Saccharomyces cerevisiae*) dispersed in fully dilutable lecithin-linker microemulsions (LLMs) with water content ranging from 0% (a water-free system known as self-microemulsifying delivery system or SMEDS) to LLMs containing 95% aqueous phase, and in 100% saline (0.9% w/v NaCl). The SMEDS contained a surfactant mixture of lecithin (Le) and polyglycerol-10-caprylate (PG10C) as hydrophilic linker (HL) at a ratio Le/HL of 2/5, which was obtained after conducting μE phase scans using ethyl oleate (EOL) as the oil phase. The weight

ratio of the surfactant mixture to EOL in the SMEDS was fixed at 60/40 (also known as a D60 dilution line). This D60 dilution line was predicted using the HLD–NAC model with parameters derived from μE phase scans fitted using a modified version of a published HLD–NAC spreadsheet. The HLD–NAC model, combined with measurements of viscosity and electrical conductivity, showed that LLMs containing between 5% and 60% aqueous phase were bicontinuous in nature and that, for systems with less than 30% aqueous phase, the transport of ions and likely other water-soluble species was very limited.

LLMs with 10% aqueous phase produced the lowest yeast viability and activity, but LLMs with 30% aqueous phase produced the highest viability and activity. For the 10%, this minimum was interpreted as being caused by the yeast being partially active, generating metabolites, but that these metabolites concentrate in a water-confined environment, likely leading to metabolite-induced toxicity. At 30% aqueous, the LLM provides the nutrient benefits of the SMEDS, enough water to enable metabolite transport, but not too much water that would induce the release of PG10C (HL) into the aqueous phase. The studies showed that the presence of this HL in water had a detrimental effect on yeast activity, explaining the second minimum in yeast activity when the aqueous phase content reached 90%. When yeast was loaded in SMEDS, the cells were stable for a 10-week period that has not been reported before for yeast in microemulsions or regular emulsions. Having near-zero water activity allows the SMEDS to keep the cells dormant for an extended period. However, the gradual absorption of water, or the gradual diffusion of HL into the dormant cell membranes are possible causes for the gradual decrease in yeast activity in SMEDS.

The longer viability and activity observed in LLMs (>1 week) and SMEDS (~10 weeks), compared to previous studies (3 days) suggests that this approach could reopen the doors to using microemulsions as solvent media in various biotransformation processes.

Author Contributions: J.D.M.: Conceptualization, Software, Methodology, Validation, Formal analysis, Investigation, Data Curation, Writing Original Draft, Writing—review and Editing, Visualization. J.D.: Conceptualization, Software, Methodology, Validation, Formal analysis, Investigation, Data Curation. M.A.A.: Methodology, Validation, Investigation, Data Curation. E.A.: Conceptualization, Software, Methodology, Formal analysis, Data Curation, Writing-review and Editing, Visualization, Supervision, Funding acquisition. All authors have read and agreed to the published version of the manuscript.

Funding: This research was funded by Natural Sciences and Engineering Research Council of Canada (NSERC), Discovery Grant Program.

Institutional Review Board Statement: Not applicable.

Informed Consent Statement: Not applicable. No human or animal subjects were used in this research.

Data Availability Statement: The data presented in this study are available on request from the corresponding author.

Conflicts of Interest: The authors declare that they have no conflicts of interest.

References

1. Pfammatter, N.; Guadalupe, A.A.; Luisi, P.L. Solubilization and Activity of Yeast Cells in Water-in-Oil Microemulsion. *Biochem. Biophys. Res. Commun.* **1989**, *161*, 1244–1251. [CrossRef] [PubMed]
2. Hoppert, M.; Mlejnek, K.; Seiffert, B.; Mayer, F. Activities of Microorganisms and Enzymes in Water-Restricted Environments: Biological Activities in Aqueous Compartments at Mm-Scale. In *Proceedings of the SPIE—The International Society for Optical Engineering*; SPIE: Bellingham, WA, USA, 1997; Volume 3111, pp. 501–509. [CrossRef]

3. Pfammatter, N.; Hochköppler, A.; Luisi, P.L. Solubilization and Growth of Candida Pseudotropicalis in Water-in-oil Microemulsions. *Biotechnol. Bioeng.* **1992**, *40*, 167–172. [CrossRef] [PubMed]
4. Prichanont, S.; Leak, D.J.; Stuckey, D.C. The Solubilisation of Mycobacterium in a Water in Oil Microemulsion for Biotransformations: System Selection and Characterisation. *Colloids Surf. A Physicochem. Eng. Asp.* **2000**, *166*, 177–186. [CrossRef]
5. Prichanont, S.; Leak, D.J.; Stuckey, D.C. Chiral Epoxide Production Using Mycobacterium Solubilized in a Water-in-Oil Microemulsion. *Enzym. Microb. Technol.* **2000**, *27*, 134–142. [CrossRef] [PubMed]
6. Stefan, A.; Palazzo, G.; Ceglie, A.; Panzavolta, E.; Hochkoeppler, A. Water-in-Oil Macroemulsions Sustain Long-Term Viability of Microbial Cells in Organic Solvents. *Biotechnol. Bioeng.* **2003**, *81*, 323–328. [CrossRef] [PubMed]
7. Zhang, H.; Xu, Y.; Wu, L.; Zheng, X.; Zhu, S.; Feng, F.; Shen, L. Anti-Yeast Activity of a Food-Grade Dilution-Stable Microemulsion. *Appl. Microbiol. Biotechnol.* **2010**, *87*, 1101–1108. [CrossRef] [PubMed]
8. Acosta, E.J.; Nguyen, T.; Witthayapanyanon, A.; Harwell, J.H.; Sabatini, D.A. Linker-Based Bio-Compatible Microemulsions. *Environ. Sci. Technol.* **2005**, *39*, 1275–1282. [CrossRef]
9. Nouraei, M.; Collymore, C.; Diosady, L.; Acosta, E. HLD-NAC Design and Evaluation of a Fully Dilutable Lecithin-Linker SMEDDS for Ibuprofen. *Int. J. Pharm.* **2021**, *610*, 121237. [CrossRef] [PubMed]
10. Sabatini, D.A.; Acosta, E.; Harwell, J.H. Linker Molecules in Surfactant Mixtures. *Curr. Opin. Colloid Interface Sci.* **2003**, *8*, 316–326. [CrossRef]
11. Yuan, J.S.; Ansari, M.; Samaan, M.; Acosta, E.J. Linker-Based Lecithin Microemulsions for Transdermal Delivery of Lidocaine. *Int. J. Pharm.* **2008**, *349*, 130–143. [CrossRef] [PubMed]
12. Zarate-Muñoz, S.; Texeira De Vasconcelos, F.; Myint-Myat, K.; Minchom, J.; Acosta, E.J. A Simplified Methodology to Measure the Characteristic Curvature (Cc) of Alkyl Ethoxylate Nonionic Surfactants. *J. Surfactants Deterg.* **2016**, *19*, 249–263. [CrossRef]
13. Nouraei, M.; Acosta, E.J. Predicting Solubilisation Features of Ternary Phase Diagrams of Fully Dilutable Lecithin Linker Microemulsions. *J. Colloid Interface Sci.* **2017**, *495*, 178–190. [CrossRef] [PubMed]
14. Acosta, E.J.; Sundar, S. How to Formulate Biobased Surfactants Through the HLD-NAC Model. In *Biobased Surfactants*; Hayes, D., Solaiman, D., Ashby, R., Eds.; AOCS Press: London, UK, 2019; pp. 471–510. [CrossRef]
15. Sundar, S.; Nouraei, M.; Latta, T.; Acosta, E. Hydrophilic-Lipophilic-Difference (HLD) Guided Formulation of Oil Spill Dispersants with Biobased Surfactants. *Tenside Surfactants Deterg.* **2019**, *56*, 417–428. [CrossRef]
16. Acosta, E.J. *Formulation Engineering with the Hydrophilic-Lipophilic-Difference (HLD) and Net-Average Curvature (NAC) HLD-NAC: Tutorial*; ResearchGate Methods: Toronto, ON, Canada, 2023; p. 12. [CrossRef]
17. Ontiveros, J.F.; Pierlot, C.; Catté, M.; Molinier, V.; Pizzino, A.; Salager, J.L.; Aubry, J.M. Classification of Ester Oils According to Their Equivalent Alkane Carbon Number (EACN) and Asymmetry of Fish Diagrams of C10E4/Ester Oil/Water Systems. *J. Colloid Interface Sci.* **2013**, *403*, 67–76. [CrossRef]
18. Acosta, E.; Natali, S. Effect of Surfactant Concentration on the Hydrophobicity of Polydisperse Alkyl Ethoxylates. *J. Surfactants Deterg.* **2022**, *25*, 79–94. [CrossRef]
19. Han, J.; Lee, M.J.; Lee, K.; Lee, Y.J.; Kwon, S.H.; Min, J.H.; Lee, E.; Lee, W.; Lee, S.W.; Kim, B.J. Role of Bicontinuous Structure in Elastomeric Electrolytes for High-Energy Solid-State Lithium-Metal Batteries. *Adv. Mater.* **2023**, *35*, e2205194. [CrossRef]
20. Mackie, T.S.; Meares, P. The Diffusion of Electrolytes in a Cation-Exchange Resin Membrane. I. Theoretical. *Proc. R. Soc. Lond. Ser. A* **1955**, *232*, 498–509. [CrossRef]
21. Kiran, S.K.; Acosta, E.J. Predicting the Morphology and Viscosity of Microemulsions Using the HLD-NAC Model. *Ind. Eng. Chem. Res.* **2010**, *49*, 3424–3432. [CrossRef]
22. Krishnan, K.; Chapman, B.; Bates, F.S.; Lodge, T.P.; Almdal, K.; Burghardt, W.R. Effects of Shear Flow on a Polymeric Bicontinuous Microemulsion: Equilibrium and Steady State Behavior. *J. Rheol.* **2002**, *46*, 529–554. [CrossRef]
23. Beuchat, L.R. Influence of Water Activity on Growth, Metabolic Activities and Survival of Yeasts and Molds. *J. Food Prot.* **1983**, *46*, 135–141. [CrossRef]
24. Galvin, K.; McDonald, J.A.; Robinson, B.H.; Knoche, W. Determination of Water Activity in Water-in-Oil Microemulsions. *Colloids Surf.* **1987**, *25*, 195–204. [CrossRef]
25. Cavanagh, R.J.; Smith, P.A.; Stolnik, S. Exposure to a Nonionic Surfactant Induces a Response Akin to Heat-Shock Apoptosis in Intestinal Epithelial Cells: Implications for Excipients Safety. *Mol. Pharm.* **2019**, *16*, 618–631. [CrossRef] [PubMed]
26. Partearroyo, M.A.; Ostolaza, H.; Goñi, F.M.; Barberá-Guillem, E. Surfactant-Induced Cell Toxicity and Cell Lysis. A Study Using B16 Melanoma Cells. *Biochem. Pharmacol.* **1990**, *40*, 1323–1328. [CrossRef] [PubMed]
27. Yang, H.; Huang, L.; Zhao, D.; Zhao, H.; Chen, Y.; Li, Y.; Zeng, Y. Protective Effect of Wheat Gluten Peptides against Ethanol-Stress Damage in Yeast Cell and Identification of Anti-Ethanol Peptides. *LWT* **2024**, *192*, 115732. [CrossRef]
28. Estela-Escalante, W.D.; Moscosa-Santillán, M.; González-Ramírez, J.E.; Rosales-Mendoza, S. Evaluation of the Potential Production of Ethanol by Candida Zemplinina Yeast with Regard to Beer Fermentation. *J. Am. Soc. Brew. Chem.* **2017**, *75*, 130–135. [CrossRef]

29. Munder, M.C.; Midtvedt, D.; Franzmann, T.; Nüske, E.; Otto, O.; Herbig, M.; Ulbricht, E.; Müller, P.; Taubenberger, A.; Maharana, S.; et al. A PH-Driven Transition of the Cytoplasm from a Fluid- to a Solid-like State Promotes Entry into Dormancy. *eLife* **2016**, *5*, e09347. [CrossRef]
30. Aukema, K.G.; Wang, M.; de Souza, B.; O'Keane, S.; Clipsham, M.; Wackett, L.P.; Aksan, A. Core-Shell Encapsulation Formulations to Stabilize Desiccated Bradyrhizobium against High Environmental Temperature and Humidity. *Microb. Biotechnol.* **2022**, *15*, 2391–2400. [CrossRef] [PubMed]
31. Kuliešienė, N.; Žūkienė, R.; Khroustalyova, G.; Chang, C.-R.; Rapoport, A.; Daugelavičius, R. Changes in Energy Status of Saccharomyces Cerevisiae Cells during Dehydration and Rehydration. *Microorganisms* **2021**, *9*, 444. [CrossRef]
32. Thomas, C.R.; Stenson, J.D.; Zhang, Z. Measuring the Mechanical Properties of Single Microbial Cells. In *High Resolution Microbial Single Cell Analytics*; Springer: Berlin/Heidelberg, Germany, 2011; Volume 124. [CrossRef]
33. Han, T.; Zhang, S.; Zhang, C. Unlocking the Secrets behind Liquid Superlubricity: A State-of-the-Art Review on Phenomena and Mechanisms. *Friction* **2022**, *10*, 1137–1165. [CrossRef]
34. Agee, S.; Rowland, T. Single-Celled Science: Yeasty Beasties. Science Buddies. Available online: www.sciencebuddies.org/science-fair-projects/project-ideas/MicroBio_p011/microbiology/yeast-activity-balloons (accessed on 24 November 2024).
35. Painting, K.; Kirsop, B. A Quick Method for Estimating the Percentage of Viable Cells in a Yeast Population, Using Methylene Blue Staining. *World J. Microbiol. Biotechnol.* **1990**, *6*, 346–347. [CrossRef]
36. Parker, R.A.; Gabriel, K.T.; Graham, K.; Cornelison, C.T. Validation of Methylene Blue Viability Staining with the Emerging Pathogen Candida Auris. *J. Microbiol. Methods* **2020**, *169*, 105829. [CrossRef]

Disclaimer/Publisher's Note: The statements, opinions and data contained in all publications are solely those of the individual author(s) and contributor(s) and not of MDPI and/or the editor(s). MDPI and/or the editor(s) disclaim responsibility for any injury to people or property resulting from any ideas, methods, instructions or products referred to in the content.

molecules

MDPI

Article

Charge Regulation in Liquid Films Stabilized by Ionic Surfactants: Change in Adsorption with Film Thickness and Phase Transitions

Iglika M. Dimitrova [1,2] and Radomir I. Slavchov [3,*]

[1] Department of Physical Chemistry, University of Chemical Technology and Metallurgy, Kliment Ohridski Blvd. 8, 1756 Sofia, Bulgaria; imd@uctm.edu
[2] Rostislaw Kaischew Institute of Physical Chemistry, Bulgarian Academy of Sciences, Acad. G. Bonchev Str., Bl. 11, 1113 Sofia, Bulgaria
[3] School of Engineering and Materials Science, Queen Mary University of London, Mile End Road, London E1 4NS, UK
* Correspondence: r.slavchov@qmul.ac.uk

Abstract: When a liquid film is thinning, the charge and the potential of its surfaces change simultaneously due to the interaction between the two surfaces. This phenomenon is an example for charge regulation and has been known for half a century for systems featuring aqueous solutions in contact with metals, salts, biological surfaces covered by protolytes, etc. Few studies, however, investigated regulation in foam and emulsion films, where the charge is carried by soluble ionic surfactants. This work presents an analysis of the phenomenon for surfactants that follow the classical Davies adsorption isotherm. The electrostatic disjoining pressure Π_{el} was analyzed, and the Davies isotherm was shown to lead to $\Pi_{\mathrm{el}} \propto h^{-1/2}$ behavior at a small film thickness h. As usual, the charge regulation regime (constant chemical potential of the surfactant) corresponded to a dependence of Π_{el} on h between those for constant charge and constant electric potential regimes. The role of the background electrolyte was also studied. At the water–air interface, many ionic surfactants exhibit a surface phase transition. We show that the interaction between the two surfaces of a foam film can trigger the phase transition (i.e., the film changes its charge abruptly), and two films of different h values can coexist in equilibrium with each other—one covered by surfactant in the 2D gaseous state and another in the 2D liquid state.

Keywords: charge regulation; foam; emulsion; surface forces; adsorption; ionic surfactants; surface phase transition

1. Introduction

All characteristics of an interface (adsorption, interfacial tension, surface potential, etc.) depend on the geometry of the heterogeneous system [1]. This dependence cannot be neglected whenever the characteristic size of the heterogeneity (the radius of curvature R, the thin film thickness h, etc.) is small compared with the characteristic thickness of the surface layer—which, for charged surfaces, is the Debye length L_{D}. Therefore, an ionic surfactant does not adsorb to the same extent on a flat surface, on nanometer-sized droplets or on extremely thin foam films. In the context of surface forces, the effect of the confinement on the state of the surface is known as *charge regulation*. As opposed to the assumptions for a constant surface charge or surface potential [2], in a thin film, both the charge and potential change with h, and the films drain under a constant chemical potential.

The chemical potential of an adsorbed species is fixed to its bulk chemical potential, and this equality sets the adsorption isotherm (the *charge regulation condition*). The charge regulation condition is system-specific. For example, Bierman used the Langmuir isotherm [3] for the ion in the adsorption layer to provide the charge regulation condition. Later, several groups assumed that only the ions in the Stern layer are charge-regulated (while the surface itself is of a fixed charge), and they used the Stern [4–8] or Stern–Grahame model [9,10] for the description of the constant chemical potential regime. Variants of these theories were used for a range of surfaces. For example, Popa et al. [11] used the approach from [7] for oppositely charged latex particles, and Carnie and Chan [12] investigated solid surfaces covered with dissociable groups using the mass action law (which resulted in a Langmuir-type isotherm). Charge regulation is not limited to films; it plays its role in confined systems of other geometries, such as nanochannels [13], ion channels [14], nano-particles [15] and macro-ions [16].

Experimental investigations focusing on charge regulation have been performed for solid-liquid-solid surface forces using the surface forces apparatus [17] and the colloidal probe technique [18,19]. For foam films, the disjoining pressure Π is accessible via modifications to the Sheludko cell [20]. Emulsion films can also be investigated [21,22]. However, no dedicated study on charge regulation in fluid films is known to us.

This work sets the fundamental theory for charge regulation in foam and emulsion films stabilized by soluble ionic surfactants, and it is a necessary first step before a subsequent experimental study on the phenomenon. We study two cases. The first one is simpler, involving an oil–water–oil emulsion film stabilized by a water-soluble ionic surfactant which follows the Davies adsorption isotherm without phase transition, suitable for water–oil (W | O) interfaces. The Van der Waals attraction is negligible for emulsion films. The second case is a foam film, where the two monolayers of the ionic surfactant exhibit a surface phase transition, which is typical for water–gas (W | G) interfaces. The two surface phases follow two different Davies isotherms. For foam films, the Van der Waals attraction is significant.

2. Results and Discussion

2.1. The Poisson–Boltzmann Equation

The electrostatic potential in the film is assumed to be the solution to the Poisson–Boltzmann equation:

$$\varepsilon \mathrm{d}^2\phi/\mathrm{d}z^2 = -\rho, \tag{1}$$

where the bulk charge density ρ follows the Boltzmann distribution:

$$\rho = eC_{\mathrm{el}}\left(\Phi - \Phi^{-1}\right); \tag{2}$$

here, $\Phi = \exp(-e\phi/kT)$ is the Boltzmann factor for a cation; e is the charge of the ions, ϕ is the electrostatic potential, z is the distance from the center of the film (a symmetric film is considered; see Figure 1), ε is the absolute dielectric permittivity of the film, and C_{el} is the concentration of the electrolytes in m^{-3}. We consider only symmetric 1:1 electrolytes. The film is aqueous, and the hydrophobic phase is insulating. Let the surfactant be anionic (e.g., sodium decyl sulfate, NaDS), of a concentration $C_{\mathrm{s}} = C_{\mathrm{DS}^-}$, where $\Phi > 1$ (i.e., the surface potential is negative). Let the background electrolyte be sodium chloride with a concentration C_{NaCl}. In this case, it is valid that

$$C_{\mathrm{el}} = C_{\mathrm{s}} + C_{\mathrm{NaCl}} = C_{\mathrm{DS}^-} + C_{\mathrm{Cl}^-} = C_{\mathrm{Na}^+} \tag{3}$$

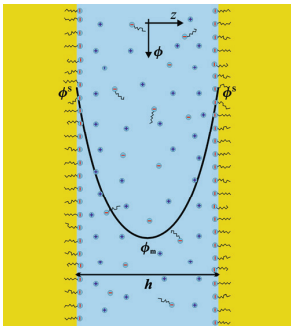

Figure 1. Illustration of thin oil–water–oil liquid film stabilized with ionic surfactant with the potential profile.

The Poisson–Boltzmann equation has serious limitations. For example it does not account for the ever-present ion-specific interactions and image forces [23], and the surface normal dipole moment (conjugated with the quadrupolarizabilities of the two phases) [24]. However, it is sufficient for a first analysis; besides, the Davies isotherm we use for the surfactant [25] is based on the same equation anyway.

Using the relation $\mathrm{d}^2\phi/\mathrm{d}z^2 = \frac{1}{2}\,\mathrm{d}E^2/\mathrm{d}\phi$, we obtain a first integral of the Poisson–Boltzmann in Equations (1) and (2):

$$\frac{\varepsilon}{2}E^2 = -\int_{\phi_\mathrm{m}}^{\phi} \rho \mathrm{d}\phi = kTC_\mathrm{el}\frac{(\Phi-\Phi_\mathrm{m})\left(\Phi-\Phi_\mathrm{m}^{-1}\right)}{\Phi}, \tag{4}$$

where $\Phi_\mathrm{m} = \exp(-e\phi_\mathrm{m}/kT)$ and ϕ_m is the extremum of the potential (where $E = 0$—see Figure 1). The square root of Equation (4) yields:

$$\frac{\mathrm{d}\phi}{\mathrm{d}z} = \pm\sqrt{\frac{2kTC_\mathrm{el}}{\varepsilon}\frac{(\Phi-\Phi_\mathrm{m})\left(\Phi-\Phi_\mathrm{m}^{-1}\right)}{\Phi}}. \tag{5}$$

For negatively charged surfaces, ϕ is maximal in the center of the film. Therefore, for $z < 0$, the positive sign should be taken, and vice versa. Separation of variables and integration leads to:

$$z = L_\mathrm{D}\int_{\Phi_\mathrm{m}}^{\Phi}\frac{\mathrm{d}\Phi}{\sqrt{\Phi(\Phi-\Phi_\mathrm{m})\left(\Phi-\Phi_\mathrm{m}^{-1}\right)}} = \frac{4L_\mathrm{D}}{\sqrt{\Phi_\mathrm{m}}}\mathrm{F}\left(\sqrt{\frac{\Phi-\Phi_\mathrm{m}}{\Phi-\Phi_\mathrm{m}^{-1}}}, \Phi_\mathrm{m}^{-1}\right). \tag{6}$$

Here, L_D is the Debye length ($L_\mathrm{D}^2 = \varepsilon kT/2e^2C_\mathrm{el}$), and F is the elliptic F integral. Integration from the center of the film ($z = 0$, $\phi = \phi_\mathrm{m}$) to one of the surfaces ($z = h/2$, $\phi = \phi^\mathrm{S}$) leads to a relation between the film thickness h and surface potential ϕ^S:

$$h = 2L_\mathrm{D}\int_{\Phi_\mathrm{m}}^{\Phi^\mathrm{S}}\frac{\mathrm{d}\Phi}{\sqrt{\Phi(\Phi-\Phi_\mathrm{m})\left(\Phi-\Phi_\mathrm{m}^{-1}\right)}} = \frac{4L_\mathrm{D}}{\sqrt{\Phi_\mathrm{m}}}\mathrm{F}\left(\sqrt{\frac{\Phi^\mathrm{S}-\Phi_\mathrm{m}}{\Phi^\mathrm{S}-\Phi_\mathrm{m}^{-1}}}, \Phi_\mathrm{m}^{-1}\right), \tag{7}$$

where $\Phi^\mathrm{S} = \exp(-e\phi^\mathrm{S}/kT)$ is the surface Boltzmann factor. This equation can be solved for Φ^S:

$$\Phi^\mathrm{S} = \Phi_\mathrm{m}^{-1} + \frac{\Phi_\mathrm{m}-\Phi_\mathrm{m}^{-1}}{\mathrm{cn}^2\left(\frac{h\sqrt{\Phi_\mathrm{m}}}{4L_\mathrm{D}}, \Phi_\mathrm{m}^{-1}\right)}, \tag{8}$$

where cn is the Jacobi cn function.

The Gauss condition relates the displacement field at the surface to the surface charge density ρ^S:

$$\varepsilon \, d\phi/dz|_{z=h/2} = \rho^S. \tag{9}$$

If the surface active species is an anion, then ρ^S is related to the adsorption Γ in the adsorption layer by the equation:

$$\rho^S = -e\Gamma. \tag{10}$$

By substituting this and the Gauss Equation (9) into the first integral, Equation (4), one obtains the *generalized Gouy equation* which accounts for the confinement:

$$\frac{L_B \Gamma^2}{2C_{el}} = \frac{\left(\Phi^S - \Phi_m\right)\left(\Phi^S - \Phi_m^{-1}\right)}{\Phi^S}; \tag{11}$$

here, $L_B = e^2/\varepsilon kT$ is the Bjerrum length (without the usual factor 4π for more concise formulae). For a very thick film ($h >> L_D$), it holds true that $\phi_m = 0$ and $\Phi_m = 1$ so that:

$$\frac{L_B \Gamma^2}{2C_{el}} = \Phi^S + \left(\Phi^S\right)^{-1} - 2, \tag{12}$$

which is Gouy's equation [26].

The dependence of the potential ϕ on z at a certain value of Φ_m is determined by Equation (6), and Φ_m itself follows from the values of Γ and Φ^S through Gouy's generalized Equation (11). The values of Γ and Φ^S are determined by the boundary condition—Equation (7), and an adsorption isotherm, which we will consider next. The dependence of ϕ on z can already be illustrated for a chosen value of Φ_m. A schematic example is given in Figure 1.

2.2. The Adsorption Isotherm

The condition for chemical equilibrium between the dissolved surfactant and the charged adsorption layer reads [3,27]:

$$\gamma^S \Gamma = K_a C_s / \Phi^S, \tag{13}$$

where K_a [m] is the adsorption constant, C_s is the concentration of surfactant, and γ^S is the surface activity coefficient, taking into account the lateral interactions between the adsorbed surface active ions. If $|e\phi^S/kT| \sim |\ln K_a C_s| >> |\ln \gamma^S \Gamma|$, then the condition predicts constant surface potential. If $|e\phi^S/kT| << |\ln K_a C_s| \sim |\ln \gamma^S \Gamma|$, then the surface charge is constant (true for densely packed monolayers in the presence of excess electrolytes). Otherwise, Equation (13) is a charge regulation condition.

The case of $\gamma^S = 1$ corresponds to "Henry's" equation of the ionic surfactant:

$$\Gamma = K_a C_s / \Phi^S. \tag{14}$$

Strictly speaking, Equation (14) is not Henry's isotherm as it accounts for the main interaction in the charged monolayer, charge-charge, through Φ^S (i.e., it is at the nonlinear Debye–Hückel level of description). Davies [25,28] combined Equation (14) with Gouy's Equation (12) under the assumption that Φ^S is an extremely large quantity (which is almost always fulfilled for a monolayer of an ionic surfactant):

$$L_B \Gamma^2 / 2C_{el} = \Phi^S. \tag{15}$$

By multiplying Equations (14) and (15) and solving them, we obtain for Γ the Davies isotherm on a single surface:

$$\Gamma_\infty = \left(\frac{2K_\mathrm{a}}{L_\mathrm{B}}\right)^{1/3} (C_\mathrm{s}C_\mathrm{el})^{1/3}. \tag{16}$$

Here, ∞ indicates that this adsorption is on an isolated surface (very thick film, $h \to \infty$). By substituting this expression back into Equation (15), we obtain the Davies equation for the surface potential (surface Boltzmann factor) of a single surface:

$$\Phi^\mathrm{S}_\infty = \frac{L_\mathrm{B}^{1/3} K_\mathrm{a}^{2/3}}{2^{1/3}} \frac{C_\mathrm{s}^{2/3}}{C_\mathrm{el}^{1/3}}. \tag{17}$$

Equations (16) and (17) work rather well for surfactants at W | O interfaces [29] in cases where the surface coverage is not too high (such that γ^S remains close to one).

Water | gas: isotherms with phase transition. In this case, a monolayer of an ionic surfactant typically exhibits two surface phases—2D gaseous and 2D liquid (known as *liquid expanded*)—with a phase transition taking place under specific conditions (concentration C_pt, adsorption Γ_pt etc.). For many ionic surfactants, both phases follow the Davies isotherm but with a different adsorption constant [29]:

$$\Gamma^\mathrm{G} = K_\mathrm{a}^\mathrm{G} C_\mathrm{s}/\Phi^\mathrm{S} \text{ and } \Gamma^\mathrm{LE} = K_\mathrm{a}^\mathrm{LE} C_\mathrm{s}/\Phi^\mathrm{S}. \tag{18}$$

It is always true that K_a^LE (the adsorption constant of the liquid expanded phase) is larger than K_a^G (the true Henry's constant); otherwise, only the gaseous phase is stable. For an isolated surface, the two equations in Equation (18) result in two Davies-like equations for Γ and Φ^S in the two phases, analogous to Equations (16) and (17) but with two different adsorption constants.

2.3. Disjoining Pressure

The local force balance in the film reads:

$$\nabla p = -\rho \nabla \phi, \tag{19}$$

where p is the isotropic mechanical pressure. This is integrated using Equation (2):

$$p = p_0 + kTC_\mathrm{el}\left(\Phi + \Phi^{-1} - 2\right), \tag{20}$$

where we treat p as a function of ϕ, and, therefore, p_0 is the pressure which corresponds to zero potential ϕ (i.e., pressure in the meniscus or in a thick film). The respective pressure tensor $\boldsymbol{P}$ (including the Maxwell tensor) is given by [30]:

$$\boldsymbol{P} = p\mathbf{U} - \varepsilon E^2 \mathbf{e}_z\mathbf{e}_z + \frac{\varepsilon}{2} E^2 \mathbf{U}. \tag{21}$$

Here, $\mathbf{U}$ is the unit tensor, and $\mathbf{e}_z$ is the unit vector in the z direction (normal to the film). This expression is approximate. For a draining film, the pressure tensor includes hydrodynamic terms [31]. When the surface carries a large dipole moment, and one of the phases is oil, the quadrupole terms of the Maxwell tensor also become important [32]. By substituting p from Equation (20) and E^2 from Equation (4) in the expression for the pressure tensor, we obtain the following result for the normal component of $\boldsymbol{P}$:

$$P_{zz} = p - \varepsilon E^2/2 = p_0 + \Pi_{\mathrm{el}}, \tag{22}$$

where Π_{el} is, by definition [2], the electrostatic disjoining pressure in the film:

$$\Pi_{\mathrm{el}} = kTC_{\mathrm{el}}\left(\Phi_{\mathrm{m}} + \Phi_{\mathrm{m}}^{-1} - 2\right). \tag{23}$$

This result was first obtained by Langmuir [33], who treated the right-hand side of this equation as the change in osmotic pressure in the center of the film, $kTC_{\mathrm{el}}(\Phi_{\mathrm{m}} + 1/\Phi_{\mathrm{m}})$, in comparison to the one in the meniscus, $2kTC_{\mathrm{el}}$.

Under the constant potential regime, the surface potential is the same as that for a single isolated surface (subscript ∞), and thus $\Phi^{\mathrm{S}} = \Phi^{\mathrm{S}}_{\infty}$. In this case, Equations (7) and (23) define Π_{el} and Φ_{m}, respectively, as functions of h (parametrically with parameter Φ_{m}).

Under the constant charge regime, it is the surfactant adsorption which is constant ($\Gamma = \Gamma_{\infty}$), while the surface potential changes with h. In this case, Equations (7) and (23) and the generalized Gouy Equation (11) (where Γ is treated as a constant) determine Π_{el}, Φ^{S}, and Φ_{m} as functions of h.

In general, a fourth equation is required to determine Π_{el}, Φ^{S}, Γ, and Φ_{m}, and this is the charge regulation condition. For this, we use the Davies isotherm for W | O, Equation (14), or two Davies isotherms with a phase transition for W | G, Equation (18).

For W | O (i.e., emulsion film), the electrostatic component given by Equation (23) dominates the disjoining pressure (the Hamaker constant for oil–water–oil is small [17]). For W | A (foam film), we must also add the Van der Waals interaction [2]:

$$\Pi = kTC_{\mathrm{el}}\left(\Phi_{\mathrm{m}} + \Phi_{\mathrm{m}}^{-1} - 2\right) - \frac{A_{\mathrm{H}}}{6\pi}\frac{1}{h^3}. \tag{24}$$

Here, A_{H} is the Hamaker constant for water.

Let us also write down the respective formulae for the membrane tension of the film. This is given by the sum of the surface tensions σ^{AL} of the adsorbed layers, the contributions from the electric double layer ($\sigma_{\mathrm{m}}^{\mathrm{DL}}$), and the Van der Waals interaction ($\sigma_{\mathrm{m}}^{\mathrm{VdW}}$):

$$\sigma_{\mathrm{m}} = 2\sigma^{\mathrm{AL}} + \sigma_{\mathrm{m}}^{\mathrm{DL}} + \sigma_{\mathrm{m}}^{\mathrm{VdW}}. \tag{25}$$

These components are calculated as follows. For σ^{AL}, Henry's equation holds true:

$$\sigma^{\mathrm{AL}} = \sigma_0 - kT\Gamma. \tag{26}$$

Here, σ_0 is the interfacial tension of the surfactant-free interface, and Equation (26) is a form of the Davies isotherm [25]. The contribution of the electric double layer follows from the Maxwell tensor and the definition of membrane tension [2]:

$$\sigma_{\mathrm{m}}^{\mathrm{DL}} = 2\int_0^{h/2} (P_{xx} - P_{zz})\mathrm{d}z. \tag{27}$$

Finally, for the Van der Waals contribution in foam films, we use the expression [17]:

$$\sigma_{\mathrm{m}}^{\mathrm{VdW}} = -\frac{A_{\mathrm{H}}}{12\pi}\frac{1}{h^2}. \tag{28}$$

Equation (28) gives the free energy of the Van der Waals interaction between the two films.

For the liquid expanded state of the monolayer, Equation (26) must be modified to account for Langmuir's liquid expanded oil-like film of hydrocarbon chains:

$$\sigma^{\mathrm{AL}} = \sigma_0^{\mathrm{LE}} - kT\Gamma = \sigma_0 + \pi_{\mathrm{coh}} - kT\Gamma, \tag{29}$$

where π_{coh} is Langmuir's cohesive pressure, a characteristic of the lateral interaction between the hydrocarbon tails in the liquid expanded film [29,34].

2.4. Charge Regulation According to the Davies Isotherm Versus Constant Charge or Potential

Constant potential. In this case, we assume that Φ^{S} is independent of h; it instead remains constant equal to $\Phi^{\mathrm{S}}_{\infty}$, as for an isolated surface. The dependence of Φ_{m} on h is determined by Equation (7) (with $\Phi^{\mathrm{S}} = \Phi^{\mathrm{S}}_{\infty}$). The dependence of Π_{el} on h is determined parametrically by Equations (7) and (23), with the parameter Φ_{m} varying from 1 at $h = \infty$ to $\Phi^{\mathrm{S}}_{\infty}$ at $h = 0$. When the potential is fixed, the adsorption of the surfactant changes with the film thickness. This $\Gamma(h)$ dependence is determined parametrically by Equation (7) and Gouy's Equation (11).

Such conditions are possible for electrode surfaces, where the potential is maintained by a potentiostat. However, for foam and emulsion films, once the film thickness h approaches the Debye length, the surface potential always changes significantly.

For the sake of comparison with the other regimes, let us give the asymptotes of the main characteristics for thick and thin films. The analysis which follows is equivalent to that of Honig and Mul [35]. We additionally assume that the surface potential is high ($\Phi^{\mathrm{S}} >> 1$) to fulfil the validity of the Davies isotherm.

For a thick film ($h >> L_{\mathrm{D}}$), the potential in the center of the film is close to zero, and $\Phi_{\mathrm{m}} \to 1$. Here, the following well-known asymptote [2,33] holds true:

$$\Pi_{\mathrm{el}} \xrightarrow{h\to\infty} 64kTC_{\mathrm{el}}\gamma^2 \mathrm{e}^{-h/L_{\mathrm{D}}}, \tag{30}$$

where $\gamma = \tanh(-e\phi^{\mathrm{S}}/4kT)$.

At high potentials, $\gamma = 1$, and thus the disjoining pressure is independent of the surface potential.

In the other limiting case of an extremely thin film ($h << L_{\mathrm{D}}$), the electrostatic potential across the film is approximately constant, and one can use $\Phi^{\mathrm{S}} \to \Phi_{\mathrm{m}}$, which simplifies Equation (7) to:

$$h \xrightarrow{\Phi^{\mathrm{S}}\to\Phi_{\mathrm{m}}} \frac{4L_{\mathrm{D}}\sqrt{\Phi^{\mathrm{S}} - \Phi_{\mathrm{m}}}}{\sqrt{\Phi_{\mathrm{m}}^2 - 1}}. \tag{31}$$

This asymptote can be inverted to the following parabolic dependence:

$$\Phi_{\mathrm{m}} = \Phi^{\mathrm{S}} - \frac{h^2}{16L_{\mathrm{D}}^2}\left(\Phi^{\mathrm{S}}\right)^2. \tag{32}$$

Then, the respective disjoining pressure asymptote follows from Equation (23):

$$\Pi_{\mathrm{el}} \xrightarrow[\Phi^{\mathrm{S}}=const]{h\to 0} kTC_{\mathrm{el}}\left[\Phi^{\mathrm{S}} - \frac{h^2}{16L_{\mathrm{D}}^2}\left(\Phi^{\mathrm{S}}\right)^2\right], \tag{33}$$

where $\Phi^{\mathrm{S}} >> 1$ was again assumed. A comparison between the two asymptotes, Equations (30) and (33), and the exact parametric dependence of Π_{el} on h is illustrated in Figure 2.

Constant charge. The results again coincide with those of Honig and Mul [35] at $\Phi^{\mathrm{S}} >> 1$. In this case, we assume that the adsorption remains independent of the film

thickness (i.e., Γ is equal to Γ_∞) of the isolated surface. The surface potential, on the other hand, changes with h. From Gouy's Equation (11), it follows that a constant charge corresponds to:

$$\Phi^{\mathrm{S}} + \left(\Phi^{\mathrm{S}}\right)^{-1} - \Phi_{\mathrm{m}} - (\Phi_{\mathrm{m}})^{-1} = \Phi^{\mathrm{S}}_{\infty} + \left(\Phi^{\mathrm{S}}_{\infty}\right)^{-1} - 2, \tag{34}$$

where $\Phi^{\mathrm{S}}_{\infty}$ refers to the isolated surface. By solving Equation (34) for Φ^{S} and substituting the solution in Equation (7) for h, we obtain h as a function of Φ_{m} for the constant Γ. We then obtain $\Pi_{\mathrm{el}}(h)$ parametrically from $h(\Phi_{\mathrm{m}})$ and $\Pi_{\mathrm{el}}(\Phi_{\mathrm{m}})$ via Equation (23).

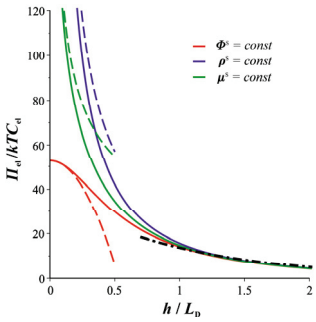

Figure 2. Comparison between the electrostatic component Π_{el} of the disjoining pressure as a function of the film thickness h (solid curves) for the three studied regimes: constant surface potential, charge, or chemical potential (see the text). The asymptote for the thick film (Equation (30)) is shown as a dashed dotted line. The asymptotes for thin films are given for the three regimes (dashed lines, Equations (33), (38), and (45)). All curves correspond to $\Phi^{\mathrm{S}}_{\infty}$ = exp(+4) for the isolated surface. The curves depend on C_{s}, C_{el}, and K_{a} only through $\Phi^{\mathrm{S}}_{\infty}$ (see Equation (17)).

The asymptote for thick films still follows Equation (30). For $h < L_{\mathrm{D}}$, however, the behavior is quite different for the two regimes. For a thin film, all potentials are very high, and $\Phi >> 1$, irrespective of the indices. Therefore, Equation (34) simplifies to

$$\Phi_{\mathrm{m}} = \Phi^{\mathrm{S}} - \Phi^{\mathrm{S}}_{\infty}. \tag{35}$$

On the other hand, we can expand Equation (8) in series:

$$\Phi^{\mathrm{S}} \xrightarrow[\Gamma=const]{h\to 0} \Phi_{\mathrm{m}} + \frac{h^2}{16L_{\mathrm{D}}^2}\Phi_{\mathrm{m}}^2. \tag{36}$$

Combining the last two equations leads to an explicit asymptote for $\Phi_{\mathrm{m}}(h)$:

$$\Phi_{\mathrm{m}} \xrightarrow[\Gamma=const]{h\to 0} \frac{4L_{\mathrm{D}}\sqrt{\Phi^{\mathrm{S}}_{\infty}}}{h}. \tag{37}$$

By substituting this Φ_{m} into Equation (23) for the disjoining pressure, we obtain the respective asymptote of Π_{el}:

$$\Pi_{\mathrm{el}} \xrightarrow[\Gamma=const]{h\to 0} kTC_{\mathrm{el}}\left(\frac{4L_{\mathrm{D}}\sqrt{\Phi^{\mathrm{S}}_{\infty}}}{h} + \frac{h}{4L_{\mathrm{D}}\sqrt{\Phi^{\mathrm{S}}_{\infty}}} - 2\right) \approx kTC_{\mathrm{el}}\left(\frac{4L_{\mathrm{D}}\sqrt{\Phi^{\mathrm{S}}_{\infty}}}{h} - 2\right). \tag{38}$$

This is compared to the exact solution in Figure 2. The exact dependence of Π_{el} versus h under a constant charge regime is calculated via Equations (23) and (7) and the generalized Gouy Equation (11) (where Γ is treated as a constant equal to Γ_∞), which determine Π_{el}, Φ^{S}, and Φ_{m} as functions of h. This is realized numerically by solving Equation (11) for Φ^{S},

substituting this Φ^{S} into Equation (7), and plotting $\Pi_{\mathrm{el}}(\Phi_{\mathrm{m}})$ from Equation (23) against $h(\Phi_{\mathrm{m}})$ from Equation (7) parametrically.

Constant chemical potential (charge regulation regime). In reality, the thinning of emulsion and foam films is under a constant chemical potential, and both Γ and Φ^{S} change with the thickness. To determine the electrostatic disjoining pressure Π_{el} for this case, we first substitute Γ from the isotherm, Equation (14), into the generalized Gouy Equation (11):

$$\frac{L_{\mathrm{B}}}{2C_{\mathrm{el}}}\frac{K_{\mathrm{a}}^2C_{\mathrm{s}}^2}{\left(\Phi^{\mathrm{S}}\right)^2}=\Phi^{\mathrm{S}}+\left(\Phi^{\mathrm{S}}\right)^{-1}-\Phi_{\mathrm{m}}-\left(\Phi_{\mathrm{m}}\right)^{-1}. \tag{39}$$

For an isolated surface (or extremely thick film of Φ_{m} = 1), the above equation simplifies to:

$$\frac{L_{\mathrm{B}}}{2C_{\mathrm{el}}}\frac{K_{\mathrm{a}}^2C_{\mathrm{s}}^2}{\left(\Phi_{\infty}^{\mathrm{S}}\right)^2}=\Phi_{\infty}^{\mathrm{S}}+\left(\Phi_{\infty}^{\mathrm{S}}\right)^{-1}-2. \tag{40}$$

The last two equations can be combined to obtain the following convenient form:

$$\frac{\Phi_{\infty}^{\mathrm{S}}\left(\Phi_{\infty}^{\mathrm{S}}-1\right)^2}{\left(\Phi^{\mathrm{S}}\right)^2}=\Phi^{\mathrm{S}}+\left(\Phi^{\mathrm{S}}\right)^{-1}-\Phi_{\mathrm{m}}-\left(\Phi_{\mathrm{m}}\right)^{-1}. \tag{41}$$

We solve Equation (41) for Φ^{S} and then we substitute the result into Equation (7) to obtain $h(\Phi_{\mathrm{m}})$. This determines $\Pi_{\mathrm{el}}(h)$ parametrically via this $h(\Phi_{\mathrm{m}})$ and $\Pi_{\mathrm{el}}(\Phi_{\mathrm{m}})$ from Equation (23).

The asymptote at a large thickness is again unchanged compared to Equation (30). To analyze the asymptote for a thin film ($h << L_{\mathrm{D}}$), we assume that all Boltzmann factors are very large, which allows us to simplify Equation (41) to:

$$\Phi^{\mathrm{S}}-\Phi_{\mathrm{m}}\approx\frac{\left(\Phi_{\infty}^{\mathrm{S}}\right)^3}{\left(\Phi^{\mathrm{S}}\right)^2} \tag{42}$$

The respective asymptote of h from Equation (7) reads as follows:

$$h\approx\frac{4L_{\mathrm{D}}}{\sqrt{\Phi_{\mathrm{m}}^2-1}}\frac{\left(\Phi_{\infty}^{\mathrm{S}}\right)^{3/2}}{\Phi^{\mathrm{S}}}\approx\frac{4L_{\mathrm{D}}}{\Phi_{\mathrm{m}}}\frac{\left(\Phi_{\infty}^{\mathrm{S}}\right)^{3/2}}{\Phi^{\mathrm{S}}} \tag{43}$$

Since for a thin film $\Phi^{\mathrm{S}}\approx\Phi_{\mathrm{m}}$, we can write the last equation as:

$$\Phi_{\mathrm{m}}\approx\frac{2\sqrt{L_{\mathrm{D}}}\left(\Phi_{\infty}^{\mathrm{S}}\right)^{3/4}}{\sqrt{h}} \tag{44}$$

This result is substituted into Langmuir's Equation (23) for Π_{el}:

$$\frac{\Pi_{\mathrm{el}}}{kTC_{\mathrm{el}}}\xrightarrow[\mu^{\mathrm{S}}=const]{h\to 0}\frac{2\sqrt{L_{\mathrm{D}}}\left(\Phi_{\infty}^{\mathrm{S}}\right)^{3/4}}{\sqrt{h}}+\frac{\sqrt{h}}{2\sqrt{L_{\mathrm{D}}}\left(\Phi_{\infty}^{\mathrm{S}}\right)^{3/4}}-2\approx\frac{2\sqrt{L_{\mathrm{D}}}\left(\Phi_{\infty}^{\mathrm{S}}\right)^{3/4}}{\sqrt{h}}-2 \tag{45}$$

Thus, the disjoining pressure of a fluid film stabilized by an ionic surfactant follows an $h^{-1/2}$ asymptote at small thicknesses. It depends solely on the surface potential of the thick film; two surfactant monolayers of the same surface potential will produce the same asymptote irrespective of the actual value of the adsorption constant K_{a}.

Let us, for completeness, also write down the asymptotes of the surface potential and the surface charge at small h values:

$$\Phi^{\mathrm{S}} \xrightarrow[\mu^{\mathrm{S}}=const]{h\to 0} \frac{2\sqrt{L_{\mathrm{D}}}}{\sqrt{h}}\left(\Phi^{\mathrm{S}}_{\infty}\right)^{3/4} + \frac{h}{4L_{\mathrm{D}}}\left(\Phi^{\mathrm{S}}_{\infty}\right)^{3/2} \tag{46}$$

$$\Gamma \xrightarrow[\mu^{\mathrm{S}}=const]{h\to 0} \sqrt{\frac{C_{\mathrm{el}}h}{2L_{\mathrm{D}}L_{\mathrm{B}}}}\left(\Phi^{\mathrm{S}}_{\infty}\right)^{3/4}. \tag{47}$$

In all of these formulae, $\Phi^{\mathrm{S}}_{\infty}$ is given by the Davies Equation (17).

The results from this section are general in the sense that they account for the presence of background electrolytes and the ion-specific effect (through the counterion-specific value of the adsorption constant K_{a} [29]). They have, however, the same limitations as the Davies isotherm; they hold for coverages of up to 30–60%, depending on the surfactant. Typically, monolayers of ionic surfactants alone are not particularly dense anyway.

2.5. Phase Transition at W | A Interface Triggered by Film Thinning

The previous section is most relevant to emulsion films stabilized by soluble ionic surfactants, where the Davies isotherm is a particularly good model [29]. What makes a foam film different is the large cohesion between the hydrocarbon tails of the adsorbed surfactant, which produces $K_{\mathrm{a}}^{\mathrm{LE}}$ in Equation (18) and π_{coh} in Equation (29). We will now consider a foam film covered with monolayers close to the phase transition point between the 2D gaseous and liquid expanded states. For an isolated surface, the phase transition point corresponds to equal surface tension of the two phases (i.e., $\sigma = \sigma^{\mathrm{AL}} + \sigma^{\mathrm{DL}}$ is the same for the two phases), where for an isolated surface, σ^{AL} is given by Equation (26) or Equation (29), and $\sigma^{\mathrm{DL}} = 2kT\Gamma$ [25,29]. Therefore, the Davies isotherms for the two phases give for the surface pressures of the two phases:

$$\pi^{\mathrm{G}} \equiv \sigma_0 - \sigma^{\mathrm{G}} = 3kT\Gamma^{\mathrm{G}} \text{ and } \pi^{\mathrm{LE}} \equiv \sigma_0 - \sigma^{\mathrm{LE}} = -\pi_{\mathrm{coh}} + 3kT\Gamma^{\mathrm{LE}}, \tag{48}$$

with Γ given by Equation (16), with two different K_{a} values for the two phases. The phase transition condition reads:

$$\pi_{\mathrm{pt}\infty} = 3kT\Gamma^{\mathrm{G}} = -\pi_{\mathrm{coh}} + 3kT\Gamma^{\mathrm{LE}}. \tag{49}$$

This equation determines the phase transition point for an isolated surface.

We determined the three parameters of the W | A isotherm—$K_{\mathrm{a}}^{\mathrm{G}}$, $K_{\mathrm{a}}^{\mathrm{LE}}$, and π_{coh}—by comparing the Davies isotherms with tensiometric data for various surfactants, which were limited to $\pi^{\mathrm{S}} < 10$ mM to make sure that the condition $\gamma^{\mathrm{S}} = 1$ is fulfilled. The procedure for determination of the parameters was like the one in [29]. The data for $C_{10}H_{21}OC_2H_4SO_3Na$ were from [36]. The data for $C_{12}H_{25}SO_4Na$ were from [37–40]; the data for $C_{10}H_{21}N(CH_3)_3Br$—from [41]; for $C_{12}H_{25}N(CH_3)_3Br$—from [42]; for $C_{12}H_{25}N(CH_3)_3Cl$—from [43]. The adsorption parameters are listed in Table 1.

In some cases ($C_{10}H_{21}OC_2H_4SO_3Na$), data for the gaseous phase were not available. It is often the case that even the lowest concentration studied experimentally is already in the liquid expanded state, as researchers are rarely interested in regions of low surface pressure. We therefore recalculated $K_{\mathrm{a}}^{\mathrm{G}}$ for the surfactant $C_{10}H_{21}OC_2H_4SO_3Na$ using the value of $K_{\mathrm{a}}^{\mathrm{G}}$ for $C_{12}H_{25}SO_4Na$, combined with Traube's rule, as described in [29].

With the parameters from Table 1, we determined the phase transition point by solving Equation (49) for C_{s} and the two adsorptions given by the Davies isotherm, Equation (16). We assumed that no background electrolyte was present, and therefore, $C_{\mathrm{el}} = C_{\mathrm{s}}$. This leads to:

$$\left(C_{s,pt\infty}\right)^{2/3} = \frac{\pi_{coh}}{3kT\left[\left(2K_a^{LE}/L_B\right)^{1/3} - \left(2K_a^{G}/L_B\right)^{1/3}\right]}. \quad (50)$$

The respective surface pressure at the phase transition for the isolated surface follows from Equation (49).

Table 1. Phase transition parameters for foam films stabilized by various surfactants.

Surfactant	Adsorption Parameters			Phase Transition for Isolated Surface (mM, mN/m)	Phase Transition in a Film	
	$\ln(K_a^G/m)$	$\ln(K_a^{LE}/m)$	π_{coh} [mN/m]		h^G [nm]	h^{LE} [nm]
$C_{10}H_{21}OC_2H_4SO_3Na$	−10.31	−7.42	−3.1	$C_{s,pt\infty}$ = 1.18 mM $\pi_{pt\infty}$ = 1.9 mN/m	C_s = 1.20 mM	
					11.0	12.8
					C_s = 1.25 mM	
					5.2	6.9
$C_{12}H_{25}SO_4Na$	−8.25	−4.64	−7.0	$C_{s,pt\infty}$ = 0.81 mM $\pi_{pt\infty}$ = 3.0 mN/m	C_s = 0.85 mM	
					4.9	6.2
					C_s = 1.00 mM	
					-	-
$C_{10}H_{21}N(CH_3)_3Br$	−11.62	−8.63	−3.5	$C_{s,pt\infty}$ = 2.51 mM $\pi_{pt\infty}$ = 2.1 mN/m	C_s = 2.53 mM	
					22.2	23.9
					C_s = 2.60 mM	
					7.3	8.9
$C_{12}H_{25}N(CH_3)_3Br$	−10.57	−5.74	−6.4	$C_{s,pt\infty}$ = 1.02 mM $\pi_{pt\infty}$ = 1.6 mN/m	C_s = 1.05 mM	
					7.2	9.9
					C_s = 1.10 mM	
					-	-
$C_{12}H_{25}N(CH_3)_3Cl$	−10.65	−7.27	−3.1	$C_{s,pt\infty}$ = 0.95 mM $\pi_{pt\infty}$ = 1.5 mN/m	C_s = 0.97 mM	
					15.2	17.6
					C_s = 1.00 mM	
					7.3	9.7

The phase transition in a foam film occurs at a slightly higher concentration compared to an isolated surface (i.e., $C_s > C_{s,pt\infty}$). For example, if we make a soap film from a solution of C_s = 0.85 mM sodium dodecyl sulfate, then the two isolated surfaces in a thick film will be in the liquid expanded state (since $C_{s,pt\infty}$ = 0.81 mM). However, as the film thins, the interactions between the two surfaces rarefy the monolayer, and eventually, a critical transition thickness is reached where LE is no longer the stable phase. At this point, the film is expected to make a phase transition to a 2D gaseous state, which is simultaneously of a smaller surface charge and surface potential and therefore thinner compared with the LE film. In Sheludko's interferometric cell, this should be observed as nucleation and growth of a darker (i.e., thinner) spot of a film covered with a gaseous monolayer within the initial lighter (thicker) film covered with a liquid expanded monolayer. The geometry of such a heterogeneous film is illustrated in Figure 3. Similar spot formations are often observed in films transiting from common films (electrostatically stabilized) to Newton black films (sterically stabilized) [44]. The phenomenon has also been observed in micellar solutions, which tend to make phase transitions through stepwise expulsion of micellar layers [45].

To our knowledge, such spot formations have never been observed for the proper surface phase transition discussed here.

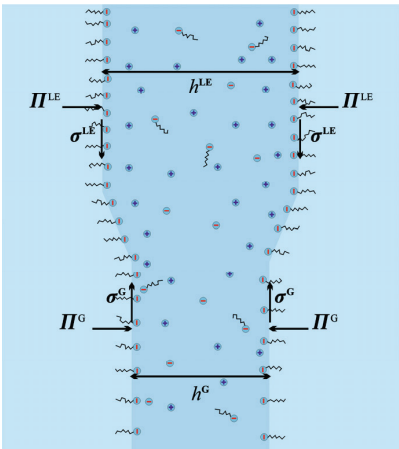

Figure 3. Illustration of phase transition in air–water–air thin liquid film.

Let us now predict the actual thicknesses at which the phase transition should be observed. The condition for chemical equilibrium was automatically fulfilled as we fixed the chemical potentials of the surfactant to that in the meniscus through the generalized Davies isotherm. The condition for mechanical equilibrium between the two films—the thicker LE and the thinner LG—requires that the membrane tensions of the two films are equal (tangential force balance) and the disjoining pressures are also equal (normal balance). The membrane tensions σ_m^{LE} and σ_m^{G} are given by Equation (25) (with the contributions from the adsorption layer, the electric double layer, and the Van der Waals interaction given by Equations (26)–(28)). These are illustrated as functions of h in Figure 4.

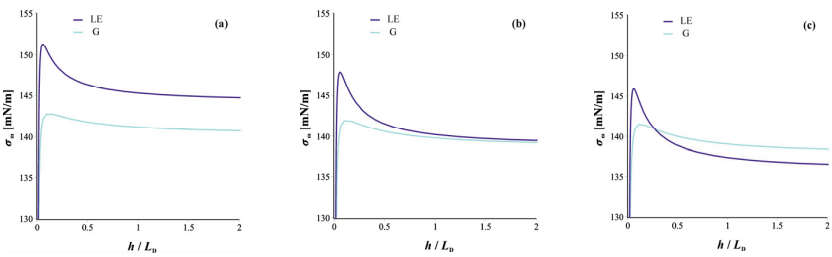

Figure 4. Membrane tension as a function of the film thickness (nondimensionalized with the Debey length L_D). The parameters are for sodium dodecyl sulfate. The three figures correspond to three concentrations: (**a**) C_s = 0.50 mM, which is below the phase transition of the isolated surface; (**b**) C_s = 0.81 mM, which is at the phase transition; (**c**) C_s = 1.00 mM, which is above the phase transition. The blue curve stands for film covered with a gaseous monolayer, and the purple is for the LE phase.

To determine the point of the phase transition, we solve the two conditions for mechanical balance simultaneously. This can be illustrated graphically by plotting the disjoining pressure $\Pi(h)$ from DLVO's Equation (24) against $\sigma_m(h)$. This is shown in Figure 5 for four different concentrations of surfactants. The first concentration is below the phase transition point of the isolated surface (Figure 5a), and the second is exactly at the phase transition point (Figure 5b). In both cases, the two curves for the gaseous and LE films cross each other, but the crossing point appears at thicknesses where the films are unstable, being below the maximum of σ_m (Figure 4), where they thin until breakage. Therefore, films stabilized by a monolayer in a 2D gaseous state remain in the gaseous state without a phase transition.

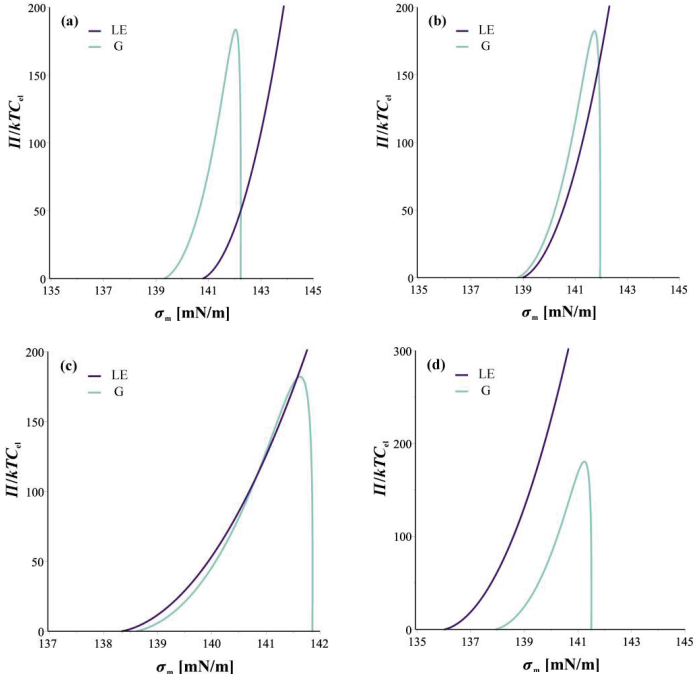

Figure 5. Determination of the point of phase transition triggered by film drainage for films stabilized with sodium dodecyl sulfate, with disjoining pressure Π versus membrane pressure σ_m. (**a**) C_s = 0.70 mM. There is a crossing point, but it corresponds to unstable equilibrium. (**b**) C_s = 0.81 mM (equal to $C_{s,pt\infty}$ of the isolated surface). Again, there is unstable equilibrium. (**c**) C_s = 0.85 mM. In this case, the crossing point near $\Pi = 100kTC_{el}$ corresponds to two films in stable equilibrium with two different thicknesses: h^G = 4.9 nm and h^{LE} = 6.2 nm. (**d**) C_s = 1.0 mM. No crossing point – no phase transition is possible.

The behavior is different for C_s = 0.85 mM, slightly higher than the concentration at the phase transition. In this case, the Π versus σ_m curves cross twice (see Figure 5c). One of the crossing points (which appears at higher Π values) corresponds to an unstable state again. The other one, however, corresponds to a stable equilibrium, with the two films coexisting as shown in Figure 3. We determined the crossing point numerically as values for Π_{pt} and $\sigma_{m,pt}$. From the obtained value of $\sigma_{m,pt}$, we calculated the thicknesses of the gaseous film and the LE film from curves like those in Figure 4. The thicknesses obtained this way are listed for a couple of surfactant concentrations in the meniscus in Table 1.

Finally, when the concentration of surfactants is much higher than C_{pt}, the two curves for the gaseous film and LE film do not cross each other (Figure 5d). Therefore, the film thinning cannot trigger a phase transition, and the film thins until breakage, remaining in the liquid expanded state.

3. Conclusions

We analyzed the surface forces in thin liquid films stabilized by ionic surfactants which drain in the charge regulation regime. We used the simplest possible Davies isotherm as a charge regulation condition for two particular systems: emulsion and foam films.

We showed that for the oil–water–oil film, this charge regulation condition predicts the electrostatic disjoining pressure between the two classical constant charge and constant potential regimes (see Figure 2). We also derived the asymptotic behavior of Π_{el} at small thicknesses, and we showed that the Davies regulation results in Π_{el} being proportional to $h^{-1/2}$, Equation (45).

We also investigated the thinning of a foam film stabilized by an ionic surfactant which forms a cohesive monolayer transiting from a 2D gaseous state to a liquid expanded state.

We showed that it is in theory possible for such foam films to make a phase transition from a thicker film, covered with liquid expanded phase, to a thinner film covered with gaseous monolayers. We analyzed the concentration range where such a transition is possible. We showed it occurs in a tight region spanning from the phase transition concentration $C_{s,pt\infty}$ of an isolated surface to one that is 10–20% higher (and varies with the surfactant). The film thicknesses of the two films in equilibrium were calculated for a few cases (Table 1).

The intention of this article is to investigate for the first time the charge regulation in fluid films, foam or emulsion, and to provide estimates of the parameters of films thinning under this regime to guide future experimental work on the phenomenon. The results show that, for single surfactant systems, charge regulation becomes important at extremely high disjoining pressures. Such pressures will be difficult to achieve in a Sheludko cell, where the compressing pressure is limited to a few tens of kPa. The phenomenon will be easier to detect in films of lower charges stabilized by a mixture of ionic and nonionic surfactants (which is the most important case in practice anyway). However, the theory in this case is more complicated and beyond the objectives of our paper. Charge regulation will also be important for microemulsions or coalescence of extremely small droplets (radius ~1 μm).

We also predicted that the thinning of a foam film can trigger a surface phase transition. This phase transition should take place with a simultaneous jump in the film thickness. The observation of such a film phase transition will be similarly difficult in a Scheludko cell for a single ionic surfactant, but it should be possible with mixed monolayers or monolayers of protolytes which are only partially charged to reduce the electrostatic repulsion to values achievable in this apparatus. The phase transition should be expected to appear in the usual way, with the formation and growth of a dark spot within the lighter initial film. The dark spot will be stabilized by a 2D gaseous monolayer of a surface charge lower than that of the surrounding film covered by an LE monolayer. A similar phase transition can be expected slightly above the phase transition concentration $C_{pt\infty}$ for any two phases of a charged monolayer.

Author Contributions: Conceptualization, R.I.S.; methodology, I.M.D. and R.I.S.; software I.M.D.; validation, R.I.S. and I.M.D.; formal analysis, I.M.D. and R.I.S.; data curation, I.M.D.; writing—original draft preparation, I.M.D. and R.I.S.; writing—review and editing, I.M.D.; visualization, I.M.D. All authors have read and agreed to the published version of the manuscript.

Funding: This study was financed by project no. BG-RRP-2.004-0002-C01, BiOrgaMCT.

Data Availability Statement: Data are contained within the article.

Conflicts of Interest: The authors declare no conflict of interest.

Abbreviations

A_H	Hamaker constant
C_{el}	total electrolyte concentration
C_s	surfactant concentration
$C_{s,pt\infty}$	phase transition concentration of an isolated surface
E	electric field
e	elementary electric charge
K_a	equilibrium adsorption constant (from the aqueous phase)
K_a^G	adsorption constant for gaseous phase
K_a^{LE}	adsorption constant for liquid expanded phase
k	Boltzmann constant

L_B	Bjerumm's length ($L_B = e^2/\varepsilon kT$)
L_D	Debye's length ($L_D^2 = \varepsilon kT/2e^2C_{el}$)
$\mathbf{P}$	pressure tensor (including the Maxwell tensor)
p	isotropic mechanical pressure
T	temperature
$\mathbf{U}$	unit tensor
z	distance from the center of the film
Γ	adsorption of the surfactant
Γ^{G}	surfactant adsorption for 2D gaseous phase
Γ^{LE}	surfactant adsorption for liquid expanded phase
γ^S	surface activity coefficient of the surfactant
ε	absolute dielectric permittivity
μ^S	chemical potential of the surface active ion
Π	disjoining pressure
Π_{el}	electrostatic disjoining pressure
π	surface pressure of the monolayer ($\pi \equiv \sigma_0 - \sigma$)
π_{coh}	Langmuir's cohesive pressure
$\pi_{pt\infty}$	phase transition surface pressure of an isolated surface
π^G	surface pressure for gaseous phase
π^{LE}	surface pressure for liquid expanded phase
ρ	charge density
ρ^S	surface charge ($\rho^S = -e\Gamma$) for ionic 1:1 surfactant
σ	surface tension of the monolayer
σ_0	surface tension of the neat surface
σ^{AL}	contribution of the adsorbed layer to the surface tension
σ_m	membrane tension
σ_m^{DL}	contribution of the electric double layer to the membrane tension
σ_m^{VdW}	Van der Waals contribution to the membrane tension
Φ	Boltzmann factor for a cation ($\Phi = \exp(-e\phi/kT)$)
Φ_m	Boltzmann factor in the center of the film ($\Phi_m = \exp(-e\phi_m/kT)$)
Φ^S	surface Boltzmann factor ($\Phi^S = \exp(-e\phi^S/kT)$)
ϕ	electrostatic potential
ϕ_m	extremum of the electrostatic potential in the center of the film
ϕ^S	surface electric potential
2D	two-dimensional
CMC	critical micelle concentration
EoS	equation of state
W | G	water–gas surface
W | O	water–oil interface

References

1. Rusanov, A.I. *Phase Transitions and Surface Phenomena*, 1st ed.; Scientific Research: Leningrad, Russia, 1967. (In Russian)
2. Derjaguin, B.V. *Theory of the Stability of Colloids and Thin Films*, 1st ed.; Scientific Research: Moscow, Russia, 1986. (In Russian)
3. Bierman, A. Electrostatic forces between nonidentical colloidal particles. *J. Colloid Interface Sci.* **1955**, *10*, 231–245. [CrossRef]
4. Melville, J.B.; Smith, A.L. Interaction between silver iodide surfaces in the presence of specifically adsorbed ions. *J. Chem. Soc. Faraday Trans. 1* **1974**, *70*, 1551–1557. [CrossRef]
5. Paunov, V.N.; Dimova, R.I.; Kralchevsky, P.A.; Broze, G.; Mehreteab, A. The hydration repulsion between charged surfaces as an interplay of volume exclusion and dielectric saturation effects. *J. Colloid Interface Sci.* **1996**, *182*, 239–248. [CrossRef]
6. Kralchevsky, P.A.; Danov, K.D.; Basheva, E.S. Hydration force due to the reduced screening of the electrostatic repulsion in few-nanometer-thick films. *Curr. Opin. Colloid Interface Sci.* **2011**, *16*, 517–524. [CrossRef]
7. Pericet-Camara, R.; Papastavrou, G.; Behrens, S.H.; Borkovec, M. Interaction between Charged Surfaces on the Poisson-Boltzmann Level: The Constant Regulation Approximation. *J. Phys. Chem. B* **2004**, *108*, 19467–19475. [CrossRef]

8. Lyklema, J.; Duval, J.F.L. Hetero-interaction between Gouy–Stern double layers: Charge and potential regulation. *Adv. Colloid Interface Sci.* **2005**, *114–115*, 27–45. [CrossRef]
9. Usui, S. Interaction between dissimilar double layers with like signs under charge regulation on the basis of the Gouy–Chapman–Stern–Grahame model. *J. Colloid Interface Sci.* **2004**, *280*, 113–119. [CrossRef]
10. Chan, D.Y.C.; Healy, T.W.; Supasiti, T.; Usui, S. Electrical double layer interactions between dissimilar oxide surfaces with charge regulation and Stern–Grahame layers. *J. Colloid Interface Sci.* **2006**, *296*, 150–158. [CrossRef] [PubMed]
11. Popa, I.; Sinha, P.; Finessi, M.; Maroni, P.; Papastavrou, G.; Borkovec, M. Importance of charge regulation in attractive double-layer forces between dissimilar surfaces. *Physical. Rev. Lett.* **2010**, *104*, 228301. [CrossRef] [PubMed]
12. Carnie, S.L.; Chan, D.Y.C. Interaction free energy between plates with charge regulation: A linearized model. *J. Colloid Interface Sci.* **1993**, *161*, 260–264. [CrossRef]
13. Fleharty, M.E.; van Swol, F.; Petsev, D.N. The effect of surface charge regulation on conductivity in fluidic nanochannels. *J. Colloid Interface Sci.* **2014**, *416*, 105–111. [CrossRef] [PubMed]
14. Aguilella, V.M.; Verdia-Baguena, C.; Alcaraz, A. Lipid charge regulation of non-specific biological ion channels. *Phys. Chem. Chem. Phys.* **2014**, *16*, 3881–3893. [CrossRef] [PubMed]
15. Wang, D.; Nap, R.J.; Lagzi, I.; Kowalczyk, B.; Han, S.; Grzybowski, B.A.; Szleifer, I. How and why nanoparticle's curvature regulates the apparent pK_a of the coating ligands. *J. Am. Chem. Soc.* **2011**, *133*, 2192–2197. [CrossRef]
16. Zheng, B.; Komura, S.; Andelman, D.; Podgornik, R. Diffusive dynamics of charge regulated macro-ion solutions. *arXiv* **2024**. [CrossRef]
17. Israelachvili, J. *Intermolecular and Surface Forces*; Academic Press: London, UK, 1992.
18. Ducker, W.A.; Senden, T.J.; Pashley, R.M. Direct measurement of colloidal forces using an atomic force microscope. *Nature* **1991**, *353*, 239–241. [CrossRef]
19. Butt, H.J. Measuring electrostatic, van der Waals, and hydration forces in electrolyte solutions with an atomic force microscope. *Biophys. J.* **1991**, *60*, 1438–1444. [CrossRef]
20. Sheludko, A. Thin liquid films. *Adv. Colloid Interface Sci.* **1967**, *1*, 391–464. [CrossRef]
21. Czarnecki, J.; Khristov, K.; Masliyah, J.; Panchev, N.; Taylor, S.D.; Tchoukov, P. Application of Scheludko–Exerowa thin liquid film technique to studies of petroleum W/O emulsions. *Colloids Surf. A Physicochem. Eng. Asp.* **2017**, *519*, 2–10. [CrossRef]
22. Yang, F.; Tchoukov, P.; Qiao, P.; Ma, X.; Pensini, E.; Dabros, T.; Czarnecki, J.; Xu, Z. Studying demulsification mechanisms of water-in-crude oil emulsions using a modified thin liquid film technique. *Colloids Surf. A Physicochem. Eng. Asp.* **2018**, *540*, 215–223. [CrossRef]
23. Slavchov, R.I.; Peychev, B.; Minkov, I. Electrolytes at uncharged liquid interfaces: Adsorption, potentials, surface tension, and the role of the surfactant monolayer. *Langmuir* **2024**, *40*, 17170–17189. [CrossRef] [PubMed]
24. Dimitrova, I.M.; Slavchov, R.I.; Ivanov, T.; Moshbach, T.S. A spherical cavity model for quadrupolar dielectics. *J. Chem. Phys.* **2016**, *144*, 114502–114519. [CrossRef] [PubMed]
25. Davies, J.T.; Rideal, E.K. *Interfacial Phenomena*, 2nd ed.; Academic Press: New York, NY, USA, 1963.
26. Gouy, L.G. Sur la constitution de la charge électrique à la surface d'un èlectrolyte. *Le J. De Phys. Et Le Radium* **1910**, *9*, 457–468. [CrossRef]
27. Reiner, E.S.; Radke, C.J. Double layer interactions between charge-regulated colloidal surfaces: Pair potentials for spherical particles bearing ionogenic surface groups. *Adv. Colloid Interface Sci.* **1993**, *47*, 59–147. [CrossRef]
28. Davies, J.T. Adsorption of long-chain ions I. *Proc. R. Soc. Lond. Ser. A* **1958**, *245*, 417–428.
29. Slavchov, R.I.; Karakashev, S.I.; Ivanov, I.B. Ionic surfactants and ion-specific effects: Adsorption, micellization, thin liquid films. In *Surfactant Science and Technology: Retrospects and Prospects*; Römsted, L., Ed.; CRC Press, Taylor&Francis Group: New York, NY, USA, 2014; Chapter 2.
30. Tamm, I.E. *Foundamentals of the Theory of Electricity*, 10th ed.; Nauka: Tolyatti, Russia, 1989. (In Russian); 9th ed.; Mir Publishers: Moscow, Russia, 1979. (In English); Chapter 2.
31. Zhang, H.; Wang, F.; Nestler, B. Multi-component electro-hydro-thermodynamic model with phase-field method. I. Dielectric. *J. Comput. Phys.* **2024**, *505*, 112907. [CrossRef]
32. Slavchov, R.I.; Dimitrova, I.M.; Ivanov, T.I. The polarized interface between quadrupolar insulators: Maxwell stress tensor, surface tension, and potential. *J. Chem. Phys.* **2015**, *143*, 154707–154721. [CrossRef]
33. Langmuir, I. The role of attractive and repulsive forces in the formation of tactoids, thixotropic gels, protein crystals and coacervates. *J. Chem. Phys.* **1938**, *6*, 873–896. [CrossRef]
34. Langmuir, I. Oil lenses on water and the nature of monomolecular expanded films. *J. Chem. Phys.* **1933**, *1*, 756–776. [CrossRef]
35. Honig, E.P.; Mul, P.M. Tables and equations of the diffuse double layer repulsion at constant potential and at constant charge. *J. Colloid Interface Sci.* **1971**, *36*, 258–272. [CrossRef]

36. Rosen, M.J. *Surfactants and Interfacial Phenomena*, 3rd ed.; Wiley: New York, NY, USA, 2004.
37. Aratono, M.; Uryu, S.; Hayami, Y.; Motomura, K.; Matuura, R. Phase transition in the adsorbed films at water/air interface. *J. Colloid Interface Sci.* **1984**, *98*, 33–38. [CrossRef]
38. Gurkov, T.D.; Dimitrova, T.D.; Marinova, K.G.; Bilke-Crause, C.; Gerber, C.; Ivanov, I.B. Ionic surfactants on fluid interfaces: Determination of the adsorption; role of the salt and the type of hydrophobic phase. *Colloids Surf. A Physicochem. Eng. Asp.* **2005**, *261*, 29–38. [CrossRef]
39. Rehfeld, S.J. Adsorption of sodium dodecyl sulfate at various hydrocarbon-water interfaces. *J. Phys. Chem.* **1967**, *71*, 738–745. [CrossRef]
40. Hines, J.D. The preparation of surface chemically pure sodium n-dodecyl sulfate by foam fractionation. *J. Colloid Interface Sci.* **1996**, *180*, 488–492. [CrossRef]
41. Bergeron, V. Disjoining pressure and film stability of alkyltrimethylammonium bromide foam films. *Langmuir* **1997**, *13*, 3474–3482. [CrossRef]
42. Aratono, M. (Kyushu University, Japan). Personal communication, 2010.
43. Uryu, S.; Aratono, M.; Yamanaka, M.; Motomura, K.; Matuura, R. Adsorption of dodecyltrimethylammonium chloride-decylammonium chloride mixtures at water/air interface. *Bull. Chem. Soc. Jpn.* **1983**, *56*, 3219–3223. [CrossRef]
44. Exerowa, D.; Nikolov, A.; Zacharieva, M. Common black and Newton film formation. *J. Colloid Interface Sci.* **1981**, *81*, 419–429. [CrossRef]
45. Anachkov, S.E.; Danov, K.D.; Basheva, E.S.; Kralchevsky, P.A.; Ananthapadmanabhan, K.P. Determination of the aggregation number and charge of ionic surfactant micelles from the stepwise thinning of foam films. *Adv. Colloid Interface Sci.* **2012**, *183–184*, 55–67. [CrossRef] [PubMed]

Disclaimer/Publisher's Note: The statements, opinions and data contained in all publications are solely those of the individual author(s) and contributor(s) and not of MDPI and/or the editor(s). MDPI and/or the editor(s) disclaim responsibility for any injury to people or property resulting from any ideas, methods, instructions or products referred to in the content.

molecules

MDPI

Article

Insight into Oil-in-Water Emulsions Stabilized by Cross-Linked and Pregelatinized Starches: The Effect of Molecular Structure, Surface Activity and Proton Molecular Dynamics

Joanna Le Thanh-Blicharz [1], Jacek Lewandowicz [1], Artur Szwengiel [2], Krystyna Prochaska [3], Hanna Maria Baranowska [4] and Grażyna Lewandowicz [5,*]

[1] Department of Food Concentrates and Starch Products, Prof. Wacław Dąbrowski Institute of Agriculture and Food Biotechnology—State Research Institute, Starołęcka 40, 61-361 Poznań, Poland; joanna.lethanh-blicharz@ibprs.pl (J.L.T.-B.); jacek.lewandowicz@ibprs.pl (J.L.)
[2] Department of Food Technology of Plant Origin, Faculty of Food Science and Nutrition, Poznan University of Life Sciences, Wojska Polskiego 31, 60-624 Poznań, Poland; artur.szwengiel@up.poznan.pl
[3] Institute of Chemical Technology and Engineering, Poznań University of Technology, Berdychowo 4, 60-965 Poznan, Poland; krystyna.prochaska@put.poznan.pl
[4] Department of Physics and Biophysics, Faculty of Food Science and Nutrition, Poznań University of Life Sciences, Wojska Polskiego 38/42, 60-637 Poznań, Poland; hanna.baranowska@up.poznan.pl
[5] Department of Biotechnology and Food Microbiology, Faculty of Food Science and Nutrition, Poznań University of Life Sciences, Wojska Polskiego 48, 60-627 Poznań, Poland
* Correspondence: grazyna.lewandowicz@up.poznan.pl

Abstract: Effective formation and stabilisation of emulsions while meeting high consumer requirements, including the so-called green label, is still a technological challenge. This is related to the multitude of emulsion destabilization mechanisms and the vastness of methods used to study them, which implies the need to develop an understanding of the phenomena occurring in emulsions. Commercial starch preparations obtained by physical and chemical modification were used to prepare model emulsions that were studied in terms of their stability. Native potato starch was the reference material. The analytical methods used included rheology, low field nuclear magnetic resonance (LF NMR), size exclusion chromatography with triple detection (SEC), and surface/interfacial tension measurements. The results showed that chemical and physical modification improved the functionality of starch in emulsions. This is due to not only chemical but also physical modifications, i.e., pregelatinization causes changes in the molecular structure of starch, including an increase in the molecular weight and the degree of branching. As a consequence, the conformation of starch macromolecules changes, which results in a change of the dynamics of protons in the continuous phase of the emulsion and the thermodynamics of starch adsorption at the water/oil interface.

Keywords: starch modification; emulsion stability; low field nuclear magnetic resonance; size exclusion chromatography; surface/interfacial tensions; rheological properties

1. Introduction

Many food products, such as mayonnaises, sauces, dips, creams, spreads, and pâtés, constitute emulsion systems. They are thermodynamically unstable, so their efficient production and stabilization is still one of the most challenging issues for food technologists. The instability of emulsions results from the fact that they are a colloidal dispersion of two immiscible liquids and their formation requires energy to increase the interfacial surface. Hence, the basic technological strategy is the introduction of surfactants, i.e., substances able to reduce the interfacial tension. Food grade surfactants are called emulsifiers. However, emulsion breakdown can occur by many different mechanisms such as coalescence, flocculation, gravitational separation or phase separation. Therefore, not only emulsifiers that primarily enable short-term stability of the emulsions, but also the so-called stabilizers

are used to improve the long-term stability of these systems. Various hydrocolloids, such as proteins and polysaccharides, especially starches, both in their native and modified form, are most often used in this task. Moreover, in relation to hydrocolloids there is no clear distinction between the terms emulsifier and stabilizer, and often they are used alternatively [1–8]. The increasing interest in particle-stabilized emulsions called Pickering emulsions has been observed in recent years. Traditional and Pickering emulsions differ fundamentally in the physicochemical properties of substances present at the oil–water interface. While traditional emulsions are produced, thanks to adsorption at the oil/water interface of the soluble, amphiphilic molecules of emulsifiers, Pickering emulsions are stabilized by the presence of insoluble, submicron particles at the oil–water interface. Some advantages of Pickering emulsions over traditional emulsions have been mentioned in the scientific literature, but in industrial practice, the latter still dominates. Moreover, a lot of theoretical and practical issues regarding traditional emulsions remain unsolved [9–12].

A multiplicity of mechanisms of destabilization of emulsions implies plurality in analytical methods for their study. The most popular are; microscopic methods; particle size measurements; and texture measurements, especially those employing rheological methods; and accelerated stability tests, mainly via centrifugation and fats oxidation analyses. Excellent, comprehensive reviews of the techniques and methodologies in this regard can be found in papers by McClements [13] and Kupikowska-Stobba et al. [14]. A less known, but very beneficial method for studying emulsions is low-field nuclear magnetic resonance (LF NMR). It is designed to study the dynamics of protons, so any system, even very complex that is rich in hydrogen, can be analysed by employing this technique. Hence, it has been used in the studies of different biological systems (including food) in their native form and environment. Most often, the proton dynamics of water molecules are studied as water is abundant in biological materials. Relaxation phenomena of protons that interact with an external magnetic field are observed. The spin-lattice relaxation time T_1, corresponding to the transfer of spin energy to the environment, and the spin-spin relaxation time T_2, corresponding to the mutual transfer of spin energy, are measured. The value of the spin-lattice relaxation time is influenced by many factors, including temperature, resonance frequency or the presence of macromolecules. The T_1 value of water increases linearly with increasing field intensity, whereas it significantly decreases as a result of the dissolution of proteins or polysaccharides [15–18]. Not only the molecular dynamics of water are studied using LF NMR but also phenomena occurring in fats, in spite of the fact that the values of relaxation times in fats are much lower than in aqueous systems. Moreover, special attention should be paid to the effect of the formation of emulsion systems on the proton relaxation phenomena. The formation of an emulsion, i.e., a colloidal dispersed system, complicates the proton relaxation processes. Two components of each relaxation time are observed, which proves that there are two proton fractions in the system, relaxing at different rates [19].

Starch is the most important source of energy in the human diet. However, its technological importance is often identified as its ability to shape the texture of food. Therefore, a lot of effort was made to control the rheological properties of starch [20–26]. As a result, both traditional physical, chemical and enzymatic processes as well as several less popular innovative methods for starch modification that change its structure are employed. This results in a change in the physicochemical and functional properties of this polysaccharide [8,27–29]. This also makes it possible to control its surface activity. Chemically modified starches can decrease interfacial tension at both air/water and oil/water interfaces to a higher extent than native starch. The effect obtained depends on both the type of modification and the degree of substitution. Further increases in the ability to reduce surface and interfacial tension can be achieved by enzymatic hydrolysis of starch preparations [30,31].

Food-grade cross-linked starches stand out among the chemically modified starches by their very low degree of substitution, an order of magnitude lower than those of

food mono-starch derivatives. For example, in cases of acetylation, maximally one in ten anhydroglucose units of starch macromolecules can contain the modifying acetyl groups;

- acetylated starch: starch–O–CO–O–CH_3,
  whereas cross-linked derivatives can be substituted at most only in one in five hundred anhydroglucose molecules [32,33];
- distarch phosphate: starch–O–PO_2–O–starch;
- distarch adipate: starch–O–CO–$(CH_2)_4$–CO–O–starch.

Nevertheless, they provide excellent technological properties thanks to an increase in the molar mass of starch that increases the viscosity of pastes, and their resistance to extended cooking times, acidity or shear stress. Distarch phosphates E1412, prevent leakage by heat treatment of meat products so they are often used in the production of ham or sausages. Double-modified starches: acetylated distarch phosphate E1414 and acetylated distarch adipate, which contain slightly hydrophobic acetyl groups and reveal higher surface activity than native starch, are often used in the manufacture of mayonnaises, sauces, margarines, or different reduced-fat products [20,34,35].

Despite chemically modified starches providing much better results, both in terms of technology and economy, consumers lately prefer foods with so-called clean labels, which in the case of starch means restrictions in the use of chemically modified ones [36,37]. Therefore, an increase in the significance of physical modification methods is observed. Pregelatinization is the most common process for physical modification of starch, despite the small decrease in the paste's viscosity. Pregelatinization in industrial practice is carried out by drying a starch suspension by employing drum dryers. It provides starch the ability to swell in cold water and create a colloidal solution due to the amorphization of its granules [38–40]. Physical modification of starch generally means the action of physical factors, such as heat, moisture, shear, radiation or pressure, without involving any chemicals. However, the production of granular cold water soluble (GCWS) starches is recognized as a physical modification despite involving heating of starches in aqueous alcohol and alcoholic alkaline treatment. This is of special importance concerning emulsion technology as pregelatinized and GCWS starches increase emulsion stability [6,35,41,42]. Other physical modification methods, including among others high-pressure homogenization of pastes, are also important for increasing the functionality of starch in emulsion systems [43]. The information presented above points to the need for further studies on the mechanisms of emulsion stabilization by starches modified by various methods. Cross-linked starches are commercially available not only in granular form but also as pregelatinized ones. Although they are a little bit more expensive, the latter is often chosen by food manufacturers. This may be related to the simplification of the technological process, but it is also suggested these starches have better functionality of pregelatinization in some applications. Therefore, this study aimed to find out the effect of sole chemical or physical as well as dual chemical-physical modification of starch on the structure, rheological properties, surface activity and functionality in emulsions of commercially available preparations of E1412, E1414 and E1422.

2. Results and Discussion

2.1. Stability of Formed Emulsions

As described in the introduction, emulsion stability is a complex concept and a lot of methods could be applied to analyse it. Nevertheless, the traditional, simple method employing the centrifugation process provides useful results and is very common. Very diverse values of creaming index data have been provided in the literature, which is related to the huge variety of emulsion recipes and methods for their production [44–48]. Nevertheless, the creaming index values are perfect for comparing different emulsifiers, stabilizers or conditions for emulsion preparation within a particular experiment. As it is presented in Figure 1, cross-linked starches revealed much better emulsifying properties than chemically unmodified starch. This applies to both cold-water and hot-water soluble

preparations. The creaming index decreased significantly after 24 h, but in cross-linked and additionally acetylated starches this decrease was only slight.

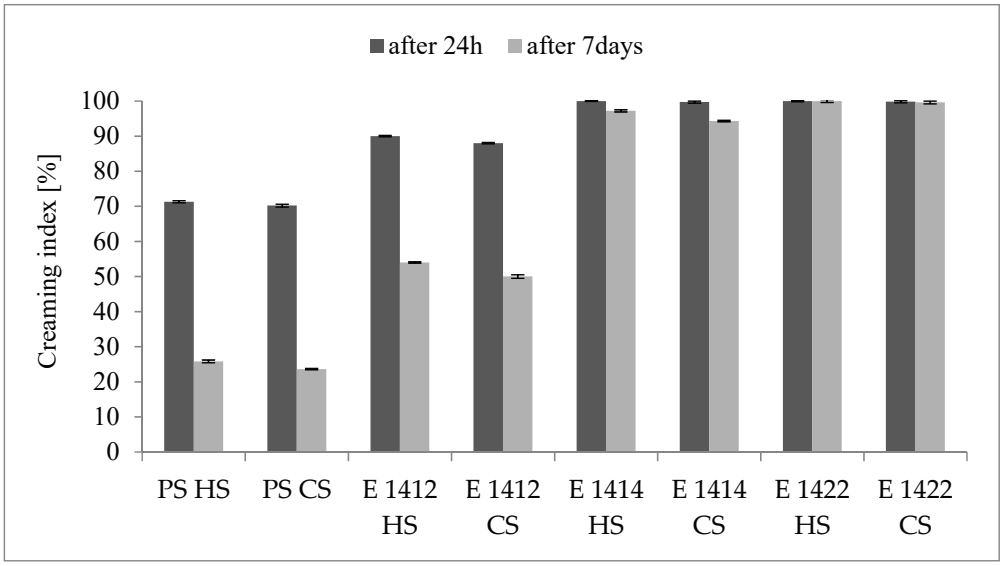

Figure 1. Changes in the creaming index of the emulsions during storage (PS—potato starch; HS—starches soluble in hot water; CS—starches soluble in cold water).

Another way to study the stability of the emulsions is to analyse colour parameters as light scattering depends on the composition and microstructure of colloidal dispersed systems [49–51]. The data presented in Table 1 indicate that chemically unmodified starch led to the production of the lowest lightness parameters (L). As in the case of the creaming index, better results were obtained for cross-linked starches, especially if they were additionally subjected to acetylation. It is also worth noting that in all cases, lighter emulsions were obtained using cold-water soluble preparations (CS) than their hot-water soluble analogues (HS). This is following the observations reported in the literature that pregelatinized starches are particularly useful in emulsion preparation [42]. Changes in lightness were accompanied by changes in parameters chromatic a* and b*. Lighter emulsions were characterized by more intense green (a) and yellow (b) colours. In the case of emulsions based on CS preparations, the shift towards the yellow colour was smaller. The lightest emulsion was obtained employing acetylated distarch adipate. Emulsions containing acetylated distarch phosphate differed in colour only slightly. More significant differences were observed for both the emulsions based on chemically unmodified starch and distarch phosphate.

Table 1. Instrumentally determined colour parameters of model emulsions with different starches in the CIE L*a*b* system.

	L (Whiteness)	a (Red–Green Balance)	b (Yellow–Blue Balance)	WI (%)
PS HS	66.85	−1.89	0.54	72.7
PS CS	67.04	−1.97	0.42	67.0
E1412 HS	69.59	−2.48	1.94	69.4
E1412 CS	72.71	−2.46	1.30	72.6
E1414 HS	83.85	−2.88	2.43	83.4
E1414 CS	85.07	−2.87	1.41	84.7
E1422 HS	86.74	−3.19	2.36	86.2
E1422 CS	85.52	−3.13	1.83	85.1

2.2. Rheological Properties of Emulsions

The measurement of the rheological properties of emulsions is of considerable practical importance as many of their sensory features correspond to specific parameters measured instrumentally. The rheological properties of an emulsion depend on many factors, the most important of which are the viscosity of the continuous phase and the concentration and structure of the dispersed phase [1,4,52]. The parameters of the Ostwald de Waele equation, which describe the flow curves of the studied emulsions, are presented in Table 2. The applied model fits the analytical data very well ($R \geq 0.98$). Among the presented data, the most noteworthy are clear differences between the rheological properties of emulsions based on cold and hot soluble starches. The values of the consistency index, which correspond to the sensory perception of the product's viscosity, in the case of emulsions with HS preparations increased as a result of the use of cross-linked starches. This particularly concerned distarch phosphate E1412, not submitted to an additional acetylation process. These increases in the consistency index were accompanied by a decrease in the flow behaviour index. In contrast, emulsions prepared with CS preparations revealed significantly smaller differences in these rheological parameters. This points to an essential effect of physical modification on the functional properties of the starches studied. As regards thixotropy, which describes the rheological instability of the fluids, it was observed that its lower values positively correlate with a higher creaming index of the emulsion. The high thixotropy values revealed emulsions based on PS CS and E1412 CS preparations. However, this phenomenon was significantly reduced in the case of starch preparations subjected to the acetylation process.

Table 2. Rheological parameters of the emulsions.

	Consistency Index K [Pa·s^n]		**Flow Behaviour Index n [−]**		**Thixotropy [Pa·s^{-1}]**		**Flow Activation Energy E [J·mol^{-1}]**	
	HS	**CS**	**HS**	**CS**	**HS**	**CS**	**HS**	**CS**
PS	1.37	4.32	0.8504	0.6824	19,480	57,465	216.1	230.1
E1412	32.48	4.05	0.3579	0.7108	−29,212	63,705	162.7	245.0
E1414	21.62	10.81	0.5593	0.6572	23,260	5960	278.3	293.1
E1422	11.66	3.48	0.6342	0.7974	15,365	−18,305	257.3	274.8

The viscosity of fluids is largely dependent on the temperature. This phenomenon is related to the energy that is supplied to the sample, which changes the interactions and intermolecular friction during flow [53–55]. The analysed cold-soluble starches created emulsions that revealed higher values of flow activation energy than their hot-soluble counterparts. A particularly large difference in activation energy values occurred in the case of E1412.

PCA analysis including the data of creaming index and lightness as the parameters describing stability of emulsions as well as rheological data is presented in Figure 2. The presented PCA plots represent over 88% of the total variation between samples. Acetylation was found important for controlling the functionality of starches in the control of emulsion rheology as four preparations of cross-linked and acetylated starches formed one group on the PCA score plot. Both preparations of chemically unmodified starch and cross-linked pregelatinized starch were also found to be similar. The most different from the other preparations was distarch phosphate HS. However, the location of vectors indicates a weak correlation of the parameters considered. The highest, albeit negative, correlation was observed for thixotropy, which is in its essence a measure of the rheological instability of the system. A slight positive correlation was observed between the creaming index and activation energy values.

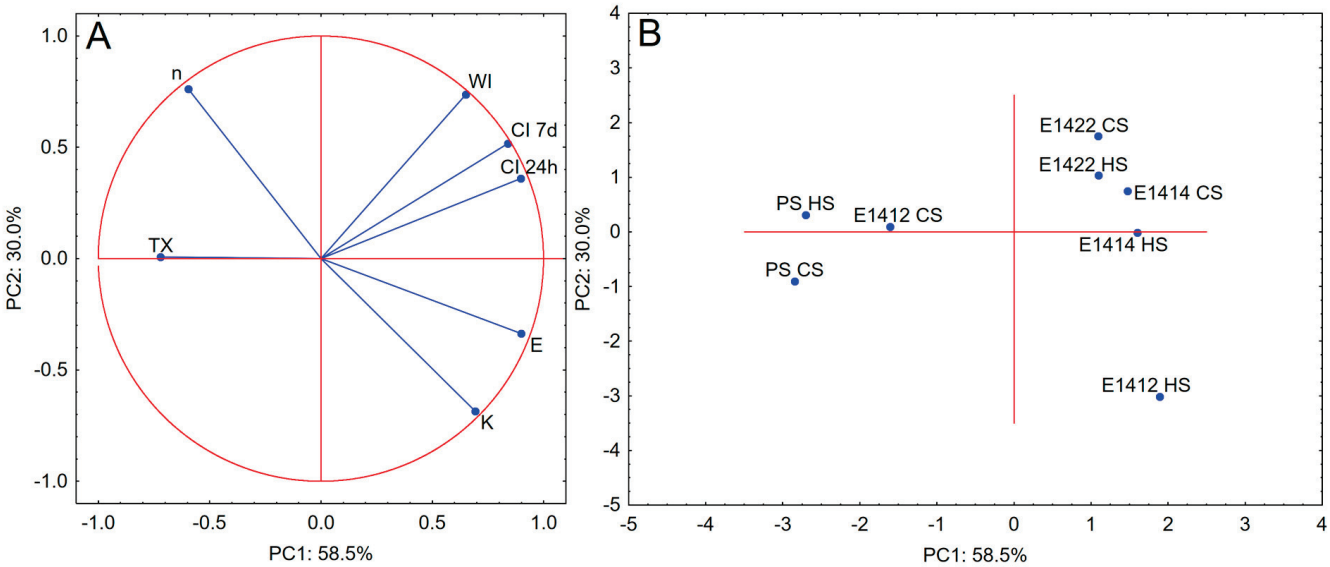

Figure 2. PCA analysis—(**A**) (loadings plot) and (**B**) (score plot) for parameters of stability of the emulsions and their rheological properties (CI 24 h—creaming index after 24 h of storage; CI 7 d—creaming index after 7 days of storage; WI—whiteness index; K—consistency index; n—flow behaviour index; E—flow activation energy; TX—thixotropy; PS HS—native potato starch; PS CS pregelatinized potato starch; E1412 HS—distarch phosphate; E1412 CS—pregelatinized distarch phosphate; E1414 HS acetylated distarch phosphate; E1414 CS—pregelatinized acetylated distarch phosphate; E1422 HS acetylated distarch adipate; E1414 CS—pregelatinized acetylated distarch adipate).

2.3. Molecular Dynamics of Emulsions

Two components of the T_1 and T_2 relaxation times were observed in the emulsion studied (Table 3). This means that there are two fractions of protons in the system that relax at different rates and that the chemical exchange between these fractions of protons is much slower than the relaxation time. Long components (T_{12} and T_{22}) reflect the relaxation processes of protons contained in the starch paste, while short components (T_{11} and T_{21}) refer to the fat fraction of the emulsion. In the emulsions formed, the values of short components were significantly lower than the values of relaxation times as in pure oil $T_1 = 102.8 \pm 0.8$ ms and $T_2 = 88.4 \pm 1.1$ ms were measured. The shortening of relaxation times depended on the type of starch and usually decreased further during storage for 24 h except emulsions based on chemically unmodified starch. An especially significant increase, in the case of the T_{11} relaxation time, was observed. That indicates some instability of the emulsion. Cross-linked starches revealed higher relaxation times; however, after 24 h, the T_{11} and T_{12} values slightly decreased. The exception are emulsions based on acetylated distarch adipate, for which no changes in the short components of relaxation times were observed. Additionally, it was found that the fat fraction of emulsions obtained from HS and CS had almost no differences. A strong decrease in the relaxation times was also observed for the continuous phase of the emulsion, as for pure water the values $T_1 = 2760$ ms and $T_2 = 2500$ ms were measured. The long components T_{12} and T_{22} of relaxation times differed due to the modification method applied (Table 3). Primarily, it is worth noting that all CS preparations formed emulsions for which the relaxation times T_{12} and T_{22} nearly did not change over time. This means that starches soluble in cold water formed emulsions that are more stable in terms of proton relaxation phenomena in the water phase.

PCA analysis including the data describing the stability of emulsions and proton relaxation times (Figure 3), in contrast to rheological properties, proves a good correlation between the analysed parameters. A positive correlation was observed between the emulsion stability parameters and the relaxation times T_{22} and T_{12}. A high negative correlation was observed for T_{11} 24 h. The relaxation times T_{21} and T_{11} 2 h did not show any significant

correlation with the creaming and whiteness indexes. The presented PCA plots represent 77% of the total variation between samples. All cross-linked and acetylated starches were very close to each other. Both samples of distarch phosphate were close to samples subjected only to physical modification. Similar to the analysis of rheological properties, native potato starch stands out from the other starches.

Table 3. The data of proton relaxation phenomena in the emulsions studied.

	Short Component of the Spin-Lattice Relaxation Time T_{11}		Short Component of the Spin-Spin Relaxation Time T_{21}		Long Component of the Spin-Lattice Relaxation Time T_{12}		Long Component of the Spin-Spin Relaxation Time T_{22}	
	2 h	**24 h**	**2 h**	**24 h**	**2 h**	**24 h**	**2 h**	**24 h**
PS HS	57.8 ± 0.9	79.2 ± 0.7	54.5 ± 3.7	69.9 ± 5.6	805.7 ± 6.1	829.2 ± 2.7	502.5 ± 6.2	451.1 ± 6.8
PS CS	60.9 ± 0.9	75.2 ± 2.0	39.2 ± 8.5	44.8 ± 5.2	841.8 ± 4.3	847.1 ± 1.1	460.5 ± 1.7	466.8 ± 5.9
E1412 HS	67.5 ± 0.9	64.1 ± 0.7	55.9 ± 3.8	39.3 ± 2.9	858.1 ± 6.0	840.1 ± 5.0	455.5 ± 6.1	394.2 ± 4.3
E1412 CS	71.5 ± 1.2	68.1 ± 2.1	57.9 ± 4.1	54.5 ± 2.2	827.7 ± 4.7	820.1 ± 3.1	395.1 ± 4.2	394.8 ± 1.5
E1414 HS	74.3 ± 0.6	69.1 ± 0.7	66.3 ± 4.9	58.9 ± 4.2	884.8 ± 2.9	829.2 ± 2.7	532.4 ± 5.8	522.1 ± 6.8
E1414 CS	66.7 ± 1.2	65.5 ± 1.2	53.6 ± 8.4	50.3 ± 1.5	850.5 ± 5.9	858.8 ± 9.9	510.5 ± 1.7	559.1 ± 2.7
E1422 HS	67.0 ± 0.5	65.8 ± 0.5	47.9 ± 8.0	490. ± 3.3	881.6 ± 3.6	862.4 ± 2.2	525.7 ± 2.0	536.3 ± 4.2
E1422 CS	670. ± 0.8	65.3 ± 1.2	49.9 ± 2.7	49.7 ± 3.4	866.5 ± 3.6	855.4 ± 3.3	559.9 ± 6.7	561.5 ± 4.4

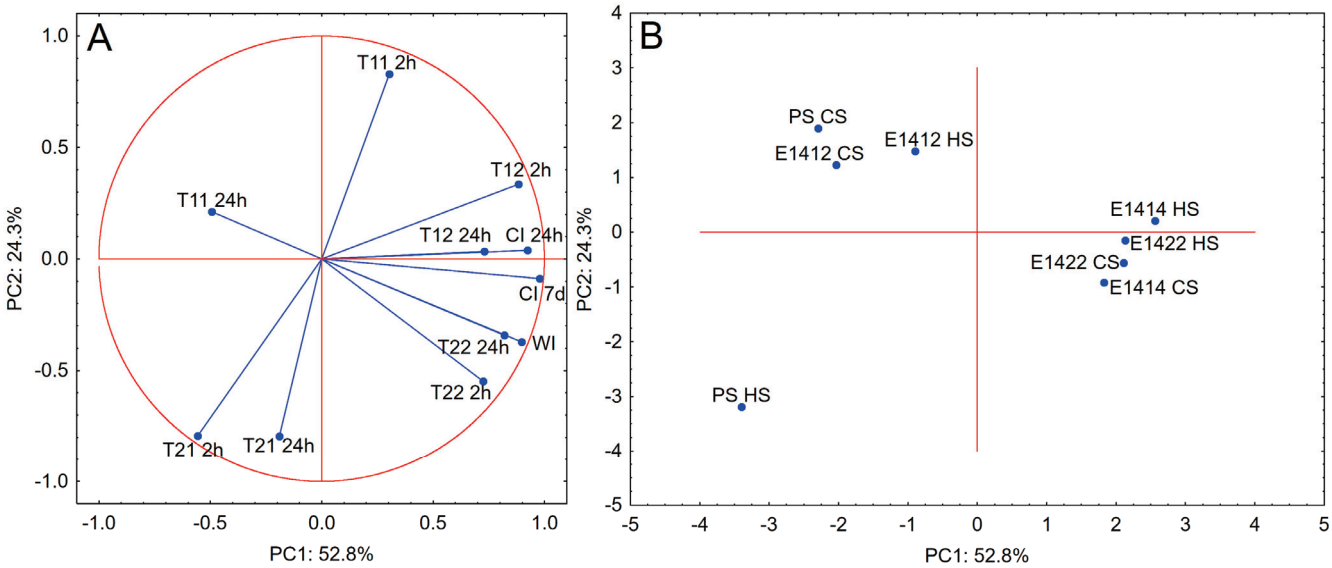

Figure 3. PCA analysis—(**A**) (loadings plot) and (**B**) (score plot) for parameters of stability of the emulsions and the parameters of proton relaxation phenomena (CI 24 h—creaming index after 24 h of storage; CI 7 d—creaming index after 7 days of storage; WI—whiteness index; T_{11}—short component of the spin-lattice relaxation time (measured after 2 h or 24 h); T_{21}—short component of the spin-spin relaxation time (measured after 2 h or 24 h); T_{12}—long component of the spin-lattice relaxation time (measured after 2 h or 24 h); T_{22}—long component of the spin-spin relaxation time (measured after 2 h or 24 h).

2.4. Molecular Structure of Starch Preparations

The functional properties of starch in aqueous media depend both on the configuration of macromolecules and their conformation in solution. The method of choice for this type of study is size exclusion chromatography with triple detection. This method, thanks to the use of refractometric, viscometric and light scattering detectors, provides information on the molecular mass distribution, as well as several parameters describing the size and shape of the starch macromolecules in the solution [56–58]. Concerning the data presented in Table 4, it is worth noting that CS preparations soluble in cold water were characterized

by significantly higher molecular mass values. In other words, hydrothermal treatment of starch, applied to obtain cold-water soluble preparations, was associated with an increase in the molecular mass of this polymer. This information may seem surprising as many years of experience of starch technologists and numerous literature reports prove the reduction of starch viscosity in the process of pregelatinization and drum-drying [38–40,59,60]. Despite that, the relationship between hydrothermal treatment and the increase in molecular weight while reducing the viscosity of pastes was presented [61]. The explanation of the observed phenomena is possible by the analysis of the derivative values calculated based on the comparison of data from the three detectors. First of all, the increase in the molecular mass of CS starch is associated with an increase in the degree of branching. Branched starches adopt such a conformation in the solution that their hydrodynamic radius does not change significantly. The radius of gyration changes slightly more, which results in changes in the Rg/Rh ratio, which is a measure of the shape of macromolecules in solution. It is assumed that compact spheres are described by the Rg/Rh value of 0.778, while coils and rods have a value > 2.0 [62]. Also, the lower than 0.5 values of the Mark–Houwink α coefficient, observed for all analysed samples, indicates the branched structure of macromolecules [63].

Table 4. Molecular masses and hydrodynamic parameters of investigated starches.

	Potato Starch		**E1412**		**E1414**		**E1422**	
Parameter	**HS**	**CS**	**HS**	**CS**	**HS**	**CS**	**HS**	**CS**
M_n [Dalton]	2.52×10^6 $\pm 3.61 \times 10^5$	6.46×10^6 $\pm 5.04 \times 10^5$	1.74×10^7 $\pm 2.25 \times 10^6$	1.08×10^7 $\pm 1.31 \times 10^6$	7.74×10^6 $\pm 1.55 \times 10^5$	3.68×10^6 $\pm 1.68 \times 10^5$	1.52×10^7 $\pm 4.53 \times 10^6$	1.27×10^7 $\pm 1.53 \times 10^6$
M_w [Dalton]	2.87×10^7 $\pm 7.71 \times 10^5$	4.20×10^7 $\pm 1.23 \times 10^6$	4.22×10^7 $\pm 1.36 \times 10^6$	4.57×10^7 $\pm 1.07 \times 10^6$	3.24×10^7 $\pm 1.20 \times 10^5$	3.48×10^7 $\pm 1.01 \times 10^6$	3.14×10^7 $\pm 2.23 \times 10^6$	3.72×10^7 $\pm 9.12 \times 10^5$
M_z [Dalton]	6.10×10^8 $\pm 6.43 \times 10^6$	9.99×10^7 $\pm 4.36 \times 10^6$	9.18×10^7 $\pm 2.29 \times 10^7$	9.59×10^7 $\pm 7.93 \times 10^6$	6.13×10^7 $\pm 1.46 \times 10^6$	9.27×10^7 $\pm 8.94 \times 10^6$	5.15×10^7 $\pm 4.44 \times 10^6$	6.16×10^7 $\pm 5.62 \times 10^6$
M_w/M_n	11.52 $\pm 1.95^{ab}$	6.51 $\pm 0.32^{ab}$	2.46 $\pm 0.40^{ab}$	4.28 $\pm 0.62^{ab}$	4.19 $\pm 0.07^{ab}$	9.48 $\pm 0.71^{ab}$	2.14 $\pm 0.49^{a}$	2.95 $\pm 0.43^{ab}$
Intrinsic viscosity [IV] [dl/g]	1.407 $\pm 0.044^{c}$	0.935 $\pm 0.097^{ab}$	1.130 $\pm 0.219^{abc}$	1.068 $\pm 0.052^{abc}$	1.372 $\pm 0.007^{c}$	0.825 $\pm 0.055^{a}$	1.343 $\pm 0.057^{c}$	1.385 $\pm 0.038^{c}$
Hydrodynamic radius R_h—[nm]	79 ± 2^{c}	77 ± 4^{bc}	85 ± 2^{cd}	82 ± 0^{cd}	80 ± 0^{cd}	66 ± 0^{ab}	83 ± 1^{cd}	87 ± 1^{d}
Radius of gyration R_g—[nm]	96 ± 6^{b}	166 ± 2^{cde}	187 ± 0^{cde}	227 ± 10^{f}	197 ± 9^{cdef}	214 ± 22^{ef}	212 ± 15^{ef}	149 ± 5^{cd}
R_g/R_h	1.22 $\pm 0.10^{ab}$	2.15 $\pm 0.13^{bcde}$	2.19 $\pm 0.06^{e}$	2.76 $\pm 0.12^{abcd}$	2.46 $\pm 0.11^{e}$	3.24 $\pm 0.30^{abcde}$	2.56 $\pm 0.15^{cde}$	1.72 $\pm 0.08^{de}$
Mark–Houwink α	0.279 $\pm 0.073^{ab}$	0.376 $\pm 0.004^{bcde}$	0.459 $\pm 0.010^{e}$	0.305 $\pm 0.011^{abcd}$	0.446 $\pm 0.001^{e}$	0.362 $\pm 0.016^{abcde}$	0.389 $\pm 0.016^{cde}$	0.406 $\pm 0.037^{de}$
Number of branching	1010 $\pm 56^{b}$	3387 $\pm 145^{c}$	2481 $\pm 347^{e}$	3322 $\pm 4^{bc}$	1488 $\pm 68^{e}$	3558 $\pm 171^{c}$	1629 $\pm 186^{d}$	1736 $\pm 155^{e}$

Explanatory notes: values marked with the same letter do not differ significantly $p > 0.05$.

Chemical modification caused significant changes in the molecular mass of starch Table 4). As expected, an increase in the number and weight of the average molecular masses was observed due to the starch cross-linking process. It may seem surprising that the z-average molecular weight of chemically unmodified starch was the highest. An explanation for this paradox is possible if is considered that each of these parameters is related to different physical quantities. The number-average molecular mass is directly defined by the number of starch macromolecules, while the weight-average molecular mass is determined by the weight fractions of individual fractions with the same molecular mass. As a consequence, the M_n value is most defined by small molecules, while the M_w value is most determined by larger ones. The z-average molecular mass is related to light

scattering processes in colloidal starch dispersions and, therefore, favours the effect of the largest molecules in the sample. Lower M_z values of cross-linked starches accompanied by increases of M_n and M_w indicated that the cross-linking process preferentially took place with the participation of smaller starch macromolecules. This hypothesis is confirmed by the lower polydispersity values (M_w/M_n) of cross-linked starches than those observed in chemically unmodified starch. Dual modified starches E1414 and E1422 were generally characterised by lower molecular masses than distarch phosphate E1412; however, in our previous work, we found only a small effect of the degree of acetylation process on the molecular structure of this polysaccharide [64].

PCA analysis (Figure 4) proved the correlation between emulsion stability parameters and some parameters of the size exclusion chromatography results. A strong positive correlation was found for the number average molecular mass, Mark–Houwink equation α parameter and stability parameters. The samples that represent this profile also show low M_w/M_n values (E1414 HS, E1422 HS and E1422 CS). It might seem that interactions between solvent–polymer and polymer–polymer are crucial here since the higher the M–H α then the more a polymer molecule attracts the surrounding solvent than the mutual attraction of the molecules. However, the highly stable emulsion sample E1414 CS was positioned among the PS CS and E1414 CS samples. These samples show high M_w, number of branches, R_g/R_h and R_g values. The position of the PS HS sample is determined by a high M_z. The E1412 HS sample is not well represented in this principal component system, being close to the origin of coordinates. The above shows that it is not possible to clearly indicate the starch parameters that are responsible for the stability of the tested emulsions. It seems that that the type of starch modification used is crucial here.

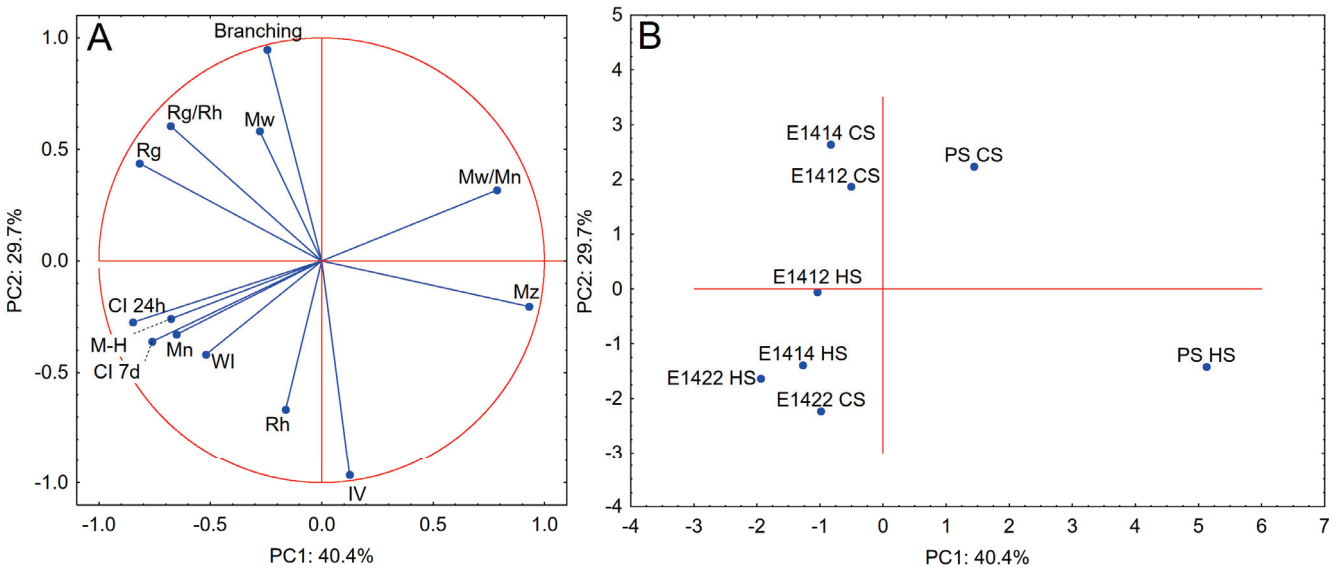

Figure 4. PCA analysis—(**A**) (loadings plot) and (**B**) (score plot) for parameters of stability of the emulsions and the parameters of proton relaxation phenomena (CI 24 h—creaming index after 24 h of storage; CI 7 d—creaming index after 7 days of storage; WI—whiteness index; M_n—number average molecular mass; M_w—weight average molecular mass; M_z—z average molecular mass; M_n/M_w—polydispersity index; R_g—radius of gyration; R_h—hydrodynamic radius; IV—intrinsic viscosity; M-H—Mark–Houwink equation α parameter; Branching—number of branches per molecule.

2.5. Surface Activity of Starch Preparations

Surface and interfacial tension γ isotherms (Figure 5) showed that modification significantly changed the surface activity of starch. The surface tension values of the water/air system were lower in the presence of chemically modified starches than in the presence of native starch. Physical modification alone did not have any effect on surface tension. The strongest increase in surface activity was observed for cross-linked and additionally

acetylated starches. In this case, physical modification caused a further decrease in the surface tension value. Similar, although less spectacular, results were obtained for the experiment at the water/toluene interface. Chemical modification of potato starch (irrespective of the type of modification) resulted in products that showed greater ability to reduce interfacial tension at the water/toluene interface compared to native starch. Also, in this case, it was observed that the physical modification of potato starch alone did not cause significant changes in the efficiency of reducing interfacial tension. However, dual physical and chemical modification resulted in higher interfacial activity of products than chemical modification alone. Similar observations were reported in the literature [65,66].

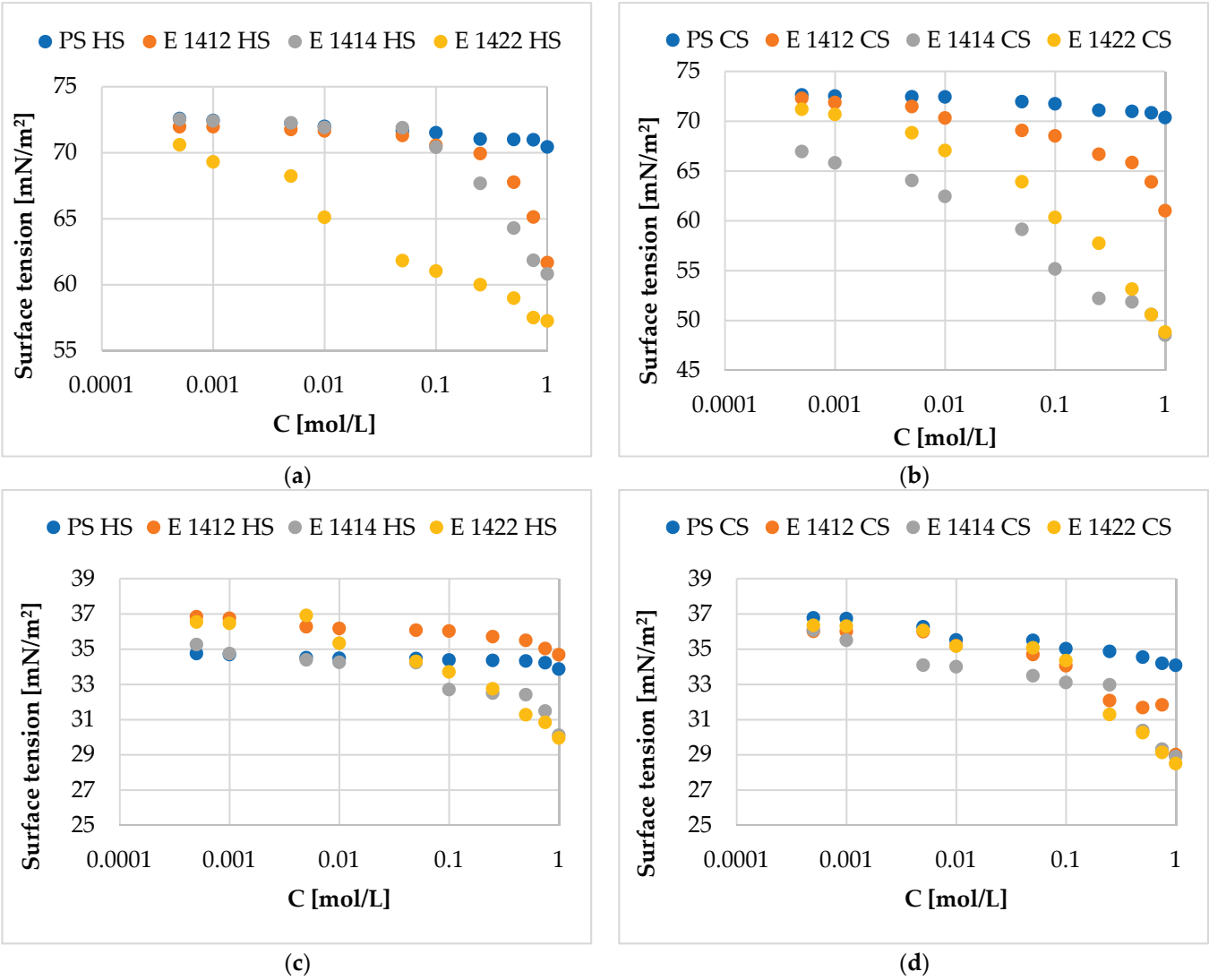

Figure 5. Surface tension (air/water system) (**a**,**b**) and interfacial tension (toluene/water system) (**c**,**d**) of the investigated starches: PS HS—native potato starch; PS CS pregelatinized potato starch; E1412 HS—distarch phosphate; E1412 CS—pregelatinized distarch phosphate; E1414 HS acetylated distarch phosphate; E1414 CS—pregelatinized acetylated distarch phosphate; E1422HS acetylated distarch adipate; E1414 CS—pregelatinized acetylated distarch adipate.

The values of the adsorption parameters resulting from the approximation of surface/interfacial tension isotherms data by the Szyszkowski equation are presented in Tables 5 and 6. Their comparative analysis for native starch and chemically and physically modified derivatives allows for assessing the impact of chemical and physical modifications on the surface properties of starch preparations. In general, it should be noted that both chemical and physical modifications of starch reduce the tendency of starch preparations

to adsorb. However, the type of modification has a significant impact on the packing and orientation of polysaccharide molecules in the saturated adsorption layer. In the relevant literature, there are very few reports that directly allow for the quantitative assessment of the effect of the starch modification process on its adsorption properties [67–69]. Only some of them concern the effect of modification (both physical and chemical) on the change in the functional properties of starch preparations, which are the effect of changes in adsorption properties. The studies were conducted for potato starch, but also for other botanical origins [70]. The value of ΔG_{ads} (Table 5) indicates that native potato starch molecules (potato HS) exhibit a strong tendency to adsorb at the water/air interface, but due to the size of the molecules, they form a loosely packed adsorption layer. As was mentioned above, the physical modification of the starch does not cause significant changes in the adsorption properties of the pregelatinized preparation PS CS. The ΔG_{ads} and Γ^{∞} values for native and gelatinized starch do not differ significantly. However, cross-linking of native starch results in a drastic reduction in the material's tendency to adsorb at the interphase. The value of free energy of adsorption for the E1412 HS derivative is almost 10 times lower compared to ΔG_{ads} for native starch. Furthermore, cross-linking of the starch molecule is accompanied by a significant (more than 3-fold) reduction in the surface concentration of the adsorption layer formed at the water/air interface. Additional pregelatinization of the cross-linked starch preparation results in a significant increase in both the tendency to adsorb and the surface concentration at the saturated interphase. It is worth noting that the double-esterified derivative (E1414 HS) forms a similarly packed monolayer as the E1412 HS preparation. However, the pregelatinization of acetylated distarch phosphate, which increases the branching of polysaccharide macromolecules, results in a marked increase in both their tendency to adsorb at the water/air interface and the area occupied by statistical macromolecules in the saturated adsorption monolayer. On the other hand, the cross-linking process of esterified starch (E1422 HS), which increases the molecular mass and leads to the formation of bridges between macromolecules, results in a starch preparation that forms a highly densely packed monolayer of macromolecules in the water/air interface. In general, the increase in branching within starch macromolecules caused by cross-linking the starch preparation leads to changes in both the polysaccharide's adsorption tendency and the packing density of the formed Gibbs adsorption layer. Pregelatinization of acetylated and cross-linked starch preparations further results in the compaction of molecules, which is reflected in the values of Γ^{∞} and A_{min}. A similar trend can be observed in the water/toluene system. However, the changes in the values of individual adsorption parameters are not as significant.

Table 5. Adsorption parameters at the water/air interface of the investigated starches.

Starch	Gibbs Free Energy of Adsorption $-\Delta G_{ads}$ [kJ/mol]	Surface Excess $\Gamma^{\infty} \times 10^7$ [mol/m^2]	Surface Area Per Macromolecule in the Saturated Adsorption Monolayer $A_{min} \times 10^{18}$ [nm^2]	Szyszkowski Isotherm Coefficient A_{sz} [mol/dm^3]	Szyszkowski Isotherm Coefficient B_{sz} [–]
potato HS	31.37	1.03	16.14	0.000003	0.0034
potato CS	28.02	1.14	14.52	0.000012	0.0038
E1412 HS	3.50	0.27	0.61	0.243	0.091
E1412 CS	15.93	6.57	2.53	0.0016	0.022
E1414 HS	5.46	0.23	0.72	0.11	0.078
E1414 CS	24.15	0.10	1.66	0.00005	0.034
E1422 HS	22.85	7.35	2.26	0.0001	0.025
E1422 CS	14.75	0.16	1.04	0.0026	0.054

The PCA analysis results showed a strong correlation between the Gibbs free energy of adsorption and the emulsion stability parameters. This indicates the crucial importance of thermodynamics in the formation and stabilization of emulsions. The other parameters

of the Szyszkowski equation did not reveal any significant significance. The data presented in Figure 6B indicate that the presence of acetyl groups in the structure of starch macromolecules was of crucial importance for the surface activity of starch. Physical modification was also important as the PS CS and E1412 CS starches are located close together on the score plot. The preparations that differed the most were PS HS and E1412 HS. This means that cross-linking significantly changed the functionality of starch concerning the surface activity of potato starch.

Table 6. Adsorption parameters at the water/toluene interface of the investigated starches.

Starch	Gibbs Free Energy of Adsorption $-\Delta G_{ads}$ [kJ/mol]	Surface Excess $\Gamma^{\infty} \times 10^7$ [mol/m^2]	Surface Area Per Macromolecule in the Saturated Adsorption Monolayer $A_{min} \times 10^{18}$ [nm^2]	Szyszkowski Isotherm Coefficient A_{sz} [mol/dm^3]	Szyszkowski Isotherm Coefficient B_{sz} [−]
Potato HS	26.44	32.08	51.76	0.00002	0.0023
Potato CS	18.40	1.53	10.87	0.0006	0.01
E1412 HS	17.72	1.07	15.55	0.0008	0.0072
E1412 CS	12.13	5.40	3.08	0.0074	0.036
E1414 HS	24.97	2.22	7.49	0.00004	0.015
E1414 CS	18.95	3.70	4.49	0.0005	0.025
E1422 HS	11.46	5.80	2.86	0.0097	0.039
E1422 CS	8.32	0.10	1.64	0.035	0.068

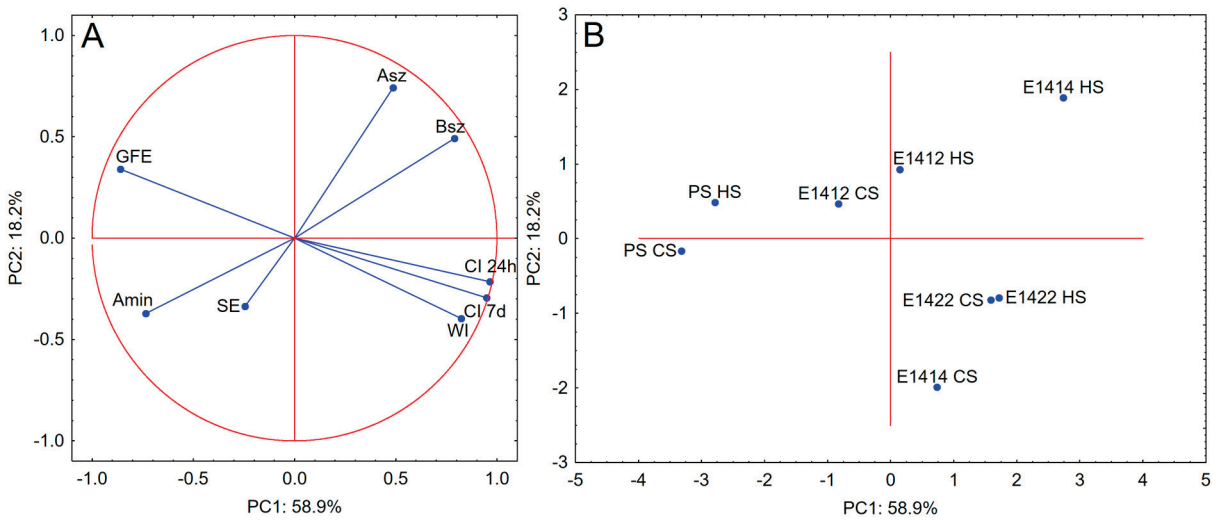

Figure 6. PCA analysis—(**A**) (loadings plot) and (**B**) (score plot) for parameters of the stability of the emulsions and the parameters of the surface activity of starches (CI 24 h—creaming index after 24 h of storage; CI 7 d—creaming index after 7 days of storage; WI—whiteness index; GFE—Gibbs free energy of adsorption (ΔG_{ads}); SE—Surface excess (Γ_{∞}); A_{min}—Surface area per macromolecule in the saturated adsorption monolayer; A_{sz}—Szyszkowski isotherm coefficient; B_{sz}—Szyszkowski isotherm coefficient.

3. Materials and Methods

3.1. Materials

Commercial food-grade chemically modified starches kindly provided by the potato processing company "Zetpezet" Ltd. (Piła, Poland) were the basic working material:

- Distarch phosphate E1412;
- Acetylated distarch phosphate E1414;
- Acetylated distarch adipate E1422.

All of the above starch variants were provided in hot and cold soluble (pregelatinized) variants. Native potato starch was used as a reference material. All samples were manufactured in the year 2018 and were produced from starch obtained during one production campaign.

3.2. Emulsion Preparation

The model emulsions were prepared with food-grade rapeseed oil and deionized water in a 1:3 ratio. A Silent Crusher homogenizer, Heidolph (Schwabach, Germany), was used to prepare the emulsion. Homogenization of the mixture was carried out for 3 min at 21,000 revolutions per second.

Emulsions using hot soluble starches (HS) were prepared based on 10% starch pastes that were gelatinized in a boiling water bath for 20 min. Oil was added to the cooled gelatinized starch pastes and afterwards, homogenization was performed to obtain an emulsion.

Emulsions from cold-soluble starch (CS) preparations were prepared similarly as is practised in the food industry for the preparation of sauces. To this end, 10% starch (*w*/*w* of water) was suspended in the oil, and subsequently, water was added and homogenization was performed to obtain an emulsion.

3.3. Methods

3.3.1. Creaming Index

The creaming index was determined according to the procedure of Titus and co-authors modified by Acton and Saffle [71]. Emulsion samples were placed in centrifuge tubes and incubated at 37 °C for 24 h and 7 days. Subsequently, the samples were centrifuged at 2500× *g* for 10 min. The creaming index (CI) was calculated from the following formula:

$$CI = (V_m - V_o)/V_m \bullet 100\%, \quad (1)$$

where: V_m—the initial volume of the emulsion [cm^3] and V_o—the volume of the separated oil [cm^3].

3.3.2. Colour Measurements

Colour measurements of the emulsions were made using the Minolta Chroma Meter CR-310 (Japan) colourimeter. Measurement conditions were chosen: observer 2°, illuminant C, colour space CIE L*a*b*. Absolute colour parameters as well as the whiteness index (WI) were determined:

$$WI = 100 - \sqrt{((100 - L)^2 + a^2 + b^2)} \quad (2)$$

where: L*—lightness, a value between 0 (black) and 100 (white); a—chromatic coordinate indicating red (positive values) and green (negative values) balance; and b—chromatic coordinate indicating yellow (positive values) and blue (negative values) balance.

3.3.3. Rotational Rheometry

The rheological properties of the emulsions were determined using a RotoVisco1 rheometer (Haake Technik GmbH, Vreden, Germany) equipped with a DC30-K10 refrigerated bath with an immersion circulator. Before the measurement, the samples were brought to 20 °C and relaxed in a measuring cylinder for 5 min. Data collection and calculations were made using RheoWin 3.61 software. The following measurements were performed:

Flow curves were determined using the Z20 DIN measurement system, within 1–600–1 s^{-1} shear rate in a time of 2 min. Obtained flow curves were described with the Ostwald de Waele equation.

Temperature versus apparent viscosity curves were determined at 100 s^{-1} shear rate in the 20 to 65 °C temperature range and a heating speed of 3 °C/min. Samples were pre-sheared at 100 s^{-1} for 180 s. The obtained curves were described by the Arrhenius Temperature–Time Superposition equation.

3.3.4. Low Field NMR

NMR relaxation times were analysed with a pulse NMR spectrometer PS15T operating at 15 MHz (Ellab, Poznań, Poland) in triplicate. The inversion–recovery (180-TI-90) pulse sequence was applied for measurements of the T_1 relaxation times. The 180 pulse was 4.8 μs, the distance between RF pulses (TI) changed from 2 to 1800 ms, and the repetition time TR between sequences was 18 s.

Measurements of the spin-spin (T_2) relaxation times were taken using the pulse train of the Carr–Purcell–Meiboom–Gill spin echoes (90-TE/2-$(180)_n$). The echo time TE was 3 ms, and the number of the spin-echoes signal (n) was 50. The five accumulations of the spin-echo trains were used. The repetition time between pulse trains was 15 s.

3.3.5. Size Exclusion Chromatography

Starch samples were dissolved in DMSO at 80 °C for 4 days with gentle stirring (Reacti-Therm, Thermo Fisher Scientific, Waltham, MA, USA). The concentration of the sample separated with SEC was 1 mg/mL. The samples were not filtered prior to analysis. The injection volume was 100 μL. SEC equipment with triple detection (Viscotek 305 TDA) was used (Malvern Practical, Malvern, UK). A conventional dual cell refractometer, viscometer, and light scattering detectors (low-angle light scattering, LALS and right-angle light scattering RALS) were employed to act together. One organic SEC column (PSS GRAM series, 3000 Å, 8 × 300 mm) with a guard column (Polymer Standard Service GmbH, Mainz, Germany) was applied. The flow rate of DMSO was 0.3 mL/min at 70 °C. The calibration was performed with the pullulan standard (113,000 g/mol). The refractive index (RI) of the solvent was 1.4595 [72]. The calculations were performed using OmiSEC 4.7 software (Malvern, TX, USA) assuming the increment in the refractive index (dn/dc) for starch in DMSO is 0.0659 mL/g. The Zimm–Stockmayer equation for a randomly branched polydisperse polymer was used to calculate the number of branches per molecule (Bn). Due to the lack of an appropriate linear standard for starch, the pullulan standard was used as a linear molecule. The determined M–H (a) = 0.710 and the M–H intercept (log K = −3.175) for pullulan in DMSO were used. The parameters obtained from the SEC separations were the mean of three independent trials.

3.3.6. Surface Properties

The surface-active properties of all starches obtained were studied by the equilibrium and dynamic surface/interfacial tension experiments performed in two systems, namely air/water and oil/water.

The equilibrium surface/interfacial tension of the starch samples was measured by the du Noüy ring method with a KRÜSS K12 tensiometer (Hamburg, Germany) [73]. The standard deviation of the surface/interfacial tension measurements was 0.05 mN/m. All measurements were carried out at 21 ± 0.1 °C and repeated three times. Twice distilled water with a conductivity of 3 μS was used as the aqueous phase. The toluene used as the organic phase for interfacial tension measurements was obtained from Aldrich Company (St. Louis, MS, USA). It is obvious that toluene cannot be used as a food additive; however, it was applied in our investigations as the model organic phase [30].

The experimentally determined surface/interfacial tension isotherms were approximated using the Szyszkowski equation. Based on the coefficients of the Szyszkowski equation, the values of adsorption parameters were estimated, such as the Gibbs free energy of adsorption, surface excess at the saturated interphase, and the area occupied by a statistical molecule adsorbed at the saturated interphase.

3.3.7. Statistical Analysis

All analyses were performed in triplicate (unless otherwise stated), and the results are presented as mean value ± standard deviation. Principal component analysis (PCA) was performed based on the correlation matrix. The statistical analyses were performed using Statistica 13.3 (TIBCO Software Inc., Palo Alto, CA, USA).

4. Conclusions

The studies presented above have shown that the stability of an emulsion is influenced by several factors but their significance varies considerably. Although the primary factor determining the functionality of starch preparations is their molecular structure, the proton relaxation phenomena occurring in the continuous phase of the emulsion, which are its consequences, turned out to be crucial for the stability of the emulsion. The thermodynamics of the adsorption of starch macromolecules at the water/oil interface was also of great importance.

Modification significantly improves the applicability of starch for emulsion stabilization. This applies not only to cross-linking and acetylation but also to physical modification. This is because not only cross-linking but also pregelatinization causes changes in the molecular structure of starch, including an increase in the molecular weight and the degree of branching of macromolecules. This implies changes in the conformation of the starch macromolecules in solution and in proton relaxation processes affects their ability to adsorb in the water/oil interface and, consequently, in their ability to stabilize the emulsion.

Author Contributions: Conceptualization, J.L.T.-B.; methodology, J.L.T.-B., J.L., A.S., K.P., H.M.B. and G.L.; software, J.L.T.-B. and J.L.; validation, J.L.T.-B.; formal analysis, J.L.T.-B. and G.L.; investigation, J.L.T.-B., J.L., A.S., K.P., H.M.B. and G.L.; resources, J.L.T.-B.; data curation, J.L.T.-B., K.P. and A.S.; writing—original draft preparation, J.L.T.-B., J.L., A.S., K.P., H.M.B. and G.L.; writing—review and editing, J.L.T.-B. and J.L.; visualization, J.L.T.-B. and J.L.; supervision, G.L.; project administration, J.L.T.-B.; funding acquisition, J.L.T.-B. and K.P. All authors have read and agreed to the published version of the manuscript.

Funding: This work was performed with the financial support of The Polish Ministry of Agriculture and Rural Development ZK-137-01 and The Polish Ministry of Science and Higher Education 0912/SBAD/2401.

Institutional Review Board Statement: Not applicable.

Informed Consent Statement: Not applicable.

Data Availability Statement: The original contributions presented in this study are included in the article; further inquiries can be directed to the corresponding author.

Conflicts of Interest: The authors declare no conflicts of interest.

References

1. Tan, C.; McClements, D.J. Application of Advanced Emulsion Technology in the Food Industry: A Review and Critical Evaluation. *Foods* **2021**, *10*, 812. [CrossRef]
2. McClements, D.J.; Jafari, S.M. Improving Emulsion Formation, Stability and Performance Using Mixed Emulsifiers: A Review. *Adv. Colloid Interface Sci.* **2018**, *251*, 55–79. [CrossRef] [PubMed]
3. Dickinson, E. Hydrocolloids as Emulsifiers and Emulsion Stabilizers. *Food Hydrocoll.* **2009**, *23*, 1473–1482. [CrossRef]
4. Tamang, N.; Shrestha, P.; Khadka, B.; Mondal, M.H.; Saha, B.; Bhattarai, A. A Review of Biopolymers' Utility as Emulsion Stabilizers. *Polymers* **2022**, *14*, 127. [CrossRef] [PubMed]
5. Waterschoot, J.; Gomand, S.V.; Fierens, E.; Delcour, J.A. Production, Structure, Physicochemical and Functional Properties of Maize, Cassava, Wheat, Potato and Rice Starches. *Starch Stärke* **2015**, *67*, 14–29. [CrossRef]
6. Ashogbon, A.O.; Akintayo, E.T. Recent Trend in the Physical and Chemical Modification of Starches from Different Botanical Sources: A Review. *Starch Stärke* **2014**, *66*, 41–57. [CrossRef]
7. Singh, J.; Kaur, L.; McCarthy, O.J. Factors Influencing the Physico-Chemical, Morphological, Thermal and Rheological Properties of Some Chemically Modified Starches for Food Applications—A Review. *Food Hydrocoll.* **2007**, *21*, 1–22. [CrossRef]
8. Kumari, B.; Sit, N. Comprehensive Review on Single and Dual Modification of Starch: Methods, Properties and Applications. *Int. J. Biol. Macromol.* **2023**, *253*, 126952. [CrossRef]
9. Shabir, I.; Dar, A.H.; Dash, K.K.; Srivastava, S.; Pandey, V.K.; Manzoor, S.; Manzoor, S.; Bashir, I. Formulation, Characterization, and Applications of Organic Pickering Emulsions: A Comprehensive Review. *J. Agric. Food Res.* **2023**, *14*, 100853. [CrossRef]
10. Almeida, R.L.J.; Monteiro, S.S.; Santos, N.C.; Rios, N.S.; dos Santos, E.S. Starch Modification and Its Application in Pickering Emulsion Stabilization: A Review. *J. Food Meas. Charact.* **2024**, *18*, 4984–5003. [CrossRef]
11. Wang, R.; Li, M.; Liu, M.; Wang, A.; Strappe, P.; Blanchard, C.; Zhou, Z. Characterization of Pickering Emulsion by SCFAs-Modified Debranched Starch and a Potent for Delivering Encapsulated Bioactive Compound. *Int. J. Biol. Macromol.* **2023**, *231*, 123164. [CrossRef]

12. Abdul Hadi, N.; Marefati, A.; Matos, M.; Wiege, B.; Rayner, M. Characterization and Stability of Short-Chain Fatty Acids Modified Starch Pickering Emulsions. *Carbohydr. Polym.* **2020**, *240*, 116264. [CrossRef] [PubMed]
13. Mcclements, D.J. Critical Review of Techniques and Methodologies for Characterization of Emulsion Stability. *Crit. Rev. Food Sci. Nutr.* **2007**, *47*, 611–649. [CrossRef] [PubMed]
14. Kupikowska-Stobba, B.; Domagała, J.; Kasprzak, M.M. Critical Review of Techniques for Food Emulsion Characterization. *Appl. Sci.* **2024**, *14*, 1069. [CrossRef]
15. Tang, F.; Vasas, M.; Hatzakis, E.; Spyros, A. Chapter Five—Magnetic Resonance Applications in Food Analysis. In *Annual Reports on NMR Spectroscopy*; Webb, G.A., Ed.; Academic Press: Cambridge, MA, USA, 2019; Volume 98, pp. 239–306. ISBN 0066-4103.
16. Blümich, B. Introduction to Compact NMR: A Review of Methods. *TrAC Trends Anal. Chem.* **2016**, *83*, 2–11. [CrossRef]
17. Blümich, B. Low-Field and Benchtop NMR. *J. Magn. Reson.* **2019**, *306*, 27–35. [CrossRef]
18. Abrami, M.; Chiarappa, G.; Farra, R.; Grassi, G.; Marizza, P.; Grassi, M. Use of Low Field NMR for the Characterization of Gels and Biological Tissues. *ADMET DMPK* **2018**, *6*, 34–46. [CrossRef]
19. Baranowska, H.M.; Rezler, R. Emulsions Stabilized Using Potato Starch. *Food Sci. Biotechnol.* **2015**, *24*, 1187–1191. [CrossRef]
20. Punia Bangar, S.; Sunooj, K.V.; Navaf, M.; Phimolsiripol, Y.; Whiteside, W.S. Recent Advancements in Cross-Linked Starches for Food Applications—A Review. *Int. J. Food Prop.* **2024**, *27*, 411–430. [CrossRef]
21. Zeng, X.; Chen, H.; Chen, L.; Zheng, B. Insights into the Relationship between Structure and Rheological Properties of Starch Gels in Hot-Extrusion 3D Printing. *Food Chem.* **2021**, *342*, 128362. [CrossRef] [PubMed]
22. Xie, F.; Halley, P.J.; Avérous, L. Rheology to Understand and Optimize Processibility, Structures and Properties of Starch Polymeric Materials. *Prog. Polym. Sci.* **2012**, *37*, 595–623. [CrossRef]
23. Makowska, A.; Dwiecki, K.; Kubiak, P.; Baranowska, H.M.; Lewandowicz, G. Polymer-Solvent Interactions in Modified Starches Pastes–Electrokinetic, Dynamic Light Scattering, Rheological and Low Field Nuclear Magnetic Resonance Approach. *Polymers* **2022**, *14*, 2977. [CrossRef] [PubMed]
24. Thanh-Blicharz, J.L.; Lewandowicz, J. Functionality of Native Starches in Food Systems: Cluster Analysis Grouping of Rheological Properties in Different Product Matrices. *Foods* **2020**, *9*, 1073. [CrossRef] [PubMed]
25. Lewandowicz, J.; Le Thanh-Blicharz, J.; Szwengiel, A. The Effect of Chemical Modification on the Rheological Properties and Structure of Food Grade Modified Starches. *Processes* **2022**, *10*, 938. [CrossRef]
26. Lewandowicz, J.; Le Thanh-Blicharz, J.; Szwengiel, A. Insight into Rheological Properties and Structure of Native Waxy Starches: Cluster Analysis Grouping. *Molecules* **2024**, *29*, 2669. [CrossRef] [PubMed]
27. Sinhmar, A.; Pathera, A.K.; Sharma, S.; Nehra, M.; Thory, R.; Nain, V. Impact of Various Modification Methods on Physicochemical and Functional Properties of Starch: A Review. *Starch Stärke* **2023**, *75*, 2200117. [CrossRef]
28. He, R.; Li, S.; Zhao, G.; Zhai, L.; Qin, P.; Yang, L. Starch Modification with Molecular Transformation, Physicochemical Characteristics, and Industrial Usability: A State-of-the-Art Review. *Polymers* **2023**, *15*, 2935. [CrossRef] [PubMed]
29. Koshenaj, K.; Ferrari, G. A Comprehensive Review on Starch-Based Hydrogels: From Tradition to Innovation, Opportunities, and Drawbacks. *Polymers* **2024**, *16*, 1991. [CrossRef] [PubMed]
30. Prochaska, K.; Kędziora, P.; Le Thanh, J.; Lewandowicz, G. Surface Activity of Commercial Food Grade Modified Starches. *Colloids Surf. B Biointerfaces* **2007**, *60*, 187–194. [CrossRef] [PubMed]
31. Konował, E.; Lewandowicz, G.; Le Thanh-Blicharz, J.; Prochaska, K. Physicochemical Characterisation of Enzymatically Hydrolysed Derivatives of Acetylated Starch. *Carbohydr. Polym.* **2012**, *87*, 1333–1341. [CrossRef]
32. FAO. FAO and WHO Compendium of Food Additive Specifications. In *Joint FAO/WHO Expert Committee on Food (JECFA), Proceedings of the 86th Meeting, Geneva, Switzerland, Italy, 12–21 June 2018*; FAO JECFA Monographs 22: Rome, Italy, 2018; ISBN 9789251311004.
33. EFSA Panel on Food Additives and Nutrient Sources added to Food (ANS); Mortensen, A.; Aguilar, F.; Crebelli, R.; Di Domenico, A.; Dusemund, B.; Frutos, M.J.; Galtier, P.; Gott, D.; Gundert-Remy, U.; et al. Re-Evaluation of Oxidised Starch (E 1404), Monostarch Phosphate (E 1410), Distarch Phosphate (E 1412), Phosphated Distarch Phosphate (E 1413), Acetylated Distarch Phosphate (E 1414), Acetylated Starch (E 1420), Acetylated Distarch Adipate (E 1422), Hydroxypropyl Starch (E 1440), Hydroxypropyl Distarch Phosphate (E 1442), Starch Sodium Octenyl Succinate (E 1450), Acetylated Oxidised Starch (E 1451) and Starch Aluminium Octenyl Succinate (E 1452) as Food Additives. *EFSA J.* **2017**, *15*, e04911. [CrossRef]
34. Cornejo-Ramírez, Y.I.; Martínez-Cruz, O.; Del Toro-Sánchez, C.L.; Wong-Corral, F.J.; Borboa-Flores, J.; Cinco-Moroyoqui, F.J. The Structural Characteristics of Starches and Their Functional Properties. *CyTA J. Food* **2018**, *16*, 1003–1017. [CrossRef]
35. Zia-ud-Din; Xiong, H.; Fei, P. Physical and Chemical Modification of Starches: A Review. *Crit. Rev. Food Sci. Nutr.* **2017**, *57*, 2691–2705. [CrossRef] [PubMed]
36. Park, S.; Kim, Y.-R. Clean Label Starch: Production, Physicochemical Characteristics, and Industrial Applications. *Food Sci. Biotechnol.* **2021**, *30*, 1–17. [CrossRef] [PubMed]
37. Grant, K.R.; Gallardo, R.K.; McCluskey, J.J. Consumer Preferences for Foods with Clean Labels and New Food Technologies. *Agribusiness* **2021**, *37*, 764–781. [CrossRef]
38. Nakorn, K.N.; Tongdang, T.; Sirivongpaisal, P. Crystallinity and Rheological Properties of Pregelatinized Rice Starches Differing in Amylose Content. *Starch Stärke* **2009**, *61*, 101–108. [CrossRef]
39. Anastasiades, A.; Thanou, S.; Loulis, D.; Stapatoris, A.; Karapantsios, T.D. Rheological and Physical Characterization of Pregelatinized Maize Starches. *J. Food Eng.* **2002**, *52*, 57–66. [CrossRef]

40. Adedokun, M.O.; Itiola, O.A. Material Properties and Compaction Characteristics of Natural and Pregelatinized Forms of Four Starches. *Carbohydr. Polym.* **2010**, *79*, 818–824. [CrossRef]
41. Lewandowicz, G. Physical Modification of Starch—Really Physical? In Proceedings of the 13th International Conference on Polysaccharides-Glycoscience, Prague, Czech Republic, 8–11 November 2017; Rapkova, R., Copikova, J., Sarka, E., Eds.; Czech Chemical Society: Prague, Czech Republic, 2017; pp. 9–14.
42. Hedayati, S.; Shahidi, F.; Koocheki, A.; Farahnaky, A.; Majzoobi, M. Influence of Pregelatinized and Granular Cold Water Swelling Maize Starches on Stability and Physicochemical Properties of Low Fat Oil-in-Water Emulsions. *Food Hydrocoll.* **2020**, *102*, 105620. [CrossRef]
43. Małyszek, Z.; Lewandowicz, J.; Le Thanh-Blicharz, J.; Walkowiak, K.; Kowalczewski, P.Ł.; Baranowska, H.M. Water Behavior of Emulsions Stabilized by Modified Potato Starch. *Polymers* **2021**, *13*, 2200. [CrossRef] [PubMed]
44. Mirzaaghaei, M.; Nasirpour, A.; Keramat, J.; Goli, S.A.H.; Dinari, M.; Desobry, S. Influence of Fatty Acid-Esterified Waxy Maize Starch Type and Concentration on Stability and Properties of Oil-in-Water Emulsions. *Int. J. Biol. Macromol.* **2023**, *233*, 123526. [CrossRef]
45. Thaiwong, N.; Thaiudom, S. Stability of Oil-in-Water Emulsion Influenced by the Interaction of Modified Tapioca Starch and Milk Protein. *Int. J. Dairy Technol.* **2021**, *74*, 307–315. [CrossRef]
46. Saari, H.; Wahlgren, M.; Rayner, M.; Sjöö, M.; Matos, M. A Comparison of Emulsion Stability for Different OSA-Modified Waxy Maize Emulsifiers: Granules, Dissolved Starch, and Non-Solvent Precipitates. *PLoS ONE* **2019**, *14*, e0210690. [CrossRef] [PubMed]
47. Hong, L.-F.; Cheng, L.-H.; Gan, C.-Y.; Lee, C.Y.; Peh, K.K. Evaluation of Starch Propionate as Emulsion Stabiliser in Comparison with Octenylsuccinate Starch. *LWT* **2018**, *91*, 526–531. [CrossRef]
48. Cheong, K.W.; Mirhosseini, H.; Hamid, N.S.A.; Osman, A.; Basri, M.; Tan, C.P. Effects of Propylene Glycol Alginate and Sucrose Esters on the Physicochemical Properties of Modified Starch-Stabilized Beverage Emulsions. *Molecules* **2014**, *19*, 8691–8706. [CrossRef] [PubMed]
49. Bortnowska, G.; Balejko, J.; Schube, V.; Tokarczyk, G.; Krzemińska, N.; Mojka, K. Stability and Physicochemical Properties of Model Salad Dressings Prepared with Pregelatinized Potato Starch. *Carbohydr. Polym.* **2014**, *111*, 624–632. [CrossRef]
50. Bortnowska, G.; Balejko, J.; Tokarczyk, G.; Romanowska-Osuch, A.; Krzemińska, N. Effects of Pregelatinized Waxy Maize Starch on the Physicochemical Properties and Stability of Model Low-Fat Oil-in-Water Food Emulsions. *Food Hydrocoll.* **2014**, *36*, 229–237. [CrossRef]
51. McClements, D.J. Theoretical Prediction of Emulsion Color. *Adv. Colloid Interface Sci.* **2002**, *97*, 63–89. [CrossRef] [PubMed]
52. Zhu, Y.; Gao, H.; Liu, W.; Zou, L.; McClements, D.J. A Review of the Rheological Properties of Dilute and Concentrated Food Emulsions. *J. Texture Stud.* **2020**, *51*, 45–55. [CrossRef]
53. Costa, H.C.B.; Arouca, F.O.; Silva, D.O.; Vieira, L.G.M. Study of Rheological Properties of Açai Berry Pulp: An Analysis of Its Time-Dependent Behavior and the Effect of Temperature. *J. Biol. Phys.* **2018**, *44*, 557–577. [CrossRef] [PubMed]
54. Park, S.; Chung, M.-G.; Yoo, B. Effect of Octenylsuccinylation on Rheological Properties of Corn Starch Pastes. *Starch Stärke* **2004**, *56*, 399–406. [CrossRef]
55. Mohamed, A.A.; Alqah, H.; Alamri, M.S.; Hussain, S.; Qasem, A.A.; Ibraheem, M.I.; Yehia, H.M.; Shamlan, G. Physicochemical Properties of Enzymatically Modified Starches. *Processes* **2021**, *9*, 2251. [CrossRef]
56. Szwengiel, A.; Kubiak, P. Molecular Dispersion of Starch as a Crucial Parameter during Size-Exclusion Chromatography. *Foods* **2020**, *9*, 1204. [CrossRef] [PubMed]
57. Gidley, M.J.; Hanashiro, I.; Hani, N.M.; Hill, S.E.; Huber, A.; Jane, J.-L.; Liu, Q.; Morris, G.A.; Rolland-Sabaté, A.; Striegel, A.M.; et al. Reliable Measurements of the Size Distributions of Starch Molecules in Solution: Current Dilemmas and Recommendations. *Carbohydr. Polym.* **2010**, *79*, 255–261. [CrossRef]
58. Gilbert, R.G.; Gidley, M.J.; Hill, S.; Kilz, P.; Rolland-Sabaté, A.; Stevenson, D.G.; Cave, R.A. Characterizing the Size and Molecular Weight Distribution of Starch: Why It Is Important and Why It Is Hard. *Cereal Foods World* **2010**, *55*, 139–143. [CrossRef]
59. Lawal, M.V.; Odeniyi, M.A.; Itiola, O.A. Material and Rheological Properties of Native, Acetylated, and Pregelatinized Forms of Corn, Cassava, and Sweet Potato Starches. *Starch Stärke* **2015**, *67*, 964–975. [CrossRef]
60. Zhang, Y.; Huang, Z.; Yang, C.; Huang, A.; Hu, H.; Gong, Z.; Sun, G.; Huang, K. Material Properties of Partially Pregelatinized Cassava Starch Prepared by Mechanical Activation. *Starch Stärke* **2013**, *65*, 461–468. [CrossRef]
61. Szwengiel, A.; Kowalczewski, P.Ł.; Wielich, F.; Małyszek, Z.; Le Thanh-Blicharz, J.; Lewandowicz, G. Changes in the Rheological Properties and Structure of Potato Starch upon Hydrothermal Treatment. In Proceedings of the 15th International Conference on Polysaccharides-Glycoscience 2019, Prague, Czech Republic, 13–15 November 2019; Řápková, R., Hinková, A., Čopíková, J., Šárka, E., Eds.; Czech Chemical Society: Prague, Czech Republic, 2019; pp. 37–41.
62. López-Franco, Y.L.; Valdez, M.A.; Hernández, J.; Calderón de la Barca, A.M.; Rinaudo, M.; Goycoolea, F.M. Macromolecular Dimensions and Mechanical Properties of Monolayer Films of Sonorean Mesquite Gum. *Macromol. Biosci.* **2004**, *4*, 865–874. [CrossRef] [PubMed]
63. Wolff, D.; Czapla, S.; Heyer, A.G.; Radosta, S.; Mischnick, P.; Springer, J. Globular Shape of High Molar Mass Inulin Revealed by Static Light Scattering and Viscometry. *Polymer* **2000**, *41*, 8009–8016. [CrossRef]
64. Szwengiel, A.; Le Thanh-Blicharz, J.; Lewandowicz, G. Molecular Structure of Acetyleted Starches with Different Degree of Substitution. In Proceedings of the 13th International Conference on Polysaccharides-Glycoscience, Prague, Czech Republic, 8–11 November 2017; Řápková, R., Čopíková, J., Šárka, E., Eds.; Czech Chemical Society: Prague, Czech Republic, 2017; pp. 180–182.

65. Nilsson, L.; Bergenståhl, B. Adsorption of Hydrophobically Modified Anionic Starch at Oppositely Charged Oil/Water Interfaces. *J. Colloid Interface Sci.* **2007**, *308*, 508–513. [CrossRef] [PubMed]
66. Konował, E.; Sulej-Chojnacka, J.; Prochaska, K. New Derivatives of Modified Starch for Food Technology. *Molecules* **2024**, *29*, 3292. [CrossRef]
67. Zahn, S.; Otto, C.; Rohm, H. Laminar Flow Cleaning of Gelatinised, Partially Hydrolysed Starch. *Int. J. Food Sci. Technol.* **2020**, *55*, 769–775. [CrossRef]
68. Li, W.; Zhang, Z.; Wu, J.; Xu, Z.; Liu, Z. Phosphorylation/Caproylation of Cornstarch to Improve Its Adhesion to PLA and Cotton Fibers. *RSC Adv.* **2019**, *9*, 34880–34887. [CrossRef] [PubMed]
69. Wiącek, A.E.; Furmaniuk, A. Starch-Based Polysaccharide Systems with Bioactive Substances: Physicochemical and Wettability Characteristics. *Int. J. Mol. Sci.* **2024**, *25*, 4590. [CrossRef] [PubMed]
70. El Farkhani, M.; Dadou, S.; El Miz, Y.; Elyoussfi, A.; El Miz, M.; Salhi, A.; Koudad, M.; Benchat, N. A Review of the Chemical Modification and Applications of Starch. *BIO Web Conf.* **2024**, *109*, 01020. [CrossRef]
71. Acton, J.C.; Saffle, R.L. Stability of Oil-in-Water Emulsions. 1. Effects of Surface Tension, Level of Oil, Viscosity and Type of Meat Protein. *J. Food Sci.* **1970**, *35*, 852–855. [CrossRef]
72. Akmarov, K.A.; Lapshov, S.N.; Sherstobitova, A.S.; Yas'kov, A.D. Optical properties of aqueous solutions of dimethyl sulfoxide and application of refractometry for monitoring their composition. *J. Appl. Spectrosc.* **2013**, *80*, 610–614. [CrossRef]
73. Rusanov, A.I.; Prokhorov, V.A. *Studies in Interface Science*; Rusanov, A.I., Prokhorov, V.A., Eds.; Elsevier: Amsterdam, The Netherlands, 1996; Volume 3, ISBN 1383-7303.

Disclaimer/Publisher's Note: The statements, opinions and data contained in all publications are solely those of the individual author(s) and contributor(s) and not of MDPI and/or the editor(s). MDPI and/or the editor(s) disclaim responsibility for any injury to people or property resulting from any ideas, methods, instructions or products referred to in the content.

molecules

MDPI

Article

Exploring the Optical Properties of Carotenoid-Based Nanoparticles: The Role of Terminal Groups

Ryuju Suzuki [1,2,*], Keigo Kinoshita [3], Takeshi Miuchi [3], Masayuki Nishino [3], Yasuhiro Shimizu [3] and Shigeru Deguchi [1,*]

[1] Research Center for Bioscience and Nanoscience, Japan Agency for Marine-Earth Science and Technology (JAMSTEC), 2-15 Natsushima-cho, Yokosuka 237-0061, Japan
[2] Department of General Engineering, National Institute of Technology, Sendai College, 48 Nodayama, Medeshima-Shiote, Natori 981-1239, Japan
[3] San-Ei Gen F.F.I. Inc., 1-1-11 Sanwa-cho, Toyonaka 561-8588, Japan
* Correspondence: r-suzuki@sendai-nct.ac.jp (R.S.); shigeru.deguchi@jamstec.go.jp (S.D.)

Abstract: Carotenoids are increasingly used as naturally occurring food colorants. For application as beverage colorants, fat-soluble carotenoids are formulated into dispersion systems via nanoparticle (NP) formation. In recent years, the antioxidant properties of carotenoids have gained immense recognition for their preventive health benefits, thereby highlighting further interest in their development as functional food ingredients. Although functional carotenoids in dispersion-based formulations are desirable, knowledge regarding the structural and optical properties of NPs of carotenoids other than those of β-carotene, and methods to efficiently produce and compare NPs of various carotenoids, remain scarce. In this study, NPs of β-carotene, lycopene, astaxanthin, and lutein were prepared using a simple reprecipitation method, with a focus on understanding the variations in the molecular self-assembly influenced by the quality of solvent used during reprecipitation. This study presents the novel finding that the terminal groups of carotenoids significantly affect the intermolecular interactions, thereby altering the structural and optical properties of the resulting NPs. Our findings are expected to contribute to the development of new technologies for controlling the color of carotenoids based on the crystal structure of the NPs.

Keywords: carotenoids; nanoparticles; reprecipitation; color; chemical structure

1. Introduction

Vegetables and fruits develop vivid colors during ripening, which play a critical ecological role in their preservation. These colors attract predators and other species, facilitating seed dispersal [1,2]. Carotenoids, which are produced via the metabolism of chlorophyll during ripening, are one of the primary pigments responsible for coloration [3,4]. All carotenoid molecules possess a polyene chain comprising eight isoprenoid units, each with various terminal groups at the chain ends. The diversity of their terminal structures is vast; over 850 carotenoids have been identified in plants, animals, and microorganisms to date [5]. Because the structures of these terminal groups influence the optical properties of the carotenoid molecules [6,7], their structural diversity enables carotenoids to absorb light across the entire visible spectrum [8,9].

Hydrophobic carotenoid molecules were previously thought to be solubilized in the cell membranes [10,11]. However, research has revealed that carotenoids exist within the cytosol in the form of nanoparticles (NPs) [12,13], suggesting that the colors of ripe vegetables and fruits arise not from the carotenoid molecules themselves, but from the colors of their microcrystalline structures. Thus, the self-assembly of carotenoids and regulation of their aggregation states are vital components for the survival strategy of these plants.

In this context, Horn et al. conducted seminal studies on β-carotene NPs, which are widely used as a natural pigments in food products [14]. They prepared β-carotene NPs of various sizes via reprecipitation from isopropanol solutions of different concentrations, which exhibited hypsochromic shifts in their absorption spectra compared to the bulk crystals. Consequently, they exhibited a yellow hue, while the bulk crystals appeared red. This color shift was attributed to the differences in the molecular arrangement between the bulk crystals and NPs [15]. Subsequent studies have highlighted the pronounced influence of pH, temperature, and water content on the aggregation patterns of carotenoids in hydrated organic solvents [16,17]. Among these factors, the volume ratio of poor solvent (e.g., water) to good solvent (e.g., alcohol) is critical for controlling the molecular assembly of NPs, particularly for those prepared using the reprecipitation method introduced by Horn et al. [18]. Although precise control of the color tone is essential for the development of food colorants, knowledge of the aggregation state of carotenoids is limited, and the properties of carotenoid-based NPs are yet to be fully explored. Because minor structural variations in the carotenoid terminal groups can significantly affect the crystal structures [19–22], they can also influence the structures and optical properties of carotenoid-based NPs, thereby offering valuable insights into the ripening process of fruits and vegetables and the formation of carotenoid-based NPs.

Further exploration of carotenoids with different terminal groups has become increasingly important from a health-maintenance perspective. Carotenoids exhibit antioxidant activity by scavenging singlet oxygen and reactive radicals, thus indicating their role in preventing chronic diseases such as cardiovascular diseases, age-related macular degeneration, and cancer [23–26]. Consequently, in addition to β-carotene, compounds such as lycopene, astaxanthin, and lutein are gaining increasing attention as functional food ingredients with the potential for development into NP-based formulations. A straightforward method for producing and comparing NPs of various carotenoids is essential for the development of carotenoid-based NPs as functional food colorants. In this study, carotenoid-based NPs were prepared using the reprecipitation method, which is a simple approach for producing organic NPs, with tetrahydrofuran (THF) as the solvent. THF effectively dissolves a wide range of carotenoids at high concentrations, and is completely miscible with water. Carotenoids such as β-carotene, lycopene, astaxanthin, and lutein, were investigated for their potential use as functional food ingredients. Specifically, the effect of the water-to-THF volume ratio during reprecipitation, which is expected to influence the molecular self-assembly, on the structural and optical properties of carotenoid-based NPs was analyzed and discussed with respect to the terminal group structures.

2. Results and Discussion

2.1. Fabrication and Structural Analysis of the Carotenoid-Based NPs

The chemical structures of the four carotenoids used in this study are shown in Figure 1. Two of them, β-carotene and lycopene, are structural isomers classified as carotenes, which solely comprise hydrocarbons (Figure 1a). Astaxanthin and lutein are classified as xanthophylls and are distinguished by their terminal groups containing hydroxyl and/or ketone functionalities (Figure 1b).

The reprecipitation method used to obtain carotenoid-based NPs involved dissolving the carotenoids in THF to obtain 5 mM solutions. Using this method, NPs are successfully formed with a good solvent-to-poor solvent ratio of 1 to 2 vol% [27]. An aliquot (0.2 mL) of each carotenoid in THF was added to an excess volume (9.8 mL) of water under vigorous stirring to achieve a final THF concentration of 2 vol%. The carotenoid-based NPs formed immediately and remained well dispersed in water without the use of stabilizing agents (Figure 2). The particle diameters, as determined via dynamic light scattering (DLS), was approximately 30 nm for β-carotene and astaxanthin, 50 nm for lutein, and 100 nm for lycopene (Figure 3). Scanning electron microscopy (SEM) analysis revealed that although some agglomeration occurred owing to the drying process required for sample preparation, the primary particles of each carotenoid were generally consistent with the DLS

measurements (Figure 4a–d). We previously confirmed that carotenoid-based NPs prepared under similar conditions were spherical when investigated using cryo-transmission electron microscopy (cryo-TEM) [28].

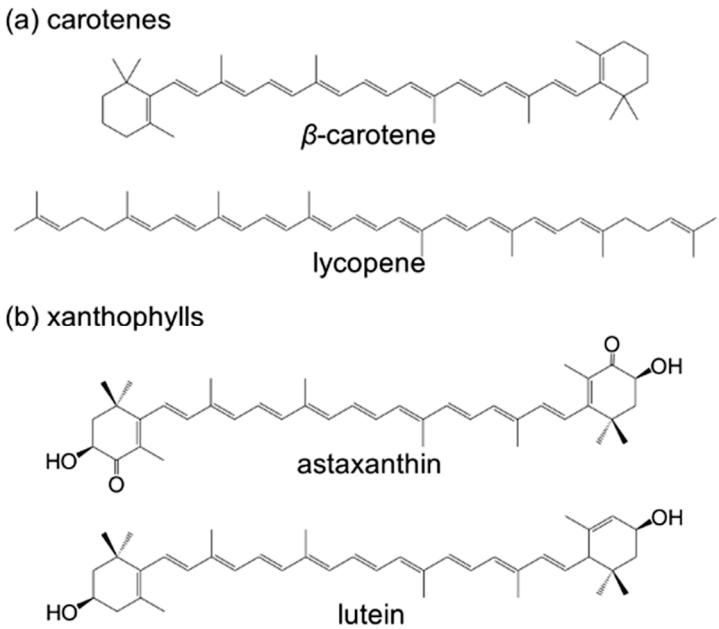

Figure 1. Chemical structures of the carotenoids: (**a**) β-carotene and lycopene (carotenes) and (**b**) astaxanthin and lutein (xanthophylls).

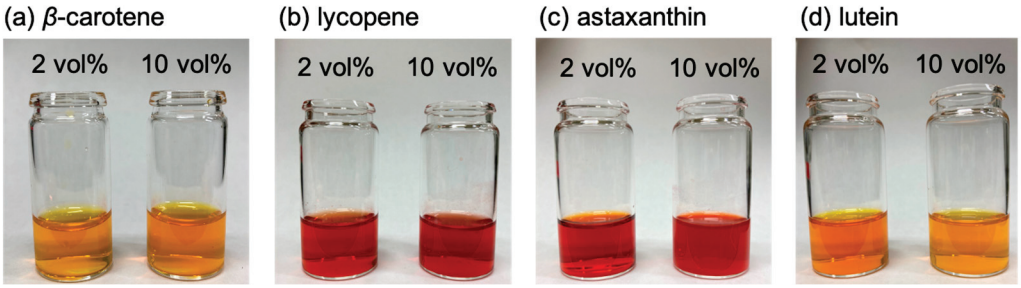

Figure 2. Nanoparticle (NP) dispersions of (**a**) β-carotene, (**b**) lycopene, (**c**) astaxanthin, and (**d**) lutein. The THF contents are (**left**) 2 and (**right**) 10 vol% in all the images.

The respective carotenoid-based NP dispersions in THF were prepared with final THF concentrations of 4, 6, 8, and 10 vol%. In a series of experiments, a solution of each carotenoid in THF was injected into a THF/water mixture rather than into pure water. THF in the mixture served to control the crystal growth rate during reprecipitation. The DLS results indicated that the sizes of the xanthophyll-based NPs (astaxanthin and lutein) increased with increasing THF content, whereas those of the carotene-based NPs (β-carotene and lycopene) showed no significant change (Figure 3). SEM images of the NPs obtained for a THF concentration of 10 vol% demonstrated that the carotene-based NPs maintained their shapes, as observed in the case of the 2 vol% samples, whereas the xanthophyll-based NPs exhibited well-developed facets (Figure 4e–h), which indicate that the NPs became more crystalline as THF content increased.

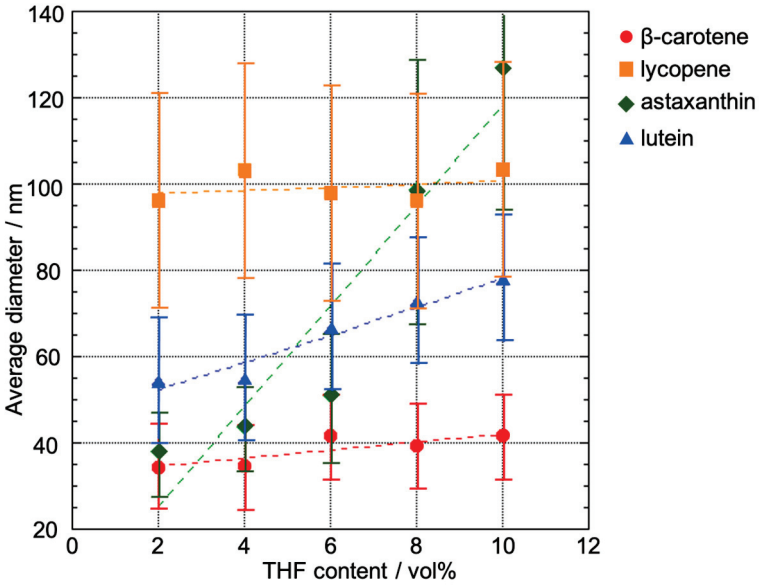

Figure 3. Relationship between the average size of the carotenoid-based NPs and the contents of THF used as a good solubilizing solvent in the reprecipitation method. The size of the NPs was measured by dynamic light scattering (DLS). Error bars show the size distribution.

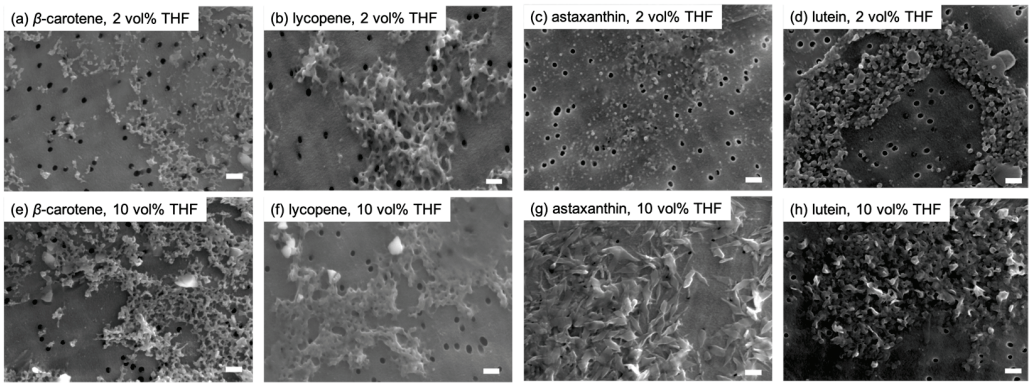

Figure 4. Scanning electron microscopy (SEM) images of the NPs of (**a**,**e**) β-carotene, (**b**,**f**) lycopene, (**c**,**g**) astaxanthin, and (**d**,**h**) lutein. The THF contents are (**a**–**d**) 2 and (**e**–**h**) 10 vol%. The black circles measuring 50 nm in diameter represent the pores of the filter membrane. Scale bars: 200 nm.

Powder X-ray diffraction (pXRD) patterns of each of the carotenoid-based NPs with THF concentrations of 2 and 10 vol% were recorded, which revealed that the XRD peaks of the xanthophyll-based NPs (astaxanthin and lutein) became clearly visible at a THF concentration of 10 vol%, indicating an increase in the crystallinity with increasing THF content (Figure 5). In contrast, the XRD peaks of the carotene-based NPs (β-carotene and lycopene) exhibited no discernible change, regardless of the THF content. The quality of the good solvent used during reprecipitation, i.e., the solubility of the target compound and its compatibility with water as a poor solvent, significantly influences the size and morphology of the resulting NPs [29]. Generally, the NP size is governed by the nucleation process, with a high degree of supersaturation favoring nucleation over crystal growth, thus resulting in the formation of smaller NPs [30]. In the present study, the solubility of xanthophylls in polar THF was higher than that of carotenes because of the presence of polar ketones and/or terminal hydroxyl groups in them. These findings suggest that an increase in the amount of THF reduces the degree of supersaturation in xanthophylls, thereby slowing the crystal growth and leading to the formation of larger and more crystalline NPs.

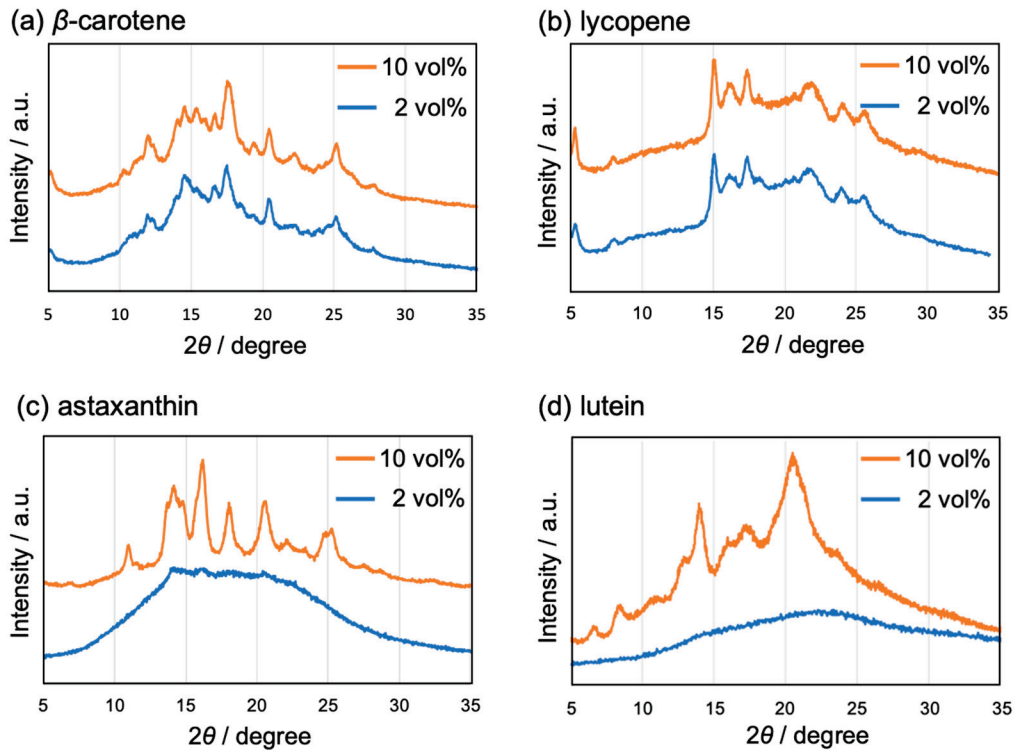

Figure 5. Powder X-ray diffraction (pXRD) patterns of the NPs of (**a**) β-carotene, (**b**) lycopene, (**c**) astaxanthin, and (**d**) lutein. The THF contents are 2 (blue line) and 10 vol% (orange line).

Carotenoid-based NPs obtained via reprecipitation exhibit a structure with a crystalline core and a surrounding amorphous shell [24]. The changes in the XRD patterns of the xanthophyll-based NPs (astaxanthin and lutein) with respect to the THF content possibly reflect a shift in the ratio of the crystalline to amorphous domains within the particles. Moreover, this variation in crystallinity influenced the conformation of the carotenoid molecules that formed these domains. Specifically, carotenoid molecules in amorphous regions are prone to molecular distortions such as rotations of the terminal rings, which were analyzed using Raman spectroscopy. A peak corresponding to the C=C stretching vibration of the polyene chain, known as ν_1, appeared at approximately 1520 cm^{-1}. It is well known that this peak shifts depending on the effective π-conjugation length of the polyene chain [31]. The shape of the ν_1 peak of the carotene-based NPs (β-carotene and lycopene) showed no significant change regardless of the THF content (Figure 6a,b). Conversely, for the xanthophyll-based NPs (astaxanthin and lutein), the ν_1 peak of the 10 vol% THF sample showed a reduced full width at half maximum (FWHM) and shifted towards lower wavenumbers compared to that of the 2 vol% THF sample (Figure 6c,d).

These peak shifts possibly reflect the changes in the proportions of the distorted molecules. Specifically, the smaller the strain of the carotenoid molecule, the longer the effective π-conjugation length, resulting in the shifting of the ν_1 peak towards a lower wavenumber [31]. In our previous study, the ν_1 peak of NPs was broader compared to that of the molecules in solution or the bulk crystals because NPs contain both distorted and undistorted molecules [28]. The proportion of molecules with varying degrees of distortions was successfully determined from the ratio of the crystalline to amorphous domains present within each carotenoid NP. The Raman spectra of the xanthophyll-based NPs (astaxanthin and lutein) indicate that the increased crystallinity with a higher THF content leads to a shift of the ν_1 peak towards a low wavenumber because the number of distorted molecules decreases and the proportion of less distorted molecules increases. The ν_1 peak did not exhibit any shift with increasing THF content in the Raman spectra of the carotene-based NPs (β-carotene and lycopene), which can be explained by the absence of any change in the degree of crystallinity. Notably, while pH can affect the structure of NPs

formed via the reprecipitation method [16,17], its influence was not a factor in this study, as the pH of the carotenoid NP dispersions did not change with the different THF contents.

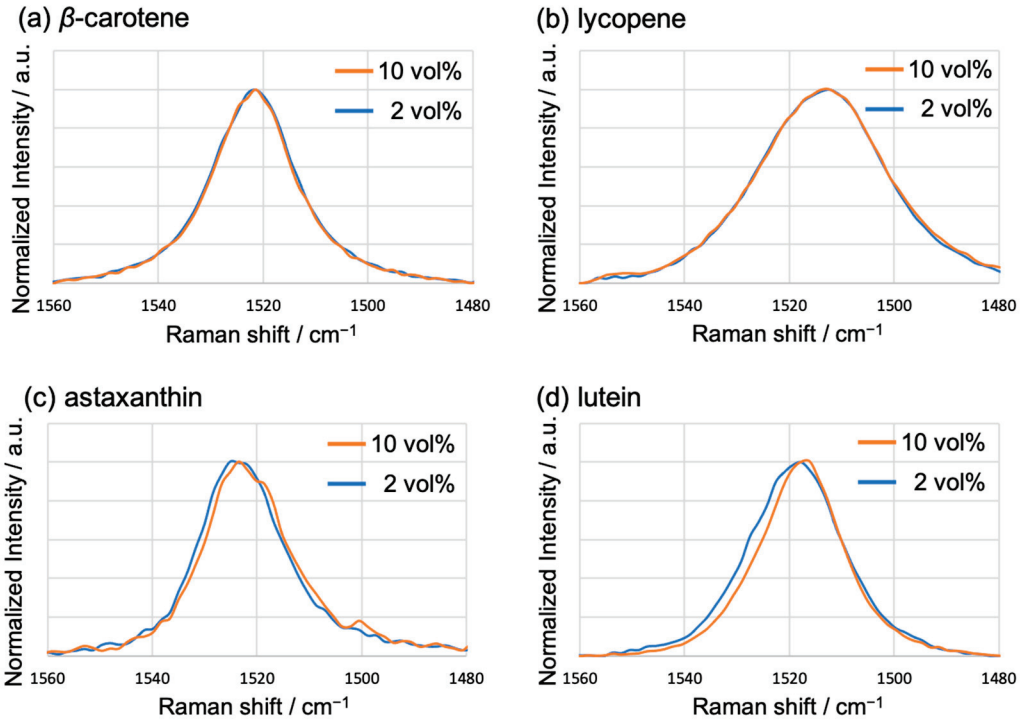

Figure 6. Raman spectra of the NPs of (**a**) β-carotene, (**b**) lycopene, (**c**) astaxanthin, and (**d**) lutein, displaying the ν_1 peak corresponding to the C=C stretching vibration. The THF contents are 2 (blue line) and 10 vol% (orange line).

2.2. Optical Properties of the Carotenoid-Based NPs

The UV-Vis absorption spectra of the carotenoid-based NPs are shown in Figure 7. In all cases, the NPs exhibited distinctly different spectra from those of the corresponding solution states. Moreover, the absorption spectra of the carotenoid-based NPs demonstrated distinctly different patterns among themselves with varying THF concentrations.

Such absorption spectral changes in carotenoids are often classified based on the aggregate type: H- and J-aggregates [19–22]. The H-aggregates exhibit a significant blue shift and a loss of vibrational structure owing to the closely packed arrangement of parallel molecules, commonly referred to as "card-pack" aggregates, in the absorption spectrum of NPs compared to that of the corresponding monomer (i.e., the solution-state spectrum). This major spectral shift is driven by excitonic interactions between the polyene chains of the carotenoid molecules. In contrast, J-aggregates consist of loosely aligned molecules in a "head to tail" arrangement, and red shifts are observed in the absorption spectrum of NPs compared to the corresponding monomer spectrum. A similar explanation can be applied to the absorption spectra of the as-prepared carotenoid-based NPs based on the type of aggregates present.

When the THF content was varied, the absorption spectra of the carotene-based NPs (β-carotene and lycopene) exhibited significant changes, despite structural analyses using XRD (Figure 5a,b) and Raman spectroscopy (Figure 6a,b) showing no significant differences. In the case of the β-carotene NPs, it has been proposed that the NPs contain multiple small self-assemblies comprising hundreds to thousands of molecules. Horn et al. also proposed a structure in which small self-assemblies coexist with amorphous domains in gelatin-protected β-carotene NPs and discussed their absorption spectra [18]. The absorption spectra of β-carotene NPs showed a decrease in the intensity of the peak obtained at 412 nm with increasing THF content, while those of the peaks at 470 nm and 510 nm increased (Figure 7a). The peak at 412 nm was attributed to the H-aggregates, whereas those at

470 and 510 nm corresponded to the J-aggregates [17]. Therefore, the spectral changes indicated a decrease in H-aggregates and an increase in J-aggregates with increasing THF content. Within a single β-carotene NP, both H- and J-aggregates coexist within the microscopic self-assembly, and their ratio is expected to vary with the THF content.

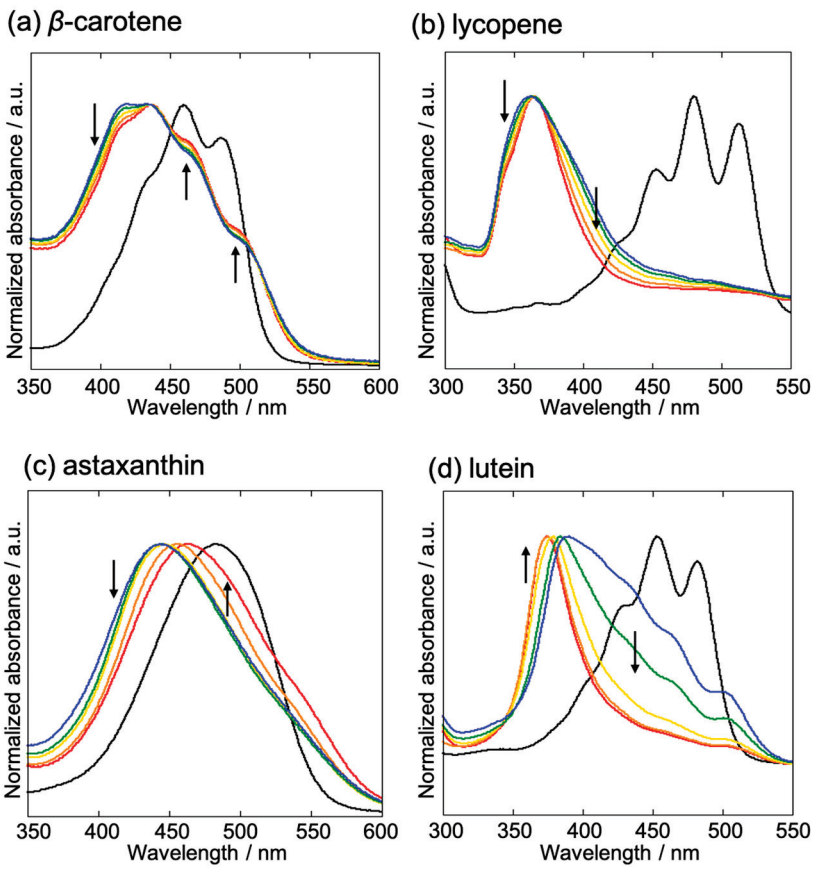

Figure 7. UV-vis absorbance spectra of (**a**) β-carotene, (**b**) lycopene, (**c**) astaxanthin, and (**d**) lutein. Each spectrum was recorded by varying the amount of THF used in the reprecipitation method, that is, 2 (blue), 4 (green), 6 (yellow), 8 (orange), and 10 (red) vol%. The direction of the arrow indicates the shift in the absorption spectrum with increasing THF content (2 vol% to 10 vol%). The black lines represent the spectra obtained for the respective carotenoids dissolved in pure THF.

The absorption spectrum of the lycopene NPs lacked a vibrational structure and exhibited the peak maximum at approximately 366 nm for a THF content of 2 vol%, indicating a significant shift compared to the corresponding solution-state spectrum (Figure 7b). This suggests that the NPs predominantly comprised H-aggregates. In addition, the spectral half-width decreased as the THF content increased. Molecular simulations suggest that H-aggregates tend to exhibit narrower linewidths in their absorption spectra when their assemblies are more ordered [19]. In other words, a greater molecular ordering implies a close packing of the molecules, increased self-assembly, and reduced number of aggregates. In these structures, several molecules are excited cooperatively, resulting in narrower spectral linewidths. These findings suggest that the rate of crystal growth in lycopene-based NPs during reprecipitation was moderated by an increase in the THF content, thereby resulting in the formation of more ordered H-aggregates.

β-carotene and lycopene are structural isomers with the molecular formula $C_{40}H_{56}$. However, in the case of β-carotene, the amount of H-aggregates decreased with increasing THF content, while that of the more loosely assembled J-aggregates increased. In contrast, lycopene formed more ordered H-aggregates with increasing THF content. This difference can be attributed to the presence or absence of sterically hindering terminal rings. Carotenes,

solely comprising hydrocarbons, stabilize their aggregates via π–π stacking interactions between the conjugated polyene chains. The presence of terminal rings twists the planar polyene chain, thereby weakening the π–π stacking between adjacent alkene chains [20]. This terminal-ring effect was also evident in the NPs. Lycopene predominantly formed H-aggregates because the absence of terminal rings allowed highly planar molecules to interact closely. Conversely, the introduction of terminal rings into β-carotene possibly inhibited the formation of tightly bound H-aggregates, thus promoting stabilization via the formation of weakly coupled J-aggregates. Notably, although changes in the absorption spectra with varying THF content were observed, they were subtle and did not alter the visible color of the dispersion to the naked eye (Figure 2).

The position and/or shape of the absorption bands of the xanthophyll-based NPs (astaxanthin and lutein) were significantly affected by the addition of varying amounts of THF (Figure 7c,d) in contrast to those of the carotene-based NPs. The absorbance band of the astaxanthin NPs observed at 442 nm for a THF content of 6 vol% or less red-shifted to 458 nm when the THF content exceeded 8 vol% (Figure 7c). Notably, the size of the astaxanthin NPs also increased when the THF content exceeded 8% (Figure 3), presumably because the higher THF concentration affected the degree of supersaturation and the kinetics of NP formation. Furthermore, increasing the THF content affected not only the size of the astaxanthin NPs, but also their crystallinity (Figure 5c). The changes in the absorption spectra of the astaxanthin NPs can also be attributed to molecular self-assembly. Because xanthophylls contain hydroxyl groups in the terminal ring, hydrogen bonding should be considered a factor that influences aggregate formation. It has been previously suggested that hydrogen bonds play a minor role in self-assembly [21]. Presumably, the terminal ring also contains keto groups in addition to hydroxyl groups, which increase steric hindrance and inhibit π–π stacking between the polyene chains. At a lower THF content, the absorption bands appeared at shorter wavelengths, indicating the formation of H-aggregates. Under these conditions (6 vol% or less), the NPs exhibited an amorphous-like structure, suggesting that the H-aggregates in astaxanthin are metastable. Conversely, at higher THF contents, the absorption spectrum exhibited a red shift, implying the formation of J-aggregates. NPs with a high crystallinity were obtained under these conditions (>8 vol%), indicating that the J-aggregates are thermodynamically stable structures.

Interestingly, lutein NPs exhibited opposite spectral behavior to that of astaxanthin NPs with varying THF content (Figure 7d). The spectrum of lutein NPs with a final THF concentration of 2 vol% showed the peak maximum at 388 nm, with dominant vibrational structures in the longer-wavelength region. These vibrational structures disappeared and the peak maximum experienced a significant blue shift to approximately 370 nm when lutein NPs were prepared with a higher THF content (>8 vol%). Notably, visible changes in the color of the dispersion were observed with the naked eye, which became lighter as the THF content increased (Figure 2d). Lutein is known to predominantly form H-aggregates because of the strong hydrogen-bonding interactions between its hydroxyl groups [22]. Similar to the astaxanthin NPs, the lutein NPs exhibited increased crystallinity at higher THF contents (Figure 5d). However, the H-aggregates were predominant in the lutein crystals. The blue shift in the absorption spectrum and disappearance of the vibrational structure indicate that densely packed H-aggregates were formed within the crystal. As the THF content decreased, the NPs became more amorphous, suggesting that the H-aggregates were loosely packed. Previous studies have suggested that when the H-aggregates of lutein become loosely packed, vibrational structures appear with a red shift in the absorption spectrum [22]. Notably, unlike the vibrational structure observed in the absorption spectrum of β-carotene NPs, the spectrum of lutein NPs does not result from the formation of J-aggregates.

By comparing the four carotenoids, it was found that the molecular structure of the carotenoid end groups influences intermolecular interactions via two key structural factors: steric hindrance and hydrogen bonding. In turn, these affect the aggregates formed and the spectral properties of the carotenoid-based NPs. Specifically, the ratio of H-aggregates to J-

aggregates appeared to vary sensitively with THF content during reprecipitation. Hydrogen bonding between the hydroxyl groups plays a crucial role in promoting the formation of H-aggregates, thereby ensuring close packing between the carotenoid molecules, as observed in the case of lutein. When lutein molecules become loosely packed due to environmental changes, they attempt to maintain H-aggregate structures despite peak shifts observed in the absorption spectrum. Conversely, some carotenoids transition to J-aggregates in response to other structural factors within their terminal rings. Steric hindrance in the terminal ring is a significant structural factor in J-aggregate formation, as observed in the case of astaxanthin, which tends to shift towards J-aggregate formation as the H-aggregates disintegrate. This steric effect is also observed in the case of carotenes that lack hydroxyl groups. For instance, lycopene, which lacks terminal rings, exhibits predominant π–π stacking between polyene chains, facilitating H-aggregate formation. However, β-carotene, with its bulky terminal rings, experiences steric hindrance that prevents H-aggregate formation, causing H-aggregates to collapse and J-aggregates to dominate. Although the prediction of NP aggregation structures solely from chemical structures is challenging because of the interplay between hydrogen bonding and steric hindrance, the reprecipitation method used in this study is a simple and versatile approach for experimentally evaluating the NP structures and optical properties of a wide range of carotenoids, many of which have significant potential for future functional applications.

3. Materials and Methods

3.1. Materials

All carotenoids (β-carotene, lycopene, astaxanthin, and lutein) were provided by San-Ei Gen F.F.I, Inc. (Osaka, Japan). THF was purchased from FUJIFILM Wako Pure Chemical Corporation (Osaka, Japan). All other reagents were commercially available and used without further purification. Water was purified to a resistance of 18.2 MΩ·cm using a PURELAB flex3 system (ELGA LabWater, Buckinghamshire, UK).

3.2. Fabrication of the Carotenoid-Based NPs

NPs in this study were prepared using the reprecipitation method [23]. Briefly, the carotenoids were separately dissolved in THF. Each solution (5 mM, 0.2 mL) was rapidly injected into vigorously stirred water (9.8 mL), which resulted in the formation of four distinct types of carotenoid-based NPs. The final THF concentration was 2 vol%. For the NP dispersions with varying THF contents (4, 6, 8, and 10 vol%), a THF/water mixture containing the desired amount of THF was used instead of pure water.

3.3. Characterization of the Carotenoid-Based NPs

The NP powders were deposited onto polycarbonate membranes via filtration (Whatman® Nucleopore Track-Etched Membranes, Sigma-Aldrich, St. Louis, MO, USA), and the sizes and morphologies of the resulting NPs were assessed using SEM (JSM-6700F, JEOL, Tokyo, Japan). DLS measurements were performed using a dynamic light scattering spectrophotometer (FPAR-1000, Otsuska Electronics Co., Ltd., Osaka, Japan). The pXRD patterns were obtained using an X-ray diffractometer (D8 ADVANCE, Bruker, Karlsruhe, Germany). Resonance Raman spectra of the NP powders were recorded using a Raman spectrophotometer (DXR, Thermo Fisher Scientific, Waltham, MA, USA, laser wavelength = 532 nm). The UV/Vis absorption spectra were recorded using a UV-Vis spectrometer (V-570, JASCO, Tokyo, Japan).

4. Conclusions

The influence of the terminal structure of carotenoid molecules on the structural and optical properties of their corresponding NPs was thoroughly investigated. The reprecipitation method employed in this study enabled the fabrication of uniform NPs of four distinct carotenoids (β-carotene, lycopene, lutein, and astaxanthin). This comparative analysis revealed that the properties of carotenoid-based NPs varied depending on the

terminal groups of the base carotenoid molecules. This was demonstrated by adjusting the amount of THF, which was used as the good solubilizing solvent during the NP fabrication process. In particular, the crystallinity of xanthophylls (astaxanthin and lutein), containing ketones and hydroxyl groups, increased with increasing THF content, leading to changes in particle size and shape. This variation in crystallinity altered the ratio of H-aggregates to J-aggregates in the xanthophyll-based NPs, which in turn affected their absorption spectrum. In contrast, for carotenes (β-carotene and lycopene) composed solely of hydrocarbons, changes in the absorption spectrum with THF content were observed despite no discernible structural changes in the XRD patterns or Raman spectra. This behavior, similar to that of xanthophylls, was attributed to changes in the self-assembly of carotene molecules. The self-assembly of carotenoids is influenced by two key factors: π–π interactions between polyene chains and hydrogen bonding in hydroxyl groups. This study concludes that the terminal groups of carotenoids are closely associated with each factor, thereby governing the structural and optical properties of carotenoid-based NPs. This significant discovery indicates the potential for controlling the color tone of various carotenoids and serves as the foundation for developing methods to regulate the colors of carotenoid-based NP dispersions, which are expected to be employed in future functional food applications. Moreover, this study accelerates the evaluation of the physical properties of NPs derived from a wide range of carotenoids. Our group is currently elucidating the detailed structures and coloration mechanisms of carotenoid-based NPs, and we will report our findings in due course.

Author Contributions: Conceptualization, R.S. and S.D.; methodology, R.S.; validation, R.S. and K.K.; formal analysis, R.S.; resources, K.K., T.M., M.N. and Y.S.; writing—original draft preparation, R.S.; writing—review and editing, R.S. and S.D.; visualization, R.S.; supervision, R.S. and S.D.; project administration, M.N.; funding acquisition, M.N., Y.S. and S.D. All authors have read and agreed to the published version of the manuscript.

Funding: This work was supported by the Adaptable and Seamless Technology Transfer Program through the target-driven R&D (A-STEP) (grant number: JPMJTR164B) from the Japan Science and Technology Agency (JST).

Institutional Review Board Statement: Not applicable.

Informed Consent Statement: Not applicable.

Data Availability Statement: The original contributions presented in the study are included in the article and further inquiries can be directed to the corresponding author.

Conflicts of Interest: Authors Keigo Kinoshita, Takeshi Miuchi are employees, and Masayuki Nishino, Yasuhiro Shimizu are part of the management team at the company San-Ei Gen F.F.I. Inc. The remaining authors declare that the research was conducted in the absence of any commercial or financial relationships that could be construed as a potential conflict of interest.

References

1. Lomáscolo, S.B.; Schaefer, H.M. Signal Convergence in Fruits: A Result of Selection by Frugivores? *J. Evol. Biol.* **2010**, *23*, 614–624. [CrossRef] [PubMed]
2. Puckey, H.L.; Lill, A.; O'Dowd, D.J. Fruit Color Choices of Captive Silvereyes (*Zosterops lateralis*). *Condor* **1996**, *98*, 780–790. [CrossRef]
3. Alboresi, A.; Dall'Osto, L.; Aprile, A.; Carillo, P.; Roncaglia, E.; Cattivelli, L.; Bassi, R. Reactive Oxygen Species and Transcript Analysis upon Excess Light Treatment in Wild-Type Arabidopsis Thaliana vs. a Photosensitive Mutant Lacking Zeaxanthin and Lutein. *BMC Plant Biol.* **2011**, *11*, 62. [CrossRef] [PubMed]
4. Havaux, M. Carotenoid Oxidation Products as Stress Signals in Plants. *Plant J.* **2014**, *79*, 597–606. [CrossRef] [PubMed]
5. Maoka, T. Carotenoids as Natural Functional Pigments. *J. Nat. Med.* **2020**, *74*, 1–16. [CrossRef]
6. Koyama, Y.; Kuki, M.; Andersson, P.O.; Gillbro, T. Singlet Excited States and the Light-Harvesting Function of Carotenoids in Bacterial Photosynthesis. *Photochem. Photobiol.* **1996**, *63*, 243–256. [CrossRef]
7. Mimuro, M.; Nagashima, U.; Nagaoka, S.I.; Takaichi, S.; Yamazaki, I.; Nishimura, Y.; Katoh, T. Direct Measurement of the Low-Lying Singlet Excited (2^1Ag) State of a Linear Carotenoid, Neurosporene, in Solution. *Chem. Phys. Lett.* **1993**, *204*, 101–105. [CrossRef]

8. Gordon, H.T.; Bauernfeind, J.C.; Furia, T.E. Carotenoids as Food Colors. In *Carotenoids as Colorants and Vitamin A Precursors: Technological and Nutritional Applications*; Bauernfeind, J.C., Ed.; Elsevier Inc.: Philadelphia, PA, USA, 1981; pp. 47–317.
9. Polívka, T.; Frank, H.A.; Enriquez, M.M.; Niedzwiedzki, D.M.; Liaaen-Jensen, S.; Hemming, J.; Helliwell, J.R.; Helliwell, M. X-ray Crystal Structure and Time-Resolved Spectroscopy of the Blue Carotenoid Violerythrin. *J. Phys Chem. B* **2010**, *114*, 8760–8769. [CrossRef]
10. Chandrika, U.G.; Jansz, E.R.; Wickramasinghe, S.M.D.N.; Warnasuriya, N.D. Carotenoids in Yellow- and Red-Fleshed Papaya (*Carica papaya* L.). *J. Sci. Food Agric.* **2003**, *83*, 1279–1282. [CrossRef]
11. Ebert, G.; Gross, J. Carotenoid Changes in the Peel of Ripening Persimmon (Diospyros Kaki) Cv Triumph. *Phytochemistry* **1985**, *24*, 29–32. [CrossRef]
12. Egea, I.; Barsan, C.; Bian, W.; Purgatto, E.; Latché, A.; Chervin, C.; Bouzayen, M.; Pech, J.C. Chromoplast Differentiation: Current Status and Perspectives. *Plant Cell Physiol.* **2010**, *51*, 1601–1611. [CrossRef] [PubMed]
13. Schweiggert, R.M.; Steingass, C.B.; Heller, A.; Esquivel, P.; Carle, R. Characterization of Chromoplasts and Carotenoids of Red- and Yellow-Fleshed Papaya (*Carica papaya* L.). *Planta* **2011**, *234*, 1031–1044. [CrossRef] [PubMed]
14. Horn, D.; Lüddecke, E. Preparation and Characterization of Nano-Sized Carotenoid Hydrosols. In *Fine Particles Science and Technology*; Pelizzetti, E., Ed.; Springer: Dordrecht, The Netherlands, 1996; pp. 761–775.
15. Auweter, H.; Haberkorn, H.; Heckmann, W.; Horn, D.; Lüddecke, E.; Rieger, J.; Weiss, H. Supramolecular Structure of Precipitated Nanosize β-Carotene Particles. *Angew. Chem. Int. Ed.* **1999**, *38*, 2188–2191. [CrossRef]
16. Billsten, H.H.; Sundström, V.; Polívka, T. Self-Assembled Aggregates of the Carotenoid Zeaxanthin: Time-Resolved Study of Excited States. *J. Phys. Chem. A* **2005**, *109*, 1521–1529. [CrossRef] [PubMed]
17. Lu, L.; Wu, J.; Wei, L.; Wu, F. Temperature Dependence of Aggregated Structure of β-Carotene by Absorption Spectral Experiment and Simulation. *Spectrochim. Acta Part A* **2016**, *169*, 116–121. [CrossRef]
18. Horn, D.; Rieger, J. Organic Nanoparticles in the Aqueous Phase—Theory, Experiment, and Use. *Angew. Chem. Int. Ed.* **2001**, *40*, 4330. [CrossRef]
19. Hempel, J.; Schädle, C.N.; Leptihn, S.; Carle, R.; Schweiggert, R.M. Structure Related Aggregation Behavior of Carotenoids and Carotenoid Esters. *J. Photochem. Photobiol. A.* **2016**, *317*, 161–174. [CrossRef]
20. Köhn, S.; Kolbe, H.; Korger, M.; Köpsel, C.; Mayer, B.; Auweter, H.; Lüddecke, E.; Bettermann, H.; Martin, H.-D. Aggregation and Interface Behaviour of Carotenoids. In *Carotenoids*; Britton, G., Liaaen-Jensen, S., Pfander, H., Eds.; Birkhäuser Basel: Basel, Switzerland, 2008; Volume 4, pp. 53–98, ISBN 978-3-7643-7498-3.
21. Köpsel, C.; Möltgen, H.; Schuch, H.; Auweter, H.; Kleinermanns, K.; Martin, H.-D.; Bettermann, H. Structure Investigations on Assembled Astaxanthin Molecules. *J. Mol. Struct.* **2005**, *750*, 109–115. [CrossRef]
22. Lu, L.; Liu, Y.; Wei, L.; Wu, F.; Xu, Z. Structures and Exciton Dynamics of Aggregated Lutein and Zeaxanthin in Aqueous Media. *J. Lumin.* **2020**, *222*, 117099. [CrossRef]
23. Barros, L.; Ferreira, M.-J.; Queirós, B.; Ferreira, I.C.F.R.; Baptista, P. Total Phenols, Ascorbic Acid, β-Carotene and Lycopene in Portuguese Wild Edible Mushrooms and Their Antioxidant Activities. *Food Chem.* **2007**, *103*, 413–419. [CrossRef]
24. Nakazawa, Y.; Sashima, T.; Hosokawa, M.; Miyashita, K. Comparative Evaluation of Growth Inhibitory Effect of Stereoisomers of Fucoxanthin in Human Cancer Cell Lines. *J. Funct. Foods* **2009**, *1*, 88–97. [CrossRef]
25. Stinco, C.M.; Rodríguez-Pulido, F.J.; Escudero-Gilete, M.L.; Gordillo, B.; Vicario, I.M.; Meléndez-Martínez, A.J. Lycopene Isomers in Fresh and Processed Tomato Products: Correlations with Instrumental Color Measurements by Digital Image Analysis and Spectroradiometry. *Food Res. Int.* **2013**, *50*, 111–120. [CrossRef]
26. Holzapfel, N.; Holzapfel, B.; Champ, S.; Feldthusen, J.; Clements, J.; Hutmacher, D. The Potential Role of Lycopene for the Prevention and Therapy of Prostate Cancer: From Molecular Mechanisms to Clinical Evidence. *Int. J. Mol. Sci.* **2013**, *14*, 14620–14646. [CrossRef] [PubMed]
27. Kasai, H.; Nalwa, H.S.; Oikawa, H.; Okada, S.; Matsuda, H.; Minami, N.; Kakuta, A.; Ono, K.; Mukoh, A.; Nakanishi, H. A Novel Preparation Method of Organic Microcrystals. *Jpn. J. Appl. Phys.* **1992**, *31*, L1132–L1134. [CrossRef]
28. Suzuki, R.; Yasuhara, K.; Deguchi, S. Effect of Molecular Distortion on the Optical Properties of Carotenoid-Based Nanoparticles. *J. Phys. Chem. C* **2022**, *126*, 2607–2613. [CrossRef]
29. Wakayama, Y.; Mitsui, T.; Onodera, T.; Oikawa, H.; Nakanishi, H. Growth Mechanism and Size Effect on Fluorescence Properties of Perylene Nanocrystals. *e-J. Surf. Sci. Nanotechnol.* **2006**, *4*, 69–73. [CrossRef]
30. Mullin, J.W. *Crystallization*, 4th ed.; Butterworth Heinemann: Oxford, UK, 2001; pp. 423–426.
31. Merlin, J.C. Resonance Raman Spectroscopy of Carotenoids and Carotenoid-Containing Systems. *Pure Appl. Chem.* **1985**, *57*, 785–792. [CrossRef]

Disclaimer/Publisher's Note: The statements, opinions and data contained in all publications are solely those of the individual author(s) and contributor(s) and not of MDPI and/or the editor(s). MDPI and/or the editor(s) disclaim responsibility for any injury to people or property resulting from any ideas, methods, instructions or products referred to in the content.

MDPI AG
Grosspeteranlage 5
4052 Basel
Switzerland
Tel.: +41 61 683 77 34

Molecules Editorial Office
E-mail: molecules@mdpi.com
www.mdpi.com/journal/molecules

Disclaimer/Publisher's Note: The title and front matter of this reprint are at the discretion of the Guest Editors. The publisher is not responsible for their content or any associated concerns. The statements, opinions and data contained in all individual articles are solely those of the individual Editors and contributors and not of MDPI. MDPI disclaims responsibility for any injury to people or property resulting from any ideas, methods, instructions or products referred to in the content.

Academic Open
Access Publishing

mdpi.com

ISBN 978-3-7258-8774-3